Universiteit Leiden
The Netherlands

Photoinduced processes in dye-sensitized photoanodes under the spotlight: a multiscale in silico investigation

Menzel, J.P.

Citation

Menzel, J. P. (2022, March 3). *Photoinduced processes in dye-sensitized photoanodes under the spotlight: a multiscale in silico investigation*. Retrieved from https://hdl.handle.net/1887/3278038

Version:	Publisher's Version
License:	Licence agreement concerning inclusion of doctoral thesis in the Institutional Repository of the University of Leiden
Downloaded from:	https://hdl.handle.net/1887/3278038

Note: To cite this publication please use the final published version (if applicable).

Photoinduced Processes in Dye-Sensitized Photoanodes under the Spotlight: A Multiscale *in Silico* Investigation

Proefschrift

ter verkrijging van
de graad van doctor aan de Universiteit Leiden,
op gezag van rector magnificus prof.dr.ir. H. Bijl,
volgens besluit van het college voor promoties
te verdedigen op donderdag 3 maart 2022
klokke 16:15 uur

door

Jan Paul Menzel
geboren te Bonn, Duitsland
in 1992

Promotor:	Prof. dr. Huub J.M. de Groot	Universiteit Leiden
Copromotor:	Dr. Francesco Buda	Universiteit Leiden

Promotiecommissie

Voorzitter:	Prof. dr. Hermen S. Overkleeft	Universiteit Leiden
Secretaris:	Prof. dr. Sylvestre A. Bonnet	Universiteit Leiden
Overige Leden:	Dr. Jörg Meyer	Universiteit Leiden
	Prof. dr. Claudia Filippi	Universiteit Twente
	Prof. dr. Lucas Visscher	Vrije Universiteit Amsterdam

Jan Paul Menzel
Photoinduced Processes in Dye-Sensitized Photoanodes under the Spotlight: A Multiscale *in Silico* Investigation
PhD. Thesis, Leiden

Cover and Bookmark designed by Anna Knörlein and Jan Paul Menzel
Printed by ProefschriftMaken

This research was performed at the Biophysical Organic Chemistry/ Solid State NMR group of the Leiden Institute of Chemistry. The work was funded by the Netherlands Organization for Scientific Research (NWO) within the Solar to Products program, grant number 733.000.007. The use of supercomputing facilities at SURFsara was sponsored by NWO Physical Sciences with financial support from NWO.

To my parents and Anna

Table of Contents

Abbreviations **5**

Chapter 1: General Introduction **9**

1.1 Solar Energy – Beyond Fossil Fuels 11

1.2 Natural and Artificial Photosynthesis 12

1.3 Dye-Sensitized Photoelectrochemical Cells 16

1.4 Aim of the Thesis and Outline 20

1.5 References 23

Chapter 2: Theoretical Background and Computational Methods **29**

2.1 The Born-Oppenheimer Approximation and Beyond 31

Non-adiabaticity and Resonant Coupling between Nearly Degenerate Electronic States and Nuclear Vibrations 35

2.2 Density Functional Theory 40

Linear Response Time Dependent DFT 43

2.3 Semi-Empirical Tight Binding Methods 45

Hückel Theory and Extended Hückel Theory 45

Density Functional Based Tight Binding 48

Geometry, Frequency, Noncovalent, eXtended Tight Binding 50

2.4 Adiabatic Ab Initio Molecular Dynamics 52

2.5 Nonadiabatic Molecular Dynamics 53

Ehrenfest Dynamics 55

AO-MO Quantum Propagation 57

2.6 References 63

Chapter 3: Understanding Coherent Charge Transfer 67

3.1 Introduction 69

3.2 Computational Methods 70

3.3 Results and Discussion 72

Photoinduced Electron Transfer and Vibronic Coupling 72

Isotope Effect 75

Dynamic Symmetry Breaking 77

Similarities with other Adiabatic Passage Processes 80

Exchange of Angular Momentum 81

3.4 Conclusion 84

3.5 References 85

3.A Appendix 88

Chapter 4: Photoinduced Electron Injection in a Fully Solvated Photoanode 99

4.1 Introduction 101

4.2 Computational Methods 106

General Procedure 106

Constructing the Photoanode 107

Generating Nuclear Trajectories 109

Electron Transfer Dynamics 111

4.3 Results and Discussion 112

Nuclear Dynamics 112

Electron Injection Properties of Anchoring Molecules 114

Electron Injection Properties of Core-Extended NDI Dyes with Different Anchoring Groups 123

4.4 Conclusion 126

4.5 References 128

4.A Appendix 133

Chapter 5: Semi-Empirical Investigation of a Water Oxidation Catalyst.....153

5.1 Introduction 155

5.2 Computational Methods 159

DFT-based Simulations.....159

GFN-xTB-based Simulations 160

Thermodynamic Computational Investigations at pH=0.....160

Comparison to Experimental Oxidation Potentials at pH=1.....161

GFN-xTB + DFT Approach for Free Energy Calculations.....163

5.3 Results 164

Energetically Preferred Spin States 164

Relative Gibbs Free Energies along the Catalytic Cycle.....165

Preferred Reaction Mechanism.....167

Relative Gibbs Free Energy using GFN-xTB+DFT 167

Comparison to Experimental Oxidation Potentials 170

5.4 Conclusion.....173

5.5 References 174

5.A Appendix 178

Chapter 6: *In Silico* Optimization of Charge Separating Dyes.....185

6.1 Introduction 187

6.2 Computational Methods 196

General Procedure.....196

GFN-xTB-based Molecular Dynamics.....196

Optimization of Extended Hückel Parameters.....197

Determination of Relevant Excitations 198

Charge Transfer Dynamics.....198

6.3 Results 200

Changing the Driving Force:

TPA-FLU-PMI vs EDG-TPA-FLU-PMI Dye.....201

DPA vs TPA Donor 203

Increasing the Bridge Length 204
Decoupling the Fragments 206
In Silico Optimization of Charge Separating Dyes 208
6.4 Conclusion 209
6.5 References 211
6.A Appendix 215

Chapter 7: Conclusions and Outlook 227
7.1 Conclusions 229
7.2 Outlook 232
Charge Transfer in a Photocatalytic WOC-Dye Complex 232
Simulating Charge Transfer in a Full Photoanode System 235
7.3 References 238
7.A Appendix 240

Summary 243

Samenvatting 247

Zusammenfassung 251

List of Publications 255

Curriculum Vitae 257

Acknowledgements 259

List of Abbreviations

ACC	Acceptor
ADF	Amsterdam Density Functional (*program*)
ADP	Adenosine Diphosphate
AIMD	Ab Initio Molecular Dynamics
ALDA	Adiabatic Linear Density Approximation (*XC kernel*)
AMS	Amsterdam Modelling Suite (program)
AO	Atomic Orbital
ATP	Adenosine Triphosphate
Ben-NDI	Benzoic acid-based core extended Naphthalene Diimide dye
BJ	Becke-Johnson (*type of damping function for D3 dispersion corrections*)
BLYP	Becke, Lee-Yang-Parr (*XC functional*)
BOA	Born-Oppenheimer Approximation
BOMD	Born-Oppenheimer Molecular Dynamics
B3LYP	Becke, 3-parameter, Lee-Yang-Parr (*XC functional*)
CAM-B3LYP	Coulomb Attenuating Method – B3LYP (*XC functional*)
Cat-NDI	Catechol-based core extended Naphthalene Diimide dye
CB	Conduction Band
COSMO	Conductor-like Screening Model (*implicit solvent model*)
CT	Charge Transfer
CTD	Charge Transfer Dynamics
CV	Cyclic Voltammetry
DCM	Dichloromethane
DFT	Density Functional Theory
DFT-D3	DFT with D3 dispersion corrections
DFTB	Density Functional based Tight Binding
DNA	Deoxyribonucleic Acid (chap 3)
DON	Donor
DOS	Density Of States
DPA	Diphenylamine
DS-PEC	Dye Sensitized Photoelectrochemical Cell
DSSC	Dye Sensitized Solar Cell
DZP	Double Zeta with one Polarization function (*basis set*)
D3	*Type of Dispersion corrections*

EDG	Electron Donating Group
EH	Extended Hückel
ET	Electron Transfer
ETD	Electron Transfer Dynamics
FC	Franck Condon
FLU	Fluorene
FLUMe	Methylated Fluorene
FT	Fourier Transform
GBSA	Generalized Born accessible Surface Area model (*implicit solvent model*)
GFN-xTB	Geometry, Frequency, Non-covalent Interactions Extended Tight Binding
GGA	Generalized Gradient Approximation
HEC	Hydrogen Evolution Catalyst
HEG	Homogeneous Electron Gas
HOMO	Highest Occupied Molecular Orbital
Hyd-NDI	Hydroxamic acid-based core extended Naphthalene Diimide dye
ISC	Intersystem Crossing
I2M	Interaction of two Metal oxo species
LC	Long-range Corrected
LDA	Local Density Approximation
LR-TDDFT	Linear Response Time Dependent Density Functional Theory
LUMO	Lowest Unoccupied Molecular Orbital
MCTDH	Multi Configurational Time Dependent Hartree
MD	Molecular Dynamics
MO	Molecular Orbital
$NADP^+$/NADPH	Nicotinamide Adenine Dinucleotide Phosphate
NAMD	Non Adiabatic Molecular Dynamics
NCAP	Nonadiabatic Conversion via Adiabatic Passage
NDI	Naphthalene Diimide
NHE	Normal Hydrogen Electrode
NMR	Nuclear Magnetic Resonance
OEC	Oxygen Evolving Complex
OPBE	Optimized exchange Perdew-Burke-Ernzerhof (*XC functional*)
PBE	Perdew-Burke-Ernzerhof (*XC functional*)

PCET	Proton Coupled Electron Transfer
PDOS	Partial Density Of States
PEM	Proton Exchange Membrane
PMI	Perylene-Monoimide
PMIMe	Methylated PMI
PSI	Photosystem I
PSII	Photosystem II
rev-DOD-BLYP	Revised, Dispersion corrected, constrained, Double hybrid-BLYP (*XC functional*)
rev-DOD-PBE	Revised, Dispersion corrected, constrained, Double hybrid-PBE (*XC functional*)
rev-DOD-PBEP86	Revised, Dispersion corrected, constrained, Double hybrid-PBEP86 (*XC functional*)
ROC	Radical Oxo Coupling
SCC-DFTB	Self-Consistent Charge Density Functional based Tight Binding
SCM	Software for Chemistry and Materials (*company*)
SPH	Single Point Hessian
STO	Slater Type Orbital
TD-DFT	Time Dependent Density Functional Theory
TEMPO	2,2,6,6-Tetramethylpiperidine 1-oxyl
TPA	Triphenylamine
TPAMe	Methylated TPA
TZP	Triple Zeta with one Polarization function (*basis set*)
VB	Valence Band
VDOS	Vibrational Density Of States
WNA	Water Nucleophilic Attack
WOC	Water Oxidation Catalyst
XC	Exchange Correlation
ZORA	Zero-Order Regular Approximation (*model for relativistic effects*)
ZPE	Zero Point Energy
ΔSCF	Delta Self Consistent Field (*method to estimate ionization potential*)

CHAPTER 1

General Introduction

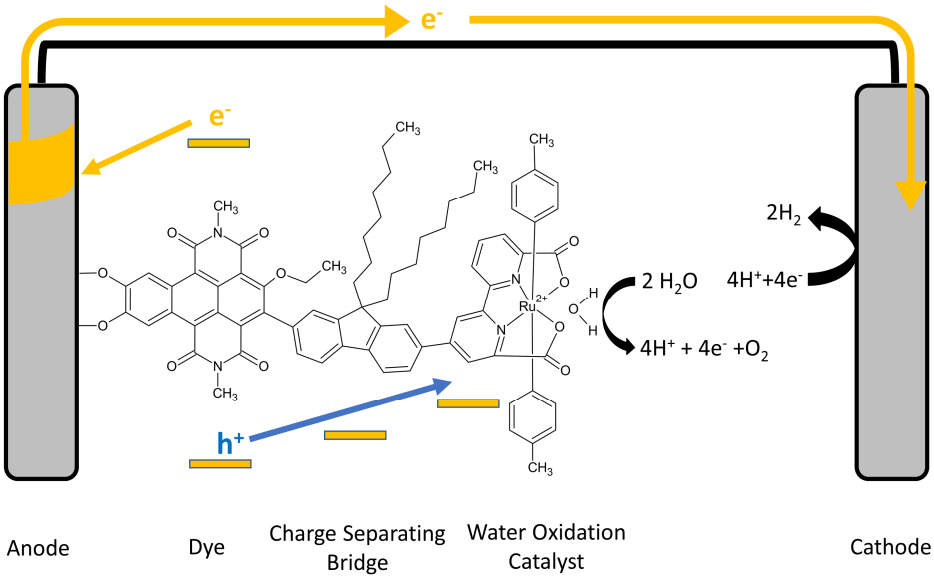

1

In this introductory chapter, the general context of this thesis is presented. The disadvantages of fossil fuels and their influence on climate change is laid out, underlining the need for alternative renewable energy sources, in particular solar based fuels. Natural solar fuel production in the form of photosynthesis is discussed, and the concept of artificial photosynthesis inspired by it is introduced. Dye-Sensitized Photoelectrochemical Cells (DS-PECs) devices are discussed, underlining the parallels with the natural photosynthetic machinery. To design efficient DS-PECs, certain requirements for the properties of all the different components involved should be achieved. The aim of this work is to use computational simulations to guide the optimization of the different components in a dye-sensitized photoanode with respect to their properties and interfaces, to fulfil the requirements laid upon each respective module. Finally, an outline of this thesis is given, discussing how these problems are tackled in this work.

1.1 Solar Energy – Beyond Fossil Fuels

The industrial revolution has increased with accelerating pace global productivity, life expectancy and global population over the last 150-200 years. This massive increase has however been fueled mainly by the unsustainable exploitation of fossil energy resources and synthetic fertilizers obtained through the energy intensive Haber-Bosch process.[1–3] With a growing population[4,5], global food and energy demand are still further increasing,[6–9] while the supply of fossil fuels remains limited.[10,11] In addition, the CO_2 waste released in the burning of carbon based fuels has been directly linked to increasing global average temperatures and climate change.[12–14] Finding renewable energy solutions is therefore one of the main challenges humanity has to tackle.

There are several candidates for renewable energy sources. Wind, hydro and tidal power can be used to generate electricity, with the first two having been used as energy supply since millennia,[15,16] however, they are unevenly accessible around the globe. By far the largest energy source available to us is the star of our planetary system, the sun. Solar irradiation is readily accessible on most places on the globe, though unevenly distributed and time dependent.[17–19] It is almost inexhaustible and provides a manifold of the energy needs that humanity is expected to have in the near future.[20,21]

Renewable energy is already a rapidly increasing part of the energy mix produced and consumed around the globe.[22] In the form of solar and wind farms, these sources of energy are used to generate electricity. However, there are drawbacks with converting solar and wind energy into electricity. Due to the seasonal and spatial difference in supply and demand of these power sources, storage is important to provide a reliable energy supply. Unfortunately, the conversion of electric energy to a more readily stored form is always accompanied by significant losses. One possible way of energy storage is in the form of chemical bonds. The direct synthesis of desirable chemical compounds through sun light is a powerful tool to generate clean

fuels that can be used to balance the production of renewables with their demand. A relatively simple chemical fuel that could be produced is molecular hydrogen.[23–25]

Hydrogen can be produced by electrochemical water splitting, also releasing oxygen in the process. When using a photovoltaic cell, the produced hydrogen would be carbon-neutral being synthesized using solar power.[26] However, a more direct process of generating hydrogen directly from sun light would be preferable.[27,28]

Hydrogen gas is already used as an energy carrier, but most of the hydrogen is obtained from natural gas, usually with a steam reforming process that is contributing to increasing green-house gas emissions.[29] When producing hydrogen as a solar fuel, CO_2-neutral hydrogen could be used in a large variety of circumstances as a clean energy source. It could also decrease the carbon foot print of the Haber-Bosch process, where even a small reduction would have a huge impact due to the massive scale of this energy intensive chemical reaction that accounts for about 1-2% of the global energy consumption.[30]

Using the solar irradiation to power chemical fuel synthesis directly without the detour of electricity generation is a promising way of producing carbon-neutral, energy rich solar fuels to feed the increasing global energy demand.

1.2 Natural and Artificial Photosynthesis

The manufacturing of energy rich chemical fuels from solar energy is a process that has been performed by plants and other photosynthetic organisms since billions of years.[31] The earliest photosynthetic organisms obtained the electrons necessary from other reductants such as H_2S and even H_2 rather than from water.[32] Oxygenic photosynthesis, where the needed electrons are gained by splitting water into oxygen, protons and electrons, has been associated with the emergence of cyanobacteria,[33,34] but recent studies revealed a more complex picture and the origin of oxygenic photosynthesis is still an active field of ongoing research.[35,36]

In oxygenic photosynthesis, energy rich, carbon based molecular compounds such as carbohydrates are produced from oxygen, water and carbon dioxide under the

influence of sun light.[37] The series of consecutive photoexcitation, charge separation and redox reactions is commonly known as Z-scheme,[38] due to the shape of the energetic diagram as seen in figure 1.1.

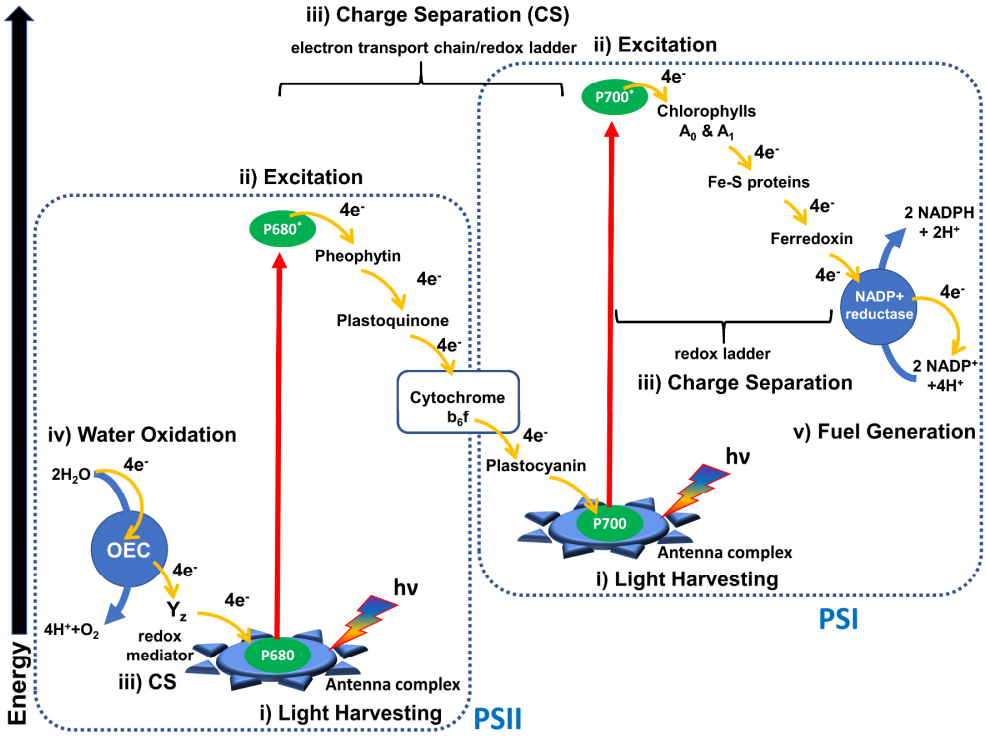

Figure 1.1. Schematic representation of the photosynthetic machinery: Light is harvested by the antenna complexes of the two Photosystems PSI and PSII. The excitation energy is collected at the chlorophyll dimers P680 and P700, where the excited electrons are transferred to the cofactors. The charge transfer state is stabilized by separating the electrons from the holes in a charge separation process (CS) via the electron transport chain and ultimately used by the $NADP^+$-reductase to generate NADPH. The hole is used by the Oxygen Evolving Complex (OEC), to split water into oxygen, electrons and protons.

The photosynthetic machinery contains two photoactive, dye-protein complexes, known as photosystems (PS) I and II, respectively. These protein assemblies contain antenna complexes that are responsible for capturing and collecting incoming photons through molecular chromophores, such as chlorophyll and carotenoids.[39,40]

The excitation energies of these chromophores are tuned by the protein environment, so that the energy of the absorbed photon is transferred coherently in the form of excitons towards the central part of the photosystem, the reaction center.[41] This coherent exciton migration is also found in the simplest light harvesting systems, chlorosomes.[42–44] Finally, at the reaction center of the PS, the exciton energy is used to photoexcite an electron in a chlorophyll *a* molecular dimer that, depending on its excitation wave length, is called P680 in PSII and P700 in PSI. The photoexcited electron is then transferred to a neighboring cofactor leading to a charge separated state, in a process that is facilitated and stabilized by specific nuclear motions.[45,46] Experimental and theoretical evidence suggest that resonances between nuclear and electronic motion play an important role in the photoinduced electron transfer in the reaction center as well.[47–53]

The hole left in the P680 at the reaction center of PSII is filled by an electron donated from the OEC[54] and obtained by splitting water into oxygen, protons and electrons as given in equation 1.1.

$$2H_2O \xrightarrow{h\upsilon} O_2 + 4\,H^+ + 4e^- \tag{1.1}$$

The photoexcited electron is further separated from the hole and the PSII through a series of consecutive electron transfer steps involving redox mediators embedded in the thylakoid membrane, regenerating the ground state of PSII.[55] (see Figure 1.1) This fast electron transfer is needed to spatially separate hole and electron and thus to prevent charge recombination during the relatively slow hole transfer and water splitting reaction steps. Electronic energy is thereby sacrificed to stabilize the charge separated state.[56] The electron then fills a hole generated by the photoexcitation of PSI. The photoexcited electron is then donated, through a smaller electron transfer chain, to the $NADP^+$ reductase, which reduces $NADP^+$ and protons to NADPH. NADPH and ATP, that is gained through the chemical potential gradient of H^+ between lumen and stroma as well the released energy by the electron transport chain, are then used in the dark reaction as reductant and energy supplier respectively. Equation 1.1 should therefore rather be described by

$$2H_2O + 2\ NADP^+ + 3\ ADP + 3\ P_i \xrightarrow{h\nu} O_2 + 2\ (NADPH + H^+) + 3\ ATP \qquad (1.2)$$

where P_i corresponds to a phosphate equivalent (PO_4^{3-}). This is also called the light reaction. As mentioned before, NADPH and ATP are then used in the dark reaction to reduce CO_2 into energy rich carbohydrates. For the example of glucose, the total chemical equation of oxygenic photosynthesis then becomes[57]

$$6CO_2 + 6H_2O \xrightarrow{h\nu} C_6H_{12}O_6 + 6O_2 \qquad (1.3)$$

For each oxygen molecule generated, at least 8 photons have to be absorbed to transfer the needed 4 electrons from water to $NADP^+$.[58]

Even though the evolutionary history of oxygenic photosynthesis has not been completely revealed, it is clear that its emergence has led to an incredible change of the terrestrial environment and ecosystem. The waste product oxygen that was released by the photosynthetic organisms into the oceans was first subdued by coprecipitation with iron ions to form oxides in the shape of banded iron formations.[59] However, after saturation of this buffering system, the released oxygen lead to a huge spike in first solvated and then atmospheric oxygen that lead to a mass extinction event called the Great Oxygen Catastrophe.[60,61]

We live on a planet that has been deeply shaped by the changes due to this event: It led to the high oxygen atmosphere and the emergence of new organisms that use oxygen for respiration.[62–65] The importance of oxygenic photosynthesis can therefore not be overstated. All of the fossil fuel we use now, has its origin in oxygenic photosynthesis performed hundreds of millions of years ago, removing CO_2 from the atmosphere.[66] If we want to generate carbon neutral chemical fuels, we need to find efficient ways of copying this process and use solar energy to directly generate the desired compounds in the form of artificial photosynthesis. To produce artificial solar fuels, two general pathways can be taken: (i) in an indirect approach, a photovoltaic cell can be coupled to an electrolyzer to use the generated electricity to split water in oxygen and the fuel hydrogen; or (ii) a direct, integrative approach can

be used where without the detour of electricity production, the photoexcited electron can be used for reduction of *e.g.* protons to hydrogen or carbon dioxide or carbon monoxide to methanol or even hydrocarbons, while the hole is used for water oxidation.

If we look at the photosynthetic machinery in a modular way, we can split it in several different components responsible for the following processes:

i) Light harvesting – antenna complexes around or associated with PSI and PSII

ii) Photoinduced excitation - P680→P680* and P700→P700* dyes

iii) Charge separation – electron transport chain/redox ladders/redox mediator

iv) Water oxidation – Oxygen Evolving Complex (OEC)

v) Fuel generation – $NADP^+$-reductase

In figure 1.1, the different processes and their respective modules are marked.

For an effective artificial photosynthesis device, it is of advantage to keep this modular approach and design components specialized in a specific function and as efficient as possible while also optimizing the interfaces between them. Each of these components can then be adapted towards the needs of the artificial photosynthesis device, dependent on reactants, products and materials involved.

1.3 Dye-Sensitized Photoelectrochemical Cells

One possible artificial photosynthesis device that has attracted much interest in recent years are Dye-Sensitized Photoelectrochemical Cells (DS-PECs).[67,68,27,69–71] A schematic of a tandem DS-PEC can be seen in figure 1.2. In DS-PECs, a semiconductor electrode, such as anatase TiO_2, is sensitized with a molecular chromophore able to absorb energy in the visible light range. The photoexcited dye at the photoanode then injects the excited electron into the Conduction Band (CB) of the semi-conductor.[72–75] The electron is transferred through an external circuit to the cathode. The hole left at the dye is then transferred to a suitable water oxidation

catalyst (WOC), which extracts electrons from water through water oxidation, regenerating the dye's ground state.[69,76–78] The released protons diffuse through a Proton Exchange Membrane (PEM) towards the cathode, where, together with the electron, fuel generation takes place via reduction of the protons through a Hydrogen Evolution Catalyst (HEC).[27] In tandem DS-PECs, this is coupled to another photoexcitation of a dye on the cathode side.[28,79]

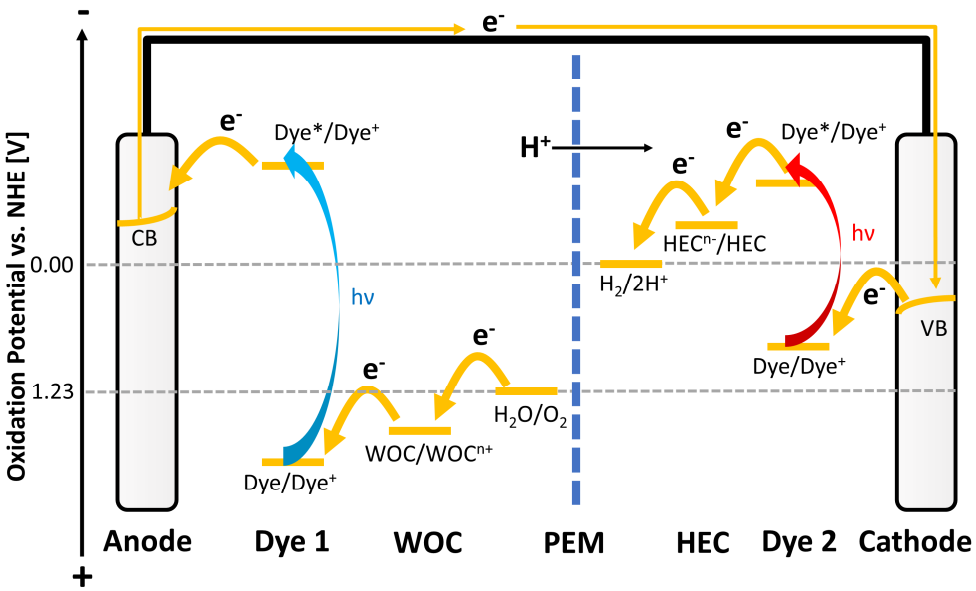

Figure 1.2. Schematic representation of a Dye-Sensitized Photo Electrochemical Cell (DS-PEC). The Photoexcited dye at the anode injects an electron into the conduction band of the electrode, which is used on the cathode side for hydrogen evolution. The hole is used by a molecular Water Oxidation Catalyst (WOC) to oxidize water, under release of oxygen and protons. The protons diffuse via a Proton Exchange Membrane (PEM) towards the cathode to be used for hydrogen evolution.

The efficiency of DS-PECs are closely linked to the optimal choice of components, their energetic alignment and their arrangement, which should favor charge separation and hinder recombination.[80,81] This holds especially true due to the large time mismatch between electron injection and water oxidation.[73] To optimize the overall process, it is of advantage to separate the DS-PEC into different modules

specialized in performing specific processes, using the same modular separation as present in natural photosynthesis (see figures 1.1 and 1.3).

A molecular dye/photosensitizer is used to absorb photons, getting photoexcited in the process.

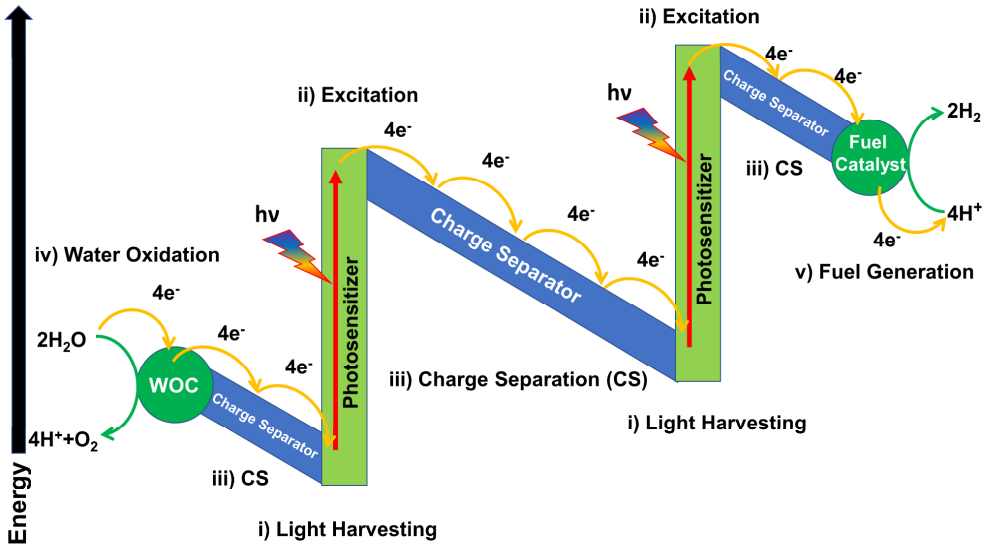

Figure 1.3. Schematic diagram of a tandem DS-PEC, showing the parallels to the z-scheme in natural photosynthesis: Light is harvested by the two photosensitizers/dyes (*i*), resulting in photoexcitation of the dyes (ii). The excited electrons are separated from the holes via charge separators (*iii*). The holes are used by a molecular WOC to oxidize water (*iv*), the electrons are ultimately used to reduce protons to hydrogen (*v*).

Since there is no commonly used additional module for light harvesting in DS-PECs, a dye needs to be an efficient light absorber in the visible light range. Large spatial charge separation can be achieved via different approaches. In the simplest DS-PECs, the separation is performed by the semiconductor electrodes, as the photoinjected electron relaxes from the band state it was injected in, to the conduction band edge, which is generally a bulk state away from the surface due to band bending. The electron is further removed by transfer to the other half-cell, the (photo)cathode. Adding further charge separators between different modules can

decrease the recombination rate: This can be done *e.g.* via molecular or redox shuttle approaches, using redox partners in the electrolyte to remove the hole from the dye, such as iodide, ferrocene, $Fe(ClO_4)_2$ or 2,2,6,6-tetramethylpiperidine 1-oxyl (TEMPO).[82–85] In a redox shuttle, however, this separation is typically non-directional, even though approaches for launching the shuttle away from the electrode exist, and back transfer still plays a large role due to the bottle neck of diffusion.[86] Several different molecular approaches can be taken:

i) implementing an energetic gradient by using either a chain of dye molecules with tuned Highest Molecular Orbital (HOMO) and Lowest Unoccupied Molecular Orbital (LUMO) energies to favor a separation of electron and hole or a push-pull dye, *ii*) inclusion of an effective barrier for either the electron or hole, by using molecular moieties with either significantly lower HOMO or higher LUMO energies or a molecular rectifier.[87–90]

Water oxidation takes place in a molecular, homogeneous transition metal-based water oxidation catalyst (WOC). This catalyst can either be bound covalently to the dye or semiconductor interface, or in solution with redox shuttles carrying the charges between photooxidized dye and WOC.

The last step, the fuel generation, takes place at the cathode. It can involve proton reduction as in figure 1.2, or *e.g.* CO_2 reduction.[71,91] This can either be driven purely electrochemically using the electrons obtained from the photoanode and their potential or can include a second photoactivation in a so-called tandem cell, mirroring the Z-scheme in natural photosynthesis. In this project we focus mainly on the processes occurring at the photoanode of a DS-PEC device.

Successful integration of the respective modules also involves the minimization of overpotential. To achieve this, three key requirements need to be fulfilled: i) to prevent back transfer and/or fluorescence, the charge separated states in the process need to be stabilized, ii) for the catalysis to proceed, overpotential for both the WOC as well as the fuel generating catalyst need to be supplied to drive their respective

chemical reactions, iii) due to the release of oxygen and hydrogen, free energy needs to be supplied for the device to run at the thermoneutral voltage.[92,93]

As mentioned above, requirement i) is often achieved by a chain of electron transfer events, where free energy is sacrificed to spatially separate hole and electron. Requirement ii) depends on the choice of catalyst, while requirement iii) corresponds to an additional 0.25 V (1.48 V vs. 1.23 V) at standard conditions.[93] Keeping losses low and still meeting these requirements demands optimal energetic alignment between the different components, while supplying enough excess energy through the excitation of the dyes with light still in the visible range. Fulfilling these demands to increase device efficiency is a challenging task of finding and integrating suitable molecular modules.

1.4 Aim of the Thesis and Outline

The production of chemical fuels from solar energy is a non-trivial task and stands or falls on both the efficiency of the single modules, but also on the optimal combination and integration of the different modules to one another. Computational simulations can be a powerful tool to design and optimize different components *in silico* to help finding promising candidates and combinations before tedious and expensive trial and error synthesis. This remains the main goal of this thesis.

However, the large variety of the involved processes demands for a wide range of computational methods. In this thesis, several diverse computational methods are employed to tackle this wide variety of chemical and physical challenges. Therefore, in chapter 2 these methods and their theoretical background are laid out and explained.

The 3rd chapter deals with the fundamental process of photoinduced charge transfer in a donor-acceptor supramolecular complex. The role of non-adiabatic coupling between nuclear and electronic motion and coherence effects is investigated. We have been able to reveal in detail how vibrational-electronic resonances facilitate the photoinduced electron transfer. Investigations of isotope

effects on the charge transfer process show how appropriate nuclear modes are selected, while dynamic symmetry breaking proves crucial for the coherent interconversion between excitonic and charge transfer state. Our simulations further emphasize the convergence of time scales between nuclear and electronic motion and angular momentum transfer between electronic and nuclear degrees of freedom.

In chapter 4, real time simulations of photoexcited electron and hole in a dye-sensitized photoanode reveal the process of electron injection into the semiconductor electrode. Both, a core extended napthalene diimide (NDI) based dye with three different anchoring moieties as well as the three anchoring molecules themselves are tested regarding their electron injection properties. Using a quantum-classical semi-empirical approach, our simulations of photoinduced electron injection within these large extended systems with full explicit solvation reveal that nuclear dynamics and trajectory averaging prove crucial in a realistic simulation of the electron injection process. Furthermore, the effect of an explicit description of the electrolyte on the electron transfer dynamics is revealed.

Chapter 5 deals with the water oxidation and introduces a computationally efficient method to investigate the catalytic cycle in a water oxidation catalyst. We introduce a novel workflow that combines Density Functional Theory (DFT) and the tight binding approach GFN-xTB to obtain reliable free-energy differences at a highly reduced computational cost.

In chapter 6, focus is laid on the spatial separation of photoexcited electron and hole via charge separating push-pull dyes and how to optimize them. It includes a study on the effect of electron donating and withdrawing properties of the push system in these interesting organic molecules. Furthermore, a systematic theoretical investigation dissects the influence of bridge length, additional phenyl groups and decoupling through sterically challenging ligands on the charge separation capabilities. These results were applied in an *in silico* optimization of such a charge separating dye, improving the charge separation efficiency significantly.

In chapter 7, an outlook is given on a system combining the components to form a full dye-sensitized Photoanode in a DS-PEC with the inclusion of the light harvesting and charge transfer component (an NDI based dye) and hole transfer to a covalently bound water oxidation catalyst.

1.5 References

(1) Smil, V. Detonator of the Population Explosion. *Nature* **1999**, *400* (6743), 415–415. https://doi.org/10.1038/22672.

(2) Carfora, A.; Pansini, R. V.; Scandurra, G. The Causal Relationship between Energy Consumption, Energy Prices and Economic Growth in Asian Developing Countries: A Replication. *Energy Strategy Reviews* **2019**, *23*, 81–85. https://doi.org/10.1016/j.esr.2018.12.004.

(3) Wrigley, E. A. Energy and the English Industrial Revolution. *Philosophical Transactions of the Royal Society A: Mathematical, Physical and Engineering Sciences* **2013**, *371* (1986), 20110568. https://doi.org/10.1098/rsta.2011.0568.

(4) Daly, H. E. Population, Migration, and Globalization. *ECOLOGICAL ECONOMICS* **2006**, 4.

(5) Fess, T. L.; Kotcon, J. B.; Benedito, V. A. Crop Breeding for Low Input Agriculture: A Sustainable Response to Feed a Growing World Population. *Sustainability* **2011**, *3* (10), 1742–1772. https://doi.org/10.3390/su3101742.

(6) Wirsenius, S.; Azar, C.; Berndes, G. How Much Land Is Needed for Global Food Production under Scenarios of Dietary Changes and Livestock Productivity Increases in 2030? *Agricultural Systems* **2010**, *103* (9), 621–638. https://doi.org/10.1016/j.agsy.2010.07.005.

(7) Edelenbosch, O. Y.; Kermeli, K.; Crijns-Graus, W.; Worrell, E.; Bibas, R.; Fais, B.; Fujimori, S.; Kyle, P.; Sano, F.; van Vuuren, D. P. Comparing Projections of Industrial Energy Demand and Greenhouse Gas Emissions in Long-Term Energy Models. *Energy* **2017**, *122*, 701–710. https://doi.org/10.1016/j.energy.2017.01.017.

(8) van Ruijven, B. J.; De Cian, E.; Sue Wing, I. Amplification of Future Energy Demand Growth Due to Climate Change. *Nat Commun* **2019**, *10* (1), 2762. https://doi.org/10.1038/s41467-019-10399-3.

(9) Semieniuk, G.; Taylor, L.; Rezai, A.; Foley, D. K. Plausible Energy Demand Patterns in a Growing Global Economy with Climate Policy. *Nat. Clim. Chang.* **2021**, *11* (4), 313–318. https://doi.org/10.1038/s41558-020-00975-7.

(10) Armaroli, N.; Balzani, V. Towards an Electricity-Powered World. *Energy Environ. Sci.* **2011**, *4* (9), 3193–3222. https://doi.org/10.1039/C1EE01249E.

(11) Capellán-Pérez, I.; Mediavilla, M.; de Castro, C.; Carpintero, Ó.; Miguel, L. J. Fossil Fuel Depletion and Socio-Economic Scenarios: An Integrated Approach. *Energy* **2014**, *77*, 641–666. https://doi.org/10.1016/j.energy.2014.09.063.

(12) Crowley, T. J.; Berner, R. A. CO2 and Climate Change. *Science* **2001**, *292* (5518), 870–872. https://doi.org/10.1126/science.1061664.

(13) Solomon, S.; Plattner, G.-K.; Knutti, R.; Friedlingstein, P. Irreversible Climate Change Due to Carbon Dioxide Emissions. *PNAS* **2009**, *106* (6), 1704–1709. https://doi.org/10.1073/pnas.0812721106.

(14) Howarth, R. W.; Santoro, R.; Ingraffea, A. Methane and the Greenhouse-Gas Footprint of Natural Gas from Shale Formations. *Climatic Change* **2011**, *106* (4), 679. https://doi.org/10.1007/s10584-011-0061-5.

(15) The Evolution of Wind-Turbines: An Historical Review. *Applied Energy* **1984**, *18* (3), 163–177. https://doi.org/10.1016/0306-2619(84)90007-2.

(16) Viollet, P.-L. From the Water Wheel to Turbines and Hydroelectricity. Technological Evolution and Revolutions. *Comptes Rendus Mécanique* **2017**, *345* (8), 570–580. https://doi.org/10.1016/j.crme.2017.05.016.

(17) Cook, T. R.; Dogutan, D. K.; Reece, S. Y.; Surendranath, Y.; Teets, T. S.; Nocera, D. G. Solar Energy Supply and Storage for the Legacy and Nonlegacy Worlds. *Chem. Rev.* **2010**, *110* (11), 6474–6502. https://doi.org/10.1021/cr100246c.

(18) Lewis, N. S.; Nocera, D. G. Powering the Planet: Chemical Challenges in Solar Energy Utilization. *PNAS* **2006**, *103* (43), 15729–15735. https://doi.org/10.1073/pnas.0603395103.

(19) Sciences, N. A. of. Correction for Lewis and Nocera, Powering the Planet: Chemical Challenges in Solar Energy Utilization. *PNAS* **2007**, *104* (50), 20142–20142. https://doi.org/10.1073/pnas.0710683104.
(20) Morton, O. A New Day Dawning?: Silicon Valley Sunrise. *Nature* **2006**, *443* (7107), 19–22. https://doi.org/10.1038/443019a.
(21) Hisatomi, T.; Domen, K. Introductory Lecture: Sunlight-Driven Water Splitting and Carbon Dioxide Reduction by Heterogeneous Semiconductor Systems as Key Processes in Artificial Photosynthesis. *Faraday Discuss.* **2017**, *198* (0), 11–35. https://doi.org/10.1039/C6FD00221H.
(22) Mitchell, C. Momentum Is Increasing towards a Flexible Electricity System Based on Renewables. *Nat Energy* **2016**, *1* (2), 1–6. https://doi.org/10.1038/nenergy.2015.30.
(23) Mazloomi, K.; Gomes, C. Hydrogen as an Energy Carrier: Prospects and Challenges. *Renewable and Sustainable Energy Reviews* **2012**, *16* (5), 3024–3033. https://doi.org/10.1016/j.rser.2012.02.028.
(24) Dincer, I.; Acar, C. Smart Energy Solutions with Hydrogen Options. *International Journal of Hydrogen Energy* **2018**, *43* (18), 8579–8599. https://doi.org/10.1016/j.ijhydene.2018.03.120.
(25) Ardo, S.; Rivas, D. F.; Modestino, M. A.; Greiving, V. S.; Abdi, F. F.; Llado, E. A.; Artero, V.; Ayers, K.; Battaglia, C.; Becker, J.-P.; Bederak, D.; Berger, A.; Buda, F.; Chinello, E.; Dam, B.; Palma, V. D.; Edvinsson, T.; Fujii, K.; Gardeniers, H.; Geerlings, H.; Hashemi, S. M. H.; Haussener, S.; Houle, F.; Huskens, J.; James, B. D.; Konrad, K.; Kudo, A.; Kunturu, P. P.; Lohse, D.; Mei, B.; Miller, E. L.; Moore, G. F.; Muller, J.; Orchard, K. L.; Rosser, T. E.; Saadi, F. H.; Schüttauf, J.-W.; Seger, B.; Sheehan, S. W.; Smith, W. A.; Spurgeon, J.; Tang, M. H.; Krol, R. van de; Vesborg, P. C. K.; Westerik, P. Pathways to Electrochemical Solar-Hydrogen Technologies. *Energy Environ. Sci.* **2018**, *11* (10), 2768–2783. https://doi.org/10.1039/C7EE03639F.
(26) Heremans, G.; Trompoukis, C.; Daems, N.; Bosserez, T.; Vankelecom, I. F. J.; Martens, J. A.; Rongé, J. Vapor-Fed Solar Hydrogen Production Exceeding 15% Efficiency Using Earth Abundant Catalysts and Anion Exchange Membrane. *Sustainable Energy Fuels* **2017**, *1* (10), 2061–2065. https://doi.org/10.1039/C7SE00373K.
(27) Yu, Z.; Li, F.; Sun, L. Recent Advances in Dye-Sensitized Photoelectrochemical Cells for Solar Hydrogen Production Based on Molecular Components. *Energy Environ. Sci.* **2015**, *8* (3), 760–775. https://doi.org/10.1039/C4EE03565H.
(28) Sherman, B. D.; McMillan, N. K.; Willinger, D.; Leem, G. Sustainable Hydrogen Production from Water Using Tandem Dye-Sensitized Photoelectrochemical Cells. *Nano Converg* **2021**, *8*. https://doi.org/10.1186/s40580-021-00257-8.
(29) Armaroli, N.; Balzani, V. The Hydrogen Issue. *ChemSusChem* **2011**, *4* (1), 21–36. https://doi.org/10.1002/cssc.201000182.
(30) Kyriakou, V.; Garagounis, I.; Vourros, A.; Vasileiou, E.; Stoukides, M. An Electrochemical Haber-Bosch Process. *Joule* **2020**, *4* (1), 142–158. https://doi.org/10.1016/j.joule.2019.10.006.
(31) Hamilton, T. L.; Bryant, D. A.; Macalady, J. L. The Role of Biology in Planetary Evolution: Cyanobacterial Primary Production in Low-Oxygen Proterozoic Oceans. *Environmental Microbiology* **2016**, *18* (2), 325–340. https://doi.org/10.1111/1462-2920.13118.
(32) Olson, J. M. Photosynthesis in the Archean Era. *Photosynth Res* **2006**, *88* (2), 109–117. https://doi.org/10.1007/s11120-006-9040-5.
(33) Hohmann-Marriott, M. F.; Blankenship, R. E. Evolution of Photosynthesis. *Annu. Rev. Plant Biol.* **2011**, *62* (1), 515–548. https://doi.org/10.1146/annurev-arplant-042110-103811.
(34) Soo, R. M.; Hemp, J.; Parks, D. H.; Fischer, W. W.; Hugenholtz, P. On the Origins of Oxygenic Photosynthesis and Aerobic Respiration in Cyanobacteria. *Science* **2017**, *355* (6332), 1436–1440. https://doi.org/10.1126/science.aal3794.
(35) Cardona, T.; Sánchez-Baracaldo, P.; Rutherford, A. W.; Larkum, A. W. Early Archean Origin of Photosystem II. *Geobiology* **2019**, *17* (2), 127–150. https://doi.org/10.1111/gbi.12322.
(36) Sánchez-Baracaldo, P.; Cardona, T. On the Origin of Oxygenic Photosynthesis and Cyanobacteria. *New Phytologist* **2020**, *225* (4), 1440–1446. https://doi.org/10.1111/nph.16249.
(37) Junge, W. Oxygenic Photosynthesis: History, Status and Perspective. *Quarterly Reviews of Biophysics* **2019**, *52*. https://doi.org/10.1017/S0033583518000112.

(38) Govindjee; Shevela, D.; Björn, L. O. Evolution of the Z-Scheme of Photosynthesis: A Perspective. *Photosynth Res* **2017**, *133* (1), 5–15. https://doi.org/10.1007/s11120-016-0333-z.
(39) Yang, H.; Liu, J.; Wen, X.; Lu, C. Molecular Mechanism of Photosystem I Assembly in Oxygenic Organisms. *Biochimica et Biophysica Acta (BBA) - Bioenergetics* **2015**, *1847* (9), 838–848. https://doi.org/10.1016/j.bbabio.2014.12.011.
(40) Zabret, J.; Bohn, S.; Schuller, S. K.; Arnolds, O.; Möller, M.; Meier-Credo, J.; Liauw, P.; Chan, A.; Tajkhorshid, E.; Langer, J. D.; Stoll, R.; Krieger-Liszkay, A.; Engel, B. D.; Rudack, T.; Schuller, J. M.; Nowaczyk, M. M. Structural Insights into Photosystem II Assembly. *Nat. Plants* **2021**, *7* (4), 524–538. https://doi.org/10.1038/s41477-021-00895-0.
(41) Fassioli, F.; Dinshaw, R.; Arpin, P. C.; Scholes, G. D. Photosynthetic Light Harvesting: Excitons and Coherence. *Journal of The Royal Society Interface* **2014**, *11* (92), 20130901. https://doi.org/10.1098/rsif.2013.0901.
(42) Li, X.; Buda, F.; de Groot, H. J. M.; Sevink, G. J. A. Contrasting Modes of Self-Assembly and Hydrogen-Bonding Heterogeneity in Chlorosomes of Chlorobaculum Tepidum. *J. Phys. Chem. C* **2018**, *122* (26), 14877–14888. https://doi.org/10.1021/acs.jpcc.8b01790.
(43) Li, X.; Buda, F.; de Groot, H. J. M.; Sevink, G. J. Agur. Molecular Insight in the Optical Response of Tubular Chlorosomal Assemblies. *J. Phys. Chem. C* **2019**, *123* (26), 16462–16478. https://doi.org/10.1021/acs.jpcc.9b03913.
(44) Li, X.; Buda, F.; de Groot, H. J. M.; Sevink, G. J. A. Dynamic Disorder Drives Exciton Transfer in Tubular Chlorosomal Assemblies. *J. Phys. Chem. B* **2020**, *124* (20), 4026–4035. https://doi.org/10.1021/acs.jpcb.0c00441.
(45) Eisenmayer, T. J.; de Groot, H. J. M.; van de Wetering, E.; Neugebauer, J.; Buda, F. Mechanism and Reaction Coordinate of Directional Charge Separation in Bacterial Reaction Centers. *J. Phys. Chem. Lett.* **2012**, *3* (6), 694–697. https://doi.org/10.1021/jz201695p.
(46) Eisenmayer, T. J.; Lasave, J. A.; Monti, A.; de Groot, H. J. M.; Buda, F. Proton Displacements Coupled to Primary Electron Transfer in the Rhodobacter Sphaeroides Reaction Center. *J. Phys. Chem. B* **2013**, *117* (38), 11162–11168. https://doi.org/10.1021/jp401195t.
(47) Vos, M. H.; Rappaport, F.; Lambry, J.-C.; Breton, J.; Martin, J.-L. Visualization of Coherent Nuclear Motion in a Membrane Protein by Femtosecond Spectroscopy. *Nature* **1993**, *363* (6427), 320–325. https://doi.org/10.1038/363320a0.
(48) Fuller, F. D.; Pan, J.; Gelzinis, A.; Butkus, V.; Senlik, S. S.; Wilcox, D. E.; Yocum, C. F.; Valkunas, L.; Abramavicius, D.; Ogilvie, J. P. Vibronic Coherence in Oxygenic Photosynthesis. *Nature Chem* **2014**, *6* (8), 706–711. https://doi.org/10.1038/nchem.2005.
(49) Romero, E.; Augulis, R.; Novoderezhkin, V. I.; Ferretti, M.; Thieme, J.; Zigmantas, D.; van Grondelle, R. Quantum Coherence in Photosynthesis for Efficient Solar-Energy Conversion. *Nature Phys* **2014**, *10* (9), 676–682. https://doi.org/10.1038/nphys3017.
(50) Ferretti, M.; Novoderezhkin, V. I.; Romero, E.; Augulis, R.; Pandit, A.; Zigmantas, D.; Grondelle, R. van. The Nature of Coherences in the B820 Bacteriochlorophyll Dimer Revealed by Two-Dimensional Electronic Spectroscopy. *Phys. Chem. Chem. Phys.* **2014**, *16* (21), 9930–9939. https://doi.org/10.1039/C3CP54634A.
(51) Novoderezhkin, V. I.; Romero, E.; Grondelle, R. van. How Exciton-Vibrational Coherences Control Charge Separation in the Photosystem II Reaction Center. *Phys. Chem. Chem. Phys.* **2015**, *17* (46), 30828–30841. https://doi.org/10.1039/C5CP00582E.
(52) Ramanan, C.; Ferretti, M.; Roon, H. van; Novoderezhkin, V. I.; Grondelle, R. van. Evidence for Coherent Mixing of Excited and Charge-Transfer States in the Major Plant Light-Harvesting Antenna, LHCII. *Phys. Chem. Chem. Phys.* **2017**, *19* (34), 22877–22886. https://doi.org/10.1039/C7CP03038J.
(53) Novoderezhkin, V. I.; Romero, E.; Prior, J.; Grondelle, R. van. Exciton-Vibrational Resonance and Dynamics of Charge Separation in the Photosystem II Reaction Center. *Phys. Chem. Chem. Phys.* **2017**, *19* (7), 5195–5208. https://doi.org/10.1039/C6CP07308E.
(54) Kern, J.; Chatterjee, R.; Young, I. D.; Fuller, F. D.; Lassalle, L.; Ibrahim, M.; Gul, S.; Fransson, T.; Brewster, A. S.; Alonso-Mori, R.; Hussein, R.; Zhang, M.; Douthit, L.; de Lichtenberg, C.; Cheah, M. H.; Shevela, D.; Wersig, J.; Seuffert, I.; Sokaras, D.; Pastor, E.; Weninger, C.; Kroll, T.; Sierra, R. G.; Aller, P.; Butryn, A.; Orville, A. M.; Liang, M.; Batyuk,

A.; Koglin, J. E.; Carbajo, S.; Boutet, S.; Moriarty, N. W.; Holton, J. M.; Dobbek, H.; Adams, P. D.; Bergmann, U.; Sauter, N. K.; Zouni, A.; Messinger, J.; Yano, J.; Yachandra, V. K. Structures of the Intermediates of Kok's Photosynthetic Water Oxidation Clock. *Nature* **2018**, *563* (7731), 421–425. https://doi.org/10.1038/s41586-018-0681-2.

(55) Rochaix, J.-D. Regulation of Photosynthetic Electron Transport. *Biochimica et Biophysica Acta (BBA) - Bioenergetics* **2011**, *1807* (3), 375–383. https://doi.org/10.1016/j.bbabio.2010.11.010.

(56) Purchase R. L.; de Groot H. J. M. Biosolar Cells: Global Artificial Photosynthesis Needs Responsive Matrices with Quantum Coherent Kinetic Control for High Yield. *Interface Focus* **2015**, *5* (3), 20150014. https://doi.org/10.1098/rsfs.2015.0014.

(57) Blankenship, R. E. *Molecular Mechanisms of Photosynthesis*; John Wiley & Sons, 2014.

(58) van Grondelle, R.; Boeker, E. Limits on Natural Photosynthesis. *J Phys Chem B* **2017**, *121* (30), 7229–7234. https://doi.org/10.1021/acs.jpcb.7b03024.

(59) Cloud, P. Paleoecological Significance of the Banded Iron-Formation. *Economic Geology* **1973**, *68* (7), 1135–1143. https://doi.org/10.2113/gsecongeo.68.7.1135.

(60) Anbar, A. D.; Duan, Y.; Lyons, T. W.; Arnold, G. L.; Kendall, B.; Creaser, R. A.; Kaufman, A. J.; Gordon, G. W.; Scott, C.; Garvin, J.; Buick, R. A Whiff of Oxygen Before the Great Oxidation Event? *Science* **2007**, *317* (5846), 1903–1906. https://doi.org/10.1126/science.1140325.

(61) Hodgskiss, M. S. W.; Crockford, P. W.; Peng, Y.; Wing, B. A.; Horner, T. J. A Productivity Collapse to End Earth's Great Oxidation. *PNAS* **2019**, *116* (35), 17207–17212. https://doi.org/10.1073/pnas.1900325116.

(62) Berkner, L. V.; Marshall, L. C. On the Origin and Rise of Oxygen Concentration in the Earth's Atmosphere. *Journal of the Atmospheric Sciences* **1965**, *22* (3), 225–261. https://doi.org/10.1175/1520-0469(1965)022<0225:OTOARO>2.0.CO;2.

(63) Canfield, D. E.; Teske, A. Late Proterozoic Rise in Atmospheric Oxygen Concentration Inferred from Phylogenetic and Sulphur-Isotope Studies. *Nature* **1996**, *382* (6587), 127–132. https://doi.org/10.1038/382127a0.

(64) Berner, R. A. Atmospheric Oxygen over Phanerozoic Time. *PNAS* **1999**, *96* (20), 10955–10957. https://doi.org/10.1073/pnas.96.20.10955.

(65) Catling, D. C.; Glein, C. R.; Zahnle, K. J.; McKay, C. P. Why O2 Is Required by Complex Life on Habitable Planets and the Concept of Planetary "Oxygenation Time." *Astrobiology* **2005**, *5* (3), 415–438. https://doi.org/10.1089/ast.2005.5.415.

(66) Sato, M. Thermochemistry of the Formation of Fossil Fuels. 14.

(67) O'Regan, B.; Grätzel, M. A Low-Cost, High-Efficiency Solar Cell Based on Dye-Sensitized Colloidal TiO 2 Films. *Nature* **1991**, *353* (6346), 737–740. https://doi.org/10.1038/353737a0.

(68) Swierk, J. R.; Mallouk, T. E. Design and Development of Photoanodes for Water-Splitting Dye-Sensitized Photoelectrochemical Cells. *Chem. Soc. Rev.* **2013**, *42* (6), 2357–2387. https://doi.org/10.1039/C2CS35246J.

(69) Yamamoto, M.; Nishizawa, Y.; Chábera, P.; Li, F.; Pascher, T.; Sundström, V.; Sun, L.; Imahori, H. Visible Light-Driven Water Oxidation with a Subporphyrin Sensitizer and a Water Oxidation Catalyst. *Chem. Commun.* **2016**, *52* (94), 13702–13705. https://doi.org/10.1039/C6CC07877J.

(70) Ooyama, Y.; Yamaji, K.; Ohshita, J. Photovoltaic Performances of Type-II Dye-Sensitized Solar Cells Based on Catechol Dye Sensitizers: Retardation of Back-Electron Transfer by PET (Photo-Induced Electron Transfer). *Mater. Chem. Front.* **2017**, *1* (11), 2243–2255. https://doi.org/10.1039/C7QM00211D.

(71) Massin, J.; Bräutigam, M.; Bold, S.; Wächtler, M.; Pavone, M.; Muñoz-García, A. B.; Dietzek, B.; Artero, V.; Chavarot-Kerlidou, M. Investigating Light-Driven Hole Injection and Hydrogen Evolution Catalysis at Dye-Sensitized NiO Photocathodes: A Combined Experimental–Theoretical Study. *J. Phys. Chem. C* **2019**, *123* (28), 17176–17184. https://doi.org/10.1021/acs.jpcc.9b04715.

(72) Duncan, W. R.; Prezhdo, O. V. Temperature Independence of the Photoinduced Electron Injection in Dye-Sensitized TiO2 Rationalized by Ab Initio Time-Domain Density Functional Theory. *J. Am. Chem. Soc.* **2008**, *130* (30), 9756–9762. https://doi.org/10.1021/ja800268x.
(73) Monti, A.; de Ruiter, J. M.; de Groot, H. J. M.; Buda, F. A Dynamic View of Proton-Coupled Electron Transfer in Photocatalytic Water Splitting. *J. Phys. Chem. C* **2016**, *120* (40), 23074–23082. https://doi.org/10.1021/acs.jpcc.6b08244.
(74) Meng, S.; Ren, J.; Kaxiras, E. Natural Dyes Adsorbed on TiO_2 Nanowire for Photovoltaic Applications: Enhanced Light Absorption and Ultrafast Electron Injection. *Nano Lett.* **2008**, *8* (10), 3266–3272. https://doi.org/10.1021/nl801644d.
(75) Monti, A.; Negre, C. F. A.; Batista, V. S.; Rego, L. G. C.; de Groot, H. J. M.; Buda, F. Crucial Role of Nuclear Dynamics for Electron Injection in a Dye–Semiconductor Complex. *J. Phys. Chem. Lett.* **2015**, *6* (12), 2393–2398.
(76) Shao, Y.; de Ruiter, J. M.; de Groot, H. J. M.; Buda, F. Photocatalytic Water Splitting Cycle in a Dye-Catalyst Supramolecular Complex: Ab Initio Molecular Dynamics Simulations. *J. Phys. Chem. C* **2019**, *123* (35), 21403–21414. https://doi.org/10.1021/acs.jpcc.9b06401.
(77) Shao, Y.; de Groot, H. J. M.; Buda, F. Proton Acceptor near the Active Site Lowers Dramatically the O–O Bond Formation Energy Barrier in Photocatalytic Water Splitting. *J. Phys. Chem. Lett.* **2019**, *10* (24), 7690–7697. https://doi.org/10.1021/acs.jpclett.9b02914.
(78) Shao, Y.; Groot, H. J. M. de; Buda, F. Tuning the Proton-Coupled Electron-Transfer Rate by Ligand Modification in Catalyst–Dye Supramolecular Complexes for Photocatalytic Water Splitting. *ChemSusChem* **2021**, *14* (1), 479–486. https://doi.org/10.1002/cssc.202001863.
(79) Li, F.; Fan, K.; Xu, B.; Gabrielsson, E.; Daniel, Q.; Li, L.; Sun, L. Organic Dye-Sensitized Tandem Photoelectrochemical Cell for Light Driven Total Water Splitting. *J. Am. Chem. Soc.* **2015**, *137* (28), 9153–9159. https://doi.org/10.1021/jacs.5b04856.
(80) Haque, S. A.; Palomares, E.; Cho, B. M.; Green, A. N. M.; Hirata, N.; Klug, D. R.; Durrant, J. R. Charge Separation versus Recombination in Dye-Sensitized Nanocrystalline Solar Cells: The Minimization of Kinetic Redundancy. *J. Am. Chem. Soc.* **2005**, *127* (10), 3456–3462. https://doi.org/10.1021/ja0460357.
(81) Maggio, E.; Martsinovich, N.; Troisi, A. Evaluating Charge Recombination Rate in Dye-Sensitized Solar Cells from Electronic Structure Calculations. *J. Phys. Chem. C* **2012**, *116* (14), 7638–7649. https://doi.org/10.1021/jp210558x.
(82) Hamann, T. W.; Farha, O. K.; Hupp, J. T. Outer-Sphere Redox Couples as Shuttles in Dye-Sensitized Solar Cells. Performance Enhancement Based on Photoelectrode Modification via Atomic Layer Deposition. *J. Phys. Chem. C* **2008**, *112* (49), 19756–19764. https://doi.org/10.1021/jp807395g.
(83) Hamann, T. W.; Ondersma, J. W. Dye-Sensitized Solar Cell Redox Shuttles. *Energy Environ. Sci.* **2011**, *4* (2), 370–381. https://doi.org/10.1039/C0EE00251H.
(84) Kageshima, Y.; Kumagai, H.; Hisatomi, T.; Minegishi, T.; Kubota, J.; Domen, K. Photoelectrochemical Solar Cells Consisting of a Pt-Modified CdS Photoanode and an Fe(ClO4)2/Fe(ClO4)3 Redox Shuttle in a Nonaqueous Electrolyte. *J. Phys. Chem. C* **2016**, *120* (20), 10781–10790. https://doi.org/10.1021/acs.jpcc.6b02406.
(85) Bruggeman, D. F.; Bakker, T. M. A.; Mathew, S.; Reek, J. N. H. Redox-Mediated Alcohol Oxidation Coupled to Hydrogen Gas Formation in a Dye-Sensitized Photosynthesis Cell. *Chemistry – A European Journal* **2021**, *27* (1), 218–221. https://doi.org/10.1002/chem.202003306.
(86) Bouwens, T.; Mathew, S.; Reek, J. N. H. P-Type Dye-Sensitized Solar Cells Based on Pseudorotaxane Mediated Charge-Transfer. *Faraday Discuss.* **2019**, *215* (0), 393–406. https://doi.org/10.1039/C8FD00169C.
(87) Ding, W.; Negre, C. F. A.; Palma, J. L.; Durrell, A. C.; Allen, L. J.; Young, K. J.; Milot, R. L.; Schmuttenmaer, C. A.; Brudvig, G. W.; Crabtree, R. H.; Batista, V. S. Linker Rectifiers for Covalent Attachment of Transition-Metal Catalysts to Metal-Oxide Surfaces. *ChemPhysChem* **2014**, *15* (6), 1138–1147. https://doi.org/10.1002/cphc.201400063.
(88) Ding, W.; Koepf, M.; Koenigsmann, C.; Batra, A.; Venkataraman, L.; Negre, C. F. A.; Brudvig, G. W.; Crabtree, R. H.; Schmuttenmaer, C. A.; Batista, V. S. Computational Design

of Intrinsic Molecular Rectifiers Based on Asymmetric Functionalization of N-Phenylbenzamide. *J Chem Theory Comput* **2015**, *11* (12), 5888–5896. https://doi.org/10.1021/acs.jctc.5b00823.

(89) Van Dyck, C.; Ratner, M. A. Molecular Rectifiers: A New Design Based on Asymmetric Anchoring Moieties. *Nano Lett.* **2015**, *15* (3), 1577–1584. https://doi.org/10.1021/nl504091v.

(90) Koepf, M.; Koenigsmann, C.; Ding, W.; Batra, A.; Negre, C. F. A.; Venkataraman, L.; Brudvig, G. W.; Batista, V. S.; Schmuttenmaer, C. A.; Crabtree, R. H. Controlling the Rectification Properties of Molecular Junctions through Molecule–Electrode Coupling. *Nanoscale* **2016**, *8* (36), 16357–16362. https://doi.org/10.1039/C6NR04830G.

(91) Szaniawska, E.; Wadas, A.; Ramanitra, H. H.; Fodeke, E. A.; Brzozowska, K.; Chevillot-Biraud, A.; Santoni, M.-P.; Rutkowska, I. A.; Jouini, M.; Kulesza, P. J. Visible-Light-Driven CO2 Reduction on Dye-Sensitized NiO Photocathodes Decorated with Palladium Nanoparticles. *RSC Adv.* **2020**, *10* (52), 31680–31690. https://doi.org/10.1039/D0RA04673F.

(92) Dau, H.; Zaharieva, I. Principles, Efficiency, and Blueprint Character of Solar-Energy Conversion in Photosynthetic Water Oxidation. *Acc. Chem. Res.* **2009**, *42* (12), 1861–1870. https://doi.org/10.1021/ar900225y.

(93) Peharz, G.; Dimroth, F.; Wittstadt, U. Solar Hydrogen Production by Water Splitting with a Conversion Efficiency of 18%. *International Journal of Hydrogen Energy* **2007**, *32* (15), 3248–3252. https://doi.org/10.1016/j.ijhydene.2007.04.036.

CHAPTER 2

Theoretical Background and Computational Methods

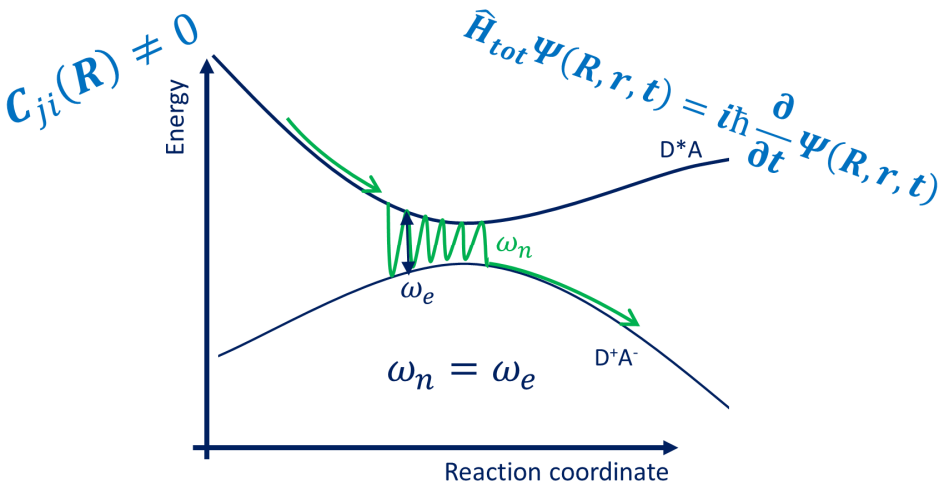

2

Simulating photoinduced processes involves transitions between electronic states. These non-adiabatic transitions go beyond the commonly used Born-Oppenheimer approximation of decoupled electronic and nuclear motions. To describe these processes, nonadiabatic effects need to be included. Due to the large diversity of system sizes and time scales within a Dye-Sensitized Photoanode, various computational methods are needed to bridge between these time and space ranges. In this chapter, the theoretical background and various computational methods used in the following chapters are introduced. If not noted otherwise, equations are given using atomic units.

2.1 The Born-Oppenheimer Approximation and Beyond

Any chemical system where relativistic effects are negligible can in principle be described by the time dependent Schrödinger equation:

$$\hat{H}_{\text{tot}}\Psi(\boldsymbol{R},\boldsymbol{r},t) = i\frac{\partial}{\partial t}\Psi(\boldsymbol{R},\boldsymbol{r},t) \tag{2.01}$$

where i is the imaginary unit, Ψ the total wavefunction describing all nuclei with coordinates $\boldsymbol{R}$ and electrons with coordinates $\boldsymbol{r}$. The total Hamiltonian $\hat{H}_{\text{tot}}$ contains the kinetic energy operators for all n electrons and N nuclei as well as electrostatic interactions between them:

$$\hat{H}_{\text{tot}} = \hat{T}_{\text{el}} + \hat{T}_{\text{nuc}} + \hat{V}_{\text{el,el}} + \hat{V}_{\text{nuc,nuc}} + \hat{V}_{\text{el,nuc}}$$

$$= -\sum_{i=1}^{n}\frac{\nabla_{\boldsymbol{r}_n}^2}{2} - \sum_{I=1}^{N}\frac{\nabla_{\boldsymbol{R}_N}^2}{2M_I} + \sum_{i=1}^{n}\sum_{j>i}^{n}\frac{1}{|\boldsymbol{r}_i - \boldsymbol{r}_j|} + \sum_{I=1}^{N}\sum_{J>I}^{N}\frac{Z_I Z_J}{|\boldsymbol{R}_I - \boldsymbol{R}_J|} - \sum_{i=1}^{n}\sum_{I=1}^{N}\frac{Z_I}{|\boldsymbol{R}_I - \boldsymbol{r}_i|} \tag{2.02}$$

Here, capital indices denote nuclei while small indices denote electrons. Consequently, $\boldsymbol{R}_I$ describes the coordinates of nucleus I, Z_I its nuclear charge and M_I the mass ratio of its nuclear mass m_I to the electron mass m_e ($M_I = \frac{m_I}{m_e}$). Similarly, $\boldsymbol{r}_i$ are the coordinates of electron i, with its charge and mass already defined within the atomic units. Solving the time-dependent Schrödinger equation in practice cannot be done without further simplifications. One of the most crucial approximations of the last century that made it possible to investigate and evaluate a myriad of chemical systems is the Born-Oppenheimer approximation (BOA).[1]

Within the BOA the separation between energy levels is considered large compared to the kinetic energy of the nuclei. Due to the large mass mismatch between electrons and nuclei, the electrons readjust instantaneously to new nuclear coordinates, decoupling electronic and nuclear subsystems. In the BOA the total

wavefunction $\Psi(\boldsymbol{R},\boldsymbol{r},t)$ can be separated into a set of pseudo time-independent electronic states $\psi_i(\boldsymbol{r};\boldsymbol{R})$ and time-dependent nuclear wave functions $\chi_i(\boldsymbol{R},t)$:

$$\Psi(\boldsymbol{R},\boldsymbol{r},t) = \sum_{i=1}^{\infty} \psi_i(\boldsymbol{r};\boldsymbol{R})\chi_i(\boldsymbol{R},t)\,, \tag{2.03}$$

where the semicolon denotes a parametrical dependence of the electronic wavefunction on the nuclear coordinates and the index i runs over the entire set of electronic eigenfunctions. The BOA provides a separation of time and spatial coordinates for the electronic motion by splitting the electron-nuclear quantum space into two subsystems: a time dependent nuclear subsystem and a time-independent electronic subsystem that readjusts instantaneously to new nuclear coordinates. For the electronic subsystem the time-independent Schrödinger equation is used:

$$\hat{H}_{\mathrm{el}}\psi_i(\boldsymbol{r};\boldsymbol{R}) = \varepsilon_i\psi_i(\boldsymbol{r};\boldsymbol{R}) \tag{2.04}$$

with

$$\hat{H}_{\mathrm{el}} = \hat{T}_{\mathrm{el}} + \hat{V}_{\mathrm{el,el}} + \hat{V}_{\mathrm{nuc,nuc}} + \hat{V}_{\mathrm{el,nuc}} \tag{2.05}$$

The nuclear subsystem keeps its direct time dependence. Inserting equations 2.03 and 2.05 into the Schrödinger equation (equation 2.01) gives

$$\left(\hat{H}_{\mathrm{el}}+\hat{T}_{\mathrm{nuc}}\right)\sum_{i=1}^{\infty}\psi_i(\boldsymbol{r};\boldsymbol{R})\chi_i(\boldsymbol{R},t) = i\frac{\partial}{\partial t}\sum_{i=1}^{\infty}\psi_i(\boldsymbol{r};\boldsymbol{R})\chi_i(\boldsymbol{R},t) \tag{2.06}$$

Multiplying with the complex conjugate ψ_j^* and integrating with $\boldsymbol{r}$ over the entire space Ω_{tot} gives

$$\int_{\Omega_{\mathrm{tot}}} d\boldsymbol{r}\,\psi_j^*(\boldsymbol{r};\boldsymbol{R})\left(\hat{H}_{\mathrm{el}} + \hat{T}_{\mathrm{nuc}}\right)\sum_{i=1}^{\infty}\psi_i(\boldsymbol{r};\boldsymbol{R})\chi_i(\boldsymbol{R},t)$$

$$= \int_{\Omega_{\mathrm{tot}}} d\boldsymbol{r}\psi_j^*(\boldsymbol{r};\boldsymbol{R})\, i\frac{\partial}{\partial t}\sum_{i=1}^{\infty}\psi_i(\boldsymbol{r};\boldsymbol{R})\chi_i(\boldsymbol{R},t) \tag{2.07}$$

The term on the right side, as χ_i is independent of $\boldsymbol{r}$, becomes

$$i\frac{\partial}{\partial t}\sum_{i=1}^{\infty}\chi_i(\boldsymbol{R},t)\int_{\Omega_{\text{tot}}} d\boldsymbol{r}\,\psi_j^*(\boldsymbol{r};\boldsymbol{R})\psi_i(\boldsymbol{r};\boldsymbol{R}) = i\frac{\partial}{\partial t}\sum_{i=1}^{\infty}\chi_i(\boldsymbol{R},t)\delta_{ij}$$

$$= i\frac{\partial}{\partial t}\chi_j(\boldsymbol{R},t) \tag{2.08}$$

For the left side of eq. 2.7, two terms, one with $\widehat{H}_{\text{el}}$ and $\widehat{T}_{\text{nuc}}$ remain with the first one being

$$\int_{\Omega_{\text{tot}}} d\boldsymbol{r}\,\psi_j^*(\boldsymbol{r},\boldsymbol{R})\widehat{H}_{\text{el}}\sum_{i=1}^{\infty}\psi_i(\boldsymbol{r};\boldsymbol{R})\chi_i(\boldsymbol{R},t)$$

$$= \int_{\Omega_{\text{tot}}} d\boldsymbol{r}\,\psi_j^*(\boldsymbol{r};\boldsymbol{R})\sum_{i=1}^{\infty}\varepsilon_i(\boldsymbol{R})\psi_i(\boldsymbol{r};\boldsymbol{R})\chi_i(\boldsymbol{R},t)$$

$$= \sum_{i=1}^{\infty}\varepsilon_i(\boldsymbol{R})\chi_i(\boldsymbol{R},t)\delta_{ji} = \varepsilon_j(\boldsymbol{R})\chi_j(\boldsymbol{R},t) \tag{2.09}$$

The second term can be simplified through the chain rule:

$$\int_{\Omega_{\text{tot}}} d\boldsymbol{r}\,\psi_j^*(\boldsymbol{r};\boldsymbol{R})\widehat{T}_{\text{nuc}}\sum_{i=1}^{\infty}\psi_i(\boldsymbol{r};\boldsymbol{R})\chi_i(\boldsymbol{R},t)$$

$$= \int_{\Omega_{\text{tot}}} d\boldsymbol{r}\,\psi_j^*(\boldsymbol{r};\boldsymbol{R})\left(-\sum_{I=1}^{N}\frac{\nabla_{\boldsymbol{R}}^2}{2M_I}\right)\sum_{i=1}^{\infty}\psi_i(\boldsymbol{r};\boldsymbol{R})\chi_i(\boldsymbol{R},t)$$

$$= \int_{\Omega_{\text{tot}}} d\boldsymbol{r}\,\psi_j^*(\boldsymbol{r};\boldsymbol{R})\left(-\sum_{I=1}^{N}\frac{1}{2M_I}\right)\sum_{i=1}^{\infty}(\nabla_{\boldsymbol{R}}^2\psi_i(\boldsymbol{r};\boldsymbol{R}))\chi_i(\boldsymbol{R},t)$$

$$+ 2\int_{\Omega_{\text{tot}}} d\boldsymbol{r}\,\psi_j^*(\boldsymbol{r};\boldsymbol{R})\left(-\sum_{I=1}^{N}\frac{1}{2M_I}\right)\sum_{i=1}^{\infty}\big(\nabla_{\boldsymbol{R}}\psi_i(\boldsymbol{r};\boldsymbol{R})\big)\big(\nabla_{\boldsymbol{R}}\chi_i(\boldsymbol{R},t)\big)$$

$$+ \int_{\Omega_{\text{tot}}} d\boldsymbol{r}\,\psi_j^*(\boldsymbol{r};\boldsymbol{R})\left(-\sum_{I=1}^{N}\frac{1}{2M_I}\right)\sum_{i=1}^{\infty}\psi_i(\boldsymbol{r};\boldsymbol{R})(\nabla_{\boldsymbol{R}}^2\chi_i(\boldsymbol{R},t))$$

$$= -\sum_{I=1}^{N} \frac{1}{2M_I} D_{ji}(\boldsymbol{R}) \sum_{i=1}^{\infty} \chi_i(\boldsymbol{R},t) - \sum_{I=1}^{N} \frac{1}{M_I} \boldsymbol{d}_{ji}(\boldsymbol{R}) \nabla_{\boldsymbol{R}} \sum_{i=1}^{\infty} \chi_i(\boldsymbol{R},t)$$

$$+ \sum_{i=1}^{\infty} \hat{T}_{\mathrm{nuc}} \chi_i(\boldsymbol{R},t) \delta_{ji}$$

$$= \sum_{i=1}^{\infty} \boldsymbol{C}_{ji}(\boldsymbol{R}) \chi_i(\boldsymbol{R},t) + \hat{T}_{\mathrm{nuc}} \chi_j(\boldsymbol{R},t) \tag{2.10}$$

with $\boldsymbol{C}_{ji}$ being the non-adiabatic coupling terms[2]

$$\boldsymbol{C}_{ji}(\boldsymbol{R}) = -\sum_{I=1}^{N} \frac{1}{2M_I} D_{ji}(\boldsymbol{R}) - \sum_{I=1}^{N} \frac{1}{M_I} \boldsymbol{d}_{ji}(\boldsymbol{R}) \nabla_{\boldsymbol{R}} \tag{2.11}$$

with respectively

$$D_{ji}(\boldsymbol{R}) = \int_{\Omega_{\mathrm{tot}}} d\boldsymbol{r}\, \psi_j^*(\boldsymbol{r};\boldsymbol{R}) \nabla_{\boldsymbol{R}}^2 \psi_i(\boldsymbol{r};\boldsymbol{R}) \tag{2.12}$$

being called the second order nonadiabatic coupling or kinetic coupling term and

$$\boldsymbol{d}_{ji}(\boldsymbol{R}) = \int_{\Omega_{\mathrm{tot}}} d\boldsymbol{r}\, \psi_j^*(\boldsymbol{r};\boldsymbol{R}) \nabla_{\boldsymbol{R}} \psi_i(\boldsymbol{r};\boldsymbol{R}) \tag{2.13}$$

the first order nonadiabatic coupling or derivative coupling term, which is a vector. It is important to note that both interactions couple between different electronic states ψ_i and ψ_j. Due to the high mass ratio in the prefactor in equation 2.11, the $\boldsymbol{C}_{ij}$ is assumed to be negligible in the BOA. As the nuclei are much heavier than the electrons, these are following the time-dependent potential energy landscape established by the nuclei, while remaining essentially in an electronic eigenstate that gradually develops over time. When inserting the results from equations 2.08, 2.09 and 2.10 into equation 2.07, we obtain

$$\left(\varepsilon_j(\boldsymbol{R}) + \hat{T}_{\mathrm{nuc}}\right) \chi_j(\boldsymbol{R},t) + \sum_{i=1}^{\infty} \boldsymbol{C}_{ji}(\boldsymbol{R}) \chi_i(\boldsymbol{R},t) = i \frac{\partial}{\partial t} \chi_j(\boldsymbol{R},t). \tag{2.14}$$

Finally, when assuming $C_{ji} = 0$, we end up with

$$\left(\varepsilon_j(\boldsymbol{R}) + \hat{T}_{\mathrm{nuc}}\right)\chi_j(\boldsymbol{R}, t) = i\frac{\partial}{\partial t}\chi_j(\boldsymbol{R}, t). \tag{2.15}$$

The nuclear wavefunctions are therefore propagated on adiabatic potential energy surfaces determined by the electronic system at nuclear positions $\boldsymbol{R}$. Neglecting $\boldsymbol{C}_{ji}$ allows for the approximate description of a wide variety of chemical problems where the chemistry proceeds while the system remains in the same electronic state. However, there are notable cases where this approximation breaks down and crossing involving different electronic states is essential to the chemical process.

Non-adiabaticity and Resonant Coupling between Nearly Degenerate Electronic States and Nuclear Vibrations

The BOA, allowing for efficient electronic structure methods and ab initio molecular dynamics (AIMD), has without a doubt led to deep insight into chemical problems and properties over time.[3–5] There are, however, significant limitations to its applicability. Employing the Hellman-Feynman theorem as described in reference [6] by Habitz and Votava, the first order terms of the non-adiabatic coupling $\boldsymbol{d}_{ji}$ can be expressed via the adiabatic states of the electronic system:

$$\boldsymbol{d}_{ji}(\boldsymbol{R}) = \frac{\int_{\Omega_{\mathrm{tot}}} d\boldsymbol{r}\, \psi_j^*(\boldsymbol{r}; \boldsymbol{R}) \nabla_{\boldsymbol{R}} \hat{H}_{\mathrm{el}} \psi_i(\boldsymbol{r}; \boldsymbol{R})}{\varepsilon_i - \varepsilon_j} \tag{2.16}$$

In this expression one can already see that the non-adiabatic coupling becomes non negligible for nearly degenerate adiabatic states. Here the BOA criterion that the energy difference is large compared to the kinetic energy of the nuclei is invalidated and the off-diagonal coupling between electronic and nuclear subsystem called nonadiabatic coupling becomes significant. A small energy difference between the electronic adiabatic states leads to an increase of the non-adiabatic terms in eq. 2.16.

If a nuclear mode with a frequency ω_{n} corresponding to the energy difference between these two states $\varepsilon_2 - \varepsilon_1 = \varepsilon_{\mathrm{e}} = \omega_{\mathrm{e}}$ is available in the system, this nuclear mode can couple to the electronic system and drive population transfer from one

state to another. This corresponds to Rabi oscillations[7] of the state populations induced by the nuclear vibration. Since this mode reaches resonance ($\omega_{\mathrm{n}} = \omega_{\mathrm{e}}$), it is filtered out by the system, effectively truncating the Hamiltonian , resulting in a system that can be represented by these two states only.[8] Inserting the nuclear wave functions $\chi_i(R,t)$ into equation 2.14 and employing a quantum-classical treatment where we exchange the quantum mechanical operators of the nuclear system by classical variables[9]

$$\begin{aligned} -\frac{\boldsymbol{d}_{ij}}{M}\nabla_R &\rightarrow -i\frac{\boldsymbol{d}_{ij}}{M}\boldsymbol{p} \\ -\frac{D_{ij}}{2M} &\rightarrow \frac{p^2}{2M}\delta_{ij} \\ \hat{T}_{\mathrm{nuc}} &\rightarrow \frac{p^2}{2M} \end{aligned} \tag{2.17}$$

the time-dependent Schrödinger equation of motion can be represented by a set of coupled equations[9]

$$\sum_{i=1}^{\infty}\left\{\varepsilon_i(\boldsymbol{R})\delta_{ji} - i\frac{\boldsymbol{p}}{M}\boldsymbol{d}_{ji}(\boldsymbol{R})\right\}\chi_i(\boldsymbol{R},t) = i\frac{\partial}{\partial t}\chi_j(\boldsymbol{R},t). \tag{2.18}$$

When a single, long living resonant mode is filtered out from a system with slowly varying geometry (i.e. the overall variation of the nuclear system measured by $\boldsymbol{R}$ is small on the timescale of the resonant nonadiabatic process) to couple two electronic states in a quasi-static environment, the displacement R_0 along the ω_{n} normal coordinate, phase φ and momentum $p = -MR_0\omega_{\mathrm{n}}\sin(\omega_{\mathrm{n}}t - \varphi)$ lead to[8]

$$\sum_{i=1,2}\left\{\varepsilon_i(R_0)\delta_{ji} + iR_0 d_{ji}(\boldsymbol{R})\omega_{\mathrm{n}}\sin(\omega_{\mathrm{n}}t - \varphi)\right\}\chi_i(\boldsymbol{R},t) = i\frac{\partial}{\partial t}\chi_j(\boldsymbol{R},t) \tag{2.19}$$

Where $d_{ji}(\boldsymbol{R})$ is now a scalar due to the multiplication with the momentum that corresponds to a single normal mode. Using equation 2.03, the two vibronic states can be represented by

$$\begin{aligned} \Psi_1(\boldsymbol{R},\boldsymbol{r},t) &= \chi_1(\boldsymbol{R},t)\psi_1(\boldsymbol{r};\boldsymbol{R}) \\ \Psi_2(\boldsymbol{R},\boldsymbol{r},t) &= \chi_2(\boldsymbol{R},t)\psi_2(\boldsymbol{r};\boldsymbol{R}) \end{aligned} \tag{2.20}$$

With only two states the equation of motion (2.19) reduces to the 2×2 matrix equation

$$\begin{pmatrix} \varepsilon_1 & iR_0 d_{12}(\boldsymbol{R})\omega_{\mathrm{n}} \sin(\omega_{\mathrm{n}} t - \varphi) \\ iR_0 d_{21}(\boldsymbol{R})\omega_{\mathrm{n}} \sin(\omega_n t - \varphi) & \varepsilon_2 \end{pmatrix} \begin{pmatrix} \chi_1(\boldsymbol{R},t) \\ \chi_2(\boldsymbol{R},t) \end{pmatrix} = i\frac{\partial}{\partial t}\begin{pmatrix} \chi_1(\boldsymbol{R},t) \\ \chi_2(\boldsymbol{R},t) \end{pmatrix}. \tag{2.21}$$

It is convenient to position the energies of the electronic states symmetrically around zero so that $\varepsilon_1 = E, \varepsilon_2 = -E$, and choose a phase $\varphi = \frac{\pi}{2}$ at $t = 0$. With $d_{12} = -d_{21}$ and using the Pauli matrices

$$\hat{\sigma}_z = \begin{pmatrix} 1 & 0 \\ 0 & -1 \end{pmatrix} = \hat{L}_z$$
$$\hat{\sigma}_z = \begin{pmatrix} 1 & 0 \\ 0 & -1 \end{pmatrix} = \hat{L}_z \tag{2.22}$$

which correspond to the angular momentum operators, we arrive at

$$\left(E\hat{L}_z - 2R_0 \boldsymbol{d}_{12}(\boldsymbol{R})\omega_{\mathrm{n}} \sin\left(\omega_{\mathrm{n}} t + \tfrac{\pi}{2}\right)\hat{L}_y\right)\begin{pmatrix} \chi_1(\boldsymbol{R},t) \\ \chi_2(\boldsymbol{R},t) \end{pmatrix} = i\frac{\partial}{\partial t}\begin{pmatrix} \chi_1(\boldsymbol{R},t) \\ \chi_2(\boldsymbol{R},t) \end{pmatrix}. \tag{2.23}$$

This matrix equation for the Hamiltonian is analogous to a system of a precessing fictitious spin S=1/2[8]

$$\hat{H} = \left(\omega_e \hat{L}_z - 2R_0 d_{12}(\boldsymbol{R})\omega_{\mathrm{n}} \sin\left(\omega_{\mathrm{n}} t + \tfrac{\pi}{2}\right)\hat{L}_y\right) = \hat{H}_0 + \hat{H}_1. \tag{2.24}$$

The $\hat{H}_0$ is the adiabatic term comprising the diagonal elements of the matrix, and the nonadiabatic $\hat{H}_1$ comprises the off-diagonal terms that are time-dependent due to the nuclear motion with frequency ω_{n}. Non adiabatic transfer is enabled in cases where the electronic and nuclear frequencies approach, finally reaching resonance $\omega_{\mathrm{n}} = \omega_{\mathrm{e}}$, with the time scales of electronic and nuclear motion converging. This allows for removing the explicit time dependency of the equations of motion, by transforming the time dependent Hamiltonian to the interaction frame of the nuclear motion to make it time-independent. For this, the $2\sin\left(\omega_{\mathrm{n}} t + \frac{\pi}{2}\right)$ term can be dcomposed into two counter rotating components, which rotate along $\hat{L}_z$ in opposite directions:

$$2\sin\left(\omega_{\mathrm{n}}t+\frac{\pi}{2}\right)\hat{L}_y = 2\cos(\omega_{\mathrm{n}}t)\hat{L}_y = 2\cos(\omega_{\mathrm{n}}t)\hat{L}_y + \sin(\omega_{\mathrm{n}}t)\,\hat{L}_x - \sin(\omega_{\mathrm{n}}t)\,\hat{L}_x = \mathrm{e}^{-i\omega_{\mathrm{n}}t\hat{L}_z}\hat{L}_y\mathrm{e}^{i\omega_{\mathrm{n}}t\hat{L}_z} + \mathrm{e}^{i\omega_{\mathrm{n}}t\hat{L}_z}\hat{L}_y\mathrm{e}^{-i\omega_{\mathrm{n}}t\hat{L}_z}. \tag{2.25}$$

This leads to

$$\hat{H}_1 = -R_0 d_{12}(\boldsymbol{R})\omega_{\mathrm{n}}\left(\mathrm{e}^{-i\omega_{\mathrm{n}}t\hat{L}_z}\hat{L}_y\mathrm{e}^{i\omega_{\mathrm{n}}t\hat{L}_z} + \mathrm{e}^{i\omega_{\mathrm{n}}t\hat{L}_z}\hat{L}_y\mathrm{e}^{-i\omega_{\mathrm{n}}t\hat{L}_z}\right). \tag{2.26}$$

The first term represents a transformation with a rotation around the z axis at frequency ω_{n}, while the second term rotates with a frequency of $-\omega_{\mathrm{n}}$. For the nuclear and electronic motion to couple, one of the two counter rotating components needs to reach resonance, while the other remains $2\omega_{\mathrm{n}}$ off resonance. In a physical, symmetric system, there is no inherent preference for one or the other component, suggesting that symmetry breaking is necessary for resonant coupling of a nuclear mode to drive population transfer between electronic states. This will be discussed further in chapter 3. Here, we assume the first term to couple to the electronic motion, while the second term is off resonance and can be neglected. To remove the time dependence of the Hamiltonian, we perform a unitary transformation with $\hat{R}_z(-\omega_{\mathrm{n}}t) = e^{i\omega_{\mathrm{n}}t}$:

$$\begin{aligned}\hat{H}_{\mathrm{int}} = \hat{R}_z(-\omega_{\mathrm{n}}t)\left(\hat{H}_0+\hat{H}_1\right)\hat{R}_z(\omega_{\mathrm{n}}t) &= \mathrm{e}^{i\omega_{\mathrm{n}}t\hat{L}_z}\omega_{\mathrm{e}}\hat{L}_z\mathrm{e}^{-i\omega_{\mathrm{n}}t\hat{L}_z} \\ -R_0 d_{12}(\boldsymbol{R})\omega_{\mathrm{n}}\mathrm{e}^{i\omega_{\mathrm{n}}t\hat{L}_z}&\left(\mathrm{e}^{-i\omega_{\mathrm{n}}t\hat{L}_z}\hat{L}_y\mathrm{e}^{i\omega_{\mathrm{n}}t\hat{L}_z}\right)\mathrm{e}^{-i\omega_{\mathrm{n}}t\hat{L}_z} \\ &= (\omega_{\mathrm{e}}-\omega_{\mathrm{n}})\hat{L}_z - R_0 d_{12}(\boldsymbol{R})\omega_{\mathrm{n}}\hat{L}_y\end{aligned} \tag{2.27}$$

With the first term vanishing at resonance condition, this leads to a simple, time independent interaction frame Hamiltonian:

$$\hat{H}_{\mathrm{int}} = -R_0 d_{12}(\boldsymbol{R})\omega_{\mathrm{n}}\hat{L}_{y.} \tag{2.28}$$

The $\hat{H}_{\mathrm{int}}$ induces coherent population transfer between the two states, that can be described with the following two, coupled equations of motion:[8]

$$\begin{aligned} i\frac{\partial}{\partial t}\chi_1(\boldsymbol{R},t) &= \frac{1}{2}R_0 d_{12}(\boldsymbol{R})\omega_{\mathrm{n}}\chi_2(\boldsymbol{R},t) \\ i\frac{\partial}{\partial t}\chi_2(\boldsymbol{R},t) &= \frac{1}{2}R_0 d_{12}(\boldsymbol{R})\omega_{\mathrm{n}}\chi_1(\boldsymbol{R},t)\end{aligned} \tag{2.29}$$

That have the solutions[8]

$$\begin{aligned}\chi_1(\boldsymbol{R},t) &= \chi_1(\boldsymbol{R},0)\left(\cos\left(\frac{1}{2}R_0 d_{12}(\boldsymbol{R})\omega_\mathrm{n} t\right)\right.\\ &\qquad\left.+\, i\chi_2(\boldsymbol{R},0)\sin\left(\frac{1}{2}R_0 d_{12}(\boldsymbol{R})\omega_\mathrm{n} t\right)\right)\\ \chi_2(\boldsymbol{R},t) &= \chi_2(\boldsymbol{R},0)\left(\cos\left(\frac{1}{2}R_0 d_{12}(\boldsymbol{R})\omega_\mathrm{n} t\right)\right.\\ &\qquad\left.+\, i\chi_1(\boldsymbol{R},0)\sin\left(\frac{1}{2}R_0 d_{12}(\boldsymbol{R})\omega_\mathrm{n} t\right)\right)\end{aligned} \tag{2.30}$$

If we take a system, that starts at a reactant state $|r\rangle$ at t=0 with $\chi_1(\boldsymbol{R},0) = 1$ and $\chi_2(\boldsymbol{R},0) = 0$, population transfer takes place resulting in a full conversion to the product state $|p\rangle$ with $\chi_1(\boldsymbol{R},\tau) = 0$ and $\chi_2(\boldsymbol{R},\tau) = 1$ after a time

$$\tau = \frac{\pi}{R_0 d_{12}(\boldsymbol{R})\omega_\mathrm{n}} \tag{2.31}$$

in a semi-classical coherent interconversion process.[8]

Photoinduced processes intrinsically include transitions between and interactions of different adiabatic states. Equations 2.30 give a straightforward description of coherent charge transfer between two adiabatic electronic states coupled to a single, long lived nuclear mode, giving deep insight into the role of electronic coherence, nuclear-electronic resonance, converging time scales of electronic and nuclear motion as well as the role of symmetry. Furthermore, due to the relaxation from the Franck-Condon region, an excited molecular system sweeps through resonance, which makes ω_e as well as d_{12} time dependent, contrary to this pseudo static approach that considers the system at the exact resonance. To model transitions between adiabatic states in complex molecular systems, the Schrödinger equation of the molecular problem given in equation 2.14 should therefore be the starting point. The non-adiabatic coupling terms need to be included to allow for transitions between adiabatic states. Several approaches of non-adiabatic molecular dynamics (NAMD) will be explained in section 2.5, while an in-depth investigation of vibronic coupling and coherence in intermolecular charge transfer is the main focus of chapter 3.

2.2 Density Functional Theory

Density Functional Theory (DFT) has proven to be the workhorse of modern computational chemistry. The main reason for its relatively low computational cost is the description of the electronic system not in terms of 4*n*-dimensional wavefunctions (3 spatial coordinates and 1 spin variable per electron), but rather an electron density dependent only on the 3 spatial coordinates. This is done on the basis of the first Hohenberg-Kohn theorem,[3] which states that a one-on-one mapping between electronic wavefunction, external potential and electron density exists,

$$\rho(\boldsymbol{r}) \leftrightarrow \hat{V}_{ext} \leftrightarrow \psi(\boldsymbol{r}) \tag{2.32}$$

so that an electron density can uniquely be assigned to a many-electron wavefunction and an external potential for any given system, and vice versa. The external potential includes the electron-nuclei interaction and can in principle also include further contributions. Since all observables of the system are a functional of the wavefunction, they can therefore also be described by a functional of the electron density, for example for the energy of the system:

$$\begin{aligned} E[\psi(\boldsymbol{r})] &= \int_{\Omega_{\text{tot}}} d\boldsymbol{r}\, \psi^*(\boldsymbol{r})\big(\hat{T}_{\text{el}} + \hat{V}_{\text{el,el}} + \hat{V}_{\text{ext}}\big)\psi(\boldsymbol{r}) \leftrightarrow \\ E[\rho(\boldsymbol{r})] &= T_{\text{el}}[\rho(\boldsymbol{r})] + V_{\text{el,el}}[\rho(\boldsymbol{r})] + V_{\text{ext}}[\rho(\boldsymbol{r})] \\ &= HK[\rho(\boldsymbol{r})] + V_{\text{ext}}[\rho(\boldsymbol{r})] \end{aligned} \tag{2.33}$$

with $HK[\rho(\boldsymbol{r})] = T_{\text{el}}[\rho(\boldsymbol{r})] + V_{\text{el,el}}[\rho(\boldsymbol{r})]$ the Hohenberg-Kohn functional. The functional for the nuclei-nuclei interaction is not included since this is a constant term within the BOA and can be added to the energy at a later stage. The ground state energy can be found by using the second Hohenberg-Kohn theorem, which states that the ground state electron density $\rho_0(\boldsymbol{r})$ minimizes the energy functional.

$$E_0 = E[\,\rho_0(\boldsymbol{r})] \leq E[\rho] \tag{2.34}$$

This means that the variational principle can be used to optimize the electron density to yield the lowest possible energy. In practice however, the form of the exact Hohenberg-Kohn Functional is unfortunately not known. The problem here are the kinetic energy functional for the electrons and the electron-electron interaction, that are both unknown for interacting electrons. To circumvent this problem, Kohn and Sham postulated that for each system of interacting electrons at a certain external potential and corresponding electron density, a hypothetical system (a 'Kohn-Sham system') of non-interacting electrons with the same electron density can be found moving in an effective potential $v_{\text{eff}}(\boldsymbol{r})$.[10] The electron density of the non-interacting system is build up by Kohn-Sham orbitals $\phi_i(\boldsymbol{r})$

$$\rho_{\text{eff}}(\boldsymbol{r}) = \sum_{i}^{n} |\phi_i(\boldsymbol{r})|^2 \tag{2.35}$$

that are found by solving *n* coupled equations for the lowest possible energy:

$$\left(-\frac{1}{2}\nabla^2 + v_{\text{eff}}(\boldsymbol{r})\right)\phi_i(\boldsymbol{r}) = \varepsilon_i \phi_i(\boldsymbol{r}) \tag{2.36}$$

With the use of the Kohn-Sham orbitals, the energy functional can be decomposed in several large known contributions and possibly smaller unknown terms that need to be approximated: The kinetic energy functional can be split into one functional for non-interacting electrons by using the non-interacting kinetic energy functional $T_{\text{eff}}[\rho(\boldsymbol{r})]$ and an unknown kinetic correlation energy term $T_{\text{corr}}[\rho(\boldsymbol{r})]$. The electron-electron interaction can also be split into a pure Coulomb interaction term $J[\rho(\boldsymbol{r})]$ and a non-classical unknown part $V_{\text{nc}}[\rho(\boldsymbol{r})]$. The two unknown funtionals are combined into the exchange correlation functional $E_{\text{XC}}[\rho(\boldsymbol{r})] = T_{\text{corr}}[\rho(\boldsymbol{r})] + V_{\text{nc}}[\rho(\boldsymbol{r})]$, and we get for the total energy functional:

$$E[\rho(\boldsymbol{r})] = T_{\text{eff}}[\rho(\boldsymbol{r})] + J[\rho(\boldsymbol{r})] + V_{\text{ext}}[\rho(\boldsymbol{r})] + E_{\text{XC}}[\rho(\boldsymbol{r})] \tag{2.37}$$

Variational optimization of this functional with respect to the Kohn-Sham orbitals subject to the orthonormality constraint leads to the Kohn-Sham equations that need to be self-consistently solved:

$$\left(-\frac{\nabla^2}{2}+\int_{\Omega_{\text{tot}}} d\boldsymbol{r}'\frac{\rho(\boldsymbol{r}')}{|\boldsymbol{r}-\boldsymbol{r}'|}+v_{\text{ext}}(\boldsymbol{r})+\varepsilon_{\text{XC}}(\boldsymbol{r})\right)\phi_i(\boldsymbol{r})=\varepsilon_i\phi_i(\boldsymbol{r}) \tag{2.38}$$

The term ε_{XC} is the functional derivative with respect to the electron density of the exchange correlation term.

For the exchange correlation (XC) functional, there are numerous approximations to be found.[11] Within the Local Density Approximation (LDA),[10] the XC-functional is based on the known exchange correlation energy of a homogeneous electron gas (HEG):

$$E_{\text{XC}}^{\text{LDA}}[\rho(\boldsymbol{r})]=\int_{\Omega_{\text{tot}}} d\boldsymbol{r}\,\varepsilon_{\text{XC}}^{\text{HEG}}\big(\rho(\boldsymbol{r})\big)\rho(\boldsymbol{r}) \tag{2.39}$$

LDA gives quite good results in systems of relatively uniform electron density distributions such as extended metal systems or semi-conductors. In systems of abrupt electron density changes such as organic molecules, it is not as reliable and instead, XC-functionals of the GGA (Generalized Gradient Approximation) family are used, where the gradient of the electron density is also taken into account:

$$E_{\text{XC}}^{\text{GGA}}[\rho(\boldsymbol{r})]=\int_{\Omega_{\text{tot}}} d\boldsymbol{r}\,\varepsilon_{\text{XC}}^{\text{HEG}}\big(\rho(\boldsymbol{r})\big)\rho(\boldsymbol{r})+\int_{\Omega_{\text{tot}}} d\boldsymbol{r}\,F_{\text{XC}}[\rho(\boldsymbol{r}),\nabla\rho(\boldsymbol{r})]\rho(\boldsymbol{r}) \tag{2.40}$$

with $F_{\text{XC}}[\rho(\boldsymbol{r}),\nabla\rho(\boldsymbol{r})]$ depending on both the electron density as well as its gradient. Examples of this family are the functionals called BLYP and PBE that are also used in this work.[12–15]

Another set of XC-functionals quite commonly used are hybrid functionals, that include a fraction of exact Hartree-Fock exchange energy. One example used in this work is the extensively used B3LYP functional.[13,16]

The choice of the XC-functional is quite crucial in describing chemical systems accurately and is highly dependent on the specific system and on the molecular properties of interest.

Linear Response Time Dependent DFT

DFT is strictly a ground state approach, describing a system in its unperturbed stable state. To model interactions with electromagnetic irradiation which perturbs the system, Runge and Gross introduced a theorem that states that for each system that evolves in a time dependent external potential $\hat{V}_{ext}(t)$, there exists a direct mapping to a time dependent electron density $\rho(\boldsymbol{r},t)$ and time dependent wave function :[4]

$$\rho(\boldsymbol{r},t) \leftrightarrow \hat{V}_{\text{ext}}(t) \leftrightarrow \psi(\boldsymbol{r},t) \tag{2.41}$$

Parallel to ground state DFT, the system can be described by non-interacting Kohn-Sham orbitals, leading to the time-dependent Kohn-Sham equations:

$$\left(-\frac{\nabla^2}{2} + \int_{\Omega_{\text{tot}}} d\boldsymbol{r}' \frac{\rho(\boldsymbol{r}',t)}{|\boldsymbol{r}-\boldsymbol{r}'|} + v_{\text{ext}}(\boldsymbol{r},t) + \varepsilon_{\text{XC}}(\boldsymbol{r},t)\right)\phi_i(\boldsymbol{r}) = i\frac{\partial}{\partial t}\phi_i(\boldsymbol{r}) \tag{2.42}$$

In Linear Response Time Dependent DFT (LR-TDDFT), the time-dependency of the electronic system is treated as the response of a ground state density $\rho_{t_0}(\boldsymbol{r})$ at time t_0 to a perturbation of frequency ω introduced through the external potential at $t>t_0$, so that

$$v_{\text{ext}}(\boldsymbol{r},\omega) = v_{t_0}^{\text{ext}}(\boldsymbol{r}) + \delta v_{\text{ext}}(\boldsymbol{r},\omega)$$
$$\rho(\boldsymbol{r},\omega) = \rho_{t_0}(\boldsymbol{r}) + \delta\rho(\boldsymbol{r},\omega) \tag{2.43}$$

This perturbation can be represented as a Taylor series. In LR-TDDFT, only the first order term, the linear response is considered. Furthermore, the response of the electron density to the external potential can again be described by a system of non-

interacting electrons responding to an effective external potential v_{eff}. The first order response in the electron density becomes

$$\delta\rho(\boldsymbol{r},\omega) = \int_{\Omega_{\text{tot}}} d\boldsymbol{r}'\, \chi(\boldsymbol{r},\boldsymbol{r}';\boldsymbol{\omega})\delta v_{\text{eff}}(\boldsymbol{r}',\omega) \tag{2.44}$$

with $\chi(\boldsymbol{r},\boldsymbol{r}';\boldsymbol{\omega})$ being called the response function, which for the non-interacting system takes the form

$$\chi(\boldsymbol{r},\boldsymbol{r}';\boldsymbol{\omega}) = \sum_{i=1}^{occ}\sum_{k=1}^{virt} 2\frac{\omega_{ki}}{\omega^2-\omega_{ki}^2}\phi_i(\boldsymbol{r})\phi_k(\boldsymbol{r})\phi_i(\boldsymbol{r}')\phi_k(\boldsymbol{r}') \tag{2.45}$$

with ϕ_{i} the occupied Kohn-Sham orbitals and ϕ_{k} the virtual and their energy difference determining $\omega_{ki} = \varepsilon_k - \varepsilon_i$. The response function displays singularities at the excitation energies.

The perturbation of the effective potential $\delta v_{\text{eff}}(\boldsymbol{r}',\omega)$ contains the change in the external potential $\delta v_{\text{ext}}(\boldsymbol{r},\omega)$ and electron density $\delta\rho(\boldsymbol{r}',\omega)$:

$$\delta v_{\text{eff}}(\boldsymbol{r}',\omega) = \delta v_{\text{ext}}(\boldsymbol{r},\omega) + \int_{\Omega_{\text{tot}}} d\boldsymbol{r}'\,\frac{\delta\rho(\boldsymbol{r}',\omega)}{|\boldsymbol{r}-\boldsymbol{r}'|}$$

$$+ \int_{\Omega_{\text{tot}}} d\boldsymbol{r}'\, f_{\text{xc}}(\boldsymbol{r},\boldsymbol{r}';\omega)\,\delta\rho(\boldsymbol{r},\omega) \tag{2.46}$$

with $f_{\text{xc}}(\boldsymbol{r},\boldsymbol{r}';\omega)$ the time dependent exchange correlation kernel, whose exact form, as the XC-Functionals, is not known and needs to be approximated. In this work, the standard ALDA (Adiabatic LDA) kernel is employed in all linear response TD-DFT calculations.

From LR-TTDFT it is possible to get relatively reliable excitation energies. However, Charge Transfer (CT) excitations are poorly described due to the long-range interactions not well described in most XC-functionals. To overcome this, a class of Long range Corrected (LC) functionals have been introduced, including the here used CAMY-B3LYP functional.[13,16–18].

2.3 Semi-Empirical Tight Binding Methods

Even though DFT is a cheap method in comparison to more elaborate wave function-based methods, it also becomes very expensive in extended systems. To describe such large systems, semi-empirical methods can be a great compromise between accuracy and computational cost. Traditional semi-empirical methods start from the Hartree-Fock approximation, but introduce simplifications in the Hamiltonian matrix and replace remaining terms with empirical parameters, which are used to include approximate correlation effects. One of the earliest of these methods was developed by Erich Hückel in the 1930s and today bears his name.[19–22]

Hückel Theory and Extended Hückel Theory

The original Hückel theory simplified the quantum mechanical description of planar hydrocarbons with extended conjugated π-systems to such an extent, that it was possible to obtain energies of π-systems and explain aromaticity on a quantum mechanical level in a time when computational tools for solving quantum mechanical problems were unavailable. The main approximation is that the electronic and energetic properties of this class of molecules are almost entirely dictated by the conjugated π-orbitals. The original Hückel method therefore disregarded sigma orbitals entirely and only took π-orbitals into consideration. The Extended Hückel (EH) theory introduced by Roald Hoffmann in 1963, expanded the description to all valence electrons, thus also including σ-orbitals.[23] The total wavefunction is described as a product of *n* one-electron wavefunctions $\psi_j(\boldsymbol{r_j})$, with *n* being the number of valence electrons, that are in turn constructed by a linear combination of *N* atomic orbitals.

$$\Psi_{tot} = \psi_1(\boldsymbol{r}_1)\psi_2(\boldsymbol{r}_2) \dots . \psi_n(\boldsymbol{r_n}) \tag{2.47}$$

$$\psi_j = \sum_{i=1}^{N} a_{ij}\varphi_i \tag{2.48}$$

The atomic orbitals φ_i are Slater Type Orbitals (STOs). Here, since the basis set is minimal, N=n. The total energy of the system can then be determined by the sum of the single electron energies ε_j, which in turn are obtained by solving

$$\hat{h}_{\text{eff}}\psi_j = \varepsilon_j\psi_j \tag{2.49}$$

with $\hat{h}_{\text{eff}}$ a single electron Hamiltonian that includes effective interactions with the other particles. These n one-electron equations can be rewritten in the form of n secular equations:

$$a_{i1}(H_{i1} - ES_{i1}) + (H_{i2} - ES_{i2}) + \cdots + a_{im}(H_{im} - ES_{im}) + a_{iN}(H_{iN} - ES_{iN}) = 0 \tag{2.50}$$

with E the energy, H_{ii} the Coulomb Integrals,

$$H_{ii} = \langle\varphi_i|\hat{h}_{\text{eff}}|\varphi_i\rangle, \tag{2.51}$$

H_{im} the Resonance Integrals

$$H_{im} = \langle\varphi_i|\hat{h}_{\text{eff}}|\varphi_m\rangle \tag{2.52}$$

and S_{im} Overlap Integrals

$$S_{im} = \langle\varphi_i|\varphi_m\rangle. \tag{2.53}$$

With the secular determinant

$$\begin{vmatrix} H_{11} - ES_{11} & H_{12} - ES_{12} & \dots & H_{1m} - ES_{1m} & \dots & H_{1N} - ES_{1N} \\ H_{21} - ES_{21} & H_{22} - ES_{22} & \cdots & H_{2m} - ES_{2m} & \dots & H_{2N} - ES_{2N} \\ \vdots & \vdots & \ddots & \vdots & \ddots & \vdots \\ H_{i1} - ES_{i1} & H_{i2} - ES_{i2} & \dots & H_{im} - ES_{im} & \dots & H_{iN} - ES_{iN} \\ \vdots & \vdots & \ddots & \vdots & \ddots & \vdots \\ H_{N1} - ES_{N1} & H_{N2} - ES_{N2} & \cdots & H_{Nm} - ES_{Nm} & \dots & H_{NN} - ES_{NN} \end{vmatrix} = 0 \tag{2.54}$$

the orbital energies, and then the orbital coefficients can be determined.

The most relevant approximation of EH, that makes it especially cost effective, is to parametrize these integrals instead of using their explicit description. Therefore, the exact expression of $\hat{h}_{\text{eff}}$ does not need to be known within the EH method. The diagonal terms of the matrix are readily evaluated: the overlap integrals S_{ii} are 1, as this is the spatial overlap between the atomic orbital φ_i with itself. The term H_{ii} is the Coulomb integral, an optimized parameter describing the kinetic and potential energy of an electron in orbital φ_i, most often described in terms of the negative of the orbital ionization potential. The off-diagonal elements include both the overlap integrals S_{im} and the Resonance Integrals H_{im}. Since the form and position of the atomic orbitals are known, S_{im} can be determined from the interatomic distances. The Resonance Integrals, describing the interaction of the electrons in orbital φ_i and φ_m are evaluated as:

$$H_{im} = \frac{1}{2} k_{im}(H_{ii} + H_{mm})S_{im}. \tag{2.55}$$

Here, k_{im} is an empirical parameter, called the Wolfsberg-Helmholz parameter. To obtain reliable energies, the EH parameters H_{ii}, k_{im} and the effective nuclear charges ζ that are embedded in the STOs are then optimized so that EH reproduces experimental or higher-level theoretical results. With that approach, the EH method can be used to obtain extremely cheap descriptions of both the electronic structure and the electronic energies. Molecular structures are not very reliable due to the non-self-consistent nature of EH, which is why this method is often used in combination with structures and trajectories of higher-level methods (even other tight binding methods as described in chapter 4 and 6).

Density Functional Based Tight Binding

A rather successfully employed semi-empirical approach, parametrized on DFT results rather than experimental data, is the Density Functional based Tight Binding (DFTB) method.[24,25] For DFTB the general expression of the energy is

$$E_{\mathrm{DFTB}} = \sum_{j}^{\mathrm{occ}} \langle \psi_j | \hat{H}_0 | \psi_j \rangle + E_{\mathrm{rep}}, \tag{2.56}$$

with $\hat{H}_0 = \hat{T}_{\mathrm{el}} + V_{\mathrm{eff}}(\boldsymbol{r})$ the unperturbed zero-order Hamiltonian. The effective potential $V_{\mathrm{eff}}(\boldsymbol{r})$ is approximated as a summation of purely atomic contributions, ψ_j the molecular orbitals, and the E_{rep} the atom-pair short range repulsion discussed later.

The molecular orbitals are expanded in STO's, similar to the EH approach in equation 2.48. The first term including the molecular orbital energies can be determined as in EH by solving the secular determinant (equation 2.54). Parametrization of the Coulomb and Resonance integrals however is done differently. The Coulomb Integral H_{ii} is determined by an LDA calculation of a free neutral pseudoatom according to

$$H_{ii} = \varepsilon_i^{\text{neutral free atom}}. \tag{2.57}$$

The resonance integrals are assumed to be 0 for the case that the orbitals in question reside on the same atom, otherwise, they are estimated by

$$H_{ij} = \langle \varphi_i^A | \hat{T}_{\mathrm{el}} + \hat{V}^A + \hat{V}^B | \varphi_j^B \rangle. \tag{2.58}$$

In equation 2.58 the potential operators for atoms A and B are included by strictly pairwise contributions of only two-center terms.

By solving the secular equations, the first term in equation 2.56 becomes a summation over all occupied Kohn-Sham orbitals with energy ε_j and occupation number n_j. The short range repulsion part E_{rep} is then taken as a function dependent

on distance R_{AB} and is determined by the difference of an LDA reference energy and the corresponding DFTB energy determined for reference structures of A and B

$$E_{\text{rep}}(R_{AB}) = \left[E_{\text{LDA}}(R_{AB}) - \sum_{j}^{\text{occ}} n_j \varepsilon_j(R_{AB})\right]_{\text{reference structure}} \tag{2.59}$$

For the practical implementation and application, a DFTB based program requires atomic parameters for each involved element including *e.g.* the STO atomic orbitals and Coulomb integral, and also pairwise parameters of each possible combination of two elements for the short range repulsion term.

The disadvantage of this tight binding approach is the negligence of long-range interactions. One extension that includes long-range Coulomb interactions is the Self-Consistent-Charge variant of DFTB, SCC-DFTB.[26–28] In this case, equation 2.56 includes an additional term

$$E_{\text{DFTB}} = \sum_{j=1}^{\text{occ}} \langle \Psi_j | \widehat{H}_0 | \Psi_j \rangle + \frac{1}{2} \sum_{A,B}^{N} q_A q_B \gamma_{AB} + E_{\text{rep}} \tag{2.60}$$

describing long-range Coulomb interactions between atoms A and B with point charges q_A and q_B, with γ_{AB} being a shorthand notation for

$$\gamma_{AB} = \frac{1}{\boldsymbol{R}_{AB}} - S(U_A, U_B, \boldsymbol{R}_{AB}). \tag{2.61}$$

$S(U_A, U_B, \boldsymbol{R}_{AB})$ is a short-range correction function that decays exponentially and is a function of the distance $\boldsymbol{R}_{AB}$ between atoms A and B and U_A, U_B are element specific Hubbard parameters of A and B.[27]

Even though the first term and the third term in equation 2.60 are the same as for canonical DFTB, the dependence of the atomic charges on the electron density and its influence on the total energy results in a self-consistent approach regarding the energy minimization.

Geometry, Frequency, Noncovalent, eXtended Tight Binding

A further development in semi-empirical methods is the GFN-xTB method developed by the Grimme group in Bonn.[29] GFN-xTB stands for Geometry, Frequency, Noncovalent, eXtended Tight Binding and as the name denotes has been optimized to accurately describe the structural properties of chemical compounds. There are no atom-pair based parameters but only global and element specific parameters, which makes GFN-xTB an extremely applicable method over a diverse range of chemical systems. The basis consists, similar to DFTB and the extended Hückel method, of a minimal basis set of STOs. Additionally, s-functions for hydrogen are augmented to improve description of hydrogen bonding, while the d-orbitals include polarization functions.

The total energy of a chemical system determined by GFN-xTB in atomic units contains the following energy terms:

$$E_{\mathrm{GFN-xTB}} = E_{\mathrm{el}} + E_{\mathrm{rep}} + E_{\mathrm{disp}} + E_{\mathrm{XB}} \tag{2.62}$$

The electronic energy term E_{el}, the repulsion energy term E_{rep} for atom-pair repulsion, the dispersion energy term E_{disp} and the E_{XB} term that includes halogen bonding effects. The atom-pair repulsion between atoms A and B with effective nuclear charges Z^{eff} and a distance R_{AB} is represented as

$$E_{\mathrm{rep}} = \sum_{A,B}^{N} \frac{Z_A^{\mathrm{eff}} Z_B^{\mathrm{eff}}}{R_{AB}} e^{-\sqrt{\alpha_A \alpha_B} R_{AB}{}^{k_{\mathrm{f}}}} \tag{2.63}$$

with α being a scaling parameter optimized for each element, while k_{f} is a global parameter with a value of 1.5[29]. The dispersion energy is determined by the common D3 dispersion corrections with BJ-damping functions.[30,31]

The halogen bonding term is described through a modified Lennard-Jones potential. Since it bears no relevance for this work, as no halogen atoms were used in any of the systems, it is not included here. A full description can be found in reference [29].

The electronic energy term is quite similar to equation 2.56 for SCC-DFTB:

$$E_{\mathrm{el}} = \sum_{i=1}^{\mathrm{occ}} n_i \langle \psi_i | \widehat{H}_0 | \psi_i \rangle + \frac{1}{2} \sum_{A,B}^{N} \sum_{l(A)}^{n_{l(A)}} \sum_{l'(B)}^{n_{l'(B)}} p_l^A p_{l'}^B \gamma_{AB,ll'}$$

$$+ \frac{1}{3} \sum_{A=1}^{N} \Gamma_A q_A^3 - T_{\mathrm{el}} S_{\mathrm{el}} \tag{2.64}$$

with the first term giving the orbital energies of the occupied orbitals ψ_i (as explained in the DFTB section) given their population n_i, and the zero-order unperturbed Hamiltonian $\widehat{H}_0$. The second term, similar in SCC-DFTB, includes the long-range Coulomb interaction between atoms A and B of a distance R_{AB}. The summation goes over all atomic shells of atom A (l) and atom B (l'), with p_l^A denoting the charge distribution of atom A and shell l. γ_{AB} is here given by

$$\gamma_{AB} = \left(\frac{1}{R_{AB}^{k_g} + \eta^{-k_g}} \right)^{1/k_g} \tag{2.65}$$

with $k_g = 2.0$ a global parameter[29] and

$$\eta = 2 \left(\frac{1}{(1 + \kappa_A^l)\eta_A} + \frac{1}{(1 + \kappa_B^{l'})\eta_B} \right)^{-1} \tag{2.66}$$

where κ_A^l and $\kappa_B^{l'}$ are scaling factors that are, as the chemical hardness η_A and η_B element specific parameters.

In the third term, q_A is the point charge of atom A, while Γ_A is the charge derivative of the atomic Hubbard parameter. These are the diagonal terms of the third-order density fluctuations. The last term is the electronic entropy, that becomes relevant in open shell systems with fractional occupations.

2.4 Adiabatic *Ab Initio* Molecular Dynamics

In general, adiabatic nuclear dynamics should be performed following equation 2.15, where the nuclei are propagated on an adiabatic PES generated by the electronic system at nuclear positions $\boldsymbol{R}$. However, as nuclei are rather heavy particles, it is often assumed that they behave as classical particles. The movement of the nuclei over time can then be described by Newton's second law of motion:

$$m_I \frac{d^2 \boldsymbol{R}_I(t)}{dt^2} = F(\boldsymbol{R}_I(t)) = -\nabla V_{\mathrm{el}}(\boldsymbol{R}_I(t)) \tag{2.67}$$

where the Force $F(\boldsymbol{R}_I)$ is determined by the electronic system through the nuclear coordinate dependent $V_{\mathrm{el}}(\boldsymbol{R}_I)$. In classical MD, this potential and with it the entire influence of the electronic system is collapsed into parametrized force fields, describing bonded interactions as covalent bond distances, angles, dihedrals, as well as non-bonded interactions by model potentials. However, these modelled interactions, often following the harmonic approximation for bonded interactions, are a stark simplification of the electronic influence on the nuclear dynamics. To describe chemical reactions, involving breaking and forming of covalent bonds, classical force fields fall short and non-harmonic potentials are necessary, for example in the framework of reactive force fields.[32] However, these electronic potentials can also be determined using quantum mechanical electronic structure methods, by using the classical limit of equation 2.15:

$$\begin{aligned} m_I \frac{d^2 \boldsymbol{R}_I(t)}{dt^2} &= -\nabla \langle \psi_0(\boldsymbol{r}; \boldsymbol{R}_I(t)) | \hat{H}_{\mathrm{el}} | \psi_0(\boldsymbol{r}; \boldsymbol{R}_I(t)) \rangle \\ &= -\nabla V_{\mathrm{el}}^0(\boldsymbol{R}_I(t)) \end{aligned} \tag{2.68}$$

The classical nuclei are evolved on a potential determined by the ground state energy of the electronic quantum system, which corresponds to the multidimensional potential energy surface of the ground state. This PES is normally calculated on the fly, with new nuclear coordinates at time *t* determining the electronic Hamiltonian and by solving the time independent Schrödinger equation for the electronic system (see equation 2.04) using the electronic structure method of choice. The gradient of

the electronic energy calculated on that point determines the forces acting on the nuclei. The forces lead to a modified nuclear geometry, that defines an updated electronic Hamiltonian. This quantum-classical method is also called Born-Oppenheimer Molecular Dynamics (BOMD). In general, the system can also be evolved in a state that is different from the ground state, using *e.g.* LR-TDDFT as the electronic structure method; however, due to the adiabatic BOA and static treatment of the electrons, non-adiabatic effects such as transitions between adiabatic states cannot be simulated.

2.5 Nonadiabatic Molecular Dynamics (NAMD)

While AIMD methods are a powerful tool to simulate chemical reactions, photochemistry is inherently non-adiabatic. Photochemical reactions therefore need to be treated with methods that allow for non-adiabatic transitions. To allow for these transitions, the electronic system needs to be treated explicitly time dependent. Usually, the time dependent electronic wavefunction is written as a linear combination of adiabatic electronic wave functions with time dependent coefficients $c_i(t)$:

$$\psi(\boldsymbol{r}, t) = \sum_{i=1}^{\infty} c_i(t)\psi_i(\boldsymbol{r}; \boldsymbol{R}(t)) \tag{2.69}$$

The direct time dependence is only in the coefficients, while the adiabatic wave functions are only indirectly dependent on time through the parametric dependence on the nuclear coordinates. The time dependent Schrödinger equation for the electrons then becomes:

$$i\sum_{i=1}^{\infty} \frac{\partial(c_i(t)\psi_i(\boldsymbol{r}; \boldsymbol{R}(t)))}{\partial t} = \widehat{H}_{\mathrm{el}} \sum_{i=1}^{\infty} c_i(t)\psi_i(\boldsymbol{r}; \boldsymbol{R}(t)) \tag{2.70}$$

Multiplying with the complex conjugate ψ_j^* and integrating over $\boldsymbol{r}$, as in equation 2.07, gives

$$i\sum_{i=1}^{\infty}\frac{\partial c_i(t)\delta_{ij}}{\partial t}+i\int_{\Omega_{\text{tot}}}d\boldsymbol{r}\psi_j^*(\boldsymbol{r};\boldsymbol{R}(t))\sum_{i=1}^{\infty}c_i(t)\frac{\partial\psi_i(\boldsymbol{r};\boldsymbol{R}(t))}{\partial t}$$

$$=\int_{\Omega_{\text{tot}}}d\boldsymbol{r}\psi_j^*(\boldsymbol{r};\boldsymbol{R}(t))\widehat{H}_{\text{el}}\sum_{i=1}^{\infty}c_i(t)\psi_i(\boldsymbol{r};\boldsymbol{R}(t)) \tag{2.71}$$

Rearranging and using equation 2.13 as well as the chain rule, we get the following coupled differential equations:

$$i\frac{\partial c_j(t)}{\partial t}=\sum_{i=1}^{\infty}c_i(t)\left[H_{ji}\big(\boldsymbol{R}(t)\big)-i\boldsymbol{d}_{ji}(\boldsymbol{R}(t))\frac{d\boldsymbol{R}(t)}{dt}\right] \tag{2.72}$$

With the Hamiltonian matrix

$$H_{ji}\big(\boldsymbol{R}(t)\big)=\int_{\Omega_{\text{tot}}}d\boldsymbol{r}\,\psi_j^*(\boldsymbol{r};\boldsymbol{R}(t))\widehat{H}_{\text{el}}\psi_i(\boldsymbol{r};\boldsymbol{R}(t)) \tag{2.73}$$

Equation 2.72 determines the time evolution of the coefficients of the adiabatic states. It is important to note, that the coefficient of state *j* depends on all other adiabatic states *i*. Both $H_{ji}\big(\boldsymbol{R}(t)\big)$ as well as $\boldsymbol{d}_{ji}(\boldsymbol{R}(t))$ allow for interaction of different adiabatic states. Both are parametrically dependent on $\boldsymbol{R}(t)$, showing the importance of the nuclear motion in the transition process. The non-adiabatic coupling vector $\boldsymbol{d}_{ji}(\boldsymbol{R}(t))$ allows for transitions from one adiabatic state to another in regions of strong coupling. The off-diagonal matrix elements of the Hamiltonian couple different states and are important in the diabatic representation or for non-orthonormal functions; they become however 0 when using an orthonormal, time independent adiabatic basis as done here. Thus, the equations for the time evolution of the coefficients becomes[33]

$$i\frac{\partial c_j(t)}{\partial t}=c_j(t)\varepsilon_i(\boldsymbol{R}(t))-i\sum_{i=1}^{\infty}\boldsymbol{d}_{ji}(\boldsymbol{R}(t))\frac{d\boldsymbol{R}}{dt} \tag{2.74}$$

The two NAMD methods used in this work differ in both the exact time evolution of the coefficients as given in equation 2.74 as well as in the time evolution of the nuclei.

Ehrenfest Dynamics

Ehrenfest dynamics is a quantum-classical mean field approach to NAMD. As in adiabatic AIMD, the nuclei are assumed to be classical particles and evolve according to forces determined quantum mechanically:[33–35]

$$m_I \frac{d^2 \boldsymbol{R}_I(t)}{dt^2} = -\nabla \langle \psi(\boldsymbol{r}, t; \boldsymbol{R}_I(t)) | \hat{H}_{\mathrm{el}} | \psi(\boldsymbol{r}, t; \boldsymbol{R}_I(t)) \rangle \tag{2.75}$$

Differently to equation 2.68, equation 2.75 does not necessarily involve the adiabatic ground state electronic wavefunction and retains the explicit time dependence of $\psi(\boldsymbol{r}, t; \boldsymbol{R}_I)$. Still, this equation shows the single configuration character of Ehrenfest dynamics, where the nuclei are evolved according to a mean potential as opposed to a multi-configuration based method as Multi Configurational Time dependent Hartree (MCTDH), which allows for propagation on different states and branching of the wave function.[36,37] The forces can be determined using the Hellmann-Feynman theorem:

$$F_I = -\langle \psi(\boldsymbol{r}, t; \boldsymbol{R}_I(t)) | \nabla_I \hat{H}_{\mathrm{el}} | \psi(\boldsymbol{r}, t; \boldsymbol{R}_I(t)) \rangle \tag{2.76}$$

Again, using time independent adiabatic basis functions with time dependent coefficients, inserting equation 2.69 into equation 2.76, we get

$$F_I = -\sum_{i,j}^{\infty} \langle c_j(t) \psi_j(\boldsymbol{r}; \boldsymbol{R}_I(t)) | \nabla_I \hat{H}_{\mathrm{el}} | c_i(t) \psi_i(\boldsymbol{r}; \boldsymbol{R}_I(t)) \rangle \tag{2.77}$$

Noting that

$$\nabla_I \langle c_j(t) \psi_j(\boldsymbol{r}; \boldsymbol{R}_I(t)) | \hat{H}_{\mathrm{el}} | c_i(t) \psi_i(\boldsymbol{r}; \boldsymbol{R}_I(t)) \rangle = \nabla_I c_j^* c_i \varepsilon_j \delta_{ji} \tag{2.78}$$

and

$$\begin{aligned}\nabla_I \langle c_j(t)\psi_j(\boldsymbol{r};\boldsymbol{R}_I(t))|\widehat{H}_{\mathrm{el}}|c_i(t)\psi_i(\boldsymbol{r};\boldsymbol{R}_I(t))\rangle \\ &= \langle \nabla_I c_j(t)\psi_j(\boldsymbol{r};\boldsymbol{R}_I(t))|\widehat{H}_{el}|c_i(t)\psi_i(\boldsymbol{r};\boldsymbol{R}_I(t))\rangle \\ &+ \langle c_j(t)\psi_j(\boldsymbol{r};\boldsymbol{R}_I(t))|\nabla_I \widehat{H}_{\mathrm{el}}|c_i(t)\psi_i(\boldsymbol{r};\boldsymbol{R}_I(t))\rangle \\ &+ \langle c_j(t)\psi_j(\boldsymbol{r};\boldsymbol{R}_I(t))|\widehat{H}_{\mathrm{el}}|\nabla_I c_i(t)\psi_i(\boldsymbol{r};\boldsymbol{R}_I(t))\rangle \\ &= \langle c_j(t)\psi_j(\boldsymbol{r};\boldsymbol{R}_I(t))|\nabla_I \widehat{H}_{\mathrm{el}}|c_i(t)\psi_i(\boldsymbol{r};\boldsymbol{R}_I(t))\rangle \\ &+ c_j^* c_i(\varepsilon_j - \varepsilon_i)\boldsymbol{d}_{ji}\end{aligned} \tag{2.79}$$

where we used that both operators are Hermitian and $-\boldsymbol{d}_{ij} = \boldsymbol{d}_{ji}$, we get

$$\begin{aligned}\langle c_j(t)\psi_j(\boldsymbol{r};\boldsymbol{R}_I(t))|\nabla_I \widehat{H}_{\mathrm{el}}|c_i(t)\psi_i(\boldsymbol{r};\boldsymbol{R}_I(t))\rangle \\ &= \nabla_I c_j^* c_i \varepsilon_j \delta_{ji} - c_j^* c_i(\varepsilon_j - \varepsilon_i)\boldsymbol{d}_{ji}\end{aligned} \tag{2.80}$$

Finally inserting into equation 2.76, we obtain the forces for the nuclei:[33]

$$F_I = -\sum_{j=1}^{\infty} |c_j|^2 \varepsilon_j + \sum_{j\neq i}^{\infty} c_j^* c_i(\varepsilon_j - \varepsilon_i)\boldsymbol{d}_{ji} \tag{2.81}$$

Therefore, the nuclei evolve on a mean potential, determined by the populations of different, mixed adiabatic states. The last term is the influence of non-adiabatic transitions between different states on the forces acting on the nuclei, that contains the non-adiabatic coupling vector $\boldsymbol{d}_{ji}$.The electronic motion is described following equation 2.74. Both subsystems are therefore coupled to each other: the nuclei move on a potential that is dependent on the average potential determined by the populations of the different adiabatic electronic states, while the electronic subsystem is coupled through the non-adiabatic coupling vector. Clearly, the nuclear motion is necessary for transitions to take place, through the $\boldsymbol{R}(t)$ dependence of $\boldsymbol{d}_{ji}$.

The single configuration approach of Ehrenfest dynamics makes this method relatively affordable in comparison to multiconfiguration based methods. However, this evolution on mean potentials comes with drawbacks: when leaving a region of strong nonadiabatic coupling, the system does not regain its adiabaticity but is instead trapped in this mean state. This holds especially true when there is a branching of wavefunctions between different adiabatic states. This over-coherence

has been recognized and decoherence corrections have been proposed to tackle this problem (see *e.g.* references [38] and [39] for recent reviews). This makes Ehrenfest dynamics a powerful tool when investigating the relaxation from the Franck-Condon region towards regions of strong non-adiabatic coupling as discussed in chapter 3, but is less reliable when leaving this region, making full conversion into the product state impossible. For simulations of photoinduced charge separation and electron injections, as treated in chapters 4, 6 and 7, Ehrenfest dynamics are less suitable, even without taking the cost for such extended systems into account.

AO-MO quantum propagation

Simulating photoinduced processes involving extended systems become prohibitively expensive when using Ehrenfest dynamics. For the simulations of photoinduced electron injection and charge separation as discussed in chapters 4, 6 and 7, an efficient, semi-classical approach of an AO-MO quantum propagation using an Extended Hückel Hamiltonian is used that was first proposed and applied by Batista *et al.*[40] The method was first used on a static nuclear geometry, but was quickly expanded to include nuclear motion.[41–45] However, instead of using excited state nuclear dynamics, the nuclear trajectories are calculated *a priori* in the ground state. This can involve the usage of classical MD following equation 2.67, or using AIMD following equation 2.68. In this work, the trajectories are obtained via AIMD ground state dynamics using one of the semi-empirical tight binding approaches discussed earlier, DFTB or GFN-xTB. The obtained nuclear trajectories are used for the quantum electron transfer dynamics (ETD).

The time evolution of the photoexcited electronic system is done by evolving a wave packet representing the photoexcited electron and one wave packet representing the hole on these predetermined nuclear trajectories. Starting from t=0, the nuclear coordinates $\boldsymbol{R}^{t=0}$ of the first geometry determine the AOs φ and the Hamiltonian $\widehat{H}_{\mathrm{el}}^{(t=0)}$. From this, the MOs $\psi_j(\boldsymbol{r};\boldsymbol{R}^{(0)})$ with their coefficients $c_j(0)$ are obtained by solving the time independent Schrödinger equation using the Extended

Hückel approach. An appropriate wave packet Ψ is chosen to represent the photoexcited electron and hole, most often corresponding to LUMO and HOMO of the excited fragment. Using the Extended Hückel approach discussed in section 2.3, these wave packets can either be described within the diabatic atomic orbital basis as given in equations 2.48, or within the adiabatic molecular orbital basis as given in equation 2.69. For the time evolution of the wave packet, we use the adiabatic MO basis. We start from the time dependent Schrödinger equation

$$i\frac{\partial\Psi(r,t;\boldsymbol{R}(t))}{\partial t} = \widehat{H}_{\mathrm{el}}\Psi(r,t;\boldsymbol{R}(t)) \tag{2.82}$$

The electronic Hamiltonian corresponds to the Extended Hückel Hamiltonian. We insert equation 2.69 into equation 2.82 and, following the derivation as given in the beginning of section 2.5, we arrive at equation 2.71, However, since we only want to propagate on a time slice δt where the nuclear geometry is assumed to be fixed, the time dependence of $\boldsymbol{R}$ as well as the Hamiltonian is removed:

$$i\sum_{i=1}^{\infty}\frac{\partial c_i(t)\delta_{ij}}{\partial t} + i\int_{\Omega_{\mathrm{tot}}} d\boldsymbol{r}\psi_j^*(\boldsymbol{r};\boldsymbol{R}^{(\delta t)})\sum_{i=1}^{\infty}c_i(t)\frac{\partial\psi_i(\boldsymbol{r};\boldsymbol{R}^{(\delta t)})}{\partial t}$$

$$= \int_{\Omega_{\mathrm{tot}}} d\boldsymbol{r}\psi_j^*(\boldsymbol{r};\boldsymbol{R}^{(\delta t)})\widehat{H}_{\mathrm{el}}^{(\delta t)}\sum_{i=1}^{\infty}c_i(t)\psi_i(\boldsymbol{r};\boldsymbol{R}^{(\delta t)}) \tag{2.83}$$

Since the MOs are now time independent, the second term on the left hand becomes zero and we obtain

$$i\frac{\partial c_j(t)}{\partial t} = \sum_{i=1}^{\infty}c_i(t)H_{ji}\left(\boldsymbol{R}^{(\delta t)}\right) = c_j(t)\varepsilon_i\left(\boldsymbol{R}^{(\delta t)}\right) \tag{2.84}$$

where again the off-diagonal elements of the Hamiltonian are zero due to the adiabatic, orthonormal character of the basis functions. Note that the difference to equation 2.74 and therefore to the electronic time propagation in Ehrenfest, is the dropping of the term including the non-adiabatic coupling. For a finite time slice δt, the new coefficients can then be obtained[43]:

$$c_j(\delta t) = c_j(0)e^{-i\varepsilon_j \delta t} \tag{2.85}$$

From this equation, one can see that non-adiabatic transitions are not possible within this time slice, since changes in the coefficients still lead to the same amplitude. Spatial movement of the wave packet is possible in the case of a superposition of adiabatic states, but population transfer between adiabatic states cannot occur. How are non-adiabatic transitions within this method then possible? The trick is in switching between adiabatic (MO) and diabatic (AO) representation of the wave function, as seen in scheme 2.1, where n_{BF} corresponds to the number of basis functions.

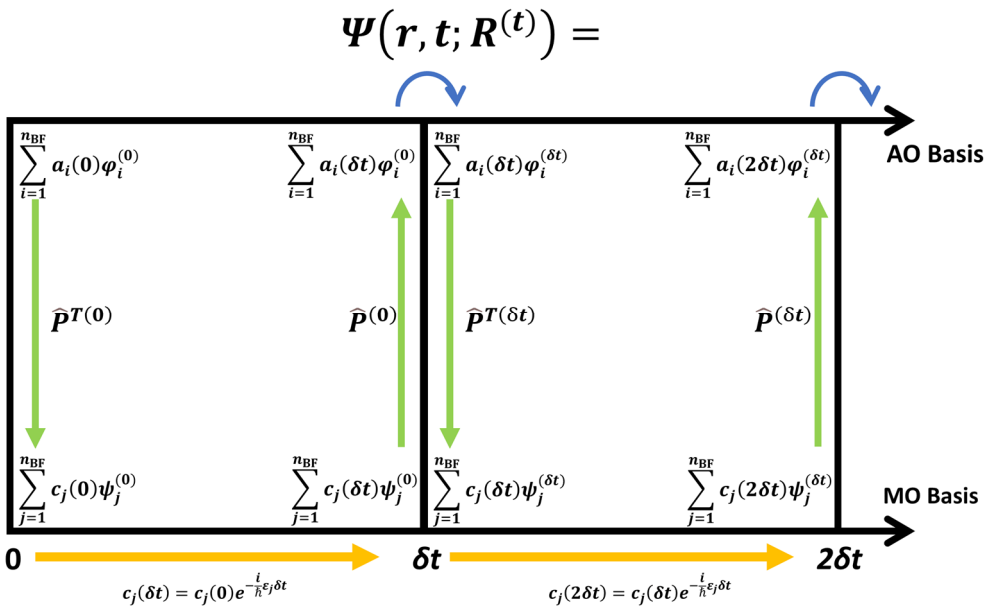

Scheme 2.1. Schematic representation of the AO/MO propagation. A wave packet representing the electron is chosen, first represented in the AO basis. After projection onto the MO basis (green arrow), the electronic time evolution is performed via the molecular orbital coefficients (orange). After projecting back onto the AO basis, the nuclei and atomic orbital basis are shifted according to the precalculated trajectory (blue). This is repeated for each consecutive time step. Note the color codes for electronic (orange) and nuclear (blue) time evolution, with green representing projection between the diabatic and adiabatic representation. Adapted from reference [43].

After the first quantum propagation of the electronic wave packet, it is projected onto the diabatic AO basis using the projection operator[43]

$$\hat{P}^{(0)}|\Psi^{(\delta t)}>=\sum_{\varphi\psi}^{n_{\mathrm{BF}}}|\varphi^{(0)}>C^{(0)}<\psi^{(0)}|, \tag{2.86}$$

where $C^{(0)}$ is the Coefficient matrix as determined by the static Extended Hückel result. The atomic orbitals are then shifted according to the new nuclear positions, assuming $|\varphi^{(0)}>\approx|\varphi^{(\delta t)}>$. The new nuclear geometry $\boldsymbol{R}^{(\delta t)}$ determines a new Hamiltonian $\hat{H}_{\mathrm{el}}^{(\delta t)}\neq\hat{H}_{\mathrm{el}}^{(0)}$, which leads to new Molecular orbitals $\psi^{(\delta t)}\neq\psi^{(0)}$.

The AO coefficients in the wave packet in the AO basis are not changed. This is where non-adiabatic transitions become possible, as the shift within the diabatic AO representation can result in changing the adiabatic state, since this wave packet in the AO representation is then projected back onto the new MO basis:

$$\hat{P}^{\mathrm{T}(\delta t)}|\Psi^{(\delta t)}>=\sum_{\varphi\psi}^{n_{\mathrm{BF}}}|\psi^{(\delta t)}>C^{\mathrm{T}(\delta t)}<\varphi^{(\delta t)}| \tag{2.87}$$

Important to note here is that the MOs as well as the coefficient matrix is different, but the AOs stay the same. This is what allows for transitions between adiabatic states. Through the change in the adiabatic MO basis, we effectively reintroduce the off-diagonal elements in the Hamiltonian matrix, since we go through the diabatic basis projecting onto a new adiabatic basis with the result of population transfer from one adiabatic state to another, which are eigenfunctions of different Hamiltonians and not orthogonal to each other.

This scheme is followed for each nuclear time step, the new nuclear positions define a new Hamiltonian and by that a new set of MOs. The wave packet is projected onto this new MO basis (see scheme 2.1). The time evolution of the MO coefficients is done following equation 2.85. After the electronic quantum propagation, the wave packet is projected back onto the AO basis and then shifted again with respect to the new coordinates. This AO-MO propagation method allows for simulating the time evolution of photoexcited electron and hole, including non-

adiabatic transitions, such as shown representatively in scheme 2.2, where a wave packet fully represented by an adiabatic state S2 evolves into S1 through non-adiabatic population transfer.

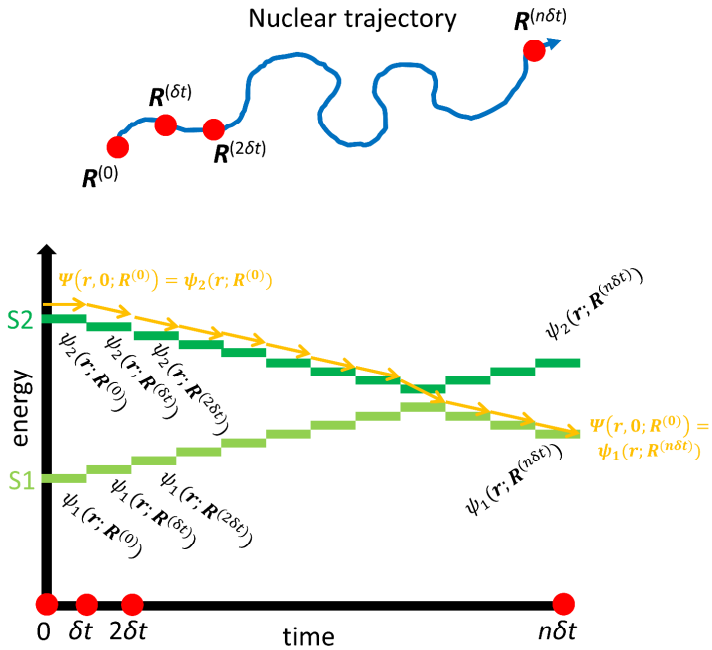

Scheme 2.2. Non-adiabatic conversion from an adiabatic state S2 to another state S1 with the AO-MO electronic propagation (yellow arrows) on a precalculated nuclear trajectory (blue arrow), starting with a wave packet equal to the adiabatic state S2. For each time step of length δt, the trajectory determines nuclear coordinates $\boldsymbol{R}^{(t)}$, which defines the molecular orbitals $\psi_i(\boldsymbol{r};\boldsymbol{R}^{(t)})$ at time t and energy of the two states S1 and S2 at the respective time step. Electronic propagation of a wave packet is performed on this MO basis. Due to the change in geometry, the wave packet is not an eigenfunction of the new Hamiltonian anymore. When the states approach each other energetically, the wave packet can only be represented by a superposition of states S2 and S1, leading to gradual population transfer between the two states. After leaving this region, the transfer is complete and the system evolves completely on state S1.

The method can be used in large, extended systems including periodic boundary conditions due to its low computational cost. It is quite reliable at elevated temperatures and large extended systems, where the approximation of the ground state trajectory is generally acceptable. Since the nuclear system evolves uninfluenced by the changed electronic structure, the electronic system cannot steer the nuclear system into resonance as with Ehrenfest dynamics. However, the electronic system can take advantage of nuclear modes available in the nuclear system due to thermal noise as shown *e.g.* in the appendix of chapter 4. All in all, the AO-MO propagator is a powerful tool for simulating photoinduced electron injection, charge transfer and charge separation in large systems in a computationally accessible way.

2.6 References

(1) Born, M.; Oppenheimer, R. Zur Quantentheorie Der Molekeln. *Ann. Phys.* **1927**, *389* (20), 457–484.

(2) Bircher, M. P.; Liberatore, E.; Browning, N. J.; Brickel, S.; Hofmann, C.; Patoz, A.; Unke, O. T.; Zimmermann, T.; Chergui, M.; Hamm, P.; Keller, U.; Meuwly, M.; Woerner, H.-J.; Vaníček, J.; Rothlisberger, U. Nonadiabatic Effects in Electronic and Nuclear Dynamics. *Struct. Dyn.* **2017**, *4* (6), 061510. https://doi.org/10.1063/1.4996816.

(3) Hohenberg, P.; Kohn, W. Inhomogeneous Electron Gas. *Phys. Rev.* **1964**, *136* (3B), B864–B871.

(4) Runge, E.; Gross, E. K. U. Density-Functional Theory for Time-Dependent Systems. *Phys. Rev. Lett.* **1984**, *52* (12), 997–1000.

(5) Car, R.; Parrinello, M. Unified Approach for Molecular Dynamics and Density-Functional Theory. *Phys. Rev. Lett.* **1985**, *55* (22), 2471–2474.

(6) Habitz, P.; Votava, C. The Hellmann–Feynman Theorem for Approximate Wave Functions and Its Application to Nonadiabatic Coupling Matrix Elements with the Aid of a Coupled Hartree–Fock Method. *J. Chem. Phys.* **1980**, *72* (10), 5532–5539. https://doi.org/10.1063/1.438971.

(7) Rabi, I. I. Space Quantization in a Gyrating Magnetic Field. *Phys. Rev.* **1937**, *51* (8), 652–654. https://doi.org/10.1103/PhysRev.51.652.

(8) Purchase, R. L.; de Groot, H. J. M. Biosolar Cells: Global Artificial Photosynthesis Needs Responsive Matrices with Quantum Coherent Kinetic Control for High Yield. *Interface focus* **2015**, *5* (3), 20150014.

(9) Akimov, A. V.; Neukirch, A. J.; Prezhdo, O. V. Theoretical Insights into Photoinduced Charge Transfer and Catalysis at Oxide Interfaces. *Chem. Rev.* **2013**, *113* (6), 4496–4565.

(10) Kohn, W.; Sham, L. J. Self-Consistent Equations Including Exchange and Correlation Effects. *Phys. Rev.* **1965**, *140* (4A), A1133–A1138.

(11) Verma, P.; Truhlar, D. G. Status and Challenges of Density Functional Theory. *Trends in Chemistry* **2020**, *2* (4), 302–318. https://doi.org/10.1016/j.trechm.2020.02.005.

(12) Becke, A. D. Density-Functional Exchange-Energy Approximation with Correct Asymptotic Behavior. *Phys. Rev. A* **1988**, *38* (6), 3098–3100.

(13) Lee, C.; Yang, W.; Parr, R. G. Development of the Colle-Salvetti Correlation-Energy Formula into a Functional of the Electron Density. *Phys. Rev. B* **1988**, *37* (2), 785–789.

(14) Perdew, J. P.; Burke, K.; Ernzerhof, M. Generalized Gradient Approximation Made Simple. *Phys. Rev. Lett.* **1996**, *77* (18), 3865–3868.

(15) Perdew, J. P.; Burke, K.; Ernzerhof, M. Generalized Gradient Approximation Made Simple [Phys. Rev. Lett. 77, 3865 (1996)]. *Phys. Rev. Lett.* **1997**, *78* (7), 1396–1396.

(16) Becke, A. D. A New Mixing of Hartree–Fock and Local Density-functional Theories. *J. Chem. Phys.* **1993**, *98* (2), 1372–1377. https://doi.org/10.1063/1.464304.

(17) Yanai, T.; Tew, D. P.; Handy, N. C. A New Hybrid Exchange–Correlation Functional Using the Coulomb-Attenuating Method (CAM-B3LYP). *Chem. Phys. Lett.* **2004**, *393* (1–3), 51–57.

(18) Akinaga, Y.; Ten-no, S. Range-Separation by the Yukawa Potential in Long-Range Corrected Density Functional Theory with Gaussian-Type Basis Functions. *Chem. Phys. Lett.* **2008**, *462* (4), 348–351. https://doi.org/10.1016/j.cplett.2008.07.103.

(19) Hückel, E. Quantentheoretische Beiträge zum Benzolproblem. I. *Z. Physik* **1931**, *70* (3), 204–286. https://doi.org/10.1007/BF01339530.

(20) Hückel, E. Quantentheoretische Beiträge zum Benzolproblem. II. *Z. Physik* **1931**, *72* (5), 310–337. https://doi.org/10.1007/BF01341953.

(21) Hückel, E. Quantentheoretische Beiträge zum Problem der aromatischen und ungesättigten Verbindungen. III. *Z. Physik* **1932**, *76* (9), 628–648. https://doi.org/10.1007/BF01341936.

(22) Hückel, E. Die freien Radikale der organischen Chemie. IV. *Z. Physik* **1933**, *83* (9), 632–668. https://doi.org/10.1007/BF01330865.

(23) Hoffmann, R. An Extended Hückel Theory. I. Hydrocarbons. *J. Chem. Phys.* **1963**, *39* (6), 1397–1412. https://doi.org/10.1063/1.1734456.
(24) Porezag, D.; Frauenheim, Th.; Köhler, Th.; Seifert, G.; Kaschner, R. Construction of Tight-Binding-like Potentials on the Basis of Density-Functional Theory: Application to Carbon. *Phys. Rev. B* **1995**, *51* (19), 12947–12957. https://doi.org/10.1103/PhysRevB.51.12947.
(25) Seifert, G.; Porezag, D.; Frauenheim, T. Calculations of Molecules, Clusters, and Solids with a Simplified LCAO-DFT-LDA Scheme. *Int. J. Quantum Chem.* **1996**, *58* (2), 185–192. https://doi.org/10.1002/(SICI)1097-461X(1996)58:2<185::AID-QUA7>3.0.CO;2-U.
(26) Elstner, M.; Porezag, D.; Jungnickel, G.; Elsner, J.; Haugk, M.; Frauenheim, Th.; Suhai, S.; Seifert, G. Self-Consistent-Charge Density-Functional Tight-Binding Method for Simulations of Complex Materials Properties. *Phys. Rev. B* **1998**, *58* (11), 7260–7268. https://doi.org/10.1103/PhysRevB.58.7260.
(27) Elstner, M.; Frauenheim, T.; Kaxiras, E.; Seifert, G.; Suhai, S. A Self-Consistent Charge Density-Functional Based Tight-Binding Scheme for Large Biomolecules. *Phys. Status Solidi B* **2000**, *217* (1), 357–376. https://doi.org/10.1002/(SICI)1521-3951(200001)217:1<357::AID-PSSB357>3.0.CO;2-J.
(28) Frauenheim, T.; Seifert, G.; Elsterner, M.; Hajnal, Z.; Jungnickel, G.; Porezag, D.; Suhai, S.; Scholz, R. A Self-Consistent Charge Density-Functional Based Tight-Binding Method for Predictive Materials Simulations in Physics, Chemistry and Biology. *Phys. Status Solidi B* **2000**, *217* (1), 41–62. https://doi.org/10.1002/(SICI)1521-3951(200001)217:1<41::AID-PSSB41>3.0.CO;2-V.
(29) Grimme, S.; Bannwarth, C.; Shushkov, P. A Robust and Accurate Tight-Binding Quantum Chemical Method for Structures, Vibrational Frequencies, and Noncovalent Interactions of Large Molecular Systems Parametrized for All Spd-Block Elements (Z = 1–86). *J. Chem. Theory Comput.* **2017**, *13* (5), 1989–2009. https://doi.org/10.1021/acs.jctc.7b00118.
(30) Grimme, S.; Antony, J.; Ehrlich, S.; Krieg, H. A Consistent and Accurate Ab Initio Parametrization of Density Functional Dispersion Correction (DFT-D) for the 94 Elements H-Pu. *J. Chem. Phys.* **2010**, *132* (15), 154104. https://doi.org/10.1063/1.3382344.
(31) Grimme, S.; Ehrlich, S.; Goerigk, L. Effect of the Damping Function in Dispersion Corrected Density Functional Theory. *J. Comput. Chem.* **2011**, *32* (7), 1456–1465. https://doi.org/10.1002/jcc.21759.
(32) van Duin, A. C. T.; Dasgupta, S.; Lorant, F.; Goddard, W. A. ReaxFF: A Reactive Force Field for Hydrocarbons. *J. Phys. Chem. A* **2001**, *105* (41), 9396–9409. https://doi.org/10.1021/jp004368u.
(33) Tully, J. C. Nonadiabatic Dynamics. In *Modern Methods for Multidimensional Dynamics Computations in Chemistry*; World Scientific, 1998. https://doi.org/10.1142/3672.
(34) Tully, J. C. Mixed Quantum–Classical Dynamics. *Faraday Discuss.* **1998**, *110* (0), 407–419. https://doi.org/10.1039/A801824C.
(35) Curchod, B. F. E.; Rothlisberger, U.; Tavernelli, I. Trajectory-Based Nonadiabatic Dynamics with Time-Dependent Density Functional Theory. *Chem. Phys. Chem.* **2013**, *14* (7), 1314–1340.
(36) Beck, M. The Multiconfiguration Time-Dependent Hartree (MCTDH) Method: A Highly Efficient Algorithm for Propagating Wavepackets. *Physics Reports* **2000**, *324* (1), 1–105. https://doi.org/10.1016/S0370-1573(99)00047-2.
(37) Worth, G. A.; Meyer, H.-D.; Köppel, H.; Cederbaum, L. S.; Burghardt, I. Using the MCTDH Wavepacket Propagation Method to Describe Multimode Non-Adiabatic Dynamics. *International Reviews in Physical Chemistry* **2008**, *27* (3), 569–606. https://doi.org/10.1080/01442350802137656.
(38) Crespo-Otero, R.; Barbatti, M. Recent Advances and Perspectives on Nonadiabatic Mixed Quantum–Classical Dynamics. *Chem. Rev.* **2018**, *118* (15), 7026–7068. https://doi.org/10.1021/acs.chemrev.7b00577.
(39) Nelson, T. R.; White, A. J.; Bjorgaard, J. A.; Sifain, A. E.; Zhang, Y.; Nebgen, B.; Fernandez-Alberti, S.; Mozyrsky, D.; Roitberg, A. E.; Tretiak, S. Non-Adiabatic Excited-State Molecular Dynamics: Theory and Applications for Modeling Photophysics in Extended Molecular

Materials. *Chem. Rev.* **2020**, *120* (4), 2215–2287. https://doi.org/10.1021/acs.chemrev.9b00447.

(40) Rego, L. G. C.; Batista, V. S. Quantum Dynamics Simulations of Interfacial Electron Transfer in Sensitized TiO_2 Semiconductors. *J. Am. Chem. Soc.* **2003**, *125* (26), 7989–7997. https://doi.org/10.1021/ja0346330.

(41) Hoff, D. A.; Silva, R.; Rego, L. G. C. Subpicosecond Dynamics of Metal-to-Ligand Charge-Transfer Excited States in Solvated [Ru(Bpy)3]2+ Complexes. *J. Phys. Chem. C* **2011**, *115* (31), 15617–15626. https://doi.org/10.1021/jp2022715.

(42) Hoff, D. A.; da Silva, R.; Rego, L. G. C. Coupled Electron–Hole Quantum Dynamics on D–π–A Dye-Sensitized TiO_2 Semiconductors. *J. Phys. Chem. C* **2012**, *116* (40), 21169–21178. https://doi.org/10.1021/jp303647x.

(43) da Silva, R.; Hoff, D. A.; Rego, L. G. C. Coupled Quantum-Classical Method for Long Range Charge Transfer: Relevance of the Nuclear Motion to the Quantum Electron Dynamics. *J. Phys.: Condens. Matter* **2015**, *27* (13), 134206. https://doi.org/10.1088/0953-8984/27/13/134206.

(44) Monti, A.; Negre, C. F. A.; Batista, V. S.; Rego, L. G. C.; de Groot, H. J. M.; Buda, F. Crucial Role of Nuclear Dynamics for Electron Injection in a Dye–Semiconductor Complex. *J. Phys. Chem. Lett.* **2015**, *6* (12), 2393–2398.

(45) da Silva Oliboni, R.; Bortolini, G.; Torres, A.; Rego, L. G. C. A Nonadiabatic Excited State Molecular Mechanics/Extended Hückel Ehrenfest Method. *J. Phys. Chem. C* **2016**, *120* (48), 27688–27698. https://doi.org/10.1021/acs.jpcc.6b09606.

CHAPTER 3

Understanding Coherent Charge Transfer: Isotope Effect and Dynamic Symmetry Breaking

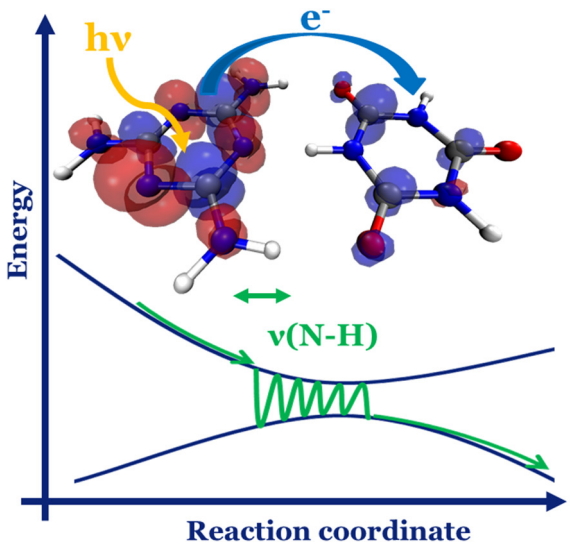

This Chapter is based on:

Jan Paul Menzel, Huub J.M. de Groot, Francesco Buda; *Journal of Physical Chemistry Letters*, **2019**, *10*, 6504-6511

3

ABSTRACT

Electron-nuclear (vibronic) coupling has emerged as an important factor in determining the efficiency of energy transfer and charge separation in natural and artificial photosynthetic systems. Here we investigate the photoinduced charge transfer process in a hydrogen bonded donor-acceptor molecular complex. By using real-time quantum-classical simulations based on time dependent Kohn-Sham we follow in detail the relaxation from the Franck-Condon point to the region of strong nonadiabatic coupling where electron transfer occurs. We elucidate how the charge transfer is coupled to specific vibrational modes and how it is affected by isotope substitution. The importance of resonance in nuclear and electron dynamics as well as the role of dynamic symmetry breaking is emphasized. Using the dipole moment as a descriptive parameter, exchange of angular momentum between nuclear and electronic subsystems in an electron-nuclear resonant process is inferred. The performed simulations support a nonadiabatic conversion via adiabatic passage process that was recently put forward. These results are relevant in deriving rational design principles for solar to fuel conversion devices.

3.1 Introduction

Photoinduced charge separation is a key process in photosynthesis. In nature, extended antenna complexes collect solar energy in the form of electronic excitations, which are then transferred to a reaction center, where the actual charge separation takes place.[1–3] Only after this separation, the photoenergy can be converted into chemical energy. Since ultrafast charge separation in combination with spatial separation play a major role in preventing charge recombination, understanding the origin of these fast and efficient processes is of crucial importance for the design of artificial photosynthesis devices.[4–8] Coherent charge transfer is an emerging concept, where, through vibronic coupling, nuclear vibrations resonate with specific electronic transitions, thus driving charge transfer efficiently.[9–14] Experimental observations and theoretical investigations underline the role of this effect in natural [12,15–21] as well as artificial systems.[22–27] For example, Falke *et al.* identified the C=C stretch and a pentagonal pinch mode to drive charge transfer from a polymer towards a fullerene in a polymer blend.[25]

Yet, essential aspects of coherent charge transfer are not well understood. In this work, using quantum-classical nonadiabatic Ehrenfest dynamics simulations, we explore which and how specific nuclear modes are selected in a donor-acceptor molecular complex and what role isotope effects and dynamic symmetry breaking play. Computer simulations of these processes provide the possibility of freezing specific nuclear coordinates or bond distances to assess how crucial these degrees of freedom are for the charge transfer. These exercises, though unphysical, can provide insight hardly accessible through experimental investigations. For this *in silico* investigation, we consider a DNA base pair mimic consisting of melamine and isocyanuric acid[22], which self-assemble through an extended two dimensional hydrogen bonding network[28]. This explicit donor-acceptor molecular complex combines relative simplicity with a realistic distribution of different chemical entities common in biological systems.[29] We investigate photoinduced coherent charge transfer and follow the onset of electron transfer (ET) upon photoexcitation in real

time. Through a comparison of the Fourier analysis of the nuclear and electronic motion along the same trajectory, relevant frequencies can be extracted. We find that modulating the frequency of key vibrational modes by isotope substitution changes their participation in the coherent process and increases the importance of other modes. Additionally, our investigations stress the importance of dynamic symmetry breaking for coherent charge transfer. Analogies are found between the simulation results of the photoinduced coherent charge transfer and the well-established adiabatic passage processes observed during nuclear magnetic resonance (NMR) adiabatic pulse[30] and chirped laser pulse optical spectroscopy experiments[31], providing additional support for the nonadiabatic conversion via adiabatic passage (NCAP)[9,32,33]. These results provide important principles to consider while designing and optimizing charge transfer and charge separation devices.[12,33]

3.2 Computational Methods

The structure of the DNA base pair mimic (melamine and isocyanuric acid) is given in scheme 3.1a. Geometry optimizations were performed with the Amsterdam Density Functional program[34,35] using Density Functional Theory (DFT). The BLYP exchange correlation functional[36,37] was used in combination with a Slater type basis set of the triple zeta with one polarization function (TZP)[38] quality. Dispersion corrections have been included following the formalism proposed by Grimme (DFT-D3)[39]. The electron transfer rate is distance dependent (see figure 3A.1 in the appendix), and we fix the nuclear coordinates of the nitrogen in the melamine tail as well as the oxygen in the isocyanuric tail that is furthest from the hydrogen bond interface. This avoids translational motion of the complex and maintains the relative distance, thereby mimicking the environment in a crystal or DNA backbone. Scheme 3.1b shows the relevant molecular orbitals involved in the photoinduced ET process. Upon excitation, an electron is transferred from the melamine HOMO to its LUMO (the LUMO+2 of the total complex, see scheme 3.1b).

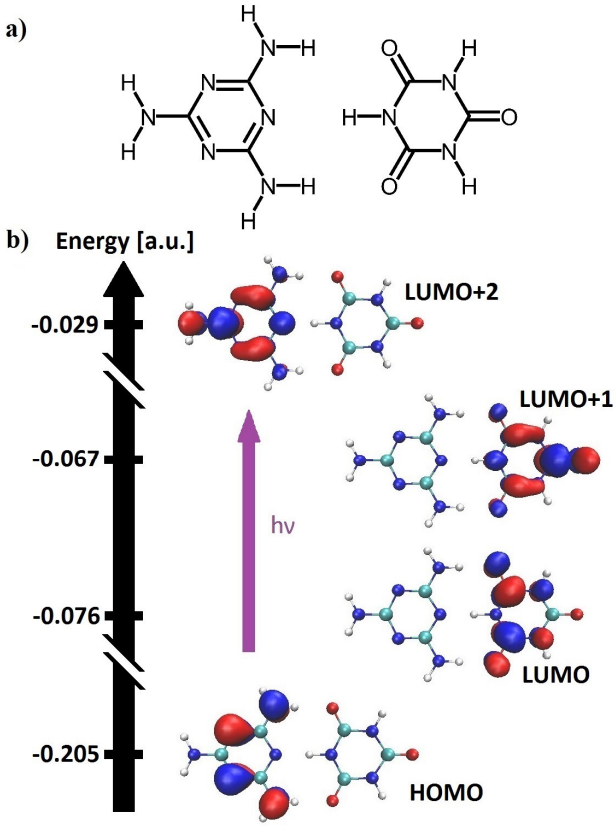

Scheme 3.1. a) Chemical structure of the pseudo base pair melamine (left, donor) and isocyanuric acid (right, acceptor) and **b)** Kohn-Sham orbitals relevant for the photoinduced charge transfer. The melamine is excited from its HOMO (HOMO of the total system) to its LUMO (the LUMO+2 of the total system), with the LUMO and LUMO+1 localized on the acceptor.

This excitation localized on the donor is higher in energy than the charge transfer state from HOMO to LUMO and from HOMO to LUMO+1. This is confirmed by TDDFT (both with BLYP and CAM-B3LYP) calculations, which show that the most relevant excitonic excitation on the donor has the highest oscillator strength in the energy range explored, while the charge transfer state has a lower energy[22] (see appendix 3A.2). This results in an energy gradient upon excitation from the excitonic to the charge transfer state. Ehrenfest dynamics simulations with BLYP[36,37] as exchange correlation functional are performed using the octopus program[40–43]. A nucleus centered spherical grid with a maximum radius of 7.56 Bohr for real space discretization was used; tests have been performed to find the optimal spacing (0.375 Bohr), resulting in a 70.18 Rydberg cut-off. Troullier-Martins pseudopotentials[44]

were used to describe the core electrons. The initial photoinduced electron configuration for the Ehrenfest dynamics was generated by moving one electron from the highest occupied β-orbital to the virtual β-LUMO+2: the β-HOMO occupation was changed to 0, while the β-LUMO+2 occupation was adapted to 1, representing a local excitation on the melamine as shown in scheme 3.1b. A time step of 1 attosecond is used for a total simulation length of 100 fs. The initial nuclear velocities are set to zero. Upon instantaneous excitation in the Franck-Condon region, the system starts to relax towards a more preferable geometry.

To quantify the electron transfer along the trajectory, we integrate the excess β-spin density localized on the acceptor. Since one β-electron is moved from the HOMO to the LUMO+2, β-spin density represents the density of the excited electron, while a lack of β-spin can be associated with the hole. This difference spin density was integrated over two halves of the simulation box, each containing the donor or acceptor molecule, respectively. The integrated density on the acceptor was then used to quantify the amount of electron density transferred during the Ehrenfest trajectory. A Fourier analysis of this electron transfer process was also done, using a gaussian window function with a sigma value of 0.8 to reduce noise.

3.3 Results and Discussion

Photoinduced Electron Transfer and Vibronic Coupling

The integrated (excited) electron density on the acceptor is reported over the trajectory from 0 to 100 fs in figure 3.1a. An oscillating character of the ET process, starting at about 10 fs, is clearly visible. The inset (top of figure 3.1) shows the difference spin density at the beginning and end of the simulation; at the beginning, HOMO and LUMO+2 can clearly be seen in the respective hole and electron densities.

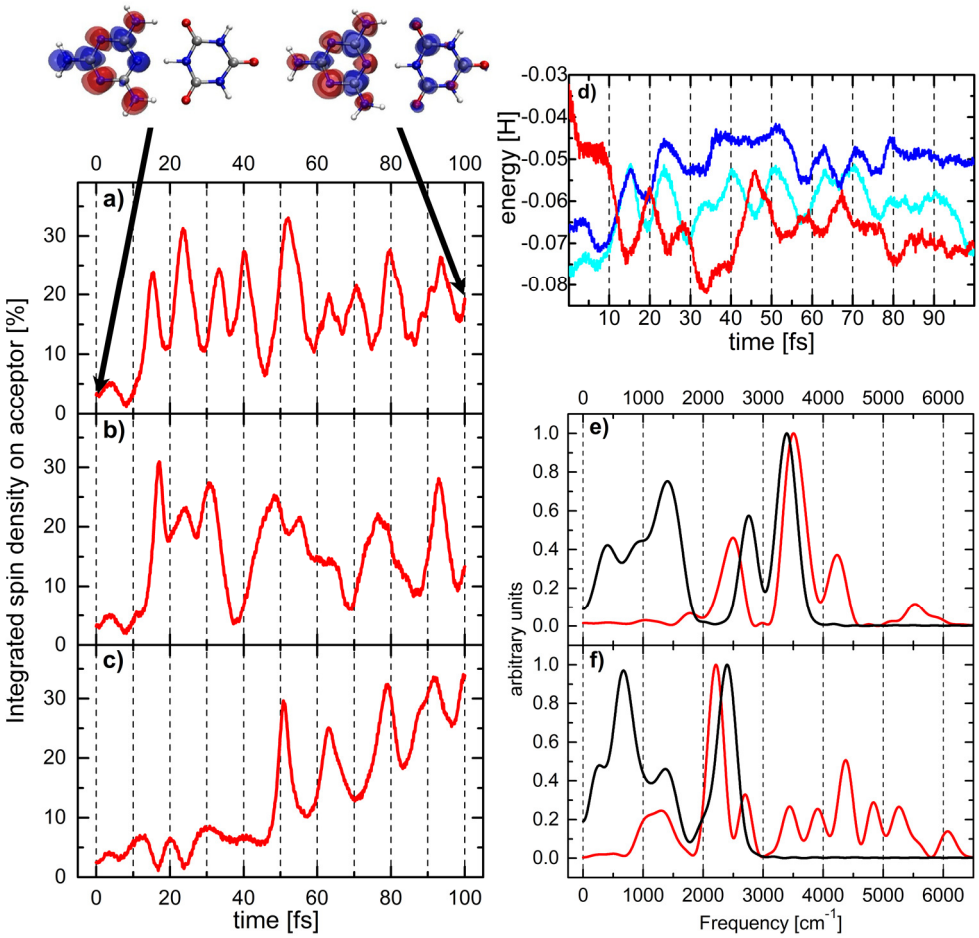

Figure 3.1. a) Electron transfer from the melamine (donor) to the isocyanuric acid (acceptor) quantified by β-spin density localized on the acceptor. Shown on top are snapshots of the difference between α and β spin density ($\rho(\beta) - \rho(\alpha)$) at the beginning and end of the simulation: blue shows excess β-spin density, corresponding to the excited electron, while red is the lack of β-spin density, which can be associated with the hole density. **b)** Electron transfer in fully deuterated melamine-isocyanuric acid system. **c)** Electron transfer for fully symmetrical starting geometry. **d)** Time evolution of the orbital energies of the LUMO+2 (red), LUMO+1 (dark blue) and LUMO (light blue) during the Ehrenfest dynamics simulation of panel a. **e)** Frequency spectrum associated to the electron transfer (red line) obtained by Fourier Transformation (FT) of the electron transfer time evolution shown in panel a and the total vibrational density of states (VDOS) of the pseudo base pair (black line) extracted from the corresponding nuclear trajectory. **f)** Electron transfer frequencies (red line) and total nuclear VDOS (black line) for the fully deuterated system corresponding to panel b.

At the end of the simulation, electron density has been transferred to the acceptor molecule partially populating the LUMO+1 and LUMO. The time evolution of the orbital energies in comparison to the electron transfer is shown in figure 3.1d).

After initial photoexcitation into the LUMO+2, a quick relaxation away from the Franck-Condon region takes place, bringing the orbital energy of the LUMO+2 closer to the LUMO and LUMO+1 energy levels in response to the nuclear motion. The orbital energies start rapidly approaching each other, crossing at approximately 12 fs, close to the first electron transfer maximum (see figure 3.1a). After the first crossing the orbital energies keep oscillating and crossing over time. However, we should keep in mind that this long-term behavior might be due to the mean field approach used, preventing the system to collapse to the lower potential energy surface. This is also the most likely reason why we do not observe complete conversion into the charge transfer state.

Noticeably, if the nuclear coordinates are fixed in the initial optimized geometry, no electron transfer is observed showing the crucial role of nuclear dynamics (see figure 3A.2 in section 3A.3 in the appendix). The Fourier transformation (FT) of the electron transfer time evolution can provide information on the characteristic frequencies associated to this process. Similarly, the total vibrational density of states (VDOS) can be extracted from the nuclear trajectory by performing a FT of the velocity autocorrelation function. In figure 3.1e, ET frequencies and the VDOS computed on the same trajectory corresponding to figure 3.1a are compared. In the frequency spectrum of the ET process, four major peaks can be distinguished at 2495, 3505, 4230 and 5525 cm^{-1} respectively. The two higher frequency peaks can be associated with electronic coherences. In particular, the peak at $\approx$ 4300 cm^{-1} can be assigned to electronic resonances close to the Franck-Condon point since it is prevalent in a purely electronic dynamics trajectory with fixed nuclear positions at the initial geometry (see figure 3A.3 in the appendix). A striking overlap between the VDOS and ET frequencies appears around 3500 cm^{-1}, corresponding to an oscillation time of 9.5 fs, suggesting strong electron-nuclear coupling. This peak in

the VDOS corresponds to the highest frequency modes, the N-H stretching vibrations (see figures 3A.4 to 3A.6 in the appendix, where peaks in the VDOS are assigned to specific nuclear motion). The lowest frequency peak in the ET spectrum at around 2500 cm^{-1} shows significant overlap with a peak in the VDOS associated to the central bridging N-H bond of the isocyanuric acid (see figure 3A.4). C=O stretches and other vibrational modes with $\nu < 2000$ cm^{-1} have a negligible effect on the ET frequency spectrum. Therefore, the N-H stretching modes appear to provide the important vibronic coupling, enabling charge transfer to take place.

Isotope Effect

If the N-H bond stretches are coupled to the photoinduced coherent charge transfer in this system, changing the corresponding vibrational frequency should affect the electron transfer process. Schnedermann *et al.* recently found that isotope effects play a significant role in the vibronically coherent process of photoisomerization of the 11-cis retinal[45]. To explore this hypothesis, we mimic *in silico* an isotope substitution experiment by exchanging all hydrogen atoms by the heavier deuterium isotope. Starting from otherwise identical initial conditions, we perform an Ehrenfest dynamics simulation for the fully deuterated system.

The isotope substitution results in a modified electron transfer pattern as shown in figure 3.1b. In particular, several oscillations at various frequencies contribute to the pattern. These frequencies are shown together with the total VDOS of the corresponding nuclear trajectory in figure 3.1f. The change in frequency of the N-D stretching modes compared to the N-H stretches is clearly visible and is proportional to about $\frac{1}{\sqrt{2}}$, as expected for a localized mode with substitution of ^{1}H by ^{2}D (see also figure 3A.7 in the appendix where a direct comparison of the VDOS for the deuterated and hydrogenated systems is shown). The two distinct N-H peaks (see figure 3.1e) merge in the N-D case, since the energy difference scales according to the isotope shift as well. The lower N-D peak appears as a shoulder at around 2000 cm^{-1}. The lower frequency bands involve C=O and C-N stretches as well as ring

modes and bending modes whose frequencies are not substantially affected by the isotope substitution.

In the high frequency region $\nu > 3000$ cm^{-1}, well resolved electronic frequencies are visible in the ET spectrum. The most dominant peak in the ET frequency spectrum $\nu \approx 2200$ cm^{-1} is resonant with the N-D stretching, as it is red shifted consistently with the shift in the N-D stretching frequency relative to the N-H mode. In addition to the N-D there is an overlap between the nuclear and electronic spectra in the lower frequency region $\nu \approx 1300$ cm^{-1} in contrast to the ^{1}H case. This indicates that also lower frequency nuclear vibrations, *e.g.* C=O and C-N stretching, couple with the ET process. These effects show that the resonance condition between the electronic energy difference and the nuclear vibrational frequencies changes upon isotope substitution. From this result we can already conclude that the N-H stretching is not uniquely essential for facilitating the electron transfer. What is important, is that these N-H modes - due to their high frequencies - are the first nuclear vibrations to match the energy difference between the electronic states during the relaxation process. The isotope substitution moves the resonance condition to lower frequencies. This is shown in a schematic potential energy plot along a generic nuclear relaxation coordinate (scheme 3.2). In the ^{2}D case additional nuclear modes couple to the electronic motion in contrast to the ^{1}H case, where the N-H frequencies are energetically isolated from all other modes.

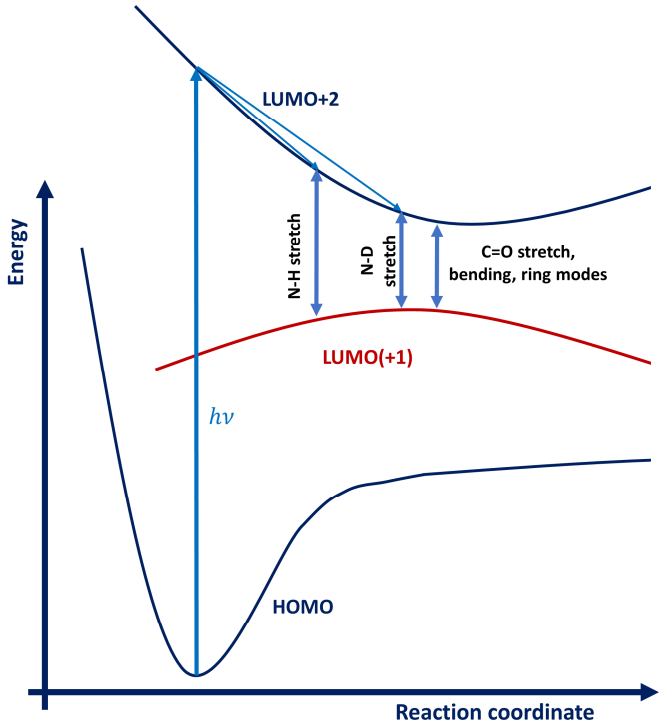

Scheme 3.2. Schematic representation of the coherent process in the investigated system. Upon excitation the system relaxes from the Franck Condon point (FC). In the ^{1}H system, the first available high energy vibrations are due to the N-H stretching and are well separated from the other modes. In the deuterated case, the N-D stretching has a vibrational energy similar to several other modes, which can therefore also couple to the electronic motion.

Dynamic Symmetry Breaking

To investigate the effect of symmetry on the photoinduced charge separation process, an Ehrenfest dynamics simulation was performed starting from an optimized geometry with enforced C_{2v} symmetry. The electron transfer pattern during this simulation can be seen in figure 3.1c, showing a delay of the first significant peak compared to the other two simulations (figure 3.1a, 3.1b). This is surprising considering that the orbital energy differences are small enough for resonant coupling with available nuclear modes within the first 10 fs (see figure 3A.8 in the appendix).

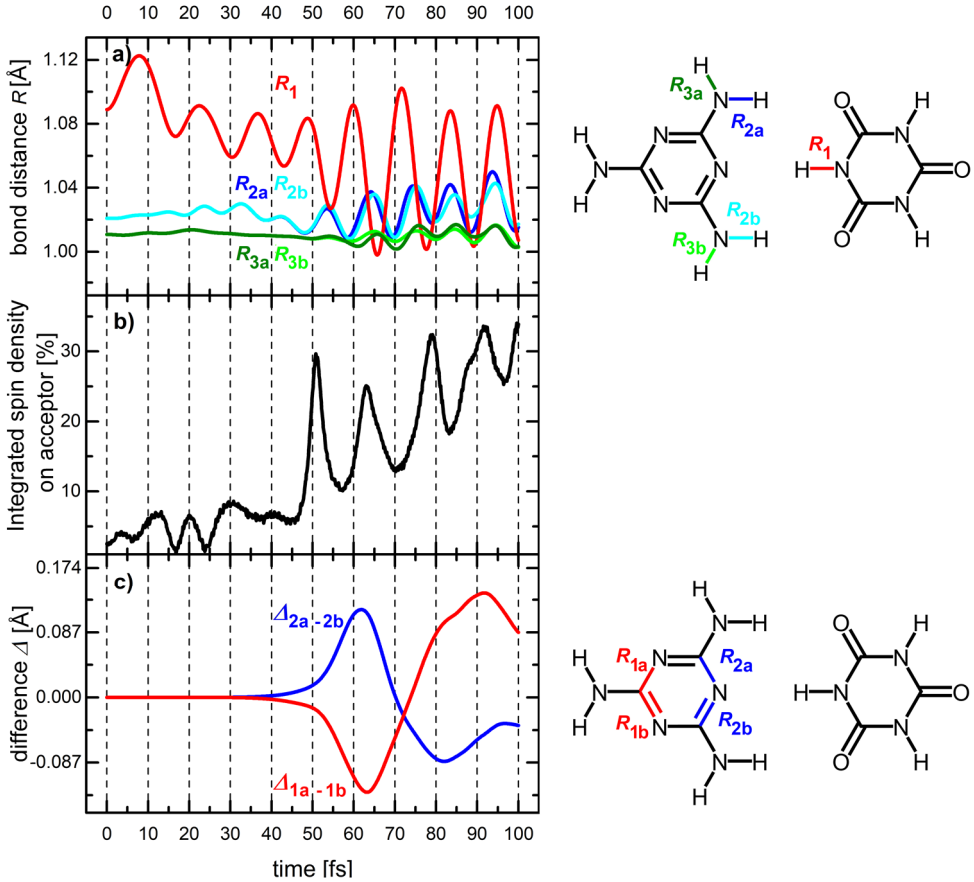

Figure 3.2. a) Time evolution of the N-H bond distances *R* for the donor-acceptor system with enforced starting C_{2v} symmetry. Different colors correspond to different bonds indicated in the chemical structure on the right. **b)** Electron transfer pattern for the same trajectory. **c)** Difference *Δ* in bond length *R* between symmetry equivalent C-N bonds shown in the chemical structure on the right.

To explain this suppression of coherent charge transfer, we need a more detailed investigation of the initial geometric relaxation. In figure 3.2a, the time evolution of the interfacial N-H bond distances (that were the most relevant in the previous cases) is compared with the electron transfer (figure 3.2b).

Two main messages can be extracted from figure 3.2a: *i*) Upon electronic excitation, symmetry equivalent bonds with respect to the C_2-axis (2a and 2b; 3a and 3b) are evolving in a perfectly identical manner, maintaining the C_{2v}-symmetry. Only when the electron transfer starts, the deviation from C_{2v}-symmetry gradually

increases from around 50 fs. *ii*) The amplitude of the N-H bond oscillations increases dramatically during the electron transfer process, suggesting that electronic energy is transferred into these nuclear vibrations.

The question arises whether the electron transfer induces this divergence from the C_{2v} symmetric motion, or conversely, it is the breaking of symmetry that allows for the electron transfer in the first place. To address this question, it is helpful to look at the difference in bond length between symmetry equivalent bonds with respect to the C_2-axis. We find that the pairs of bonds that first diverge from perfect symmetric motion are C-N bonds in the aromatic ring of the donor molecule (see figure 3A.9 in the appendix showing all symmetry equivalent pairs). In figure 3.2c, the bond length difference $\Delta_{1a-1b} = R_{1a} - R_{1b}$between the two bonds 1a and 1b, as well as the bond length difference $\Delta_{2a-2b} = R_{2a} - R_{2b}$ between bonds 2a and 2b are shown. At $t \approx$ 35 fs, the bond lengths start to diverge: bond 1a shortens, while 1b elongates and at the same time bond 2a increases while bond 2b decreases in length. The combination of these concerted expansions and compressions corresponds to a normal mode of the donor molecule of the A_2' irreducible representation of the D3h group which is the point group of both melamine and isocyanuric acid when in isolation. This A_2' irreducible representation also includes rotation around the *z* axis which is oriented perpendicular to the molecular plane. This motion breaks the initial C_{2v}-symmetry. Two equivalent modes rotating in opposite directions around the *z*-axis exist that could be excited. Once a small preference, for instance due to numerical noise in the integration of the equations of motion, is given to a rotation in one direction in favor of its counter rotating equivalent, asymmetric motion will emerge. About 45 fs into the simulation, which is around 10 fs after the onset of the asymmetric motion, the electron transfer process starts, responding to the breaking of symmetry. This underlines the importance of dynamic symmetry breaking in photoinduced coherent charge transfer. In a system interacting with its environment, there will always be a slight preference to one component over the other, resulting in symmetry breaking. This holds especially true when coupled to a thermal bath or in a chiral environment.

The displacement from the symmetric geometry, at t = 45 fs, when the ET process starts, is about 0.01 Å. This small displacement will already be present at extremely low temperatures. Still, these results already suggest a design principle for systems to optimize coherent charge transfer: breaking the symmetry as initial condition, *e.g.* by using chiral motifs. This principle is well in line with natural photosynthetic systems, which are built from chiral proteins and cofactors.[46,47]

Similarities with other Adiabatic Passage Processes

We stress the similarity between the coherent charge transfer and the well-established adiabatic passage processes observed during adiabatic pulses in both NMR and optical spectroscopy[30,31]: In this work we have a process that can be described as population change between two states - an excitonic and a charge transfer state. The two states have an energy difference corresponding to a radial frequency ω_e, that is modulated over time due to relaxation from the Franck Condon point (see scheme 3.2). This closely mirrors the radiofrequency ω_{rf} in an NMR adiabatic pulse experiment and the laser frequency ω_L in a chirped laser pulse in optical spectroscopy. In all three cases, we sweep towards a resonance condition, in our case $\omega_e = \omega_n$, with ω_n being an available nuclear frequency. As we approach the resonance, nonadiabatic coupling increases significantly. The electronic motion slows down, the time scales of nuclear and electronic motion converge, making exchange between the nuclear and electronic system possible by vibronic coupling. As in the two adiabatic passage processes mentioned earlier, (*i*) the NMR adiabatic pulse for reversal of magnetization, and (*ii*) chirped laser pulses with change of orbital angular momentum, a change of population from the excitonic state to the charge transfer state can be observed (see electron transfer in figure 3.1a-c), showing characteristic oscillations of frequency ω_n. Moving into the interaction frame corresponding to this ω_n, this exchange should then be smooth, again similar to the mentioned other processes. Within the interaction frame of the electronic frequency ω_e however, similarly to the case of the interaction frame of the laser pulse in optical

spectroscopy or the radio frequency in an adiabatic pulse experiment in NMR, there is a precession around the interaction frame axis, due to the mismatch of ω_e and ω_n when sweeping ω_e. At the resonance condition $\omega_e = \omega_n$, the nonadiabatic coupling is strongest and the populations of state 1 and 2 will be $p_1 = p_2 = ½$ each. As the system moves out of resonance, with $\omega_e < \omega_n$, the system further evolves into full conversion with $p_1 = 0$ and $p_2 = 1$. In our simulation, due to the mean field approach used, we cannot observe this full conversion, since the system is trapped in the coherent superposition state and does not collapse into an adiabatic state (see chapter 2.5). Still, due to the many parallels observed between this coherent charge transfer process on one side and adiabatic pulses and chirped laser pulse experiments on the other side, our results support a nonadiabatic conversion via adiabatic passage (NCAP) process.

Exchange of Angular Momentum

Since the system evolves from one quantum state to another, a change of quantum number is involved. Normally, transitions between electronic states follow selection rules, leading to transitions only being allowed via *e.g.* the release or absorption of a photon carrying an angular momentum. Also for the non-radiative exciton to charge transfer transition in our study the change in quantum number has to be accompanied by a change of an associated physical quantity. In a publication by Purchase *et al.*, the authors stressed the importance of convergence of time scales of nuclear and electronic circulating motion in a molecule for coherent charge transfer and suggested the exchange of angular momentum between the electronic and nuclear subsystems in a semiclassical coherent process.[32] Coupling of quantum and classical rotation is well established in other fields of chemistry and chemical physics, where it has been shown that transitions in quantum subspaces give rise to observable rotations in a suitable interaction frame of the classical motion.[48] Since in the Ehrenfest simulations, the conservation of total angular momentum is not enforced, we rather monitor collective motion in both the electronic as well as nuclear

subsystems by following the orientational change in the electronic and nuclear components of the dipole moment, which we introduce here as a descriptive parameter for the process. The generated charge transfer state results in a large electronic dipole moment change along the *x*-axis, potentially masking any other orientational change. Therefore, we focus on the dipole moment associated with the α-electrons since they are not directly involved in the charge transfer process and yet still respond to the electron transfer. The orientation of this dipole moment in the *x*-*y* plane during the Ehrenfest dynamics with symmetric starting condition is shown in figure 3.3a.

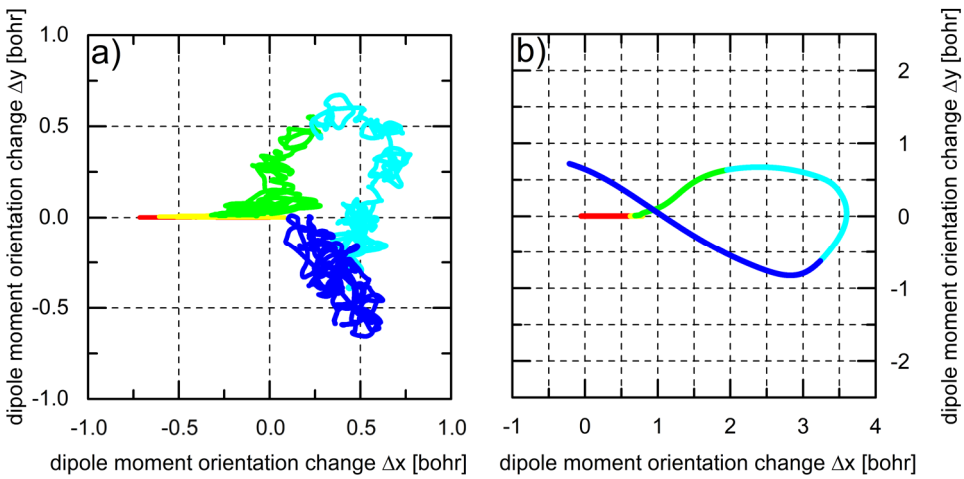

Figure 3.3. a) Orientation of the dipole moment associated with *α*-electrons in the *x*-*y* plane for the simulation starting with enforced symmetric geometry. The colors correspond to consecutive time intervals, starting from red (0<*t*<20 fs) to yellow (20<*t*<40 fs), green (40<*t*<60 fs), light blue (60<*t*<80 fs) and dark blue (80<*t*<100 fs). The rotational character starting around *t* = 40 fs is clearly visible. **b)** Change of orientation of the dipole moment associated with the nitrogen and hydrogen nuclei involved in the N-H stretches coupled to the electron transfer process. The colors correspond to consecutive time intervals, starting from red (0<*t*<20 fs) to yellow (20<*t*<40 fs), green (40<*t*<60 fs), light blue (60<*t*<80 fs) and dark blue (80<*t*<100 fs). The correlation between this nuclear dipole moment orientation and the electronic dipole moment orientation in a) is apparent.

Within the first ~35 fs, the dipole moment only changes along the *x*-axis, conserving symmetry. Upon the breaking of symmetry, the dipole moment starts to deviate from its initial orientation along the *x*-axis. At around *t* = 45 fs, when the

electron transfer process starts, a clear clockwise rotation with an angular momentum in the negative z-axis direction starts.

According to Purchase *et al.*, this change in electronic angular momentum should be associated with a net rotation in the interaction frame of the nuclear motion of the coupled mode.[32] We should therefore see the same rotational behavior if we plot the dipole moment orientation change of all the nuclei involved in N-H covalent bond vibrations, which we have shown to be crucial for the coherent photoinduced charge transfer. The change in this nuclear dipole moment orientation reflects the net rotation in the interaction frame associated with the nuclear mode and is shown in figure 3.3b. There is a clear correlation in the rotation of this nuclear dipole moment and the rotation of the dipole moment associated with the α-electrons. After about 35 fs, the symmetry breaks, leading to deviation of both dipole moment orientations from the x-axis. At around $t = 45$ fs, at the onset of electron transfer, both the nuclear as well as electronic dipole moment start to rotate in unison in the molecular plane, maintaining correlation until about 80 fs into the simulation, where noise in the electronic system appears to obscure this connection. The change in quantum number therefore involves the gradual exchange of angular momentum between the electronic and nuclear system. For completeness, the dipole moment associated with the β-spin density in the symmetric case and the dipole moment associated with the α-electrons in the asymmetric simulation shown in figures 3A.10 and 3A.11 in the appendix.

3.4 Conclusion

In summary, the photoinduced coherent charge transfer in this donor-acceptor system can be described as follows: Upon excitation into the Franck-Condon region in the excited state localized on the donor molecule, the system relaxes towards lower energetic regions of the excited state PES. During this relaxation, the system explores regions of strong coupling between the excitonic and lower energy charge transfer states as they approach each other energetically. As soon as the energy difference between these two states (one occupied, one unoccupied), is in resonance with a nuclear vibration available in the system, the nuclear vibration couples to the electronic motion and drives the electron transfer in a resonant process. A crucial condition for an efficient conversion process is the dynamic breaking of symmetry. Furthermore, the change in quantum number associated with the non-radiative transition between quantum states leads to a net exchange of angular momentum into the coupled vibrational state. Which particular nuclear mode first reaches the resonance condition depends on the specific potential energy surfaces involved in the electron transfer process. Thus, the process is robust as it self-selects a rapid channel to the output. In the melamine-isocyanuric acid system the highest N-H bond frequencies are the first and most important modes reaching the resonance condition. Due to the energetic gap between the N-H stretches and all other modes, the N-H bonds drive the electron transfer almost exclusively. This results in a relatively clean oscillatory pattern in the electron transfer process. When exchanging hydrogens by deuterium, the system relaxes to a region where the involved states are closer in energy. The difference between the N-D stretches and the lower frequency modes is now smaller and thus additional modes can drive the charge transfer. Therefore, more frequencies are involved and a more complex electron transfer pattern emerges. In spite of the specificity of this donor-acceptor complex, we believe these principles are playing a role in natural systems and might help interpreting experimental data on coherent charge transfer.

3.5 References

(1) Groot, M. L.; Pawlowicz, N. P.; Wilderen, L. J. G. W. van; Breton, J.; Stokkum, I. H. M. van; Grondelle, R. van. Initial Electron Donor and Acceptor in Isolated Photosystem II Reaction Centers Identified with Femtosecond Mid-IR Spectroscopy. *PNAS* **2005**, *102* (37), 13087–13092.

(2) Durrant, J. R.; Klug, D. R.; Kwa, S. L.; Grondelle, R. van; Porter, G.; Dekker, J. P. A Multimer Model for P680, the Primary Electron Donor of Photosystem II. *PNAS* **1995**, *92* (11), 4798–4802.

(3) Romero, E.; van Stokkum, I. H. M.; Novoderezhkin, V. I.; Dekker, J. P.; van Grondelle, R. Two Different Charge Separation Pathways in Photosystem II. *Biochemistry* **2010**, *49* (20), 4300–4307.

(4) Faunce, T. A.; Lubitz, W.; Rutherford, A. W. (Bill); MacFarlane, D.; Moore, G. F.; Yang, P.; Nocera, D. G.; Moore, T. A.; Gregory, D. H.; Fukuzumi, S.; Yoon, K. B.; Armstrong, F. A.; Wasielewski, M. R.; Styring, S. Energy and Environment Policy Case for a Global Project on Artificial Photosynthesis. *Energy Environ. Sci.* **2013**, *6* (3), 695–698.

(5) Faunce, T.; Styring, S.; Wasielewski, M. R.; Brudvig, G. W.; Rutherford, A. W.; Messinger, J.; Lee, A. F.; Hill, C. L.; deGroot, H.; Fontecave, M.; MacFarlane, D. R.; Hankamer, B.; Nocera, D. G.; Tiede, D. M.; Dau, H.; Hillier, W.; Wang, L.; Amal, R. Artificial Photosynthesis as a Frontier Technology for Energy Sustainability. *Energy Environ. Sci.* **2013**, *6* (4), 1074–1076.

(6) Tachibana, Y.; Vayssieres, L.; Durrant, J. R. Artificial Photosynthesis for Solar Water-Splitting. *Nat Photon* **2012**, *6* (8), 511–518.

(7) Kim, D.; Sakimoto, K. K.; Hong, D.; Yang, P. Artificial Photosynthesis for Sustainable Fuel and Chemical Production. *Angew. Chem. Int. Ed.* **2015**, *54* (11), 3259–3266.

(8) Yu, Z.; Li, F.; Sun, L. Recent Advances in Dye-Sensitized Photoelectrochemical Cells for Solar Hydrogen Production Based on Molecular Components. *Energy Environ. Sci.* **2015**, *8* (3), 760–775.

(9) Scholes, G. D. Coherence from Light Harvesting to Chemistry. *J. Phys. Chem. Lett.* **2018**, *9* (7), 1568–1572.

(10) Jumper, C. C.; Rafiq, S.; Wang, S.; Scholes, G. D. From Coherent to Vibronic Light Harvesting in Photosynthesis. *Current Opinion in Chemical Biology* **2018**, *47*, 39–46.

(11) Scholes, G. D.; Fleming, G. R.; Olaya-Castro, A.; van Grondelle, R. Lessons from Nature about Solar Light Harvesting. *Nat Chem* **2011**, *3* (10), 763–774.

(12) Romero, E.; Augulis, R.; Novoderezhkin, V. I.; Ferretti, M.; Thieme, J.; Zigmantas, D.; van Grondelle, R. Quantum Coherence in Photosynthesis for Efficient Solar-Energy Conversion. *Nat Phys* **2014**, *10* (9), 676–682.

(13) Scholes, G. D.; Fleming, G. R.; Chen, L. X.; Aspuru-Guzik, A.; Buchleitner, A.; Coker, D. F.; Engel, G. S.; van Grondelle, R.; Ishizaki, A.; Jonas, D. M.; Lundeen, J. S.; McCusker, J. K.; Mukamel, S.; Ogilvie, J. P.; Olaya-Castro, A.; Ratner, M. A.; Spano, F. C.; Whaley, K. B.; Zhu, X. Using Coherence to Enhance Function in Chemical and Biophysical Systems. *Nature* **2017**, *543* (7647), 647–656.

(14) Chenu, A.; Scholes, G. D. Coherence in Energy Transfer and Photosynthesis. *Annual Review of Physical Chemistry* **2015**, *66* (1), 69–96.

(15) Engel, G. S.; Calhoun, T. R.; Read, E. L.; Ahn, T.-K.; Mančal, T.; Cheng, Y.-C.; Blankenship, R. E.; Fleming, G. R. Evidence for Wavelike Energy Transfer through Quantum Coherence in Photosynthetic Systems. *Nature* **2007**, *446* (7137), 782–786.

(16) Fuller, F. D.; Pan, J.; Gelzinis, A.; Butkus, V.; Senlik, S. S.; Wilcox, D. E.; Yocum, C. F.; Valkunas, L.; Abramavicius, D.; Ogilvie, J. P. Vibronic Coherence in Oxygenic Photosynthesis. *Nature Chemistry* **2014**, *6* (8), 706–711.

(17) Collini, E.; Wong, C. Y.; Wilk, K. E.; Curmi, P. M. G.; Brumer, P.; Scholes, G. D. Coherently Wired Light-Harvesting in Photosynthetic Marine Algae at Ambient Temperature. *Nature* **2010**, *463* (7281), 644–647.

(18) Tiwari, V.; Peters, W. K.; Jonas, D. M. Electronic Resonance with Anticorrelated Pigment Vibrations Drives Photosynthetic Energy Transfer Outside the Adiabatic Framework. *PNAS* **2013**, *110* (4), 1203–1208.
(19) Thyrhaug, E.; Tempelaar, R.; Alcocer, M. J. P.; Žídek, K.; Bína, D.; Knoester, J.; Jansen, T. L. C.; Zigmantas, D. Identification and Characterization of Diverse Coherences in the Fenna–Matthews–Olson Complex. *Nature Chemistry* **2018**, *10* (7), 780–786.
(20) Ma, F.; Romero, E.; Jones, M. R.; Novoderezhkin, V. I.; van Grondelle, R. Vibronic Coherence in the Charge Separation Process of the Rhodobacter Sphaeroides Reaction Center. *J. Phys. Chem. Lett.* **2018**, *9* (8), 1827–1832.
(21) Chin, A. W.; Prior, J.; Rosenbach, R.; Caycedo-Soler, F.; Huelga, S. F.; Plenio, M. B. The Role of Non-Equilibrium Vibrational Structures in Electronic Coherence and Recoherence in Pigment-Protein Complexes. *Nat Phys* **2013**, *9* (2), 113–118.
(22) Eisenmayer, T. J.; Buda, F. Real-Time Simulations of Photoinduced Coherent Charge Transfer and Proton-Coupled Electron Transfer. *ChemPhysChem* **2014**, *15* (15), 3258–3263.
(23) Akimov, A. V.; Neukirch, A. J.; Prezhdo, O. V. Theoretical Insights into Photoinduced Charge Transfer and Catalysis at Oxide Interfaces. *Chem. Rev.* **2013**, *113* (6), 4496–4565.
(24) Monti, A.; Negre, C. F. A.; Batista, V. S.; Rego, L. G. C.; de Groot, H. J. M.; Buda, F. Crucial Role of Nuclear Dynamics for Electron Injection in a Dye–Semiconductor Complex. *J. Phys. Chem. Lett.* **2015**, *6* (12), 2393–2398.
(25) Falke, S. M.; Rozzi, C. A.; Brida, D.; Maiuri, M.; Amato, M.; Sommer, E.; Sio, A. D.; Rubio, A.; Cerullo, G.; Molinari, E.; Lienau, C. Coherent Ultrafast Charge Transfer in an Organic Photovoltaic Blend. *Science* **2014**, *344* (6187), 1001–1005.
(26) Andrea Rozzi, C.; Maria Falke, S.; Spallanzani, N.; Rubio, A.; Molinari, E.; Brida, D.; Maiuri, M.; Cerullo, G.; Schramm, H.; Christoffers, J.; Lienau, C. Quantum Coherence Controls the Charge Separation in a Prototypical Artificial Light-Harvesting System. *Nat Commun* **2013**, *4*, 1602.
(27) Park, M.; Im, D.; Rhee, Y. H.; Joo, T. Coherent and Homogeneous Intramolecular Charge-Transfer Dynamics of 1-Tert-Butyl-6-Cyano-1,2,3,4-Tetrahydroquinoline (NTC6), a Rigid Analogue of DMABN. *J. Phys. Chem. A* **2014**, *118* (28), 5125–5134.
(28) Perdigão, L. M. A.; Champness, N. R.; Beton, P. H. Surface Self-Assembly of the Cyanuric Acid–Melamine Hydrogen Bonded Network. *Chem. Commun.* **2006**, *0* (5), 538–540.
(29) Prokhorenko, V. I.; Picchiotti, A.; Pola, M.; Dijkstra, A. G.; Miller, R. J. D. New Insights into the Photophysics of DNA Nucleobases. *The Journal of Physical Chemistry Letters* **2016**, *7* (22), 4445–4450.
(30) Tannús, G. Adiabatic Pulses. *NMR IN BIOMEDICINE* **1997**, *10*, 12.
(31) Wollenhaupt, M.; Präkelt, A.; Sarpe-Tudoran, C.; Liese, D.; Baumert, T. Quantum Control by Selective Population of Dressed States Using Intense Chirped Femtosecond Laser Pulses. *Appl. Phys. B* **2006**, *82* (2), 183–188.
(32) Purchase R. L.; de Groot H. J. M. Biosolar Cells: Global Artificial Photosynthesis Needs Responsive Matrices with Quantum Coherent Kinetic Control for High Yield. *Interface Focus* **2015**, *5* (3), 20150014.
(33) Purchase, R.; Cogdell, R.; Breitling, F.; Stadler, V.; van Hulst, N.; Kramer, G.-J.; Ramirez, A.; Zwijnenberg, R.; Kallergi, A.; de Baan, J. B.; Rudra, I.; de Groot, H. J. M. Semi-Synthetic Responsive Matrices for Artificial Photosynthesis. In *Series on Chemistry, Energy and the Environment*; WORLD SCIENTIFIC, 2019; pp 47–69.
(34) Velde, G. te; Bickelhaupt, F. M.; Baerends, E. J.; Fonseca Guerra, C.; van Gisbergen, S. J. A.; Snijders, J. G.; Ziegler, T. Chemistry with ADF. *J. Comput. Chem.* **2001**, *22* (9), 931–967.
(35) ADF2013, http://www.scm.com, SCM, Theoretical Chemistry, Vrije Universiteit, Amsterdam, The Netherlands. .
(36) Becke, A. D. Density-Functional Exchange-Energy Approximation with Correct Asymptotic Behavior. *Phys. Rev. A* **1988**, *38* (6), 3098–3100.
(37) Lee, C.; Yang, W.; Parr, R. G. Development of the Colle-Salvetti Correlation-Energy Formula into a Functional of the Electron Density. *Phys. Rev. B* **1988**, *37* (2), 785–789.

(38) Van Lenthe, E.; Baerends, E. J. Optimized Slater-Type Basis Sets for the Elements 1–118. *Journal of Computational Chemistry* **2003**, *24*, 1142–1156.
(39) Grimme; others. A Consistent and Accurate Ab Initio Parametrization of Density Functional Dispersion Correction (DFT-D) for the 94 Elements H-Pu. *J. Chem. Phys.* **2010**, *132* (715).
(40) Andrade, X.; Alberdi-Rodriguez, J.; Strubbe, D. A.; Oliveira, M. J. T.; Fernando Nogueira; Castro, A.; Muguerza, J.; Arruabarrena, A.; Louie, S. G.; Aspuru-Guzik, A.; Angel Rubio; Marques, M. A. L. Time-Dependent Density-Functional Theory in Massively Parallel Computer Architectures: The Octopus Project. *J. Phys.: Condens. Matter* **2012**, *24* (23), 233202.
(41) Castro, A.; Appel, H.; Oliveira, M.; Rozzi, C. A.; Andrade, X.; Lorenzen, F.; Marques, M. a. L.; Gross, E. K. U.; Rubio, A. Octopus: A Tool for the Application of Time-Dependent Density Functional Theory. *physica status solidi (b)* **2006**, *243* (11), 2465–2488.
(42) Marques, M. A. L.; Castro, A.; Bertsch, G. F.; Rubio, A. Octopus: A First-Principles Tool for Excited Electron–Ion Dynamics. *Computer Physics Communications* **2003**, *151* (1), 60–78.
(43) Castro, A.; Marques, M. A. L.; Rubio, A. Propagators for the Time-Dependent Kohn–Sham Equations. *The Journal of Chemical Physics* **2004**, *121* (8), 3425–3433.
(44) Troullier, N.; Martins, J. L. Efficient Pseudopotentials for Plane-Wave Calculations. *Phys. Rev. B* **1991**, *43* (3), 1993–2006.
(45) Schnedermann, C.; Yang, X.; Liebel, M.; Spillane, K. M.; Lugtenburg, J.; Fernández, I.; Valentini, A.; Schapiro, I.; Olivucci, M.; Kukura, P.; Mathies, R. A. Evidence for a Vibrational Phase-Dependent Isotope Effect on the Photochemistry of Vision. *Nature Chem* **2018**, *10* (4), 449–455.
(46) Eisenmayer, T. J.; de Groot, H. J. M.; van de Wetering, E.; Neugebauer, J.; Buda, F. Mechanism and Reaction Coordinate of Directional Charge Separation in Bacterial Reaction Centers. *J. Phys. Chem. Lett.* **2012**, *3* (6), 694–697.
(47) Moore, L. J.; Zhou, H.; Boxer, S. G. Excited-State Electronic Asymmetry of the Special Pair in Photosynthetic Reaction Center Mutants: Absorption and Stark Spectroscopy. *Biochemistry* **1999**, *38* (37), 11949–11960.
(48) Boender, G. J.; Vega, S.; Groot, H. J. M. D. A Physical Interpretation of the Floquet Description of Magic Angle Spinning Nuclear Magnetic Resonance Spectroscopy. *Molecular Physics* **1998**, *95* (5), 921–934.

3.A Appendix

3A.1 Geometries and Effect of Intermolecular Distance

In figure 3A.1, we show the electron transfer time evolution for a trajectory with an intermolecular distance increased by 1 Å compared to the optimized geometry. As is clearly visible, this is already enough to inhibit the charge transfer process on the time scale of the simulation.

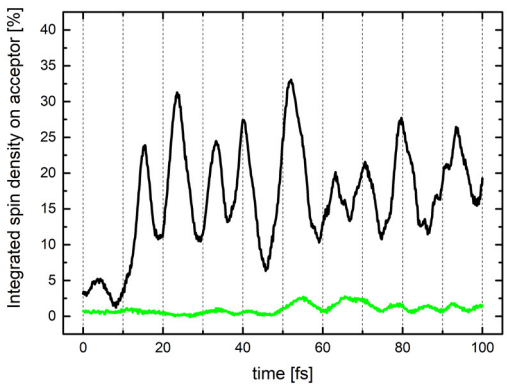

Figure 3A.1. Comparison of the electron transfer pattern starting from optimized geometry (black) and a geometry with an intermolecular distance increased by 1Å (green). This increase in intermolecular distance is enough to inhibit the charge transfer process within the time scale investigated.

The initial geometries used for the Ehrenfest dynamics are given in tables 3A.1

Table 3A.1. Initial geometry (in Bohr) used for the Ehrenfest dynamics a) without enforced C_{2v}-symmetry and b) with enforced C_{2v}-symmetry. The fixed atoms are marked with *

a)

N	-2.001614	0.031842	0.000000
C	-3.426373	-2.135237	0.000000
C	-3.379525	2.278876	0.000000
N	-5.992697	-2.227231	0.000000
N	-5.949866	2.399089	0.000000
C	-7.117530	0.115311	0.000000
N	-2.123401	4.418507	0.000000
N	-2.233755	-4.326562	0.000000
N	-9.614457	0.117436	0.000000 *
H	-0.114494	4.450706	0.000000
H	-3.121367	6.044066	0.000000
H	-3.274394	-5.947841	0.000000
H	-0.239847	-4.434270	0.000000
H	-10.533707	1.851824	0.000000
H	-10.585442	-1.583609	0.000000
C	8.517469	-0.165043	0.000000
N	7.061556	-2.324476	0.000000
N	7.095488	2.110390	0.000000
C	4.427971	-2.407892	0.000000
C	4.517363	2.253758	0.000000
N	3.358169	-0.044253	0.000000
O	10.757456	-0.132269	0.000000 *
O	3.346296	4.294753	0.000000
O	3.319715	-4.429777	0.000000
H	7.996239	-3.989308	0.000000
H	8.097476	3.783894	0.000000
H	1.213266	-0.002685	0.000000

b)

N	-2.603536	0.000000	0.000000
C	-3.999683	-2.168130	0.000000
C	-3.999683	2.168130	0.000000
N	-6.546495	-2.279433	0.000000
N	-6.546495	2.279433	0.000000
C	-7.692047	0.000000	0.000000
N	-2.739492	4.396637	0.000000
N	-2.739492	-4.396637	0.000000
N	-10.268718	0.000000	0.000000 *
H	-0.811858	4.473371	0.000000
H	-3.780779	5.997919	0.000000
H	-3.780779	-5.997919	0.000000
H	-0.811858	-4.473371	0.000000
H	-11.205478	1.663445	0.000000
H	-11.205478	-1.663445	0.000000
C	7.978317	0.000000	0.000000
N	6.508749	-2.192863	0.000000
N	6.508749	2.192863	0.000000
C	3.868282	-2.314315	0.000000
C	3.868282	2.314315	0.000000
N	2.646694	0.000000	0.000000
O	10.286523	0.000000	0.000000 *
O	2.763579	4.365135	0.000000
O	2.763579	-4.365135	0.000000
H	7.449109	-3.869490	0.000000
H	7.449109	3.869490	0.000000
H	0.588848	0.000000	0.000000

3A.2 Excitation energies with Time dependent DFT

To classify important electronic excitations of the pseudo base pair system, linear-response time dependent DFT calculations were performed with the Amsterdam Density Functional program (ADF)[1,2]. Since BLYP[3,4] is known to poorly describe charge transfer excitations, we calculated the first 30 excitations using also the long range corrected CAM-B3LYP[5] exchange correlation functional and a TZP[6] basis set with D3 dispersion corrections[7]. The relative orbital alignment of the relevant orbitals for BLYP and CAM-B3LYP are given as energy differences in table 3A.2.

Table 3A.2. Orbital energy differences between HOMO/LUMO, LUMO/LUMO+1 and LUMO+1/LUMO+2 for BLYP and CAM-B3LYP.

Transition	BLYP	CAM-B3LYP
ΔE LUMO-HOMO [Hartree]	0.129	0.308
ΔE (LUMO+1)-LUMO [Hartree]	0.009	0.006
ΔE (LUMO+2)-(LUMO+1) [Hartree]	0.038	0.031

As expected for a hybrid functional, the HOMO-LUMO gap is significantly increased in CAM-B3LYP in comparison to the GGA BLYP. However, there is no rearrangement in the four relevant orbitals active in the charge transfer process. Excitation energies and oscillator strengths for the most relevant excitonic and charge transfer excitations are reported in table 3A.3. As expected for a GGA functional, BLYP strongly underestimates the charge transfer excitation energy. However, for both functionals, the energy of the excitonic state is higher in comparison to the charge transfer state. Furthermore, the oscillator strength of the excitonic state is in both cases larger than for the charge transfer state.

Table 3A.3. Excitation energies and Oscillator strength for the most relevant charge transfer and exciton excited states in the melamine-isocyanuric acid pseudo base pair determined by TDDFT with BLYP and CAM-B3LYP.

	BLYP		CAM-B3LYP	
	Energy [eV]	Oscillator strength	Energy [eV]	Oscillator strength
Charge transfer excitation	3.680	0.0037	6.407	0.1220
Excitonic excitation localized on the donor	6.1834	0.2767	6.905	0.6140

3A.3 Ehrenfest dynamics with frozen nuclear geometry

Electron dynamics simulations were performed with fixed nuclear degrees of freedom. Two different geometries were investigated: the initial geometry at the start of the Ehrenfest dynamics (from here on called simulation G0) and the geometry from the Ehrenfest trajectory at 10.7 fs, approximately the time where the electron transfer process starts (named simulation G1). The latter geometry lies therefore within the region where the involved electronic states are closely coupled. The total simulation time was 50 fs with a time step of 1 as. The integrated spin density on the acceptor as a function of time is shown in figure 3A.2.

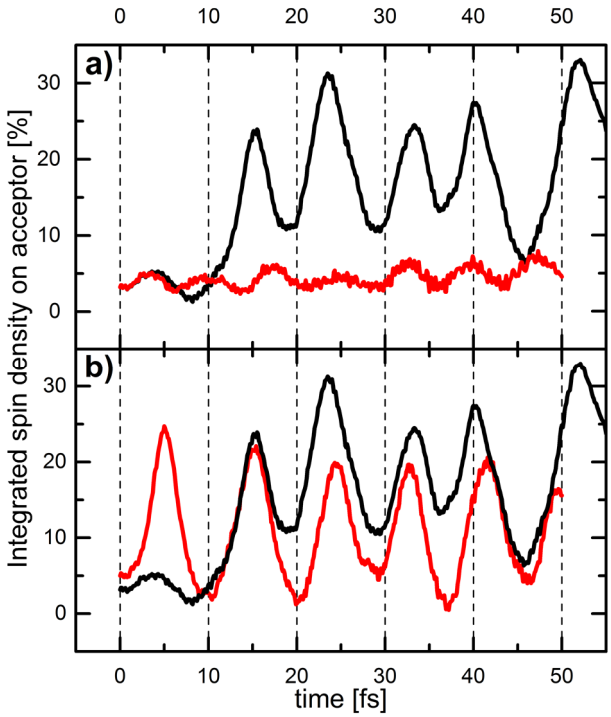

Figure 3A.2. Comparison of the electron transfer pattern for unconstrained nuclear degrees of freedom (black) with the transfer pattern of a simulation with the nuclear coordinates kept fixed at the initial geometry (simulation G0, **a**, red) and with the pattern for fixed nuclear coordinates at the geometry taken at 10.7 fs of the original trajectory, when the electron transfer starts (simulation G1, **b**, red).

A frequency analysis of the electron transfer patterns of these three simulations is presented in figure 3A.3 The peaks at around 4300 cm^{-1} and 5500 cm^{-1} corresponding to the trajectory with free nuclei show significant overlap with the frequencies of electron density oscillations in the case of the frozen initial geometry (simulation G0). This strongly suggests that the high frequency oscillations are due to the coupling between electronic states at a geometry close to the Franck-Condon point. The main peak at about 3500 cm^{-1} shows instead significant overlap with the electron

density oscillation frequency extracted from simulation G1, where the nuclei were fixed at a geometry in the strong coupling regime. This is also the peak that has a large overlap with the N-H bond vibrations. This shows that at this specific geometry, a resonance between electronic energy difference and nuclear vibration (the N-H stretches) has emerged.

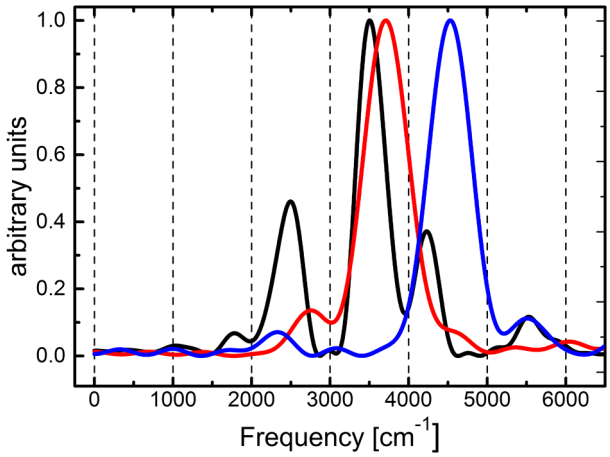

Figure 3A.3. Frequencies of electron transfer processes: in black, ET pattern during Ehrenfest simulation with free nuclear degrees of freedom, in blue ET transfer frequencies with nuclear degrees of freedom kept fixed at the initial geometry (simulation G0), in red ET transfer frequencies with nuclear degrees of freedom fixed for the geometry at the onset of electron transfer (approx. t = 10.7 fs, simulation G1).

3A.4 Assignment of relevant peaks in the total VDOS

The bond distances were extracted from the nuclear trajectory. FTs were performed on these bond distances to obtain the corresponding vibrational frequencies. By performing a FT on the velocity autocorrelation function, a total VDOS of the entire system was obtained. A gaussian window function with a sigma value of 0.8 was chosen to filter out noise in the FT. In order to assign specific peaks in the total VDOS, we analyze the time evolution of specific localized geometric parameters such as bond distances and angles extracted from the trajectory. FTs reveal the underlying frequencies. We find that the highest frequency band at $\nu \approx 3500$ cm^{-1} can clearly be associated with N-H stretching modes as shown in figure 3A.4. The N-H bond involved in the central N···H-N hydrogen bond shows instead a considerably lower frequency, giving rise to a red shifted peak in the total VDOS at $\nu \approx 2700$ cm^{-1}. This can be explained by the relatively strong hydrogen bond, with the hydrogen almost being shared between the two nitrogen atoms. As shown in figures 3A.5 and 3A.6, the peak centered around 1500 cm^{-1} consists of several contributions from C=O stretches, C-N stretches and some bending modes. The overlap between many modes close in frequency make a direct association for ν < 2000 cm^{-1} in general

complicated. What clearly emerges through this vibrational analysis is the separation in frequency of the N-H bonds compared to all other vibrational modes.

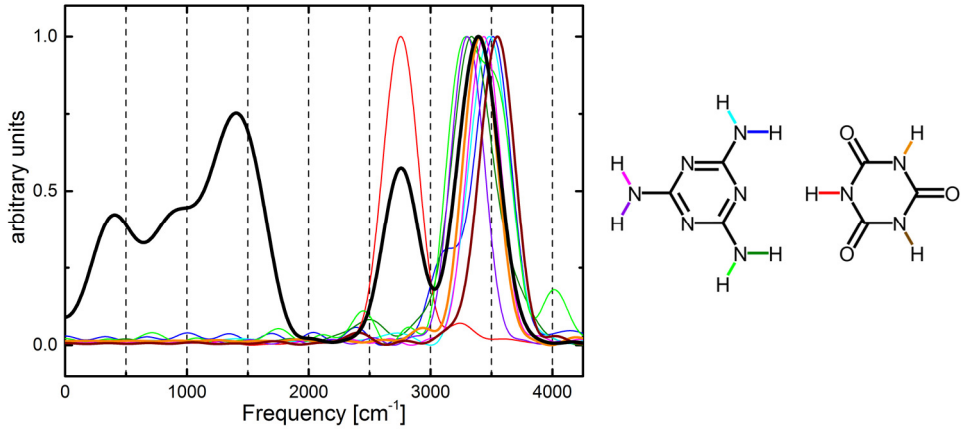

Figure 3A.4. VDOS of the pseudo base pair obtained via FT of the velocity autocorrelation function extracted from the Ehrenfest trajectory (black). Shown in color are all frequencies of the N-H stretches obtained via FT of the bond distances extracted from the Ehrenfest trajectory. The corresponding bonds are color-coded in the chemical structure shown on the right. Interesting is the shifted frequency of the central N-H bond on the donor-acceptor interface, as its frequency is significantly shifted to lower values due to the weakening of the bond through the strong hydrogen bond formed.

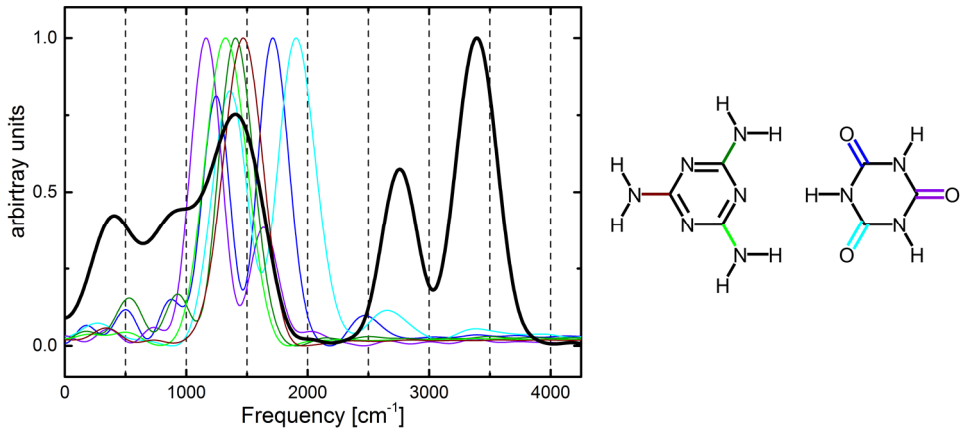

Figure 3A.5. VDOS of the pseudo base pair obtained via FT of the velocity autocorrelation function extracted from the Ehrenfest trajectory (black). Shown in color are frequencies of C=O stretches and C-N stretches obtained via FT of the bond distances extracted from the Ehrenfest trajectory. The corresponding bonds are color-coded in the chemical structure shown on the right.

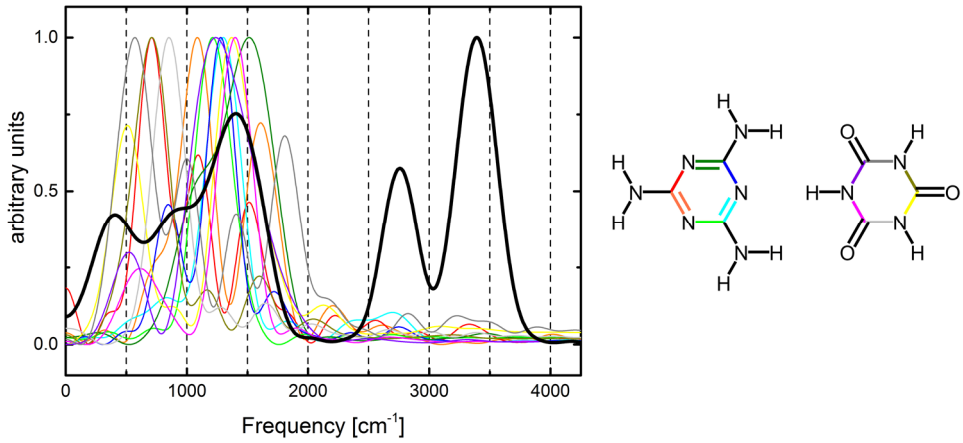

Figure 3A.6. VDOS of the pseudo base pair obtained via FT of the velocity autocorrelation function extracted from the Ehrenfest trajectory (black). Shown in color are frequencies of ring vibrations obtained via FT of the bond distances extracted from the Ehrenfest trajectory. The corresponding bonds are color-coded in the chemical structure shown on the right.

Figure 3A.7 shows the total VDOS for the two simulations using ^{1}H and ^{2}D respectively. The N-H (N-D) stretches are shifted as expected on the basis of the mass difference.

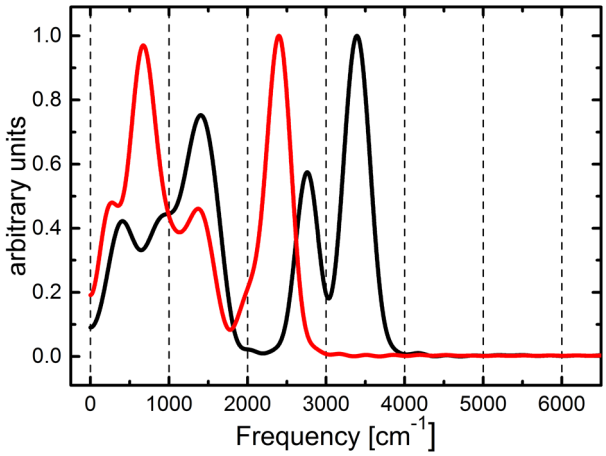

Figure 3A.7. Total VDOS of the ^{2}D substituted (red) and ^{1}H systems (black), obtained by performing a FT of the velocity autocorrelation functions using the respective trajectories.

3A.5 Dynamic Symmetry breaking

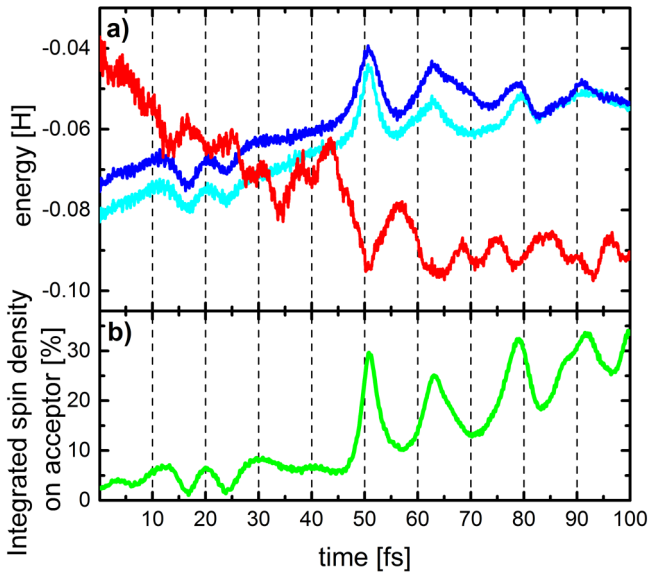

Figure 3A.8. Time evolution of the orbital energies (**a**) of the LUMO+2 (red), LUMO+1 (dark blue) and LUMO (light blue) in comparison to the electron transfer (green, **b**) during the Ehrenfest dynamics simulation starting with a C_{2v}-enforced initial geometry.

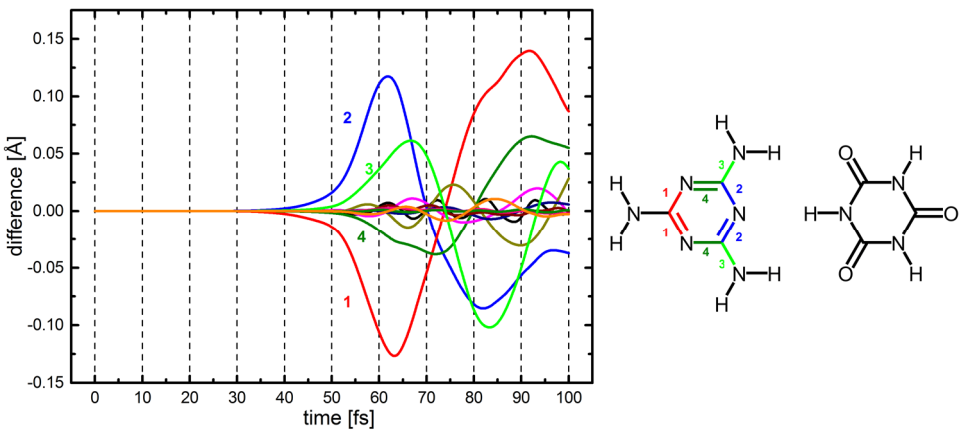

Figure 3A.9. Difference in bond distance between symmetry equivalent bond pairs. Here, the bond distance of the bonds shown as lower in the chemical structure is subtracted from the bond distance of their respective symmetry equivalent bond above. Color-coded are the four bond pairs first diverging from perfectly symmetric behavior.

3A.6 Dipole moment orientation

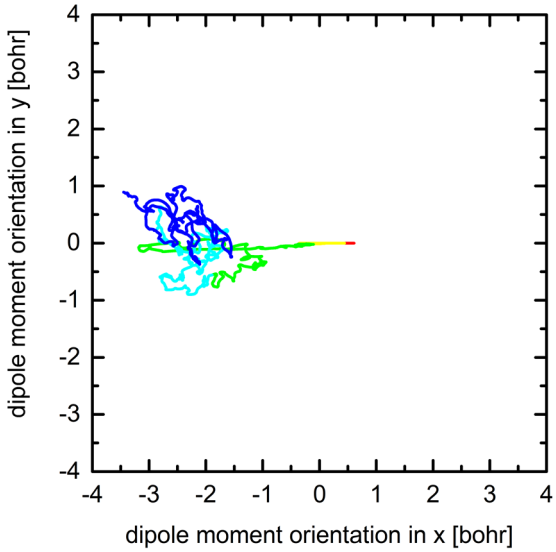

Figure 3A.10. Orientation of the dipole moment associated with β-electrons in the x-y plane for the simulation with enforced symmetric starting geometry. The colors correspond to consecutive time intervals, starting from red ($0<t<20$ fs) over yellow ($20<t<40$ fs), green ($40<t<60$ fs), light blue ($60<t<80$ fs) and dark blue ($80<t<100$ fs). A rotational character is visible in this case as well, but seems to be obscured by the large change in x due to the generated charge transfer state.

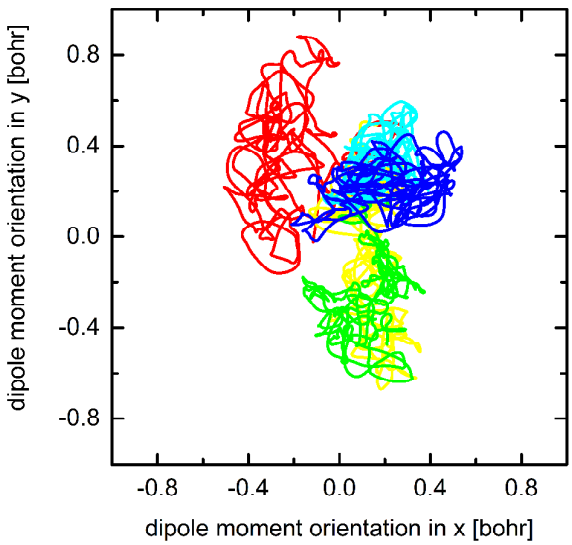

Figure 3A.11. Orientation of the dipole moment associated with α-electrons in the x-y plane for the simulation without enforced symmetry. The colors correspond to consecutive time intervals, starting from red ($0<t<20$ fs) over yellow ($20<t<40$ fs), green ($40<t<60$ fs), light blue ($60<t<80$ fs) and dark blue ($80<t<100$ fs). Rotational character, yet noisy, is apparent also in this simulation.

3A.7 Estimated non-adiabaticity of the process via the two level model by Purchase et al.[8]

Following the model discussed in chapter 2 and in Purchase *et al* [8], we consider the formula (see equation 2.31) for the period τ needed to convert the reactant state to the product state during the nonadiabatic process:

$$\tau = \frac{\pi}{R_0 d_{12} \omega_n}$$

We should keep in mind, that this result is obtained for a simple two state model that is coupled to a single nuclear vibrational mode of frequency ω_n with displacement R_0. Due to sweep of the resonance condition between the nuclear vibration and energy difference between the electronic states, the two state model gives a good description of the conversion process as the resonance leads to truncation of the full Hamiltonian, collapsing to two states.[8] To get a rough estimate of the nonadiabatic coupling term d_{12} for our donor-acceptor molecular complex, we therefore choose the most relevant nuclear mode which is coupled to the electronic motion. We consider the case with symmetric starting conditions (figure 3.1c), where the central N-H bond vibration is the most relevant mode, with $\omega_n \sim 2\pi*2700$ cm^{-1} (see figure 3A.4). The displacement R_0 of this mode is determined from the trajectory to be approximately 0.04 Å (see figure 3.2a). As a rough estimate for the complete charge transfer process, we take the time from the onset of electron transfer to the end of the simulation (55 fs, see figure 3.1c) and multiply by 3 to extrapolate to full electron transfer. In this way we estimate a period τ = 165 fs. By using these parameters extracted from our system, we estimate a value of 0.94 Å^{-1} for d_{12}.

3A.8 References

(1) Velde, G. te; Bickelhaupt, F. M.; Baerends, E. J.; Fonseca Guerra, C.; van Gisbergen, S. J. A.; Snijders, J. G.; Ziegler, T. Chemistry with ADF. *J. Comput. Chem.* **2001**, *22* (9), 931–967.

(2) ADF2013, http://www.scm.com, SCM, Theoretical Chemistry, Vrije Universiteit, Amsterdam, The Netherlands. .

(3) Becke, A. D. Density-Functional Exchange-Energy Approximation with Correct Asymptotic Behavior. *Phys. Rev. A* **1988**, *38* (6), 3098–3100.

(4) Lee, C.; Yang, W.; Parr, R. G. Development of the Colle-Salvetti Correlation-Energy Formula into a Functional of the Electron Density. *Phys. Rev. B* **1988**, *37* (2), 785–789.

(5) Yanai, T.; Tew, D. P.; Handy, N. C. A New Hybrid Exchange–Correlation Functional Using the Coulomb-Attenuating Method (CAM-B3LYP). *Chem. Phys. Lett.* **2004**, *393* (1–3), 51–57.

(6) Van Lenthe, E.; Baerends, E. J. Optimized Slater-Type Basis Sets for the Elements 1–118. *Journal of Computational Chemistry* **2003**, *24*, 1142–1156.

(7) Grimme; others. A Consistent and Accurate Ab Initio Parametrization of Density Functional Dispersion Correction (DFT-D) for the 94 Elements H-Pu. *J. Chem. Phys.* **2010**, *132* (715).

(8) Purchase, R. L.; de Groot, H. J. M. Biosolar Cells: Global Artificial Photosynthesis Needs Responsive Matrices with Quantum Coherent Kinetic Control for High Yield. *Interface focus* **2015**, *5* (3), 20150014.

CHAPTER 4

Photoinduced Electron Injection in a Fully Solvated Dye-Sensitized Photoanode: A Dynamical Semi-Empirical Study

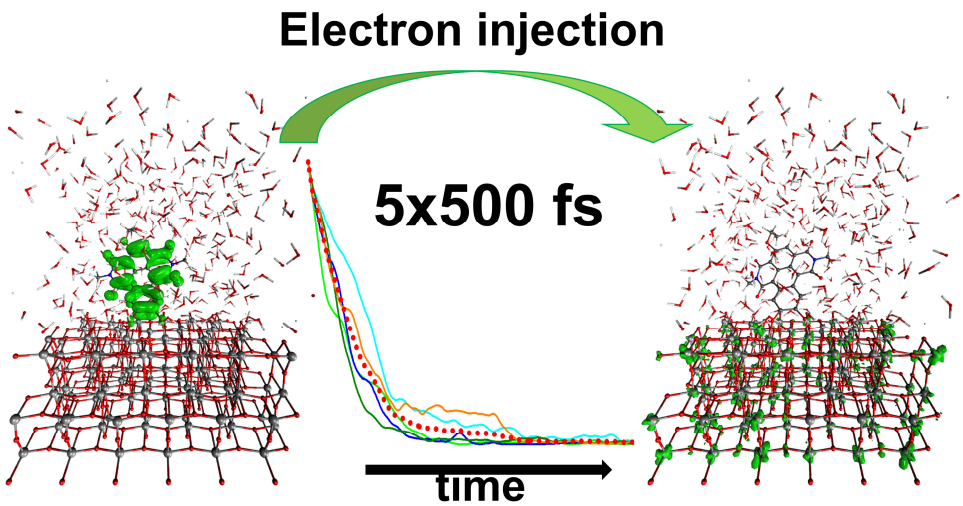

This Chapter is based on:
Jan Paul Menzel, Anastasios Papadopoulos, Jelena Belić, Huub J.M. de Groot, Lucas Visscher, Francesco Buda; *Journal of Physical Chemistry C*, **2020**, *124*, 27965-27976

4

ABSTRACT

Dye Sensitized Solar Cells (DSSCs) and Dye Sensitized Photoelectrochemical Cells (DS-PECs) have attracted much interest in recent years for solar energy conversion. More effort is still required to increase the efficiency of these devices, which is closely linked to the crucial process of photoinduced charge separation. Computational studies can provide insight into this fundamental process and suggest molecular components and interfaces that feature optimal energy level alignment before time consuming trial-and-error experimental realization. Here, we use a combination of Density Functional based Tight Binding (DFTB) and an extended Hückel approach to perform quantum-classical simulations of photoinduced electron injection in a TiO_2 Dye-Sensitized Photoanode with explicit solvation at a reasonable computational cost. In particular, we evaluate injection capabilities of core extended Napthalene Diimide (NDI) dyes with three different anchoring groups. Our results stress the importance of nuclear motion as well as conformational and trajectory sampling for a realistic description of the injection process. Furthermore, explicit solvation highly influences the conformational space explored by the dye and anchoring molecules, especially concerning the adsorption mode. Taking these effects into account, the core extended NDI with a catechol based anchoring moiety shows to be the most promising ultrafast electron injector. Our strategy allows for a more systematic computational search for appropriate molecular chromophores in dye-sensitized devices for solar energy conversion.

4.1 Introduction

In the search for environmentally friendly, renewable energy sources, Dye-Sensitized Solar Cells (DSSCs) have a high potential as a cost-effective alternative to silicon based photovoltaic cells in solar energy conversion.[1–3] These devices consist of semiconductor-based electrodes, which have been sensitized with photoactive molecular chromophores that absorb in the visible light range. DSSCs can also be extended by including molecular catalysts for direct conversion of solar energy to chemical fuel (Dye-Sensitized Photoelectrochemical Cells or DS-PECs). Both of these devices have attracted continued scientific interest.[4–8]

The anode or the cathode can be dye-sensitized to activate redox processes in the two half-cells. In this work we will focus on the design of a dye-sensitized photoanode, with a schematic set-up shown in figure 4.1. A semiconductor electrode (here TiO_2) is sensitized with a molecular dye (here a core extended NDI). The dye is attached via an anchoring group (here catechol).

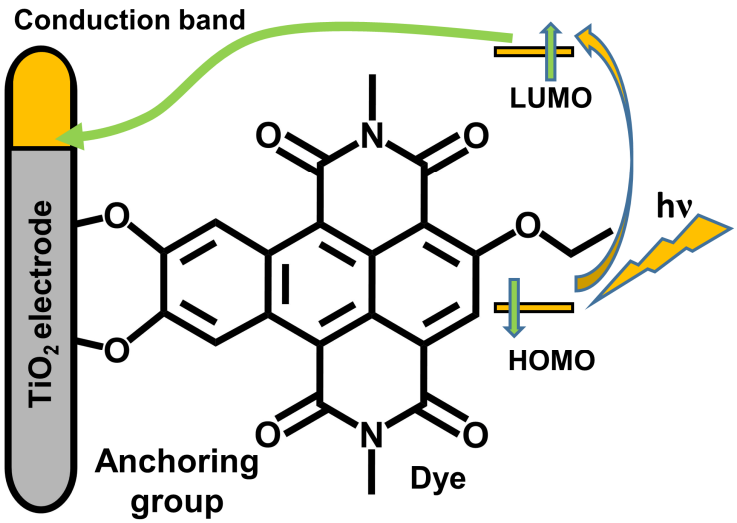

Figure 4.1. Characteristic set-up of a dye-sensitized photoanode: a dye molecule is attached via an anchoring group to a semiconductor electrode. Upon photoexcitation to the LUMO, the dye injects an electron into the conduction band of the semiconductor.

Upon photoexcitation with visible light, the excited electron is injected from the dye's LUMO into the conduction band of the electrode. This electron is then transferred via an external circuit towards the cathode. In DSSCs, electron flow from the cathode towards the anode via the electrolyte is then carried by redox mediators, which pick up the electron, diffuse towards the anode and reduce the photooxidized dye, completing the cycle. In the case of DS-PECs, the photooxidized dye is regenerated by electrons extracted from water splitting via a suitable water oxidation catalyst (WOC), generating oxygen and protons in the process. The protons diffuse via a proton exchange membrane (PEM) towards the cathode, where, in combination with the electron, the chemical fuel is produced, *e.g.* hydrogen from proton reduction or carbon based fuel from CO_2 reduction.[9]

For both types of devices (DSSCs and DS-PECs), the energetic alignment of the involved electronic states is absolutely crucial for obtaining a high forward reaction yield. The thermodynamic driving force and the electronic coupling between the molecular excited state and the semiconductor conduction band need to be tailored for rapid electron injection from the dye into the electrode, while suppressing wasteful back transfer and charge recombination.[10,11] To find a good compromise between these two contrasting but related requirements remains challenging.

Computational chemistry can provide insight into specific fundamental processes involved, such as interfacial electron transfer and charge separation.[12,13] It can deliver tools to screen through potential molecular dyes and interfaces to propose candidates before time consuming synthesis and tedious experimental investigations.[14] Density Functional Theory (DFT) based methods are often used to compare orbital energies of the molecular dyes with the electrodes' conduction band states and localization of the involved frontier orbitals.[15–18] Unfortunately, limitations of standard exchange correlation functionals may hinder the comparison with experimental values. For isolated molecular dyes, Linear Response Time Dependent DFT (LR-TDDFT) gives much more reliable results.[19–21]

However, these static approaches cannot capture changes in the electronic wave functions as the molecular conformations change. In addition, delocalization and localization effects, as well as changing orbital character due to *e.g.* forming or breaking of conjugation are not described either. These effects can be included in a limited way by ensemble averaging, taking geometries from equilibrated molecular dynamics (MD) runs. However, changes in the geometry during the injection process itself remain elusive. Finally, interaction of different electronic states can turn out to provide a pathway dominating the injection process when the electronic system is propagated.

Real-time evolution of the photoexcited electron can provide important insight into the dynamic aspect of these ultrafast injection processes. Non-adiabatic molecular dynamics (NAMD) approaches would be a favorable method, since they include the coupling between electronic and nuclear dynamics, but in practice this is still very expensive to use in these extensive systems over long time scales.[22–26] Both surface hopping and Ehrenfest-type approaches based on (TD)DFT have been successfully used to simulate electron injection processes[27–31]. These methods are computationally demanding and thus strongly limited with respect to the size of the system that can be investigated, especially if one is interested in performing several trajectories and compare numerous dye-semiconductor systems and their respective performances.

An alternative, computationally very efficient route to simulate the electron injection from photoexcited dye molecules was put forward by Rego and Batista.[32] In this method, the photoinduced electron dynamics is modelled via quantum dynamics based on an extended Hückel Hamiltonian. The approach was first demonstrated with a simulation of photoinduced electron injection from catechol into a TiO_2 anode.[32] It has been successfully used to elucidate electron transfer processes in a range of systems, including TiO_2 based electrodes with organic dyes,[32–38] DSSCs with transition metal complex based sensitizers,[39–46] nanocrystals[47,48] and charge separation dynamics in metal complexes.[49,50] While in

earlier simulations using this approach, the electron dynamics was done on fixed nuclear geometries, later implementations included the use of precalculated nuclear trajectories to model the effect of nuclear dynamics on the electron injection process.[37,49,51] Within this efficient, semiclassical approach, switching between the adiabatic MO basis and the diabatic AO basis allows for nonadiabatic population transfer. More recently, this method has also been extended to use the nonadiabatic elements derived from the quantum mechanically treated electronic system as an additional force in the classical MD to allow for persistent change of the nuclear trajectory in response to the evolution of the electronic subsystem.[52–55]

Here, we investigate electron injection properties of an extended core Naphthalene Diimide (NDI) dye with different anchoring groups in a TiO_2 based-dye sensitized photoanode using a combination of Self Consistent Charge Density Functional Based Tight Binding (SCC-DFTB) for the nuclear dynamics and the before mentioned extended Hückel method for the electron transfer dynamics (ETD). The main goal is to give an overview of the relative importance of nuclear motion, influence of different initial conformations and trajectories as well as inclusion of explicit solvation. In particular, explicit solvation can have several different effects on the photoinduced electron injection process: (*i*) the solvent can change the absorption properties of the molecular dye, (*ii*) it has an influence on the configurational space explored specifically at the dye-electrode interface, (*iii*) water tends to coadsorb onto the semiconductor interface and polarize the surface, thereby changing the band structure and the energy of the surface states, (*iv*) the water can interact directly with the anchored dye via breaking bonds between anchor and electrode, or by forming hydrogen bonds.

We aim to determine the most appropriate anchoring group for our dye with respect to their electronic conductivity and injection properties. For this, three benzene – derived anchoring moieties were chosen: benzoic acid, catechol and benzohydroxamic acid. Carboxylic acids are probably the most widely used anchoring groups but lack chemical stability, catechol and benzohydroxamic acid

show reasonable chemical stability and high estimated electron injection capabilities.[56] The investigated anchoring molecules are shown in figure 4.2a-c.

As molecular photosensitizer, an NDI-based dye was used, as NDIs are powerful light absorbers. They have a high extinction coefficient and can be tuned over the entire visible light range by introduction of electron withdrawing- or donating groups.[14,57,58] In figure 4.2d-f, the investigated core extended ethoxy NDIs, with the anchoring moieties fused into the extended core, are shown, which will be named cat-NDI, ben-NDI and hyd-NDI, according to their respective anchoring group.

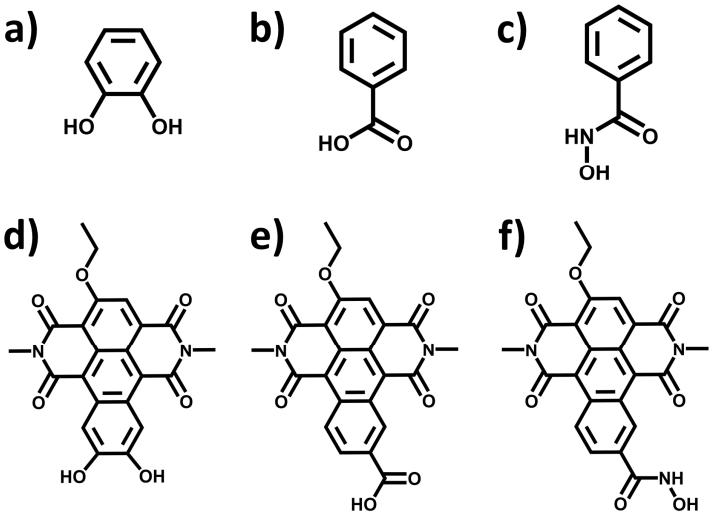

Figure 4.2. Investigated anchoring and dye molecules: **a)** catechol, **b)** benzoic acid, **c)** benzohydroxamic acid, **d)** core extended ethoxy-NDI with catechol anchoring group (cat-NDI), **e)** core extended ethoxy-NDI with carboxylic acid anchoring group (ben-NDI), **f)** core extended ethoxy-NDI with hydroxamic acid anchoring group (hyd-NDI).

The chapter is organized as follows: first, a description of the computational methods is given, which includes a short overview of the general procedure, the construction of the photoanode system *in silico*, treatment of the nuclear subsystem and finally the electron transfer dynamics. In the following section, we discuss our

results, with special focus on the effect of nuclear dynamics, trajectory averaging and explicit solvation. Conclusions are given in the last section.

4.2 Computational Methods

General Procedure

To evaluate the performance of the chosen dye and anchoring molecules, a quantum-classical semiempirical method is used, which allows for simulations of the full photoanode system at relatively low computational cost. Interfacial electron transfer simulations based on quantum dynamics using the AO/MO propagator and an extended Hückel Hamiltonian[50] are performed on *a priori* generated nuclear trajectories obtained at the SCC-DFTB-MD level.[59–61] The extended Hückel Hamiltonian is parametrized on DFT results (see section 4.A1 in the appendix for detailed information). The general workflow is described in scheme 4.1.

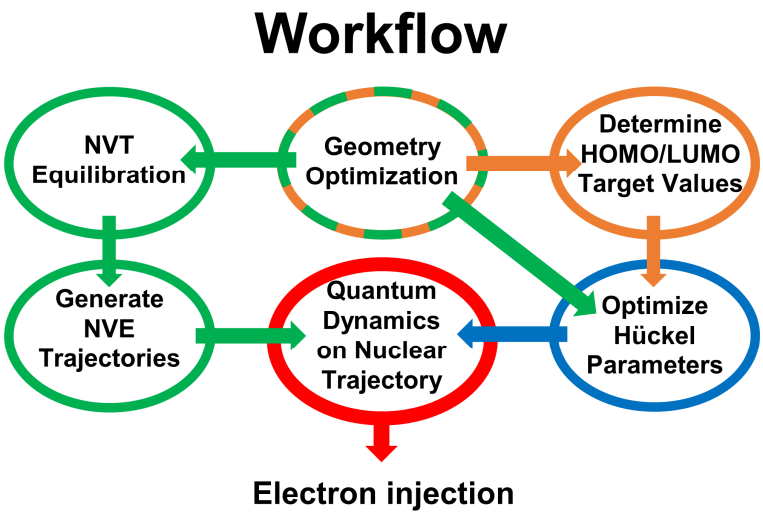

Scheme 4.1. Preparation of nuclear trajectories and extended Hückel parameters used in the semi-empirical quantum classical simulations of photoinduced electron injection. Colors refer to different computational methods: green for SCC-DFTB, orange for DFT/B3LYP, blue for Hückel parameter optimization, red for the AO/MO propagation using the extended Hückel Hamiltonian. DFT-based geometries are used for HOMO/LUMO target values determination, while DFTB-based geometries are used for the trajectory generation and for the parameter optimization.

The DFTB module of the Amsterdam Density Functional (ADF) program was used for simulating the nuclear dynamics (green box in Scheme 4.1).[62,63] The tiorg-0-1 parameter set, which is optimized to describe bulk Ti and TiO_2 as well as TiO_2 surfaces with and without organic adsorbants, was chosen for the SCC-DFTB.[64] The ADF program was also used for determining the DFT target values for the parameter optimization (orange box in Scheme 4.1). The ETD simulations were performed using the code developed by Rego and Batista (red circle in Scheme 4.1).[32]

Constructing the Photoanode

The TiO_2 was assumed to be in the anatase phase, since this phase is photocatalytically more active than rutile TiO_2 and most often used for photoelectrodes.[65] To model the TiO_2 anatase electrode, first a bulk optimization was performed using a supercell of 48 atoms in total (16 titanium atoms, 32 oxygen atoms) and periodic boundary conditions. The box size was optimized as well. The resulting geometry can be seen in figure 4.3.

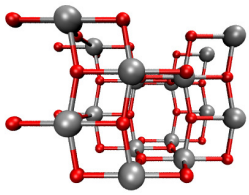

Figure 4.3. Optimized geometry of bulk anatase. Only one supercell is shown.

A supercell of 3 layers for a total of 144 atoms and cell dimensions of 10.045 Å x 15.234 Å x 70 Å with the surface normal into the *z* direction was used to model the anatase(101) surface starting from the optimized bulk geometry. The TiO_2 surface slab was reoptimized to model surface relaxation effects while the lowest layer was kept frozen in the bulk geometry. All anchoring groups were attached via bidentate bridging mode. The dissociating protons were adsorbed on the anatase surface to

keep the unit cell overall neutral. For the benzohydroxamic acid, the protonation state 1 was chosen (one proton is dissociated, one remains) as determined by Rudshteyn *et al.*[66] The optimized geometries of these anatase-anchor complexes are shown in figure 4.4.

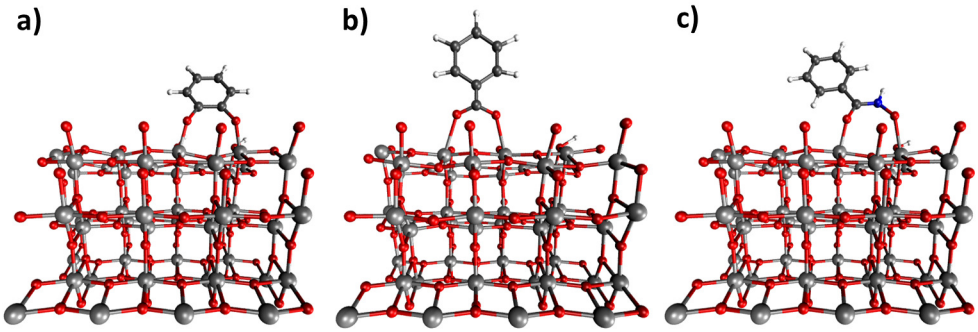

Figure 4.4. Optimized geometry of catechol **(a)**, benzoic acid **(b)** and benzohydroxamic acid **(c)** on anatase (101) surface.

Water molecules were added to obtain a total density of 1 g/ml. These water layers were constructed using a configuration extracted from bulk water equilibrated at 300K. Figure 4.5a shows this simulation box specifically for benzoic acid, containing a total of 453 atoms. SCC-DFTB based molecular dynamics simulations were performed while freezing the lowest TiO_2 layer to keep bulk geometry, as well as a layer of water on top to prevent evaporation. The simulation box for the ben-NDI, including a total of 1329 atoms and box dimensions of 20.091 Å x 22.851 Å x 70 Å is shown in figure 4.5b. Periodic boundary conditions are applied in all the directions. To avoid spurious interactions along the *z* direction, we add a vacuum layer of about 40 Å.

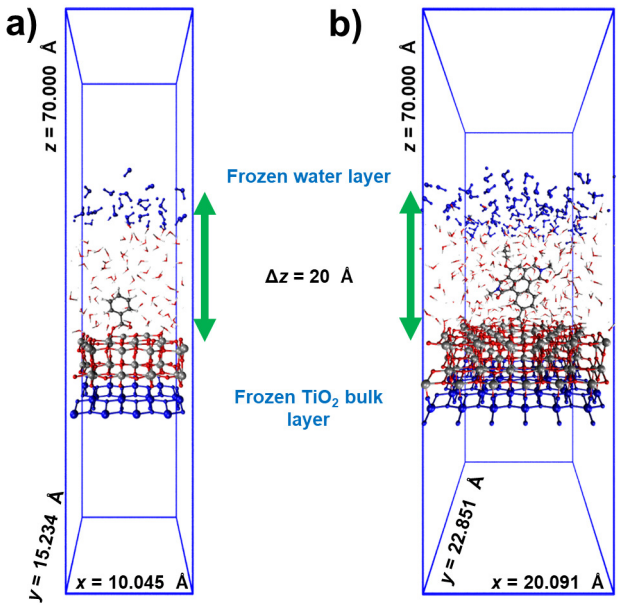

Figure 4.5. Simulation boxes for **a)** benzoic acid and **b)** ben-NDI attached to a TiO_2 -slab including explicit solvation. Periodic boundary conditions are enforced in *x*, *y* and *z*. Shown in blue are atoms kept frozen to mimic TiO_2 bulk geometry and to prevent evaporation and diffusion of the water molecules towards the opposite side of the TiO_2 slab.

Generating Nuclear Trajectories

In scheme 4.2, the general procedure to generate the nuclear trajectories is shown. First, a MD equilibration run in the NVT ensemble, using a Berendsen thermostat[67] at 300 K was performed for 5 ps with a time step of 1 fs. This was followed by a total of 1.5 ps in the NVE ensemble for the anchoring groups, while 2.5 ps were produced for the core extended NDI dyes. A time step of 0.1 fs was used for both. This short time step is necessary for stable ETD simulations. The resulting trajectory was then split into 15 parts of 100 fs each in the case of the anchoring groups. For the dyes, 5 slices of 500 fs each were taken. The initial geometries of these shorter trajectories were used for the ETD simulations on a fixed geometry.

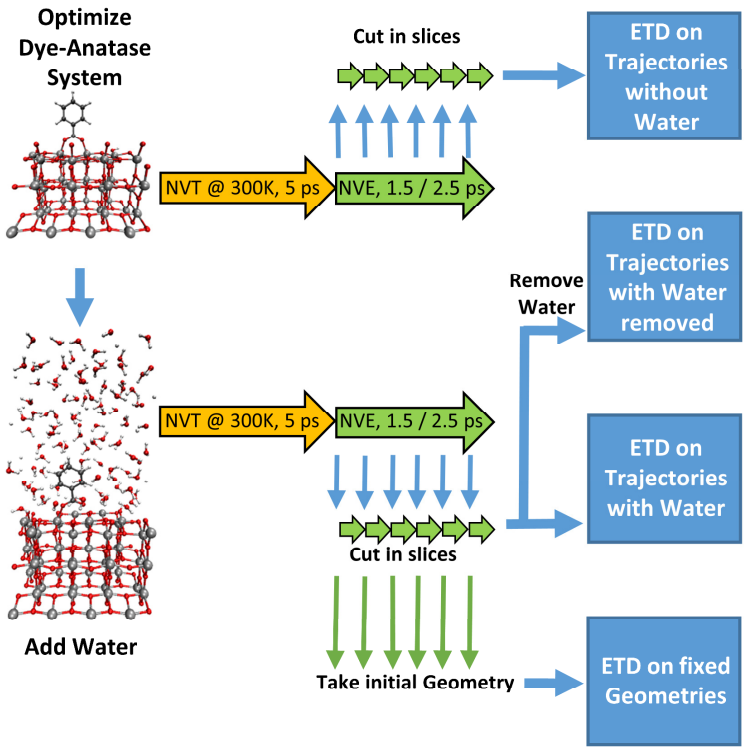

Scheme 4.2. Geometry and trajectory generation for usage in the ETD simulations. After an initial NVT equilibration at 300 K (yellow arrow), an NVE production run is performed (green arrow). This trajectory is then split into different slices for the quantum propagation. This procedure is performed twice, with and without explicit solvation. ETD simulations on static nuclear geometries were performed on the initial geometries of the trajectory slices.

To estimate the influence of explicit solvation, three different cases were investigated: (*i*) full explicit solvation during the nuclear trajectory generation and the ETD; (*ii*) the same nuclear trajectories but removing the water molecules for the ETD; (*iii*) nuclear trajectories and ETD without any water molecules. In this way, we can disentangle pure polarization effects due to the solvent from changes in the conformations explored during the dynamics, especially associated to formation of hydrogen bonds and changes of adsorption mode.

Electron Transfer Dynamics

The ETD simulations were performed using an extended Hückel Hamiltonian that is based on parametrization of Coulomb and overlap integrals. For the water molecules and anatase electrode the standard Hückel parameters were used.[68] The Hückel parameters for the dye and anchor molecules were optimized to achieve good relative energy alignment of the conduction band edge of the anatase on one hand and the frontier orbitals of the organic molecule on the other hand as determined by experimental values and DFT results. Consistent with the interpretation of the eigenvalues of the Hückel Hamiltonian as single particle energies, Hückel parameters were optimized on the dye and anchoring molecules in implicit water using ΔSCF derived values for the HOMO and ΔSCF plus excitation energy (TDDFT or experimental) for the LUMO energies at the DFT - B3LYP[69,70]/DZP[71] level with implicit COSMO[72] (Conductor-like Screening Model) water. A more detailed description and comparison to available experimental values is given in section 4A.1 in the appendix.

The excitation of each organic molecule is modelled by localizing the photoexcited electron on the LUMO of the corresponding adsorbed molecule, with the hole being localized at its HOMO. Even though there is evidence that catechol adsorbed to an anatase surface is excited directly to a charge transfer state with the electron already in the conduction band of the TiO_2,[73] the local excitonic state is used here, since we are interested in the ability of catechol to inject a photoexcited electron donated by an excited dye. We chose the same time step of 0.1 fs for nuclear and electronic propagation. This short time step is necessary for a stable ETD simulation since the time independence of the Hamiltonian during a nuclear time step is a reasonable approximation. The propagation is done for a total of 100 fs (anchoring molecules) or 500 fs (core extended NDIs). During the time evolution of the wave packets, the electron and hole population were calculated for the following fragments: the anatase electrode, the adsorbed organic molecule and the water molecules.

4.3 Results and Discussion

Nuclear Dynamics

During the equilibration dynamics with explicit solvent, water adsorption onto the anatase surface is observed in all systems considered in this work. Thereby, initial hydrogen bond formation towards the oxygen located on the surface steps (figure 4.6a) is followed by covalent attachment of the water oxygen to titanium (figure 4.6b). After adsorption, hydrogen bond formation to the surface oxygen, coadsorbed water molecules and bulk water is also common (see also 4.6b). These findings are consistent with work by Selli *et al*. and Aschauer *et al.* that found these geometries for multilayers of water on anatase(101).[74,75]

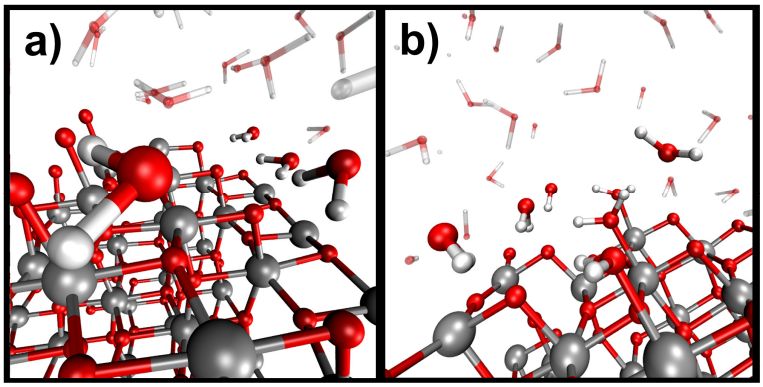

Figure 4.6. Adsorption of water on the anatase(101) surface: **a)** Initially, water molecules associate via hydrogen bonds to the oxygen on the surface step; the corresponding adsorbed water molecules are shown in ball and stick representation. **b)** Covalent bonds to Ti atoms are formed and hydrogen bonds to the bulk water create further water layers that remain relatively dynamic.

Interestingly, the adsorption mode of benzohydroxamic acid changes during the molecular dynamics. While the bidentate adsorption is most stable in vacuum, with explicit water it switches spontaneously to a monodentate mode with hydrogen bond formation to a coadsorbed water molecule. This happens via a water molecule in solution that attacks the oxygen-titanium bond by forming a hydrogen bond to the hydroxamic acid oxygen (figure 4.7a). Afterwards, the molecule rearranges to form a hydrogen bond to a neighboring adsorbed water molecule (see figure 4.7b). This

mode was also found to be the energetically most favorable with monolayer water present by Rudshteyn *et al.*[66] It is noteworthy that SCC-DFTB based MD is able to predict this correctly.

This change in adsorption mode from monodentate to bidentate is also present for ben-NDI and hyd-NDI. However, it also happens without explicit water, contrary to the benzohydroxamic acid. This change seems to be due to the steric stress of the imide part of the NDI that points towards the surface.

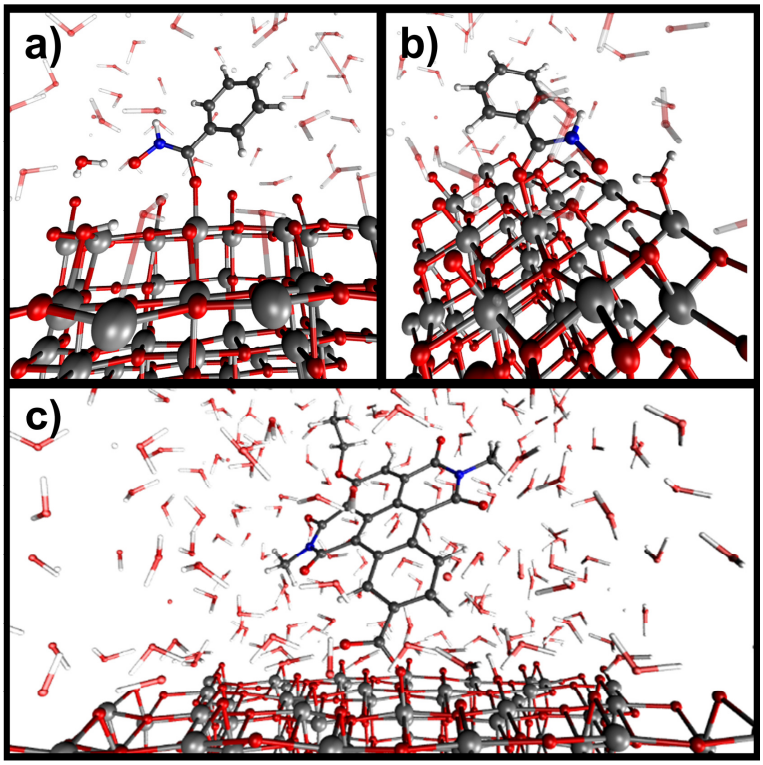

Figure 4.7. Change of the benzohydroxamic acid adsorption mode from bidentate to monodentate via **a)** attack of a water molecule (highlighted) and **b)** rearrangement forming a hydrogen bond to the highlighted coadsorbed water molecule; **c)** monodentate adsorption of ben-NDI due to steric stress induced by the imide part of the NDI pointing towards the surface.

This leads to angular strain on the anchoring group, that is released by breaking one of the bonds to the surface. An example is shown in figure 4.7c. In the case

without explicit water, the attractive interaction between the π-system and the anatase surface also plays a role, while the adsorbed water prevents this interaction when including explicit solvation. In the hyd-NDI case, this leads to π-stacking between the entire aromatic plane of the NDI and the surface.

Electron Injection Properties of Anchoring Molecules

The electron injection over time for one ETD simulation on a single trajectory with explicit solvation is given in figure 4.8a for the benzohydroxamic acid, where we show the electron population on different fragments over time.

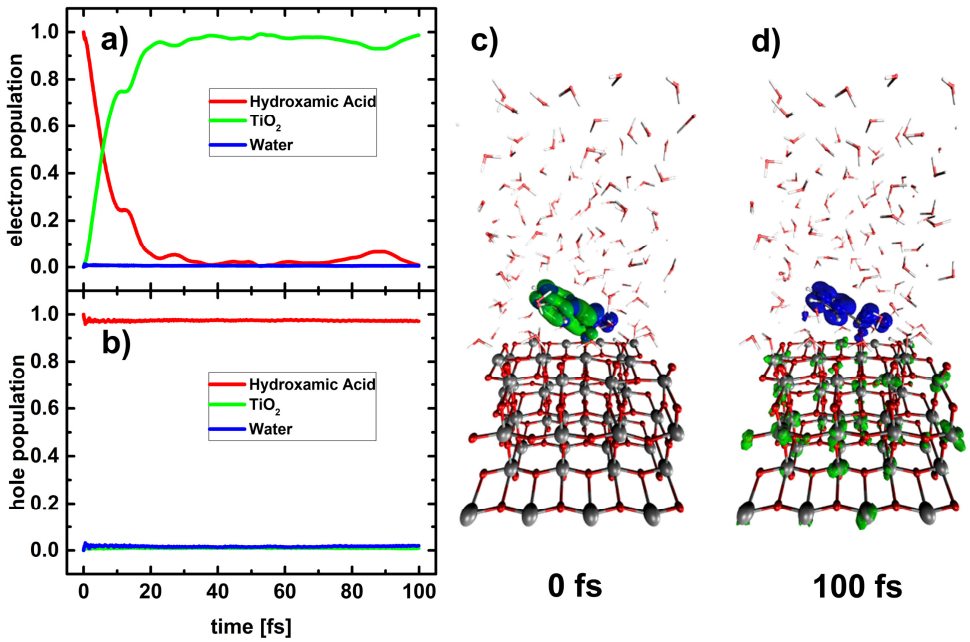

Figure 4.8. Electron **(a)** and hole **(b)** populations on the different fragments: Benzohydroxamic acid (red), TiO_2 (green) and water (blue) with full explicit solvation; **c)** electron (green) and hole (blue) density at the beginning of the simulation, both fully localized on the benzohydroxamic acid. **d)** electron (green) and hole (blue) density after 100fs. The electron is injected into the TiO_2 electrode, while the hole remains stable on the benzohydroxamic acid.

At the beginning of the simulation, both the hole and the electron are completely localized on the benzohydroxamic acid, occupying the respective HOMO and LUMO orbital (see figure 4.8c).

During the quantum dynamics evolution, the photoexcited electron is transferred from the benzohydroxamic acid to the anatase electrode. As can be seen, electron injection is complete within 20 fs (see figure 4.8a). No electron density is donated to the explicit water molecules. The hole population (see figure 4.8b) remains stable on the benzohydroxamic acid. At the end of the simulation, the electron is therefore injected into the electrode, while the hole remains on the benzohydroxamic acid: charge separation has occurred (see figure 4.8d).

However, one single trajectory can be misleading in drawing conclusions on the injection process. To obtain a reasonable estimate of the electron injection rate, several ETD results have to be averaged. In figure 4.9a, the photoinduced electron injection from the benzohydroxamic acid to the anatase electrode is averaged over all 15 ETD simulations performed on nuclear trajectories with explicit water. The same is shown for the hole in figure 4.9b.

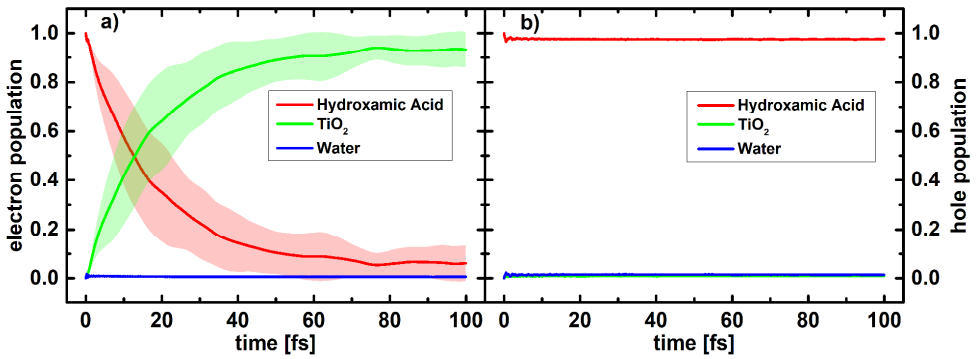

Figure 4.9. Electron **(a)** and hole **(b)** populations on the different fragments: Benzohydroxamic acid (red), TiO_2 (green) and water (blue) with full explicit solvation, averaged over 15 trajectories. The lines denote the mean values, the shaded area the standard deviation centered on the mean value.

Photoinduced electron injection is observed; however, the average rate is significantly lower than for the single trajectory discussed earlier: within about 60 fs on average, the injection is basically complete. This highlights the importance of appropriate statistics by averaging over multiple simulations in determining the injection rate. Some general statements can be made for all simulations and for all investigated molecules: (*i*) no significant electron population is observed on the water molecules, (*ii*) the hole remains stable on the organic molecule. Figures of electron and hole survival for all cases and molecules can be found in the appendix.

The importance of averaging over several geometries or trajectories is evident in figure 4.10a – 4.10d, where we report the electron injection evolution for each of the 15 geometries (4.10a) and trajectories (4.10c) of benzohydroxamic acid in explicit water, with the mean value and the standard deviation also included (figures 4.10b and 4.10d). Figure 4.10a shows that the choice of the initial geometry can lead to qualitatively different results: from almost no injection to a very fast process finished within 20 fs. Correspondingly, this leads to a high standard deviation and a slow, incomplete injection when considering the mean value, shown in figure 4.10b. We have analyzed in some more detail these different conformations to search for characteristic geometrical features that might affect the injection properties. While some features, such as a large dihedral angle between phenyl group and hydroxamic acid, as well as a large distance between anchoring group and TiO_2 often slow down the injection process, more complex collective geometric variables seem to be involved, not only including the chromophore but also the solvent and the semiconductor surface. It is therefore challenging to disentangle these features.

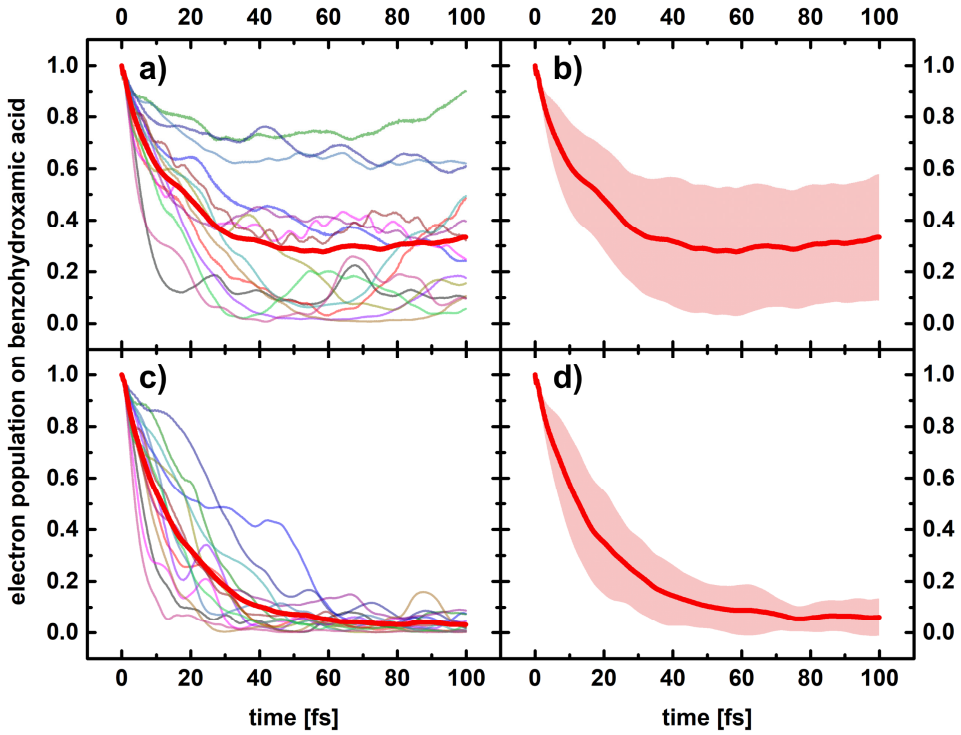

Figure 4.10. Variation of electron population on benzohydroxamic acid: **a)** all 15 ETDs on static geometries with the mean value in bold; **b)** the corresponding standard deviation (shaded area) centered on the mean value (bold line); **c)** all 15 ETDs on nuclear trajectories with the mean value in bold, **d)** the corresponding standard deviation (shaded area) centered on the mean value (bold line).

The effect of including dynamics is shown in figure 4.10c. Here, more geometries are explored during the trajectory and the rates change significantly compared to the static case. This means that if injection is hindered at a certain geometry, injection might be slowed down in the dynamic case, but not completely inhibited. For example, the value of the dihedral angle between anchoring group and aromatic system can prevent electron flow from the molecule to the anatase surface, but when a more favorable conformation is explored during the trajectory, the injection channel is opened (see a more detailed description in 4A.2). In previous investigations of photoinduced electron transfer processes, coherent effects between

nuclear and electronic motion have been shown to be relevant in facilitating the charge separation (see also chapter 3).[24,26,37,52] Here, we have also explored possible resonances between electronic and nuclear frequencies and show an example in section 4A.3 in the appendix. This suggests that the electronic system is able to take advantage of nuclear modes of appropriate frequency.

A further effect of the nuclear dynamics is the larger conformational sampling within the simulation leading to a significant decrease in the standard deviation (see figure 4.10d). The benzohydroxamic acid is the most extreme case, for the benzoic acid and catechol the variation between single ETD runs is significantly lower (see appendix 4A.4 and 4A.5).

The lower injection rate and large standard deviation of the static case is a consequence of the high variation between single trajectories and charge oscillations between surface and molecule visible in figure 4.10a. These oscillations are an effect of the finite size of the system that has been overcome in the past by including absorbing potentials in the lowest TiO_2 layer.[32,34,46] However, the oscillations are greatly reduced when including nuclear dynamics (see figure 4.10c), since dynamic disorder rapidly localizes the charge within the surface slab. This points to a sufficient size of our system without the need of using an artificial absorbing potential, as localized low energetic states are available through thermal noise in the TiO_2 slab. Since this is a dynamic effect within the electrode, the TiO_2 slab needs to be treated dynamically, as freezing the surface leads to the same oscillatory behavior observed in the completely static system (see figure 4A.10 in the appendix).

To check the relative importance of nuclear dynamics, trajectory averaging and explicit solvation on the electron injection process, we compare the average electron population over time on all three anchoring molecules for these different cases in figure 4.11. In all panels, only the electron population on the anchoring molecule averaged over all 15 ETDs is shown. Single runs and standard deviations are omitted for clarity and reported in the appendix (sections 4A.4 – 4A.6).

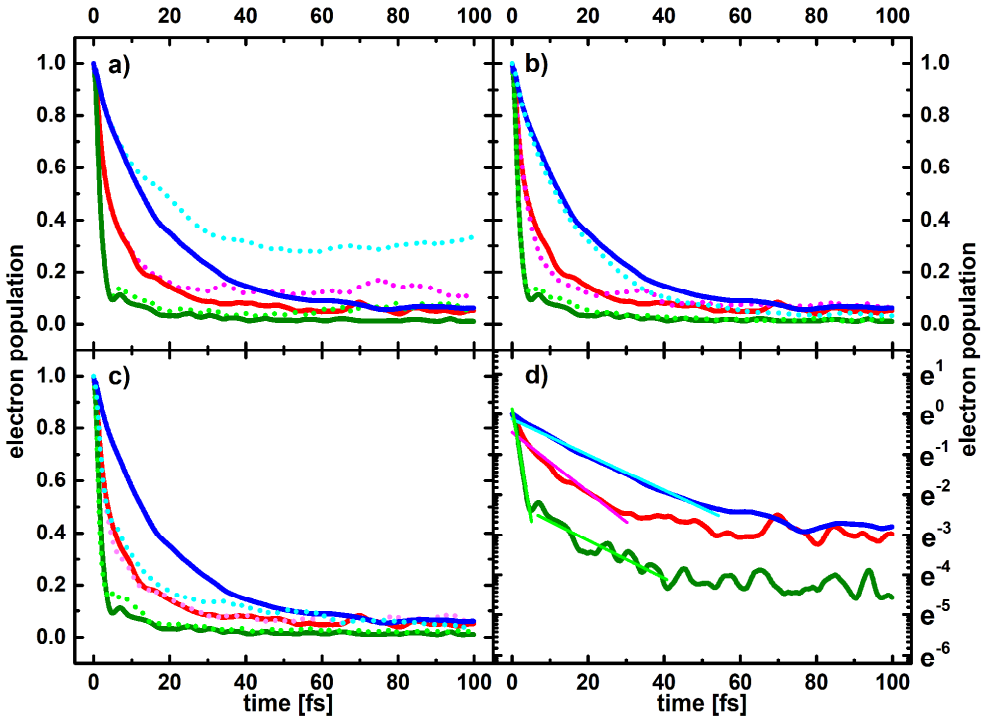

Figure 4.11. Electron population on catechol (red), benzoic acid (green) and benzohydroxamic acid (blue) averaged over 15 ETD simulations each. In different panels we compare the results obtained with the nuclear trajectories with explicit water (full lines) with the results obtained with **a)** static nuclear geometries (dotted lines), **b)** the same nuclear trajectories with the water molecules subsequently removed for the ETD (dotted lines), **c)** trajectories obtained without explicit solvation (dotted lines). Panel **d)** shows the electron injection for the fully solvated, dynamic case on a ln scale including a linear fit indicated in a lighter color.

In figure 4.11a, the average electron population over time on all three anchoring molecules are given for the static vs. the dynamic case. It is important to note that the geometries chosen are the initial structures from the trajectories (see scheme 4.2), meaning that the initial conditions for the static and dynamic cases are identical. The importance of nuclear dynamics for the description of the injection process is clearly visible. The electron injection is slower and less complete for all static cases in comparison to the dynamic ones due to larger differences in rate between single ETD

runs as well as oscillations between anchoring molecule and electrode. However, this effect varies by anchoring molecule. While for the benzoic acid especially the initial injection seems quite well described on static geometries, the difference between static geometries and nuclear trajectories is quite significant for catechol and very large for the benzohydroxamic acid. All in all, nuclear dynamics are quite important in the electron injection process. More conformations are explored during the trajectory, leading to smaller differences between single ETD runs. Conformations that inhibit electron injection do not prevent the process, as over time, other parts of conformational space are explored that allow for electron flow. Furthermore, dynamic disorder inhibits oscillations between the different fragments.

The importance of including explicit solvation is less straightforward. As mentioned earlier, to disentangle pure polarization effects from influence of the water on the conformational space explored, we investigated three cases: (*i*) nuclear trajectories obtained with full explicit solvation, (*ii*) the same trajectories but with the water molecules subsequently removed, thus keeping the effect on nuclear dynamics but removing polarization effects, and (*iii*) trajectories obtained in vacuum.

We first consider the pure polarization effect by comparing the ETDs of the full explicit solvation model and the same nuclear trajectories with the water molecules removed for the quantum dynamics, as given in figure 4.11b. For all three anchoring molecules, the difference between full explicit solvation and removing the water molecules for the ETD is quite small. The presence of the water slightly slows down the injection into the TiO_2 electrode for the benzohydroxamic acid, while the benzoic acid remains almost unchanged. For the catechol, injection without water is slightly increased at the beginning, but a small peak at 35 fs denotes minor back transfer that is suppressed when including explicit water. The differences decrease over the course of the simulation. We expect that the polarization effect is so small due to the tight binding character of the Hückel method, which poorly describes long range effects.

While the polarization effect of the water in our simulations is small, the effect of excluding water in the nuclear dynamics can be significant, as seen in figure 4.11c. While the conformational space explored with water seems to be very similar for catechol, as there is almost no difference in injection rate, this is not the case for the other two anchoring molecules. There is a quite clear back transfer peak after initial injection (at 5 fs) in the case of the benzoic acid that is significantly higher when excluding water. This can partially be explained by the missing polarization effects, as was the case in figure 4.10b, but is more pronounced and might hint at a lower dynamic disorder in the system. In both cases, full injection is achieved after about 40 fs. For the benzohydroxamic acid, the effect of explicit solvation is quite striking as the electron injection is a lot slower. This is most likely due to the changed adsorption mode discussed earlier, where the benzohydroxamic acid adsorbs bidentally in vacuum, but switches to monodentate adsorption mode when including explicit water (as was shown in figure 4.7). Explicit solvation therefore seems to be very important for the benzohydroxamic acid, less so for benzoic acid, and negligible for catechol. In addition, conformational differences induced by the water and direct interaction via formation of hydrogen bonds appear more important than polarization effects in this tight binding framework.

To compare injection rates for the three anchoring molecules, we give the electron population over time on a semi-logarithmic scale in figure 4.11d. Here we only focus on the fully solvated dynamic case. For all three anchoring molecules, the injection behavior seems to follow exponential behavior, until less than 10 % electron population remains on the dye. After that, noise takes over. A linear fit is given for this part of the electron injection plot, to estimate the rate. The slope, adjusted R^2 values, estimated rates and mean life time for the three anchoring molecules are given in table 4.1.

Table 4.1. Slope, adjusted R^2 values and estimated electron injection rates for catechol, the two regimes of the benzoic acid and the benzohydroxamic acid determined from the linear fits on the semi logarithmic mean value of 15 ETD simulations performed on fully solvated nuclear trajectories.

Molecule	Slope [fs^{-1}]	Adjusted R^2	Estimated Electron injection rate [s^{-1}]	Mean life time [fs]
Catechol	-0.074	0.95397	7.4×10^{13}	13.6
Benzoic Acid	-0.547	0.98888	5.5×10^{14}	1.8
	-0.048	0.87008	4.8×10^{13}	21.1
Benzohydroxamic Acid	-0.043	0.99302	4.3×10^{13}	22.8

The benzoic acid seems to have two distinct regimes: within the first 5 fs a very rapid injection, followed by a slower rate comparable to the other two anchoring groups. This is most likely a relaxation effect due to the strong coupling between TiO_2 surface states and the oxygens of the benzoic acid, as can be seen in the density of states (DOS) given in the appendix (figure 4A.2). The injection rates are all in the order of 10^{13} s^{-1}, with the first regime of the benzoic acid showing an even higher rate of the order of 10^{14} s^{-1}.

All in all, conformational averaging and inclusion of nuclear dynamics are crucial in describing the exponential decay of the injection process, while explicit solvation seems important for the correct description of nuclear dynamics, but not in the ETD simulations. While the injection rates vary when including or excluding nuclear dynamics and explicit solvation, the relative trend of the anchoring molecules stays the same.

Electron Injection Properties of Core-Extended NDI Dyes with Different Anchoring Groups

The electron injection properties of the excited anchoring molecules give some insight into the effects of nuclear motion and explicit solvation on these molecules as well as an estimate of their performance. In this section we focus on the electron injection properties of the whole photoanode system including the NDI based dyes shown in figure 4.2d-f.

A comparison of the average electron population over time on these NDI based dyes is given in figures 4.12a-d. Here we focus on the time evolution of the mean values averaged over 5 ETD simulations of 500 fs each. Figures with single trajectories and standard deviations can be found in the appendix (section 4A.7 to 4A.9). In figure 4.12a, we compare the electron injection evolution obtained with ETDs on static geometries with those performed on nuclear trajectories. Again, the geometries correspond to the initial structures of the trajectories, meaning that initial conditions are the same.

In general, electron injection here is significantly slower in comparison to the corresponding benzene derived anchoring molecules. This might be associated to both lower LUMO energies (and therefore lower driving force) and lower coupling of the molecules' LUMO to the conduction band states, as the distance between donor and acceptor is increased. While cat-NDI fully injects the photoexcited electron within 150 fs in the dynamic case, the exclusion of nuclear dynamics leads to a far lower injection with an electron population on the dye molecule of still 20 % after 500 fs. The same holds true for ben-NDI, where the electron population left on the dye rises from 10 % in the dynamic to approximately 50 % in the static case. For the hyd-NDI, this is even more striking: while the electron population on the dye is about 35 % after 500 fs when including nuclear dynamics, in the static case it actually rises from a minimum of 45 % at 300 fs to about 60 % after 500 fs.

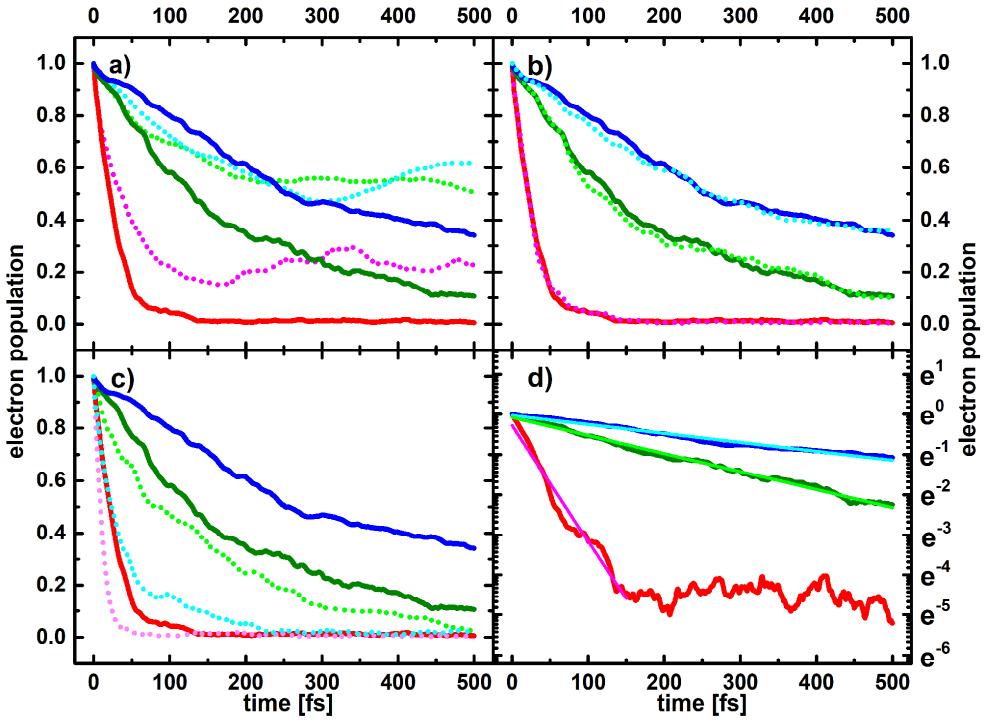

Figure 4.12. Electron population on cat-NDI (red), ben-NDI (green) and hyd-NDI (blue) averaged over 5 ETD simulations each. In different panels we compare the results obtained with the nuclear trajectories with explicit water (full lines) with the results obtained with **a)** static nuclear geometries (dotted lines), **b)** the same nuclear trajectories with the water molecules subsequently removed for the ETD (dotted lines), **c)** trajectories obtained without explicit solvation (dotted lines). Panel **d)** shows the electron injection for the fully solvated, dynamic case on a ln scale including a linear fit indicated in a lighter color.

Furthermore, the importance of explicit solvation in the trajectory generation is much more obvious here than for the benzene derivatives. While the removal of water molecules for the ETD leads to very little change (dotted lines in figure 4.12b in comparison to the full lines), the electron injection rate is significantly higher for all dye molecules when using nuclear trajectories obtained without explicit solvation (dotted lines in figure 4.12c). Interestingly, the trend of the injection properties changes also qualitatively. While in all cases, electron injection is quicker without explicit water, the hyd-NDI shows an extreme increase in injection rate and surpasses

the ben-NDI. This extreme change can be explained by the π-stacking of the hyd-NDI onto the surface that was mentioned earlier. Such an interaction leads to very strong electronic coupling between the NDI and TiO_2, that allows for direct injection between dye and surface without crossing the anchoring molecule (see figure 4.13). Consequently, it is absolutely crucial to include explicit solvation for the generation of nuclear trajectories to predict the performance of a molecular dye.

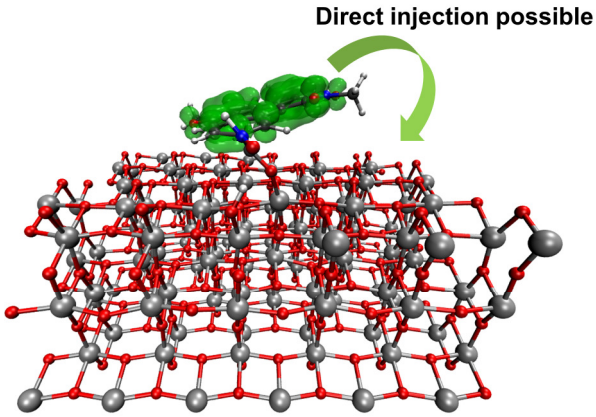

Figure 4.13. Representative geometry of hyd-NDI without explicit solvation. The close interaction between the π-system of the dye with the anatase surface allows for direct injection. The electron density (shown in green) does not need to pass through the anchoring moiety.

In figure 4.12d, the electron population on the core-extended NDI dyes averaged over 5 ETDs on trajectories with explicit water is shown on a semi-logarithmic scale. This allows for a linear fit to estimate injection rates. In comparison to the anchoring groups, the exponential behavior is even more evident. Slopes, adjusted R^2 values, estimated rates and mean survival time are given in table 4.2. The rates of injection are significantly lower than for the anchoring molecules. Still, the slowest injection (the hyd-NDI) has a mean life time of about 500fs, still 4-5 orders shorter than a typical fluorescence life time. The most effective anchor-dye complex is thus cat-NDI, which is one order of magnitude faster than the other two molecules. Ben-NDI

and hyd-NDI have comparable rates, with ben-NDI approximately twice as fast. Contrary to the benzene derived anchoring molecules, the catechol-based dye injects faster than the dye attached via a carboxylic acid group. This lower relative rate of the carboxylic acid integrated in the dye can be explained by the change of adsorption mode: while the benzoic acid stays in bidentate mode, the ben-NDI prefers monodental adsorption due to steric constraints, leading to a comparably lower injection rate.

Table 4.2. Slope, adjusted R^2 values and estimated electron injection rates for cat-NDI, ben-NDI and hyd-NDI determined from the linear fits on the semi logarithmic mean value of 5 ETD simulations performed on fully solvated nuclear trajectories.

Molecule	Slope [fs^{-1}]	Adjusted R^2	Estimated Electron injection rate [s^{-1}]	Mean life time [fs]
cat-NDI	-0.028	0.96446	$2.8x10^{13}$	35
ben-NDI	$-4.37x10^{-3}$	0.99203	$4.37x10^{12}$	224
hyd-NDI	$-2.21\ x10^{-3}$	0.97753	$2.21x10^{12}$	452

4.4 Conclusion

We have investigated the photoinduced electron injection from three different anchoring molecules (catechol, benzoic acid, benzohydroxamic acid) as well as from core extended NDI based dyes with these three anchoring moieties. An evaluation of the importance of nuclear dynamics, conformational averaging and explicit solvation for the injection process was done. Nuclear dynamics are crucial for describing the electron injection process, suppressing oscillations back to the dye molecules and localizing the electron through dynamic disorder. Conformational and trajectory averaging has a profound impact, especially in the benzoic acid and hydroxamic acid derivatives. This is further underlined by the fact that the injection rate is strongly dependent on the anchoring mode (bidentate bridging vs

monodentate). Explicit solvation is of importance regarding the correct adsorption mode of anchoring groups and correct overall dynamics of the dyes. This holds especially true for the hydroxamic acid. For the nuclear trajectory generation, explicit water should therefore be included. Explicit solvent polarization effects are low due to the tight binding character of the Hamiltonian. Concerning all anchor-dye complexes explored, the cat-NDI emerged as the most effective (full injection within 150 fs). The ben-NDI (with 90 % within 500 fs) and hyd-NDI (65 % within 500 fs) showed lower injection rates. The computational strategy employed, including the effect of nuclear dynamics, trajectory averaging and explicit solvation at a still reasonable computational cost, allows for a more unbiased screening of potential molecular dyes and may be relevant in the development of new dye sensitized photoanodes for solar energy conversion.

4.5 References

(1) O'Regan, B.; Grätzel, M. A Low-Cost, High-Efficiency Solar Cell Based on Dye-Sensitized Colloidal TiO 2 Films. *Nature* **1991**, *353*, 737–740.

(2) Cao, Y.; Saygili, Y.; Ummadisingu, A.; Teuscher, J.; Luo, J.; Pellet, N.; Giordano, F.; Zakeeruddin, S. M.; Moser, J.-E.; Freitag, M.; Hagfeldt, A.; Grätzel, M. 11% Efficiency Solid-State Dye-Sensitized Solar Cells with Copper(II/I) Hole Transport Materials. *Nature Communications* **2017**, *8*, 15390.

(3) Zhang, L.; Yang, X.; Wang, W.; Gurzadyan, G. G.; Li, J.; Li, X.; An, J.; Yu, Z.; Wang, H.; Cai, B.; et al. 13.6% Efficient Organic Dye-Sensitized Solar Cells by Minimizing Energy Losses of the Excited State. *ACS Energy Lett.* **2019**, *4*, 943–951.

(4) Hagfeldt, A.; Boschloo, G.; Sun, L.; Kloo, L.; Pettersson, H. Dye-Sensitized Solar Cells. *Chem. Rev.* **2010**, *110*, 6595–6663.

(5) Li, F.; Fan, K.; Xu, B.; Gabrielsson, E.; Daniel, Q.; Li, L.; Sun, L. Organic Dye-Sensitized Tandem Photoelectrochemical Cell for Light Driven Total Water Splitting. *J. Am. Chem. Soc.* **2015**, *137*, 9153–9159.

(6) Yamamoto, M.; Nishizawa, Y.; Chábera, P.; Li, F.; Pascher, T.; Sundström, V.; Sun, L.; Imahori, H. Visible Light-Driven Water Oxidation with a Subporphyrin Sensitizer and a Water Oxidation Catalyst. *Chem. Commun.* **2016**, *52*, 13702–13705.

(7) Jiang, J.; Spies, J. A.; Swierk, J. R.; Matula, A. J.; Regan, K. P.; Romano, N.; Brennan, B. J.; Crabtree, R. H.; Batista, V. S.; Schmuttenmaer, C. A.; Brudvig, G. W. Direct Interfacial Electron Transfer from High-Potential Porphyrins into Semiconductor Surfaces: A Comparison of Linkers and Anchoring Groups. *J. Phys. Chem. C* **2018**, *122*, 13529–13539.

(8) Massin, J.; Bräutigam, M.; Bold, S.; Wächtler, M.; Pavone, M.; Muñoz-García, A. B.; Dietzek, B.; Artero, V.; Chavarot-Kerlidou, M. Investigating Light-Driven Hole Injection and Hydrogen Evolution Catalysis at Dye-Sensitized NiO Photocathodes: A Combined Experimental–Theoretical Study. *J. Phys. Chem. C* **2019**, *123*, 17176–17184.

(9) Yu, Z.; Li, F.; Sun, L. Recent Advances in Dye-Sensitized Photoelectrochemical Cells for Solar Hydrogen Production Based on Molecular Components. *Energy Environ. Sci.* **2015**, *8*, 760–775.

(10) Haque, S. A.; Palomares, E.; Cho, B. M.; Green, A. N. M.; Hirata, N.; Klug, D. R.; Durrant, J. R. Charge Separation versus Recombination in Dye-Sensitized Nanocrystalline Solar Cells: The Minimization of Kinetic Redundancy. *J. Am. Chem. Soc.* **2005**, *127*, 3456–3462.

(11) Maggio, E.; Martsinovich, N.; Troisi, A. Evaluating Charge Recombination Rate in Dye-Sensitized Solar Cells from Electronic Structure Calculations. *J. Phys. Chem. C* **2012**, *116*, 7638–7649.

(12) Mai, S.; González, L. Molecular Photochemistry: Recent Developments in Theory. *Angewandte Chemie International Edition* **2020**, *59*, 16832–16846.

(13) Persico, M.; Granucci, G. Photochemistry. A Modern Theoretical Perspective.; Springer: Cham (Switzerland), 2018.

(14) Belić, J.; van Beek, B.; Menzel, J. P.; Buda, F.; Visscher, L. Systematic Computational Design and Optimization of Light Absorbing Dyes. *J. Phys. Chem. A* **2020**, *124*, 6380–6388.

(15) Le Bahers, T.; Labat, F.; Pauporté, T.; Lainé, P. P.; Ciofini, I. Theoretical Procedure for Optimizing Dye-Sensitized Solar Cells: From Electronic Structure to Photovoltaic Efficiency. *J. Am. Chem. Soc.* **2011**, *133*, 8005–8013.

(16) De Angelis, F.; Fantacci, S.; Selloni, A.; Grätzel, M.; Nazeeruddin, M. K. Influence of the Sensitizer Adsorption Mode on the Open-Circuit Potential of Dye-Sensitized Solar Cells. *Nano Lett.* **2007**, *7*, 3189–3195.

(17) Cheng, J.; Sulpizi, M.; Van de Vondele, J.; Sprik, M. Hole Localization and Thermochemistry of Oxidative Dehydrogenation of Aqueous Rutile TiO2(110). *ChemCatChem.* **2012**, *4*, 636–640.

(18) Yang, L.; Lindblad, R.; Gabrielsson, E.; Boschloo, G.; Rensmo, H.; Sun, L.; Hagfeldt, A.; Edvinsson, T.; Johansson, E. M. J. Experimental and Theoretical Investigation of the Function

of 4-Tert-Butyl Pyridine for Interface Energy Level Adjustment in Efficient Solid-State Dye-Sensitized Solar Cells. *ACS Appl. Mater. Interfaces* **2018**, *10*, 11572–11579.

(19) Pastore, M.; Mosconi, E.; De Angelis, F.; Grätzel, M. A Computational Investigation of Organic Dyes for Dye-Sensitized Solar Cells: Benchmark, Strategies, and Open Issues. *J. Phys. Chem. C* **2010**, *114*, 7205–7212.

(20) Pastore, M.; Fantacci, S.; De Angelis, F. Ab Initio Determination of Ground and Excited State Oxidation Potentials of Organic Chromophores for Dye-Sensitized Solar Cells. *J. Phys. Chem. C* **2010**, *114*, 22742–22750.

(21) De Angelis, F.; Fantacci, S.; Gebauer, R. Simulating Dye-Sensitized TiO2 Heterointerfaces in Explicit Solvent: Absorption Spectra, Energy Levels, and Dye Desorption. *J. Phys. Chem. Lett.* **2011**, *2*, 813–817.

(22) Akimov, A. V.; Neukirch, A. J.; Prezhdo, O. V. Theoretical Insights into Photoinduced Charge Transfer and Catalysis at Oxide Interfaces. *Chem. Rev.* **2013**, *113*, 4496–4565.

(23) Curchod, B. F. E.; Rothlisberger, U.; Tavernelli, I. Trajectory-Based Nonadiabatic Dynamics with Time-Dependent Density Functional Theory. *Chem. Phys. Chem.* **2013**, *14*, 1314–1340.

(24) Rozzi, A. C.; Falke, M. S.; Spallanzani, N.; Rubio, A.; Molinari, E.; Brida, D.; Maiuri, M.; Cerullo, G.; Schramm, H.; Christoffers, J.; Lienau, C. Quantum Coherence Controls the Charge Separation in a Prototypical Artificial Light-Harvesting System. *Nature Communications* **2013**, *4*, 1602.

(25) Eisenmayer, T. J.; Buda, F. Real-Time Simulations of Photoinduced Coherent Charge Transfer and Proton-Coupled Electron Transfer. *ChemPhysChem* **2014**, *15*, 3258–3263.

(26) Menzel, J. P.; de Groot, H. J. M.; Buda, F. Photoinduced Electron Transfer in Donor–Acceptor Complexes: Isotope Effect and Dynamic Symmetry Breaking. *J. Phys. Chem. Lett.* **2019**, *10*, 6504–6511.

(27) Meng, S.; Ren, J.; Kaxiras, E. Natural Dyes Adsorbed on TiO_2 Nanowire for Photovoltaic Applications: Enhanced Light Absorption and Ultrafast Electron Injection. *Nano Lett.* **2008**, *8*, 3266–3272.

(28) Duncan, W. R.; Prezhdo, O. V. Temperature Independence of the Photoinduced Electron Injection in Dye-Sensitized TiO2 Rationalized by Ab Initio Time-Domain Density Functional Theory. *J. Am. Chem. Soc.* **2008**, *130*, 9756–9762.

(29) Meng, S.; Kaxiras, E. Electron and Hole Dynamics in Dye-Sensitized Solar Cells: Influencing Factors and Systematic Trends. *Nano Lett.* **2010**, *10*, 1238–1247.

(30) Kolesov, G.; Grånäs, O.; Hoyt, R.; Vinichenko, D.; Kaxiras, E. Real-Time TD-DFT with Classical Ion Dynamics: Methodology and Applications. *J. Chem. Theory Comput.* **2016**, *12*, 466–476.

(31) Long, R.; Casanova, D.; Fang, W.-H.; Prezhdo, O. V. Donor–Acceptor Interaction Determines the Mechanism of Photoinduced Electron Injection from Graphene Quantum Dots into TiO_2: π-Stacking Supersedes Covalent Bonding. *J. Am. Chem. Soc.* **2017**, *139*, 2619–2629.

(32) Rego, L. G. C.; Batista, V. S. Quantum Dynamics Simulations of Interfacial Electron Transfer in Sensitized TiO_2 Semiconductors. *J. Am. Chem. Soc.* **2003**, *125*, 7989–7997.

(33) Rego, L. G. C.; Abuabara, S. G.; Batista, V. S. Coherent Optical Control of Electronic Excitations in Functionalized Semiconductor Nanostructures. *Quantum Info. Comput.* **2005**, *5*, 318–334.

(34) Rego, L. G. C.; Abuabara, S. G.; Batista, V. S. Model Study of Coherent Quantum Dynamics of Hole States in Functionalized Semiconductor Nanostructures. *The Journal of Chemical Physics* **2005**, *122*, 154709.

(35) Rego, L. G. C.; Abuabara, S. G.; Batista, V. S. Coherent Control of Tunnelling Dynamics in Functionalized Semiconductor Nanostructures: A Quantum-Control Scenario Based on Stochastic Unitary Pulses. *Journal of Modern Optics* **2006**, *53*, 2519–2532.

(36) Xiao, D.; Martini, L. A.; Snoeberger, R. C.; Crabtree, R. H.; Batista, V. S. Inverse Design and Synthesis of Acac-Coumarin Anchors for Robust TiO2 Sensitization. *J. Am. Chem. Soc.* **2011**, *133*, 9014–9022.

(37) Monti, A.; Negre, C. F. A.; Batista, V. S.; Rego, L. G. C.; de Groot, H. J. M.; Buda, F. Crucial Role of Nuclear Dynamics for Electron Injection in a Dye–Semiconductor Complex. *J. Phys. Chem. Lett.* **2015**, *6*, 2393–2398.
(38) Poddutoori, P. K.; Thomsen, J. M.; Milot, R. L.; Sheehan, S. W.; Negre, C. F. A.; Garapati, V. K. R.; Schmuttenmaer, C. A.; Batista, V. S.; Brudvig, G. W.; van der Est, A. Interfacial Electron Transfer in Photoanodes Based on Phosphorus(V) Porphyrin Sensitizers Co-Deposited on SnO_2 with the Ir(III)Cp* Water Oxidation Precatalyst. *J. Mater. Chem. A* **2015**, *3*, 3868–3879.
(39) McNamara, W. R.; Snoeberger III, R. C.; Li, G.; Richter, C.; Allen, L. J.; Milot, R. L.; Schmuttenmaer, C. A.; Crabtree, R. H.; Brudvig, G. W.; Batista, V. S. Hydroxamate Anchors for Water-Stable Attachment to TiO2 Nanoparticles. *Energy Environ. Sci.* **2009**, *2*, 1173.
(40) Lim, G. N.; Hedström, S.; Jung, K. A.; Smith, P. A. D.; Batista, V. S.; D'Souza, F.; van der Est, A.; Poddutoori, P. K. Interfacial Electron Transfer Followed by Photooxidation in N,N-Bis(p-Anisole)Aminopyridine–Aluminum(III) Porphyrin–Titanium(IV) Oxide Self-Assembled Photoanodes. *J. Phys. Chem. C* **2017**, *121*, 14484–14497.
(41) Lee, S. H.; Regan, K. P.; Hedström, S.; Matula, A. J.; Chaudhuri, S.; Crabtree, R. H.; Batista, V. S.; Schmuttenmaer, C. A.; Brudvig, G. W. Linker Length-Dependent Electron-Injection Dynamics of Trimesitylporphyrins on SnO2 Films. *J. Phys. Chem. C* **2017**, *121*, 22690–22699.
(42) Tichnell, C. R.; Miller, J. N.; Liu, C.; Mukherjee, S.; Jakubikova, E.; McCusker, J. K. Influence of Electrolyte Composition on Ultrafast Interfacial Electron Transfer in Fe-Sensitized TiO2-Based Solar Cells. *J. Phys. Chem. C* **2020**, *124*, 1794–1811.
(43) Shahroosvand, H.; Abaspour, S.; Pashaei, B.; Bideh, B. N. On How Ancillary Ligand Substitution Affects the Charge Carrier Dynamics in Dye-Sensitized Solar Cells. *RSC Adv.* **2018**, *8*, 19465–19469.
(44) Shahroosvand, H.; Abbasi, P.; Bideh, B. N. Dye-Sensitized Solar Cell Based on Novel Star-Shaped Ruthenium Polypyridyl Sensitizer: New Insight into the Relationship between Molecular Designing and Its Outstanding Charge Carrier Dynamics. *ChemistrySelect* **2018**, *3*, 6821–6829.
(45) Abuabara, S. G.; Cady, C. W.; Baxter, J. B.; Schmuttenmaer, C. A.; Crabtree, R. H.; Brudvig, G. W.; Batista, V. S. Ultrafast Photooxidation of Mn(II)−Terpyridine Complexes Covalently Attached to TiO_2 Nanoparticles. *J. Phys. Chem. C* **2007**, *111*, 11982–11990.
(46) Mukherjee, S.; Liu, C.; Jakubikova, E. Comparison of Interfacial Electron Transfer Efficiency in [Fe(Ctpy)2]2+–TiO2 and [Fe(CCNC)2]2+–TiO2 Assemblies: Importance of Conformational Sampling. *J. Phys. Chem. A* **2018**, *122*, 1821–1830.
(47) McNamara, W. R.; Snoeberger, R. C.; Li, G.; Schleicher, J. M.; Cady, C. W.; Poyatos, M.; Schmuttenmaer, C. A.; Crabtree, R. H.; Brudvig, G. W.; Batista, V. S. Acetylacetonate Anchors for Robust Functionalization of TiO_2 Nanoparticles with Mn(II)−Terpyridine Complexes. *J. Am. Chem. Soc.* **2008**, *130*, 14329–14338.
(48) Negre, C. F. A.; Young, K. J.; Oviedo, Ma. B.; Allen, L. J.; Sánchez, C. G.; Jarzembska, K. N.; Benedict, J. B.; Crabtree, R. H.; Coppens, P.; Brudvig, G. W.; Batista, V. S. Photoelectrochemical Hole Injection Revealed in Polyoxotitanate Nanocrystals Functionalized with Organic Adsorbates. *J. Am. Chem. Soc.* **2014**, *136*, 16420–16429.
(49) Hoff, D. A.; Silva, R.; Rego, L. G. C. Subpicosecond Dynamics of Metal-to-Ligand Charge-Transfer Excited States in Solvated [Ru(Bpy)3]2+ Complexes. *J. Phys. Chem. C* **2011**, *115*, 15617–15626.
(50) da Silva, R.; Hoff, D. A.; Rego, L. G. C. Coupled Quantum-Classical Method for Long Range Charge Transfer: Relevance of the Nuclear Motion to the Quantum Electron Dynamics. *J. Phys.: Condens. Matter* **2015**, *27*, 134206.
(51) Hoff, D. A.; da Silva, R.; Rego, L. G. C. Coupled Electron–Hole Quantum Dynamics on D−π–A Dye-Sensitized TiO_2 Semiconductors. *J. Phys. Chem. C* **2012**, *116*, 21169–21178.
(52) Torres, A.; Oliboni, R. S.; Rego, L. G. C. Vibronic and Coherent Effects on Interfacial Electron Transfer Dynamics. *J. Phys. Chem. Lett.* **2015**, *6*, 4927–4935.

(53) da Silva Oliboni, R.; Bortolini, G.; Torres, A.; Rego, L. G. C. A Nonadiabatic Excited State Molecular Mechanics/Extended Hückel Ehrenfest Method. *J. Phys. Chem. C* **2016**, *120*, 27688–27698.
(54) Torres, A.; Prado, L. R.; Bortolini, G.; Rego, L. G. C. Charge Transfer Driven Structural Relaxation in a Push–Pull Azobenzene Dye–Semiconductor Complex. *J. Phys. Chem. Lett.* **2018**, *9*, 5926–5933.
(55) Oliboni, R. S.; Yan, H.; Fan, H.; Abraham, B.; Avenoso, J. P.; Galoppini, E.; Batista, V. S.; Gundlach, L.; Rego, L. G. C. Vibronic Effects in the Ultrafast Interfacial Electron Transfer of Perylene-Sensitized TiO2 Surfaces. *J. Phys. Chem. C* **2019**, *123*, 12599–12607.
(56) Ambrosio, F.; Martsinovich, N.; Troisi, A. What Is the Best Anchoring Group for a Dye in a Dye-Sensitized Solar Cell? *J. Phys. Chem. Lett.* **2012**, *3*, 1531–1535.
(57) Sakai, N.; Mareda, J.; Vauthey, E.; Matile, S. Core-Substituted Naphthalenediimides. *Chem. Commun.* **2010**, *46*, 4225–4237.
(58) Narsaria, A. K.; Ruijter, J. D.; Hamlin, T. A.; Ehlers, A. W.; Guerra, C. F.; Lammertsma, K.; Bickelhaupt, F. M. Performance of TDDFT Vertical Excitation Energies of Core-Substituted Naphthalene Diimides. *Journal of Computational Chemistry* **2020**, *41*, 1448–1455.
(59) Elstner, M.; Porezag, D.; Jungnickel, G.; Elsner, J.; Haugk, M.; Frauenheim, Th.; Suhai, S.; Seifert, G. Self-Consistent-Charge Density-Functional Tight-Binding Method for Simulations of Complex Materials Properties. *Phys. Rev. B* **1998**, *58*, 7260–7268.
(60) Elstner, M.; Frauenheim, T.; Kaxiras, E.; Seifert, G.; Suhai, S. A Self-Consistent Charge Density-Functional Based Tight-Binding Scheme for Large Biomolecules. *physica status solidi (b)* **2000**, *217*, 357–376.
(61) Frauenheim, T.; Seifert, G.; Elsterner, M.; Hajnal, Z.; Jungnickel, G.; Porezag, D.; Suhai, S.; Scholz, R. A Self-Consistent Charge Density-Functional Based Tight-Binding Method for Predictive Materials Simulations in Physics, Chemistry and Biology. *physica status solidi (b)* **2000**, *217*, 41–62.
(62) ADF 2019.3, SCM, Theoretical Chemistry, Vrije Universiteit, Amsterdam, The Netherlands, http://www.scm.com.
(63) Velde, G. te; Bickelhaupt, F. M.; Baerends, E. J.; Fonseca Guerra, C.; van Gisbergen, S. J. A.; Snijders, J. G.; Ziegler, T. Chemistry with ADF. *J. Comput. Chem.* **2001**, *22*, 931–967.
(64) Dolgonos, G.; Aradi, B.; Moreira, N. H.; Frauenheim, T. An Improved Self-Consistent-Charge Density-Functional Tight-Binding (SCC-DFTB) Set of Parameters for Simulation of Bulk and Molecular Systems Involving Titanium. *J. Chem. Theory Comput.* **2010**, *6*, 266–278.
(65) Luttrell, T.; Halpegamage, S.; Tao, J.; Kramer, A.; Sutter, E.; Batzill, M. Why Is Anatase a Better Photocatalyst than Rutile? - Model Studies on Epitaxial TiO 2 Films. *Scientific Reports* **2014**, *4*, 4043.
(66) Rudshteyn, B.; Negre, C. F. A.; Oliboni, R. S.; Monti, A.; Chen, J.; Crabtree, R. H.; Rego, L. G. C.; Batista, V. S. Inferring Protonation States of Hydroxamate Adsorbates on TiO_2 Surfaces. *J. Phys. Chem. C* **2017**, *121*, 11985–11990.
(67) Berendsen, H. J. C.; Postma, J. P. M.; van Gunsteren, W. F.; DiNola, A.; Haak, J. R. Molecular Dynamics with Coupling to an External Bath. *J. Chem. Phys.* **1984**, *81*, 3684–3690.
(68) Alvarez, S. Table of Parameters for Extended Huckel Calculations, Collected by Santiago Alvarez, Universitat de Barcelona (1995). **1995**.
(69) Becke, A. D. A New Mixing of Hartree–Fock and Local Density-functional Theories. *J. Chem. Phys.* **1993**, *98*, 1372–1377.
(70) Lee, C.; Yang, W.; Parr, R. G. Development of the Colle-Salvetti Correlation-Energy Formula into a Functional of the Electron Density. *Phys. Rev. B* **1988**, *37*, 785–789.
(71) Van Lenthe, E.; Baerends, E. J. Optimized Slater-Type Basis Sets for the Elements 1–118. *Journal of Computational Chemistry* **2003**, *24*, 1142–1156.
(72) Pye, C. C.; Ziegler, T. An Implementation of the Conductor-like Screening Model of Solvation within the Amsterdam Density Functional Package. *Theor Chem Acc* **1999**, *101*, 396–408.
(73) Ooyama, Y.; Yamaji, K.; Ohshita, J. Photovoltaic Performances of Type-II Dye-Sensitized Solar Cells Based on Catechol Dye Sensitizers: Retardation of Back-Electron Transfer by PET (Photo-Induced Electron Transfer). *Mater. Chem. Front.* **2017**, *1*, 2243–2255.

(74) Selli, D.; Fazio, G.; Seifert, G.; Di Valentin, C. Water Multilayers on TiO2 (101) Anatase Surface: Assessment of a DFTB-Based Method. *J. Chem. Theory Comput.* **2017**, *13*, 3862–3873.

(75) Aschauer, U. J.; Tilocca, A.; Selloni, A. Ab Initio Simulations of the Structure of Thin Water Layers on Defective Anatase TiO2(101) Surfaces. *International Journal of Quantum Chemistry* **2015**, *115*, 1250–1257.

4.A Appendix

4A.1 Extended Hückel parameter optimization

In the quantum dynamics calculations, the correct energetic values of the involved orbitals are crucial, since they determine the thermodynamic driving force as well as the time evolution of the electronic wave packets. They are obtained using the tight binding Hamiltonian based on Extended Hückel theory that was described in chapter 2. To obtain reliable results, we need to optimize the semi-empirical parameters defining the matrix elements of the Extended Hückel Hamiltonian in such a way that they reproduce experimental values. As there is only limited experimental information on some of the investigated molecules, an alternative to experimental values is needed for parameter optimization. Here, we use ΔSCF[1,2] values obtained in implicit solvation to obtain the ionization potential that is related to the HOMO via the Koopmans theorem.[3] Thereby, a geometry optimization of the neutral species was performed, as well as an unrestricted calculation on this same geometry with one electron removed. The energy difference between these two SCF calculations is then a reasonable estimate of the experimental oxidation potential. These values were calculated with the ADF program by SCM (Software for Chemistry and Materials)[4,5] at the DFT/B3LYP[6–8] level using a Double Zeta with one Polarization Function (DZP) basis set[9] and D3 dispersion corrections with BJ-damping[10,11] within COSMO[12] implicit water solvation. This combination was chosen, since the ΔSCF results in the corresponding implicit solvation agree reasonably well with available experimental oxidation potentials (see table 4A.1).

Table 4A.1: Experimental oxidation potential, ΔSCF estimate using B3LYP/DZP, D3-BJ and COSMO solvation of the solvent used in the experiment and COSMO water.

Molecule	Solvent used in experiment	ΔSCF in experimental solvent [eV]	Experimental Oxidation Potential [V]	ΔSCF in COSMO water [eV]
Catechol	Acetonitrile	-5.86	-5.83[13]	-5.79
Benzoic acid	Water	-7.07	-	-7.07
Benzhydroxamic acid	Water	-6.74	-	-6.74
NDI	Dichloromethane (DCM)	-7.01	-7.07[14]	-6.94
NDI_2OEt	DCM	-6.31	-6.16[14]	-6.05
NDI_2NHEt	DCM	-5.45	-5.35[14]	-5.20
NDI_NHEt_OEt	DCM	-5.81	-5.75[14]	-5.55

For the NDI based dyes, the LUMO target energy was obtained by using the before mentioned ΔSCF value for the HOMO energy and adding the TD-DFT excitation energy obtained on the same geometry with the same settings. These values agree reasonably well with experimental values for several tested NDIs (see table 4A.2). Recently, also Narsaria *et al.* showed that B3LYP excitation energies for NDIs have a strong correlation with experimental excitation energies.[15]

Table 4A.2: Experimental oxidation potential, ΔSCF estimate using B3LYP/DZP, D3-BJ and COSMO solvation of the solvent used in the experiment, ΔSCF + TDDFT excitation energy estimate, experimental reduction potential. Values differing more than 0.2 eV marked in bold.

Molecule	Solvent used in experiment	ΔSCF in experim. solvent [eV]	Experim. Oxidation Potential [V]	ΔSCF + TDDFT Excitation energy (in brackets)	Experim. Reduction Potential [V]
Catechol	Acetonitrile	-5.86	-5.83[13]	**-0.93 (4.93)**	**-1.65**[13]
NDI	DCM	-7.01	-7.07[14]	-3.91 (3.10)	-4.01[14]
NDI_2OEt	DCM	-6.31	-6.16[14]	-3.77 (2.55)	-3.82[14]
NDI_ 2NHEt	DCM	-5.45	-5.35[14]	-3.52 (1.94)	-3.56[14]
NDI_ NHEt_OEt	DCM	-5.81	-5.75[14]	-3.62 (2.20)	-3.75[14]

Unfortunately, for the benzene based anchoring groups, this method does not give an accurate estimate and thus a different approach has been taken. The ΔSCF value still describes the experimental oxidation potential reasonably well and therefore is still taken as a reference for the HOMO energy. For the LUMO energy, the ΔSCF value plus the experimental onset of the first UV-Vis absorption peak is taken as reference, since also in experiments, difficult redox potentials are often estimated using this onset value and subtracting / adding it to the more easily obtained redox potential (reduction / oxidation potential).[13,14]

To summarize, the target energies for the frontier orbitals are obtained as follows: For all molecules, the ΔSCF values in water (COSMO) were used as HOMO target value. For the anchoring molecules catechol, benzoic acid and benzohydroxamic acid, the experimental first absorption peak onset energy was added to the ΔSCF value to obtain an estimate for the LUMO energy. For the NDI-derived molecules, the TDDFT excitation energies in COSMO using B3LYP/DZP for the excitation with the largest oscillator strength (here always the HOMO-LUMO excitation) were added to the ΔSCF values as an estimate for the LUMO energy. The values are reported in table 4A.3.

Optimization of the parameters was performed on the free dye and anchor molecules: they were optimized in their neutral (thus protonated) form before dissociative adsorption on the TiO_2 surface. Since the nuclear dynamics were performed using SCC-DFTB[16–18] with the tiorg-0-1 parameter set[19], the geometry optimization was performed with the same settings. Since the conduction band edge of the TiO_2 with the Extended Hückel Hamiltonian is at -10.00 eV and the experimental value for the anatase conduction band edge is at approximately -4.05 eV[20], the target values of the frontier orbitals of the molecules are shifted by -5.95 eV to give the correct energetic alignment. The optimization procedure itself was performed using a genetic algorithm and cost function that are described elsewhere.[21]

Table 4A.3: Target energies for HOMO (ΔSCF) and LUMO (either ΔSCF + TDDFT excitation energy or ΔSCF + experimental absorption peak onset energy).

Molecule	**Target HOMO [eV]**	**Target LUMO [eV]**	
	ΔSCF (water)	ΔSCF + TDDFT excitation energy in water (brackets)	ΔSCF + experimental absorption peak onset (brackets)
Catechol	-5.79		-1.61 (4.18[13])
Benzoic Acid	-7.07		-2.77 (~4.3[22])
Benzohydroxamic Acid	-6.74		-2.44 (~4.3[22])
2OEt-NDI	-6.05	-3.56 (2.50)	
Cat-NDI	-5.55	-3.50 (2.05)	
Ben-NDI	-6.06	-3.88 (2.18)	
Hyd-NDI	-6.04	-3.88 (2.16)	

Only HOMO and LUMO energies were used as targets. In table 4A.4 we compare the HOMO and LUMO energies obtained with standard parameters, the target values and the energies obtained with the optimized parameters.

Table 4A.4: HOMO/LUMO energies for the different molecules obtained with standard Hückel parameters, target values generated above with linear shift of -5.95 eV and obtained with optimized Hückel parameters.

Molecule	**Standard Hückel Parameters [eV]**		**Target values [eV]**		**Optimized Hückel parameters [eV]**	
	HOMO	LUMO	HOMO	LUMO	HOMO	LUMO
Catechol	-12.20	-8.17	-11.74	-7.56	-11.75	-7.55
Benzoic Acid	-12.81	-9.62	-13.02	-8.72	-13.02	-8.72
Benzohydroxamic Acid	-12.69	-9.43	-12.69	-8.39	-12.70	-8.39
2OEt-NDI	-12.14	-10.63	-12.00	-9.51	-12.00	-9.52
Cat-NDI	-11.96	-10.76	-11.50	-9.45	-11.50	-9.45
Ben-NDI	-12.10	-10.84	-12.01	-9.83	-12.01	-9.83
Hyd-NDI	-12.07	-10.83	-11.99	-9.83	-11.96	-9.81

The spatial distribution of the frontier orbitals was checked against their respective B3LYP counter parts to exclude unphysical orbitals. For the anchoring molecules, this was extended to HOMO-1 and LUMO+1 as well, since their high symmetry results in several near degenerate states that might mix and cross due to changing nuclear geometries. In tables 4A.5 and 4A.6, the spatial distribution of the frontier orbitals using B3LYP/COSMO and Extended Hückel using the optimized parameters are shown for the anchoring molecules and dyes. The optimized parameters give frontier orbital energies as well as spatial distributions that are very close to the B3LYP results.

Table 4A.5: Spatial distribution of HOMO-1, HOMO, LUMO and LUMO+1 for the three anchoring molecules, using B3LYP and the Extended Hückel method with optimized parameters

Molecule /Method	HOMO-1	HOMO	LUMO	LUMO+1
Catechol				
B3LYP		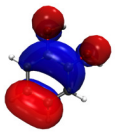	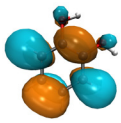	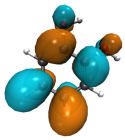
Extended Hückel Optimized	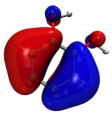	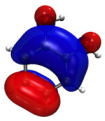	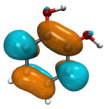	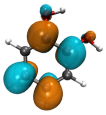
Benzoic Acid				
B3LYP	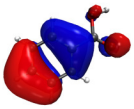	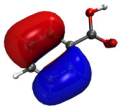	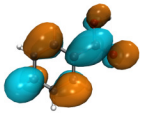	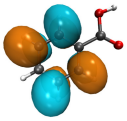
Extended Hückel Optimized	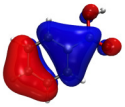	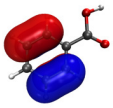	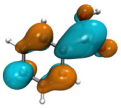	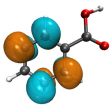
Benzohydroxamic Acid				
B3LYP	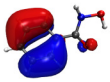	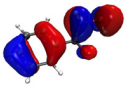	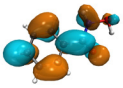	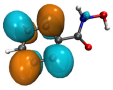
Extended Hückel Optimized	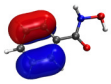	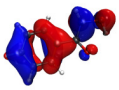	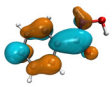	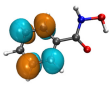

Table 4A.6: Spatial distribution of HOMO and LUMO for the NDI-based dyes, using B3LYP and the Extended Hückel method with optimized parameters

	HOMO		***LUMO***	
	B3LYP	*Extended Hückel*	*B3LYP*	*Extended Hückel*
2OEt-NDI	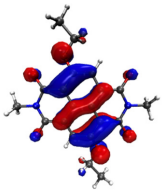	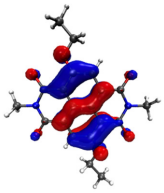	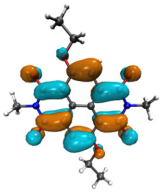	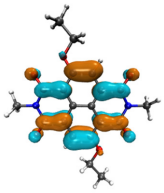
Cat-NDI	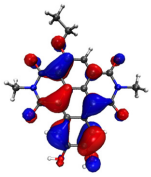	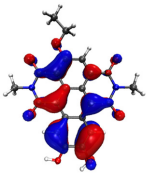	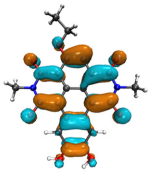	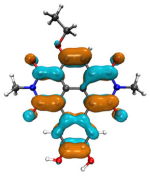
Ben-NDI	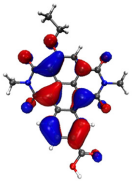	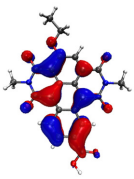	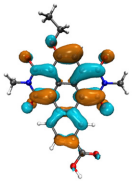	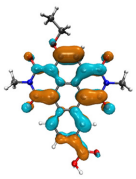
Hyd-NDI	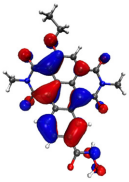	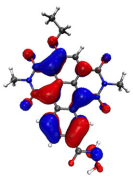	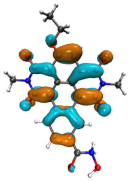	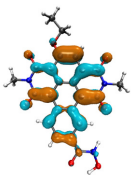

In figure 4A.1, the energetic alignment of the frontier orbitals of all optimized molecules are shown in comparison to the TiO_2 conduction band edge. As can be seen, all molecules have sufficient driving force to inject into the conduction band. The benzene derived anchoring groups have significantly higher LUMO energies than the NDI derived dyes. The carboxylic acid and hydroxamic acid-based core extended ethoxy NDIs have very similar LUMO energies close to the conduction band edge, while the catechol increases both the HOMO and LUMO energy values of the NDI in comparison to the other two anchoring groups.

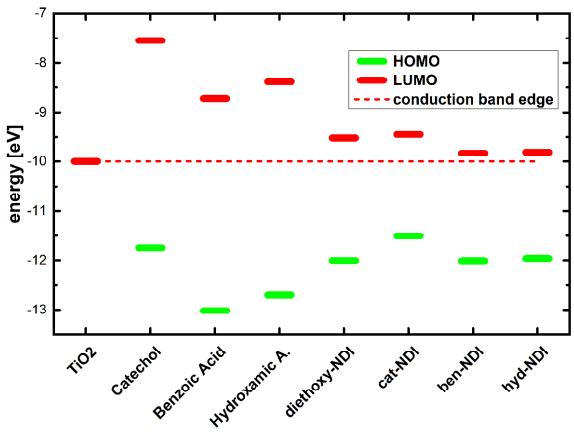

Figure 4A.1. HOMO and LUMO energies of the investigated anchoring molecules and dyes in comparison to the conduction band edge of anatase (dashed line) obtained with the Extended Hückel method using the optimized parameters.

Of course, this alignment might change during the attachment of the molecules on the TiO_2 surface and also during the dynamics. In figure 4A.2, the Partial Density of States (PDOS) of TiO_2 and the investigated anchoring molecules from the full photoanode system, with anchoring molecules attached to the electrode and explicit solvent is shown for comparison. All three anchoring molecules have a LUMO energy that is well within the conduction band of the TiO_2. Therefore, there is a driving force to inject a photoexcited electron into the conduction band. Catechol has the highest LUMO, followed by the benzohydroxamic acid and then the benzoic acid. The benzoic acid has a low amount of state density below the LUMO that comes from conduction band states that extend over the carboxylic acids' oxygens. This overlap might also explain the initial ultrafast injection of the benzoic acid, where the electron wave packet rapidly expands from the fragment LUMO onto states involving the TiO_2. In general, the HOMO – LUMO gap of the anchoring molecules is quite high and the LUMO well above the conduction band edge.

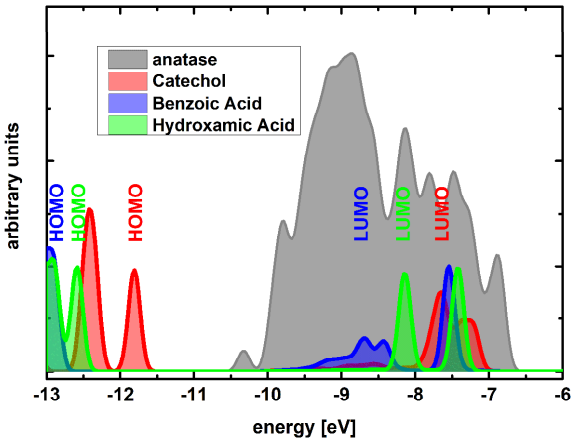

Figure 4A.2. Partial Densities of States (PDOS) in band gap and conduction band of the TiO_2 electrode (grey) and the adsorbed anchoring molecules catechol (red), benzoic acid (blue) and benzohydroxamic acid (green). The TiO_2 PDOS has been divided by 5 for easier comparison. Frontier orbitals are marked.

In figure 4A.3, the PDOS of the core extended ethoxy NDI molecules is shown in comparison to the TiO_2. HOMO-LUMO gaps are significantly lower than for the respective anchoring molecules. Cat-NDI has the highest LUMO energy, above the conduction band edge. Ben-NDI and Hyd-NDI show very similar PDOS, with their LUMOs slightly above the conduction band edge.

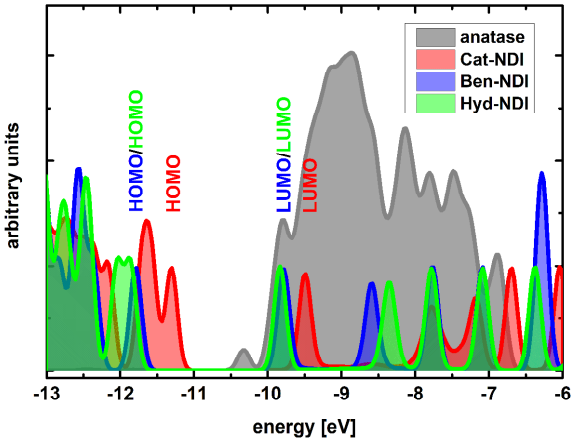

Figure 4A.3. Partial Densities of States (PDOS) in band gap and conduction band of the TiO_2 electrode (grey) and the adsorbed anchoring molecules cat-NDI (red), ben-NDI (blue) and hyd-NDI (green). The TiO_2 PDOS has been divided by 5 for easier comparison. Frontier orbitals are marked.

Here, the driving force is significantly lower than for the anchoring molecules, which is reflected in their significantly lower injection rates. However, the HOMO-LUMO gap lies for all three NDI molecules well in the visible light range and alignment seems favorable.

4A.2 Influence of dihedral angle on electron injection

In some of the ETD simulations, the observed delay in the injection can be tightly associated to the dihedral angle between the anchoring group and the aromatic system of the organic molecule. One such example is shown in figure 4A.4, where electron injection from benzohydroxamic acid is shown.

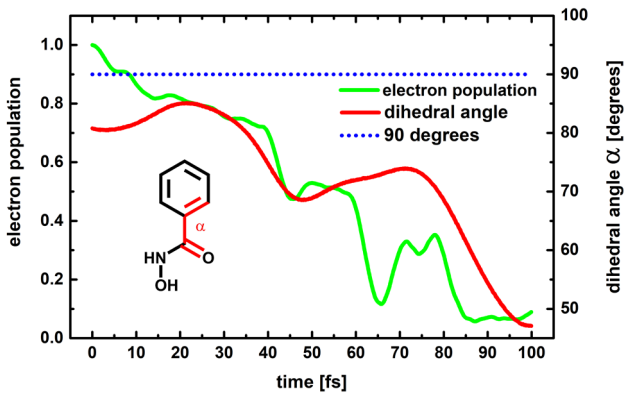

Figure 4A.4. Electron population on ben-NDI over time (green) in comparison to dihedral angle α (red) shown in the inlet structure. The dotted blue line corresponds to 90 degrees. Electron injection is hindered when the dihedral angle is close to 90 degrees, breaking conjugation.

A simulation with delayed injection was chosen and compared to the associated change in dihedral angle shown in the inset chemical structure. Injection is hindered when the angle approaches 90 degrees, breaking possible conjugation between the benzene group and the hydroxamate subsystem.

In figure 4A.5, an example is given from the ben-NDI case. The initial electron injection is fast, but at around 150 fs is stagnating, while the dihedral angle approaches 90 degrees with the aromatic system and anchoring group perpendicular to each other. For about 250 fs, the injection process is halted and only starts again

when the dihedral angle leaves the region around 90 degrees, opening a channel via the anchoring group.

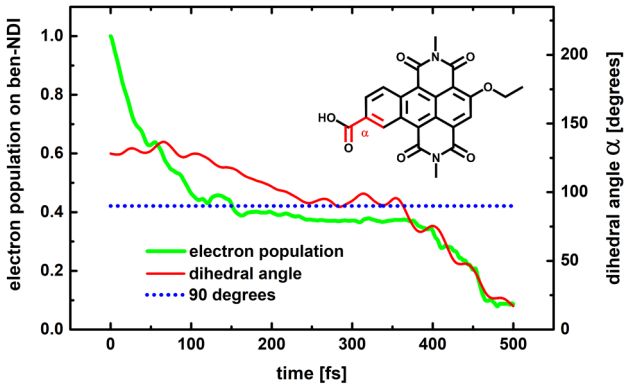

Figure 4A.5. Electron population on ben-NDI over time (green) in comparison to dihedral angle (red) shown in the inlet structure. The dotted blue line corresponds to 90 degrees. Electron injection is hindered when the dihedral angle is close to 90 degrees, breaking conjugation.

4A.3 Resonance coupling in the electron transfer process

As shown before, the nuclear geometries can allow or prohibit electron flow from the photoexcited dye towards the electrode. However, the nuclear motion itself can also be used by the electron for a rapid injection by taking advantage of resonant coupling. Whereas the electronic system is not able to activate nuclear modes and slow down the nuclear motion in the sense of coherent conversion from reactant to product state, it can use present modes available through the incoherent thermal noise for a nonadiabatic population transfer. As the LUMO of the dye molecules lays energetically within the conduction band of the TiO_2 electrode, the energy difference between electronic states is very small and a myriad of different states can couple to another. This leads to a very rich selection of modes that the electronic system can couple to in the region w/2p < 1000 cm^{-1}. Both, the electronic frequencies as well as the total nuclear vibrational density of states (VDOS) of a single electron injection trajectory of the photoexcited hyd-NDI molecule, are given in figure 4A.6. Water molecules are omitted from the VDOS for clarity. As is clear from the figure, most electronic frequencies (red) lie in the region w/2p < 1000 cm^{-1}, where a large variety of nuclear modes (blue) is available.

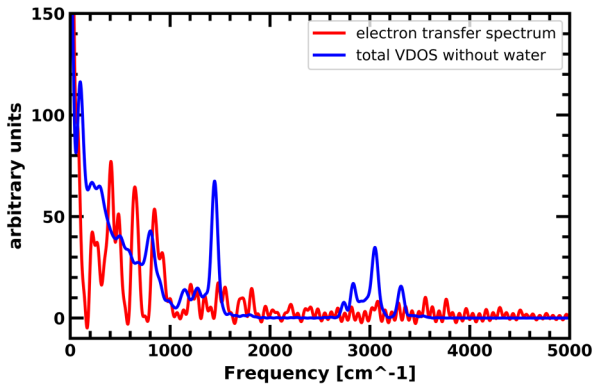

Figure 4A.6. Electron transfer frequencies (red) and total VDOS (blue) of a single trajectory of electron injection from photoexcited hydNDI with explicit water. The water molecules are removed from the VDOS for clarity. Notable are the large peaks in the electron transfer frequencies at low wavenumbers and the abundance of nuclear modes in the same region. A gaussian window function with a sigma value of 5 was used to reduce noise.

Over the course of the injection process, the electronic system can therefore couple to several nuclear modes, with some modes becoming more pronounced over the trajectory and others whose role diminishes. We note that this huge variety of possible pathways also leads to a significant speed-up of the conversion, especially within the electrode, since the high density of electronic states in the conduction band lead to a quick conversion to low lying states. In this system, the role of resonant coupling plays therefore an important role, but which exact modes couple to this process is of less relevance since there is a wide collection of modes available, that have very similar frequencies: there will always be a mode of correct frequency available.

Nevertheless, we show an example of resonant coupling between the electronic system and a specific nuclear mode below in figure 4A.7, that becomes so dominant in a part of the trajectory, that it can clearly be associated to the conversion process. The electronic frequencies and VDOS of the dihedral angle shown in the inset are given for the time 150-250 fs, where the coupling is most pronounced.

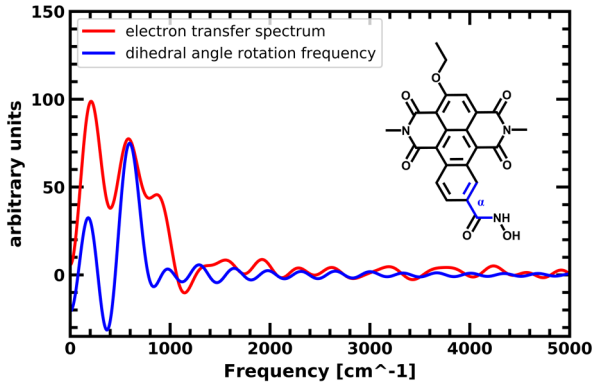

Figure 4A.7. Electron transfer frequency (red) and frequencies of the dihedral angle rotation (blue) marked in the inlet for the same trajectory as above between 150 and 250 fs. There is a clear resonance between the nuclear mode and the electron transfer frequencies with a peak at around 570 cm^{-1}. A gaussian window function with a sigma of 1 was used to reduce noise.

4A.4 Photoinduced electron injection – Catechol

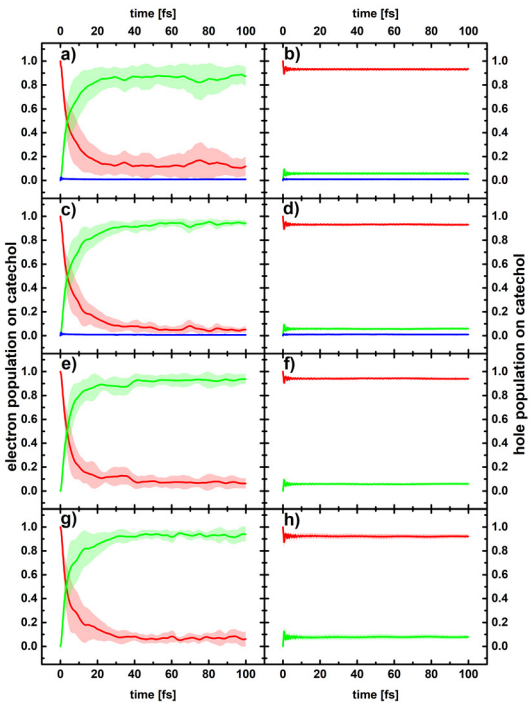

Figure 4A.8. Electron population (left panels) and hole population (right panels) on catechol (red), TiO_2 (green) and water (blue) averaged over 15 ETDs on
a)/b) static geometries,
c)/d) nuclear trajectories with explicit solvation,
e)/f) nuclear trajectories with explicit water removed,
g)/h) nuclear trajectories without water.
The bold lines denote the mean value, the shaded areas represent the standard deviation centered on the mean value.

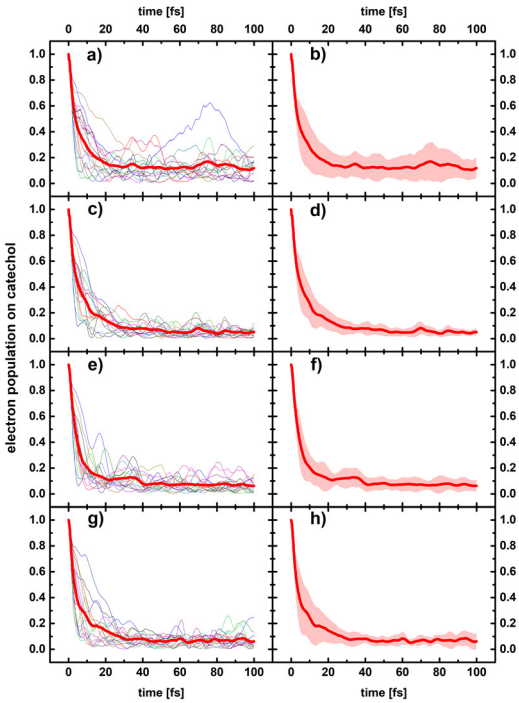

Figure 4A.9. Electron population on catechol. The left panels show the 15 single ETD runs in narrow lines, the resulting mean average in bold red; the right panels give this same mean average in bold red with the shaded areas representing the standard deviation. Results obtained on
a/b) static geometries,
c/d) nuclear trajectories with explicit water,
e/f) nuclear trajectories with water removed,
g/h) nuclear trajectories without water.

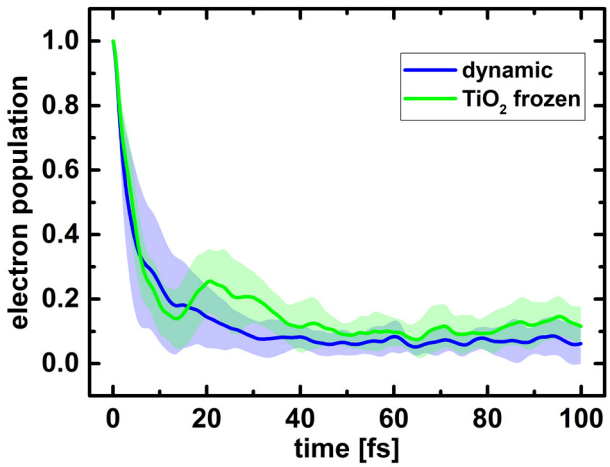

Figure 4A.10. Electron population on catechol averaged over 15 ETDs without explicit solvation allowing for TiO_2 nuclear dynamics (blue) and when freezing the TiO_2 electrode (green). The bold lines represent the mean value, the shaded areas the standard deviation.

4A.5 Photoinduced electron injection – Benzoic acid

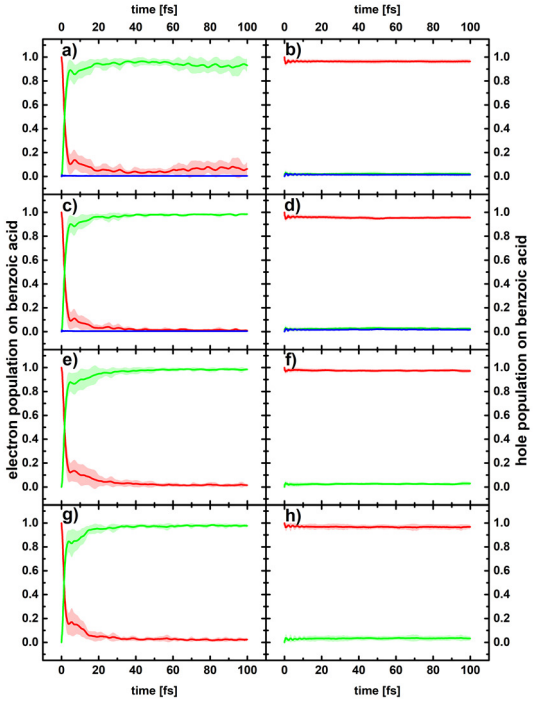

Figure 4A.11. Electron population (left panels) and hole population (right panels) on benzoic acid (red), TiO_2 (green) and water (blue) averaged over 15 ETDs on
a)/b) static geometries,
c)/d) nuclear trajectories with explicit solvation,
e)/f) nuclear trajectories with explicit water removed,
g)/h) nuclear trajectories without water.
The bold lines denote the mean value, the shaded areas represent the standard deviation centered on the mean value.

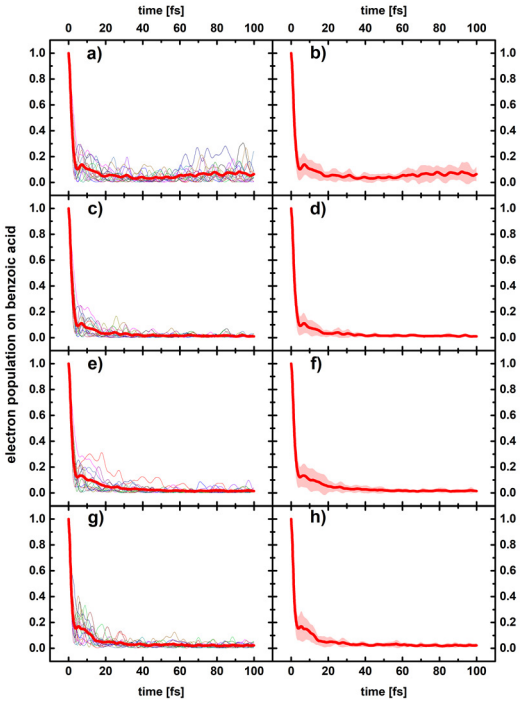

Figure 4A.12. Electron population on benzoic acid. The left panels show the 15 single ETD runs in narrow lines, the resulting mean average in bold red, the right panels give this same mean average in bold red with the shaded areas representing the standard deviation. Results obtained on
a/b) static geometries,
c/d) nuclear trajectories with explicit water,
e/f) nuclear trajectories with water removed,

4A.6 Photoinduced electron injection – Benzohydroxamic acid

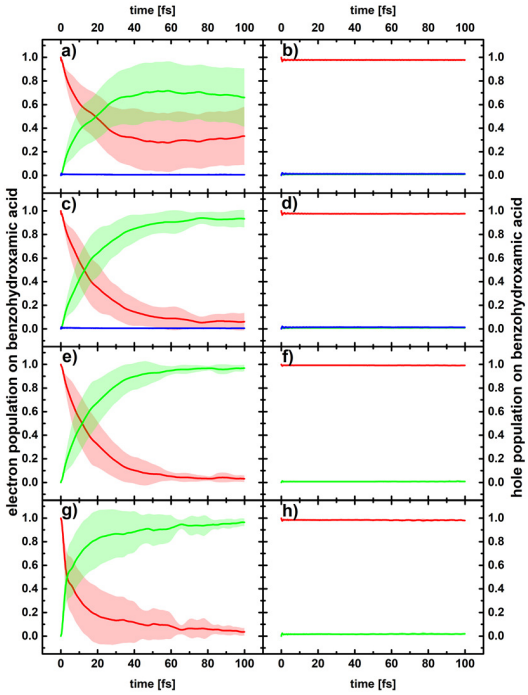

Figure 4A.13. Electron population (left panels) and hole population (right panels) on benzohydroxamic acid (red), TiO_2 (green) and water (blue) averaged over 15 ETDs on
a)/b) static geometries,
c)/d) nuclear trajectories with explicit solvation,
e)/f) nuclear trajectories with explicit water removed,
g)/h) nuclear trajectories without water.
The bold lines denote the mean value, the shaded areas represent the standard deviation centered on the mean value.

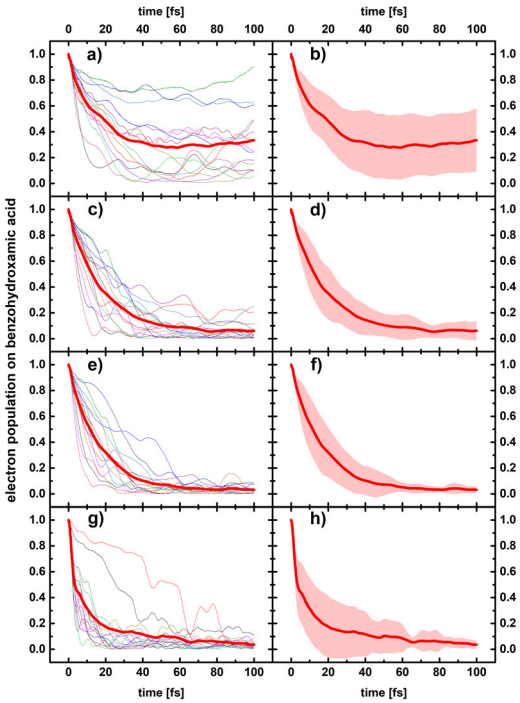

Figure 4A.14. Electron population on benzohydroxamic acid. The left panels show the 15 single ETD runs in narrow lines, the resulting mean average in bold red, the right panels give this same mean average in bold red with the shaded areas representing the standard deviation. Results obtained on
a/b) static geometries,
c/d) nuclear trajectories with explicit water,
e/f) nuclear trajectories with water removed,
g/h) nuclear trajectories without water.

4A.7 Photoinduced electron injection – Cat-NDI

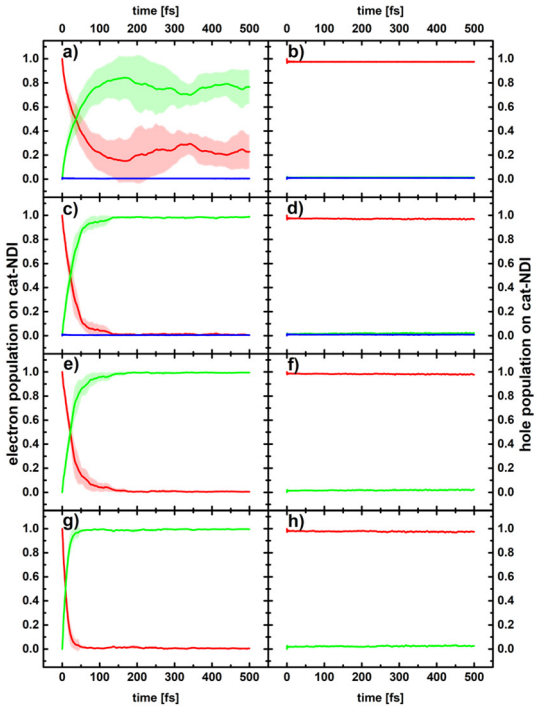

Figure 4A.15. Electron population (left panels) and hole population (right panels) on cat-NDI (red), TiO_2 (green) and water (blue) averaged over 5 ETDs on
a)/b) static geometries,
c)/d) nuclear trajectories with explicit solvation,
e)/f) nuclear trajectories with explicit water removed,
g)/h) nuclear trajectories without water. The bold lines denote the mean value, the shaded areas represent the standard deviation centered on the mean value.

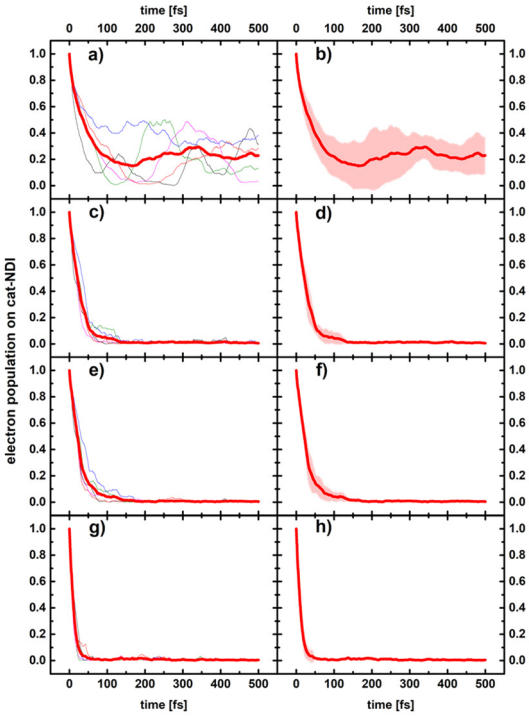

Figure 4A.16. Electron population on cat-NDI. The left panels show the 5 single ETD runs in narrow lines, the resulting mean average in bold red, the right panels give this same mean average in bold red with the shaded areas representing the standard deviation. Results obtained on
a/b) static geometries,
c/d) nuclear trajectories with explicit water,
e/f) nuclear trajectories with water removed,
g/h) nuclear trajectories without water.

4A.8 Photoinduced electron injection – Ben-NDI

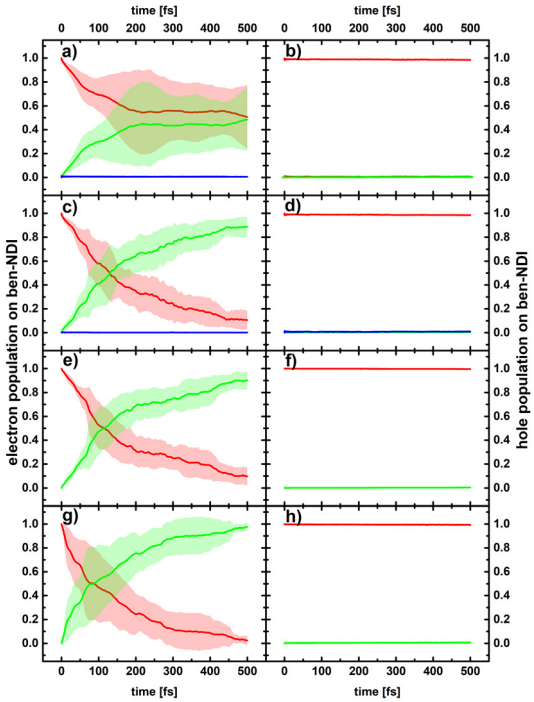

Figure 4A.17. Electron population (left panels) and hole population (right panels) on ben-NDI (red), TiO_2 (green) and water (blue) averaged over 5 ETDs on
a)/b) static geometries,
c)/d) nuclear trajectories with explicit solvation,
e)/f) nuclear trajectories with explicit water removed,
g)/h) nuclear trajectories without water. The bold lines denote the mean value, the shaded areas represent the standard deviation centered on the mean value.

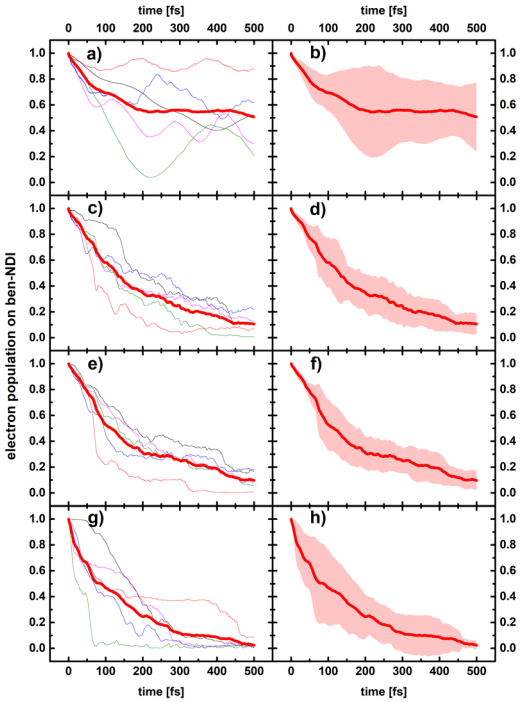

Figure 4A.18. Electron population on ben-NDI. The left panels show the 5 single ETD runs in narrow lines, the resulting mean average in bold red, the right panels give this same mean average in bold red with the shaded areas representing the standard deviation. Results obtained on
a/b) static geometries,
c/d) nuclear trajectories with explicit water,
e/f) nuclear trajectories with water removed,
g/h) nuclear trajectories without water.

4A.9 Photoinduced electron injection – Hyd-NDI

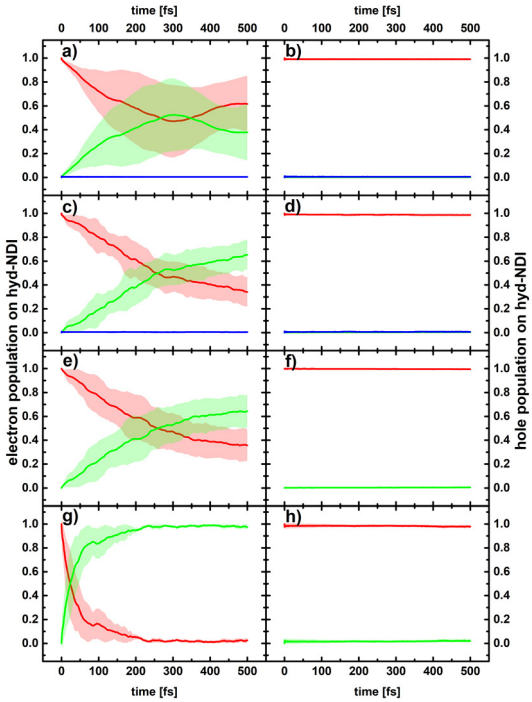

Figure 4A.19. Electron population (left panels) and hole population (right panels) on hyd-NDI (red), TiO_2 (green) and water (blue) averaged over 5 ETDs on
a)/b) static geometries,
c)/d) nuclear trajectories with explicit solvation,
e)/f) nuclear trajectories with explicit water removed,
g)/h) nuclear trajectories without water.
The bold lines denote the mean value, the shaded areas represent the standard deviation centered on the mean value.

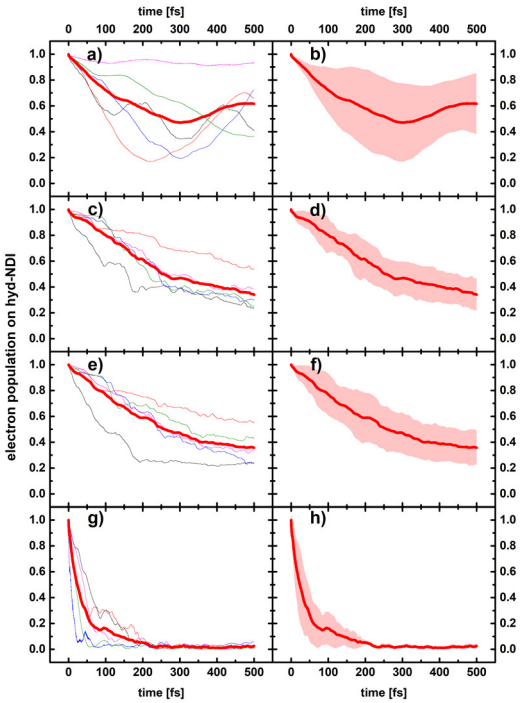

Figure 4A.20. Electron population on hyd-NDI. The left panels show the 5 single ETD runs in narrow lines, the resulting mean average in bold red, the right panels give this same mean average in bold red with the shaded areas representing the standard deviation. Results obtained on
a/b) static geometries,
c/d) nuclear trajectories with explicit water,
e/f) nuclear trajectories with water removed,
g/h) nuclear trajectories without water.

4A.10 References

(1) Gunnarsson, O.; Lundqvist, B. I. Exchange and Correlation in Atoms, Molecules, and Solids by the Spin-Density-Functional Formalism. *Phys. Rev. B* **1976**, *13* (10), 4274–4298.

(2) Jones, R. O.; Gunnarsson, O. The Density Functional Formalism, Its Applications and Prospects. *Rev. Mod. Phys.* **1989**, *61* (3), 689–746.

(3) Koopmans, T. Über die Zuordnung von Wellenfunktionen und Eigenwerten zu den Einzelnen Elektronen Eines Atoms. *Physica* **1934**, *1* (1), 104–113.

(4) Velde, G. te; Bickelhaupt, F. M.; Baerends, E. J.; Fonseca Guerra, C.; van Gisbergen, S. J. A.; Snijders, J. G.; Ziegler, T. Chemistry with ADF. *J. Comput. Chem.* **2001**, *22* (9), 931–967.

(5) ADF 2019.3, SCM, Theoretical Chemistry, Vrije Universiteit, Amsterdam, The Netherlands, http://www.scm.com. .

(6) Becke, A. D. Density-Functional Exchange-Energy Approximation with Correct Asymptotic Behavior. *Phys. Rev. A* **1988**, *38* (6), 3098–3100.

(7) Becke, A. D. A New Mixing of Hartree–Fock and Local Density-functional Theories. *J. Chem. Phys.* **1993**, *98* (2), 1372–1377.

(8) Lee, C.; Yang, W.; Parr, R. G. Development of the Colle-Salvetti Correlation-Energy Formula into a Functional of the Electron Density. *Phys. Rev. B* **1988**, *37* (2), 785–789.

(9) Van Lenthe, E.; Baerends, E. J. Optimized Slater-Type Basis Sets for the Elements 1–118. *Journal of Computational Chemistry* **2003**, *24*, 1142–1156.

(10) Grimme, S.; Antony, J.; Ehrlich, S.; Krieg, H. A Consistent and Accurate Ab Initio Parametrization of Density Functional Dispersion Correction (DFT-D) for the 94 Elements H-Pu. *J. Chem. Phys.* **2010**, *132* (15), 154104.

(11) Grimme, S.; Ehrlich, S.; Goerigk, L. Effect of the Damping Function in Dispersion Corrected Density Functional Theory. *Journal of Computational Chemistry* **2011**, *32* (7), 1456–1465.

(12) Pye, C. C.; Ziegler, T. An Implementation of the Conductor-like Screening Model of Solvation within the Amsterdam Density Functional Package. *Theor Chem Acc* **1999**, *101* (6), 396–408.

(13) Ooyama, Y.; Yamaji, K.; Ohshita, J. Photovoltaic Performances of Type-II Dye-Sensitized Solar Cells Based on Catechol Dye Sensitizers: Retardation of Back-Electron Transfer by PET (Photo-Induced Electron Transfer). *Mater. Chem. Front.* **2017**, *1* (11), 2243–2255.

(14) Sakai, N.; Mareda, J.; Vauthey, E.; Matile, S. Core-Substituted Naphthalenediimides. *Chem. Commun.* **2010**, *46* (24), 4225–4237.

(15) Narsaria, A. K.; Ruijter, J. D.; Hamlin, T. A.; Ehlers, A. W.; Guerra, C. F.; Lammertsma, K.; Bickelhaupt, F. M. Performance of TDDFT Vertical Excitation Energies of Core-Substituted Naphthalene Diimides. *Journal of Computational Chemistry* **2020**, *41* (15), 1448–1455.

(16) Elstner, M.; Porezag, D.; Jungnickel, G.; Elsner, J.; Haugk, M.; Frauenheim, Th.; Suhai, S.; Seifert, G. Self-Consistent-Charge Density-Functional Tight-Binding Method for Simulations of Complex Materials Properties. *Phys. Rev. B* **1998**, *58* (11), 7260–7268.

(17) Elstner, M.; Frauenheim, T.; Kaxiras, E.; Seifert, G.; Suhai, S. A Self-Consistent Charge Density-Functional Based Tight-Binding Scheme for Large Biomolecules. *physica status solidi (b)* **2000**, *217* (1), 357–376.

(18) Frauenheim, T.; Seifert, G.; Elsterner, M.; Hajnal, Z.; Jungnickel, G.; Porezag, D.; Suhai, S.; Scholz, R. A Self-Consistent Charge Density-Functional Based Tight-Binding Method for Predictive Materials Simulations in Physics, Chemistry and Biology. *physica status solidi (b)* **2000**, *217* (1), 41–62.

(19) Dolgonos, G.; Aradi, B.; Moreira, N. H.; Frauenheim, T. An Improved Self-Consistent-Charge Density-Functional Tight-Binding (SCC-DFTB) Set of Parameters for Simulation of Bulk and Molecular Systems Involving Titanium. *J. Chem. Theory Comput.* **2010**, *6* (1), 266–278.

(20) Fujisawa, J.; Eda, T.; Hanaya, M. Comparative Study of Conduction-Band and Valence-Band Edges of TiO2, SrTiO3, and BaTiO3 by Ionization Potential Measurements. *Chemical Physics Letters* **2017**, *685*, 23–26.

(21) Monti, A.; Negre, C. F. A.; Batista, V. S.; Rego, L. G. C.; de Groot, H. J. M.; Buda, F. Crucial Role of Nuclear Dynamics for Electron Injection in a Dye–Semiconductor Complex. *J. Phys. Chem. Lett.* **2015**, *6* (12), 2393–2398.

(22) Glorius, M.; Moll, H.; Bernhard, G. Complexation of Uranium(VI) with Aromatic Acids in Aqueous Solution – a Comparison of Hydroxamic Acids and Benzoic Acid. *Radiochimica Acta* **2007**, *95* (3), 151–157.

CHAPTER 5

Efficient Workflow for the Investigation of the Catalytic Cycle of Water Oxidation Catalysts: Combining GFN-xTB and DFT

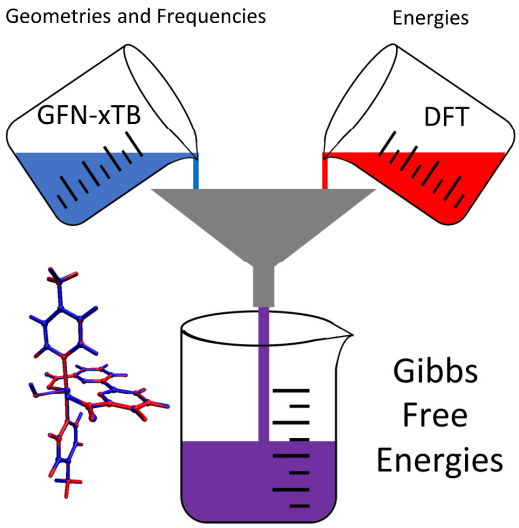

This Chapter is based on:

Jan Paul Menzel, Martijn Kloppenburg, Jelena Belić, Huub J.M. de Groot, Lucas Visscher, Francesco Buda; *Journal of Computational Chemistry*, **2021**, *42*, 1885-1894

5

ABSTRACT

Photocatalytic water oxidation remains the bottleneck in many artificial photosynthesis devices. The efficiency of this challenging process is inherently linked to the thermodynamic and electronic properties of the chromophore and the water oxidation catalyst (WOC). Computational investigations can facilitate the search for favorable chromophore-catalyst combinations. However, this remains a demanding task due to the requirements on the computational method that should be able to correctly describe different spin and oxidation states of the transition metal, the influence of solvation and the different rates of the charge transfer and water oxidation processes. To determine a suitable method with favorable cost/accuracy ratios, the full catalytic cycle of a molecular ruthenium based WOC is investigated using different computational methods, including density functional theory (DFT) with different functionals (GGA, Hybrid, Double Hybrid) as well as the semi-empirical tight binding approach GFN-xTB. A workflow with low computational cost is proposed that combines GFN-xTB and DFT and provides reliable results. GFN-xTB geometries and frequencies combined with single-point DFT energies give free energy changes along the catalytic cycle that closely follow the full DFT results and show satisfactory agreement with experiment, while significantly decreasing the computational cost. This workflow allows for cost efficient determination of energetic, thermodynamic and dynamic properties of WOCs.

5.1 Introduction

Chemical fuels produced by solar energy have shown potential as a clean energy alternative to carbon-based fossil fuels. Fuel production most commonly involves proton or CO_2 reduction. The electrons needed for this reduction can be obtained through the oxidation of water into protons, molecular oxygen and electrons. Therefore, water splitting dye-sensitized photoelectrochemical cells and other photoelectrochemical devices for solar energy production have been intensely investigated in the recent decades.[1–3] Still, the efficiency of such devices remains quite low as the water oxidation usually requires a high overpotential, well in excess to what is thermodynamically required, leading to significant energy losses beyond the thermodynamic limit. Although the overpotential can in principle be lowered by molecular catalysts, their operation with a sufficiently high turnover number and turnover frequency is a challenge. The development of a combination of a photosensitizer and a (transition metal-based) stable and rapid catalyst in a photocatalytic complex is thus a crucial step forward in the realization of more efficient devices. Ru-based transition metal complexes have in this respect in the last decade emerged as promising water oxidation catalyst (WOC) candidates.[4–8]

In addition to the catalyst itself, also the coupling of the WOC to a suitable photooxidative dye is challenging due to the different requirements for oxidation potentials and HOMO energies for the different catalytic steps that involve a number of oxidation states of the transition metal. Electronic configurations change through the catalytic cycle, which affects the nature of the HOMO and its energy. Computational investigations with *e.g.* estimation of redox potentials, orbital energies and excitation energies can help in finding suitable combinations of dye and WOC candidates.[9] Dynamics and solvent effects should also be taken into account to simulate both water oxidation as well as the initial photooxidation of a dye-WOC complex to obtain reliable insight in electron and hole transfer processes.[10] DFT-based *ab initio* molecular dynamics coupled with enhanced sampling techniques have been employed quite successfully in determining reaction barriers for water

oxidation processes with oxidized WOCs,[11–14] redox mediators[15,16] or photo-oxidized dyes.[17–20] However, these simulations are computationally very demanding as they require a quantum mechanical description of the entire system, including explicit solvation, since the water solvent participates actively in the catalytic reaction. Methods that well describe the organic molecular dyes, transition metal complexes and water are therefore needed, but this is complicated due to the open shell nature of the systems and the different spin states that need to be taken into account. Finding a computationally affordable and yet reliable method to determine thermodynamic requirements, oxidation potentials and dynamic properties remains challenging.

A semiempirical method that has shown great potential in the structural characterization of transition metal complexes is the GFN-xTB (Geometries, Frequencies, Non-covalent interactions extended Tight Binding) method developed by Grimme *et al.*[21] This method is based on atomic and global parameters that are optimized on basis of DFT. GFN-xTB has been used successfully for the description of transition metal complexes[21–23] and lanthanoides[24]. This method has been also extended on several fronts, including the GFN-2xTB, that is founded on more physically relevant parameters than GFN-xTB and the GFN-FF,[25,26] a force field parametrized on GFN-xTB results. Both GFN-xTB and GFN-2xTB have already been used in the determination of redox potentials with low computational cost.[27–29]

In this work, we determine whether GFN-xTB is a viable alternative to describe a Ru-based catalyst developed by Duan *et al.*[4], also with respect to potential molecular dynamics simulations. Therefore, we investigated the performance of GFN-xTB on this Ru-based WOC in comparison to DFT with different exchange correlation functionals and to available experimental data. We propose a computationally efficient workflow that combines GFN-xTB calculations for geometries and frequencies and B3LYP for energies, which leads to accurate relative Gibbs free energies along the catalytic cycle.

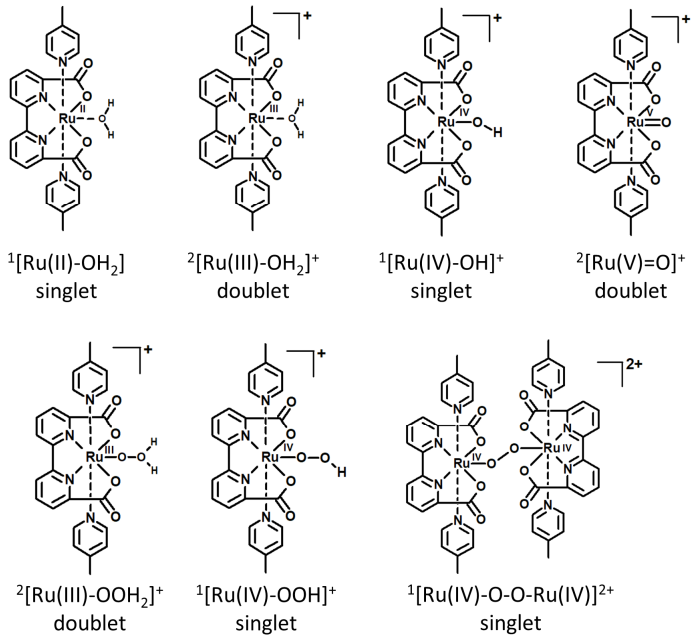

Scheme 5.1. Chemical structures, abbreviations used throughout the publication and favored spin state of all catalytic intermediates.

The possible catalytic intermediates of the WOC are shown in scheme 5.1, with their chemical structure, nomenclature used throughout the manuscript and their favored spin states. This class of catalysts has two possible catalytic pathways branching from the ^{2}[Ru(V)=O]$^+$ intermediate shown in scheme 5.2. One is the water nucleophilic attack (WNA)[30,31] pathway, where a water molecule attacks the oxygen of the ^{2}[Ru(V)=O]$^+$ as a nucleophile, leading to the ^{2}[Ru(III)-OOH$_2$]$^+$.[30] The other possible pathway involves two ^{2}[Ru(V)=O]$^+$ forming the ^{1}[Ru(IV)-O-O-Ru(IV)]$^{2+}$ dimer through a radical coupling mechanism: this mechanism has been called interaction of two metal oxo species (I2M) or radical oxo coupling (ROC) in the literature.[32,33] This binuclear reaction pathway often shows higher turnover frequencies and lower overpotentials than the WNA pathway. It also circumvents the problem of scaling relations between the Ru-OH and Ru-OOH bond strength that makes optimizing catalysts far from trivial due to the interdependence of these two parameters.[34,35]

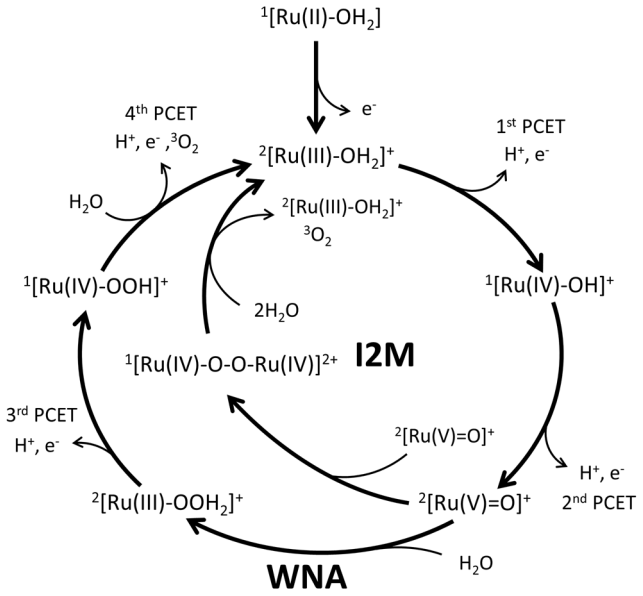

Scheme 5.2. Catalytic cycle with the two possible pathways from $^{2}[Ru(V)=O]^{+}$, water nucleophilic attack (WNA) and interaction of 2 metal oxo species (I2M).

However, the reaction rate in the I2M mechanism depends on the catalyst concentration, since two catalysts in the correct oxidation state have to encounter to form a dimer. This process can be accelerated by increasing the local concentration, *e.g.* through accumulation in self-assembling nanospheres.[36]

The investigated catalyst has been shown experimentally to perform via the I2M mechanism.[4] However, by exchanging both equatorial or axial ligands, the catalyst can be tailored and the I2M mechanism can be made either more dominant or less favorable, to the point where the WNA mechanism is enforced over the I2M route.[37–40] In general, complexes with excess spin density on the oxygen and attractive interactions between axial ligands of two complexes lead to I2M mechanisms, whereas stabilization of positive partial charge on the same oxygen (and thus a higher electrophilicity) and steric hindrance between two complexes leads to a preferred WNA.[32,38,39] Since both reaction mechanisms are possible for the investigated complex in different regimes, such as low concentration, immobilizing the catalyst on a surface etc., it is crucial that the computational methods used to investigate the

catalyst describe both mechanisms reasonably well and are able to discriminate between the two to predict the right mechanism. We therefore also evaluate the different methods with respect to predicting the correct catalytic pathway.

5.2 Computational Methods

All geometry optimizations as well as the vibrational analysis were performed with the Amsterdam Density Functional (ADF) and Density Functional Tight-Binding (DFTB) engines of the Amsterdam Modelling Suite (AMS) program package.[41–43] We decide to use structures including only the first coordination shell. Previous studies have also considered a small cluster of hydrogen bonded water molecules.[44] However, the attachment of this tight water network results in considerable deformation of the original Ru complex, such as elongation of Ru-N distances, deforming the bipyridine backbone. Moreover, these hydrogen bond networks remain stable only if the released protons are still attached to the complex without diffusing into bulk solution.

DFT-based Simulations

Four different exchange correlation functionals were used in the DFT-based investigations: B3LYP,[45,46] BLYP,[46,47] PBE[48,49] and OPBE.[48–50] All DFT-based simulations were performed with the Slater type TZP (triple-ζ polarized) basis set.[51] D3 dispersion corrections with BJ-damping were used.[52] Scalar Relativistic effects were included via the Zero-Order Regular Approximation (ZORA).[53–55] The solvent environment was included through the COSMO implicit-water model.[56] Geometry optimizations were performed with unrestricted DFT, considering all possible spin states involving the d-orbitals. Vibrational analysis was performed only for the geometries corresponding to the most stable spin state.

GFN-xTB-based Simulations

For a semi-empirical description of the Ru-based water oxidation catalyst, the GFN-xTB was used as implemented in the AMS2019 program package.[21,43] This was done to keep the same optimization and numerical frequency methods as for the DFT-based calculations for a better direct comparison. Solvation was implicitly included via the Generalized Born accessible Surface Area (GBSA) model as implemented in AMS.[57] Geometry optimizations were performed with fractional occupations corresponding to the different possible spin states, since unrestricted calculations are not supported yet.

Thermodynamic Computational Investigations at pH=0

The Gibbs free energy was determined using DFT with the four tested exchange correlation functionals mentioned above, as well as using GFN-xTB. After optimization of the geometries of all catalytic intermediates in the lowest spin state and obtaining their binding energy (*E*), the zero-point energy (*ZPE*), *pV* and entropic terms (*TS*) were estimated via vibrational analysis to determine the Gibbs free energy as given in equation 5.1.

$$G = E + pV + ZPE - TS_{(T=298.15K)} \tag{5.1}$$

This was also done for H_2O, O_2 and H_2. Given the proton coupled electron transfer (PCET) character of the reaction steps, the free energy of H^+ and e^- is computed as the free energy of ½ H_2, as first proposed by Nørskov and co-workers.[58–60] The relative Gibbs free energy of each catalytic step is therefore taken as the difference between consecutive catalytic intermediates (including water, H_2 and O_2). Due to equating the free energy of a proton and electron with half hydrogen molecule, the Gibbs free energies are taken at standard NHE conditions. This means that all values, if not declared differently, are taken at pH=0. The zero of the free energy is taken as the free energy of the first catalytic intermediate, the ^{2}[Ru(III)-OH_2]$^+$ plus two water molecules.

Comparison to Experimental Oxidation Potentials at pH=1

To compare the computational results with experimental data, oxidation potentials for the first few catalytic steps were estimated from our Gibbs free energy calculations via Gibbs free energy difference between consecutive catalytic steps as first proposed and implemented by Nørskov and coworkers.[58] Oxidation potentials were determined for the three oxidation reactions given in equations 5.2-5.4, since for these steps there are experimental data available in the literature.[4]

$$^{1}[\mathrm{Ru(II)-OH_2}] \rightarrow {}^{2}[\mathrm{Ru(III)-OH_2}]^{+} + \mathrm{e}^{-} \tag{5.2}$$

$$^{2}[\mathrm{Ru(III)-OH_2}]^{+} \rightarrow {}^{1}[\mathrm{Ru(IV)-OH}]^{+} + \mathrm{H}^{+} + \mathrm{e}^{-} \tag{5.3}$$

$$^{1}[\mathrm{Ru(IV)-OH}]^{+} \rightarrow {}^{2}[\mathrm{Ru(V)=O}]^{+} + \mathrm{H}^{+} + \mathrm{e}^{-} \tag{5.4}$$

The first oxidation potential was determined by ΔSCF (Delta Self Consistent Field),[61,62] from the difference between the energy of the precatalyst ^{1}[Ru(II)-OH$_2$] and its oxidized form ^{2}[Ru(III)-OH$_2$]$^{+}$ at the same geometry. Since this oxidation is pH independent and does only involve an electron transfer, the relaxation of the environment can be neglected as it is slow in comparison to the fast electron transfer. We also note that intake of water for the Ru(II) oxidation state is quite challenging and could in our model only be achieved by breaking a coordination bond between one carboxylic acid group and the ruthenium, with formation of a hydrogen bond between water and this carboxylate. A representative geometry is shown in figure 5A.1 in section 5A.2 in the appendix. This finding supports the suggestion that the complex is not stable in the 7-coordinated state at this low oxidation state and water coordinates to the complex under breaking of one of the other coordination bonds to form a 6-coordinated complex.[6] Since the reaction involves the extraction of an electron without a coupled proton transfer, the energy difference is essentially determined against the absolute electrode potential (as in comparison to an electron at rest in vacuum). Therefore, the energy needs to be converted to the normal

hydrogen electrode (NHE) used in the experiment by subtracting the NHE potential energy versus vacuum (4.44 eV). This is also the only step, in which the number of electrons differs from the reactant to product states. GFN-xTB has a particularly large self-interaction energy that is corrected here by an empirical energy shift for the single point energy of the oxidized state in the ΔSCF by -5.70 eV as determined and employed by Neugebauer *et al.* [27]

The other two reaction steps involve a proton coupled electron transfer. Here, the reorganization of the complex is necessary for the oxidation to take place, especially the coupled proton transfer. Therefore, Gibbs free energy differences between the reactants and products are used to obtain the oxidation potentials. As mentioned earlier, the proton and electron release is assumed to be equivalent to the release of half a hydrogen molecule. These potentials are therefore already versus NHE at pH = 0 since this corresponds to the energy needed to reduce a proton at standard conditions. As the experimental values were determined at pH=1, the computed oxidation potentials were adjusted to this pH value by shifting the H^+ potential using the Nernst equation as shown in equation 5.5.

$$G_{\mathrm{H}^+,\mathrm{pH}=1} = G^0_{\mathrm{H}^+,\mathrm{pH}=0} + k_B T * \ln([\mathrm{H}^+]) = 0 - k_B T \ln(10) * \mathrm{pH}_{=1} \approx -0.059\ eV \tag{5.5}$$

Here, $G^0_{\mathrm{H}^+,\mathrm{pH}=0}$ is the standard Gibbs free energy at standard conditions with pH=0, which is 0 eV by definition in NHE, k_B=8.617 eV/K is the Boltzmann constant and T is the temperature at standard conditions (T=298,15 K). Following the Nernst equation for a single electron event, the computationally determined oxidation potentials involving a PCET step were shifted by -0.059 V to obtain the values vs NHE at pH=1.

GFN-xTB + DFT Approach for Free-Energy Calculations

For a good compromise between accuracy and computational cost, a combination of DFT and GFN-xTB calculations was performed to estimate the Gibbs free energy. Since the geometries obtained at the GFN-xTB and B3LYP level are remarkably similar (see figure 5A.2 and table 5A.6 in section 5A.3 in the appendix), geometry optimization and vibrational analysis can be done with GFN-xTB, thereby significantly speeding up the process. The composite free energy consists of a DFT based energy to which the ZPE and entropic contributions obtained by GFN-xTB are added (see equation 5.6).

$$G_{\mathrm{GFN-xTB+DFT}} = E_{\mathrm{DFT}}^{\mathrm{GFN-xTB\ geometry}} + ZPE_{\mathrm{GFN-xTB}} + pV_{\mathrm{GFN-xTB}} - TS_{\mathrm{GFN-xTB}} \tag{5.6}$$

The procedure is also visualized in scheme 5.3. This workflow was tested using B3LYP, OPBE and the double hybrid functionals rev-DOD-PBE, rev-DOD-PBEP86 and rev-DOD-BLYP.[63–65] The settings for the double hybrid calculations were the same as for the other DFT based simulations (thus including COSMO water, D3 (BJ) corrections, relativistic effects via ZORA), except for the higher basis set TZ2P.[51–56] We also note that in a very recent work by Spicher *et al.*, the Single Point Hessian (SPH) method has been introduced, which combines GFN-xTB/GFN-FF methods with DFT to obtain reliable free energies in non-equilibrium geometries, *e.g.* obtained with a different level of theory or from molecular dynamics snapshots.[66]

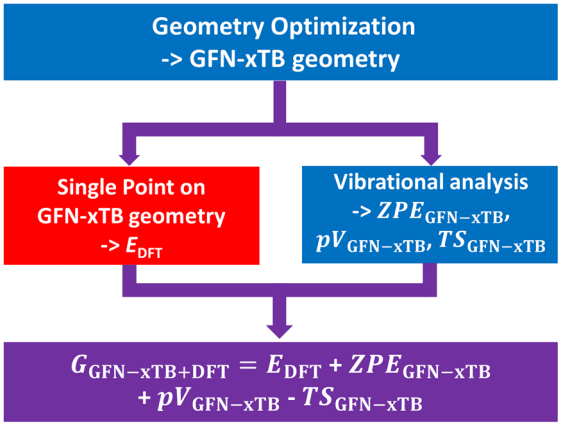

Scheme 5.3. Workflow for the GFN-xTB+DFT combined method. The colors denote the different computational methods used: blue represents GFN-xTB, red DFT. Purple denotes the combination of both. After a GFN-xTB based geometry optimization, vibrational analysis with GFN-xTB is performed, and the calculation is completed with a single point DFT at this geometry. The combination of these results gives an estimate of the Gibbs free energy (purple box).

5.3 Results

Energetically Preferred Spin States

For all catalytic intermediates, the energetically favored state turned out to be the one with the lowest possible spin multiplicity. This is due to the 7-coordinated environment of the Ru, breaking the octahedral symmetry and thus removing the t2g orbitals degeneracy. This result is consistently found using both GFN-xTB and DFT with all exchange correlation functionals considered in this work (see appendix). The corresponding favored spin state is reported in scheme 5.1 for all intermediates. It should also be noted that for all cases, the states of higher multiplicity lie significantly higher in energy than the ground-state (see tables 5A.1-5A.5 in section 5A.1 in the appendix) and are therefore neglected in further investigations. We note however, that an Intersystem Crossing (ISC) event is necessary for the release of oxygen from the dimer. Formation of the dimer is a radical coupling mechanism that necessitates two antiferromagnetically coupled ^{2}[Ru(V)=O]$^+$ species, since the formation of the new covalent bond is due to radical coupling of these two unpaired

electrons. If the spins are parallel, thus ferromagnetically coupled, the bond formation has much less of a radical coupling character and thus requires a higher activation energy. This bond formation was studied computationally by Nyhlén *et al*, who also found a higher barrier for the ferromagnetically coupled ^{2}[Ru(V)=O]$^+$ pair.[44] For the formation of $^3O_2$, an ISC from singlet to triplet state is necessary. The authors showed that the dimer in the triplet state has a very low barrier towards oxygen release.[44] In the WNA mechanism, the last step also necessitates an ISC for $^3O_2$ release.

Relative Gibbs Free Energy along the Catalytic Cycle

The Gibbs free energy differences of all catalytic intermediates at pH=0 with respect to the first intermediate (^{2}[Ru(III)-OH$_2$]$^+$+2H$_2$O) are given in figure 5.1, as well as table 5.1. The steps for the hybrid functional (B3LYP) are indicated with a solid line, the results for the GGA functionals (BLYP, PBE, OPBE) in dashed lines, while the GFN-xTB trace is shown as a dotted line. With the exception of GFN-xTB, all methods agree qualitatively with each other.

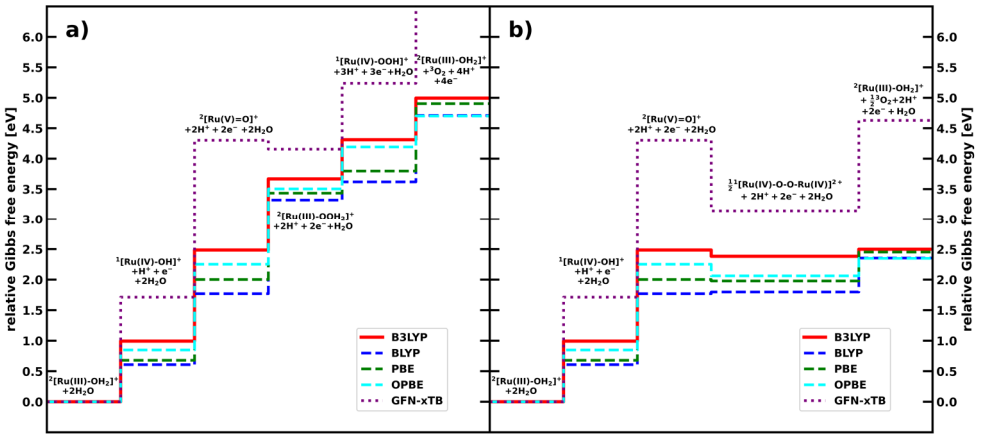

Figure 5.1. Gibbs Free energies at pH=0 relative to the first catalytic step along the catalytic pathways for a) the WNA mechanism and b) the I2M mechanism obtained with: B3LYP (red, solid line), BLYP (blue, dashed), PBE (green, dashed), OPBE (cyan, dashed) and GFN-xTB (purple, dotted).

For the WNA pathway, all catalytic steps are endergonic for all methods with the exception of GFN-xTB, that gives a slightly exergonic nucleophilic attack step. In general, the Gibbs free energy obtained with GFN-xTB deviates significantly from the other methods, with for example the oxygen release step 4.26 eV higher than the closest DFT value, obtained with B3LYP. The large energetic difference is most likely due to use of the fractional occupations instead of a properly unrestricted calculation of the oxygen molecule using GFN-xTB. This choice of occupations leads to energies that are always higher than obtained for a closed shell singlet state. Therefore, the formation energy of molecular oxygen is overestimated. Also for the ^{2}[RuV=O]$^{+}$ intermediate, GFN-xTB gives a free energy 1.81 eV higher than the next closest method (B3LYP). The conclusion from these results is that GFN-xTB in the present form, *i.e.* not allowing for unrestricted calculations, appears to be unsuitable for correctly describing the energetic and thermodynamic properties of the different catalytic intermediates. We note that this is not surprising, since GFN-xTB has been developed with the goal of computing accurate geometries and frequencies, but not primarily for accurate energetics.

Table 5.1. Gibbs free energy difference in eV at pH=0 for all catalytic steps and tested methods relative to the first catalytic intermediate.

Method	**^{2}[Ru(III)-OH$_2$]$^{+}$ +2H$_2$O**	**^{1}[Ru(IV)-OH]$^{+}$ +H^{+}+e^{-}+2H$_2$O**	**^{2}[Ru(V)=O]$^{+}$ +2H^{+} +2e^{-}+ 2H$_2$O**	**^{2}[Ru(III)-OOH$_2$]$^{+}$ +2H^{+}+2e^{-}+H$_2$O**	**^{1}[Ru(IV)- OOH]$^{+}$ +3H^{+}+3e^{-}+H$_2$O**	**½^{1}[Ru(IV)-O-O-Ru(IV)]$^{2+}$ +2H^{+}+2e^{-}**	**^{2}[Ru(III)-OH$_2$]$^{+}$ +4H^{+}+4e^{-}+^{3}O$_2$**
B3LYP	0.00	0.99	2.49	3.67	4.31	2.38	5.00
BLYP	0.00	0.61	1.77	3.32	3.62	1.80	4.71
PBE	0.00	0.68	2.00	3.43	3.80	1.98	4.91
OPBE	0.00	0.85	2.25	3.50	4.19	2.06	4.70
GFN-xTB	0.00	1.71	4.30	4.16	5.24	3.14	9.26
GFN-xTB+ B3LYP	0.00	0.99	2.57	3.93	4.45	2.49	5.12
GFN-xTB+ OPBE	0.00	1.01	2.46	3.83	4.41	2.38	4.82

Preferred Reaction Mechanism

Experimental investigations on the catalyst showed that it operates via the I2M radical coupling mechanism[4]. All investigated methods predict this correctly. As visible in figure 5.1b, the radical coupling between two $^{2}[Ru(V)=O]^{+}$ species leads to the energetically lower $^{1}[Ru(IV)\text{-}O\text{-}O\text{-}Ru(IV)]^{2+}$ dimer species. This downhill process is in contrast with the thermodynamically unfavorable formation of $^{2}[Ru(III)\text{-}OOH_2]^{+}$ via water nucleophilic attack. The only exception to this is GFN-xTB, where both processes, I2M as well as WNA, are downhill. However, the free energy difference between $^{2}[Ru(V)=O]^{+}$ and the dimer is much larger than between $^{2}[Ru(V)=O]^{+}$ and $^{2}[Ru(III)\text{-}OOH_2]^{+}$, also predicting the I2M mechanism to be much more likely. All methods show the oxygen release from the dimer to be endergonic under standard conditions. However, we note that this endergonic behavior might be an artifact of the missing explicit water solvation, as the water uptake is highly sensitive to the hydrogen bonding network.[44] Furthermore, an ISC event is necessary before triplet oxygen can be released. The triplet state of the dimer, as seen in the appendix (see tables 5A.1-5A.5), is considerably higher in energy than the singlet for all investigated methods, making the oxygen release favorable and irreversible. While for the DFT based methods, the Gibbs free energy difference between the dimer and the final catalytic step to regenerate the $^{2}[Ru(III)\text{-}OH_2]^{+}$ under the release of oxygen is relatively small, it is quite large for GFN-xTB. Although this does not change the preference for the I2M mechanism, it underlines again that GFN-xTB alone is not suited to describe the energetics in the catalytic cycle in a satisfactory manner.

Relative Gibbs Free Energy using GFN-xTB+DFT

While GFN-xTB did not prove to be reliable for the energies, it provides geometries and frequencies that are quite similar to the B3LYP results (see root mean square displacements and the Internal Energy and entropic terms in table 5A.6 in the Appendix). For this reason, a combination of GFN-xTB geometries and frequencies

with single point energies from B3LYP were also tested (see Scheme 5.3). Using a geometry optimization and vibrational analysis from GFN-xTB in combination with a single point energy from B3LYP significantly reduced computational cost while still providing reliable results for the free energy. The relative Gibbs free energy of the catalytic intermediates for both the WNA and the I2M mechanism is given in figure 5.2 and table 5.1 for both B3LYP and GFN-xTB+B3LYP. As can be seen in figure 5.2, the GFN-xTB+B3LYP method predicts the correct reaction mechanism and follows very closely the B3LYP results: the deviation from B3LYP is quite small, around 0.1 eV for all the steps except one deviating by 0.26 eV. While the energy differences between consecutive steps are in excellent agreement, the accumulation of small errors lead to larger deviations for the later intermediates, as they are taken relative to the first step. The relatively large structural difference for the ^{2}[Ru(III)-OOH$_2$]$^+$ intermediate (see table 5A.6 in the Appendix) between the two methods might explain the slightly larger deviation at this step.

While this combination of B3LYP and GFN-xTB gives almost quantitatively the same results as the B3LYP, the computational cost is drastically reduced as only one single point calculation with the hybrid functional is needed, thus avoiding the demanding geometry optimization, and more importantly, frequency calculation. As the computational cost for GFN-xTB is extremely small compared to B3LYP (see table 5A.6 in the appendix), this leads to a speed up of a minimum of 2 orders of magnitude for this system, as 2*3N (>300 in this case, as the number of atoms in the ^{1}[Ru(III)-OH$_2$]$^+$ monomer for example is N=56) points need to be calculated for the numerical differentiation of the analytical gradient of the energy in the frequency analysis.

The extreme speed of GFN-xTB leads to the possibility of describing large, extended systems for the cost of essentially only one single point calculation of a higher-level method such as B3LYP, with this calculation being the limiting factor. This combined method therefore effectively scales as a single point calculation of the higher-level method. For systems that can be treated with a single point DFT

calculation, the combined method allows for accurate Gibbs free energies with little additional cost. The semi-quantitative agreement with a much lower computational cost also holds true when using OPBE for the single point energies (table 5.1, last row).

It is quite remarkable that GFN-xTB describes the geometries and frequencies of these challenging transition metal complexes so well, especially considering the different oxidation and spin states involved. Furthermore, although GFN-xTB was not developed for this purpose, it can be extended by just one additional single point calculation based on DFT to give remarkably accurate Gibbs free energies.

All in all, this combination of DFT and GFN-xTB shows great potential in obtaining results close to the DFT description while being much more efficient computationally.

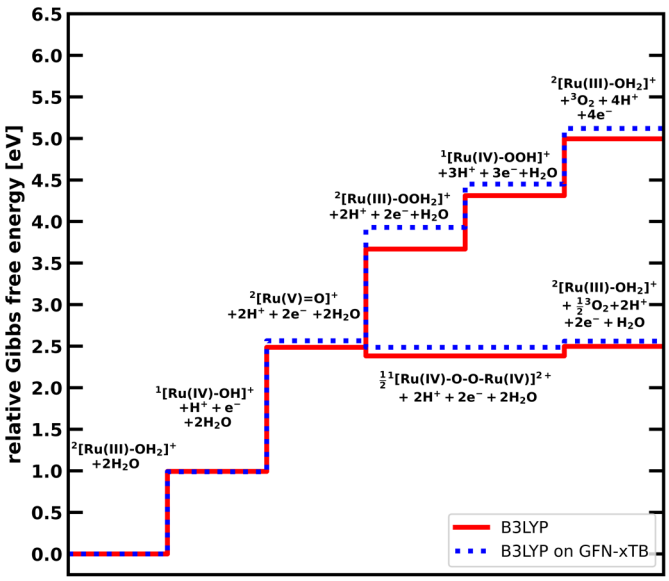

Figure 5.2. Gibbs Free energies at pH=0 relative to the first catalytic step along both catalytic pathways obtained by B3LYP (red, solid line) and by the GFN-xTB+B3LYP combined approach (blue, dotted line)

Comparison to Experimental Oxidation Potentials

The experimentally determined oxidation potential of the ^{1}[Ru(II)-OH$_2$] -> ^{2}[Ru(III)-OH$_2$]$^+$, ^{2}[Ru(III)-OH$_2$]$^+$ -> ^{1}[Ru(IV)-OH]$^+$ and ^{1}[Ru(IV)-OH]$^+$ -> ^{2}[Ru(V)=O]$^+$ steps are given in table 5.2 and compared to the calculated oxidation potentials vs NHE at pH=1 for all investigated methods. The results are also shown graphically in figure 5.3.

In addition to the results reported in table 5.1, also single point energies of three double hybrid functionals, rev-DOD-PBE, rev-DOD-PBEP86 and rev-DOD-BLYP in combination with GFN-xTB geometries and frequencies are included here. All methods show the same trend for the three oxidative steps, with an increasing oxidation potential.

The B3LYP and the OPBE results are in good agreement with experimental values, the largest absolute deviation from experimental results being 0.18 V for B3LYP and 0.28 V for OPBE. Interestingly, our results using B3LYP are very close to the results obtained in ref. [44], even though the model used and the approach to compute the free energy were different.

Table 5.2. Oxidation potentials in V vs NHE at pH=1 for the given oxidative steps obtained for all used computational methods and experimental values.

Method	**^{1}[Ru(II)-OH$_2$] → ^{2}[Ru(III)-OH$_2$]$^+$ + e$^-$**	**^{2}[Ru(III)-OH$_2$]$^+$ → ^{1}[Ru(IV)-OH]$^+$ + H$^+$ + e$^-$**	**^{1}[Ru(IV)-OH]$^+$ → ^{2}[Ru(V)=O]$^+$ + H$^+$ + e$^-$**
B3LYP	0.65	0.93	1.43
BLYP	0.52	0.55	1.10
PBE	0.57	0.62	0.93
OPBE	0.56	0.79	1.35
GFN-xTB	1.28[b]	1.65	2.53
GFN-xTB+B3LYP	0.62	0.93	1.52
GFN-xTB+OPBE	0.51	0.95	1.39
GFN-xTB+rev-DOD-PBE	0.76	0.88	1.92
GFN-xTB+rev-DOD-PBEP86	0.73	0.91	1.92
GFN-xTB+rev-DOD-BLYP	0.80	0.88	2.03
Experiment	**0.60[a]**	**1.07[a]**	**1.25[a]**

[a] from reference[4]. [b] including self-interaction correction[27].

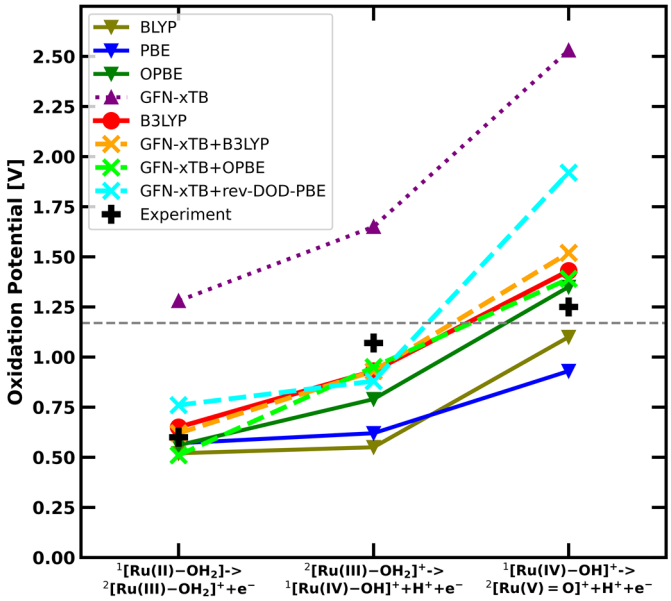

Figure 5.3. Computed oxidation potentials vs NHE at pH=1 between catalytic steps in comparison to experimental data (black crosses): B3LYP (red circles), BLYP (olive triangles), PBE (blue triangles), OPBE (green triangles), GFN-xTB (purple triangles), GFN-xTB+B3LYP (orange crosses), GFN-xTB+OPBE (lime crosses) and the double hybrid rev-DOD-PBE with GFN-xTB geometry and frequencies (cyan crosses). The lines connecting the symbols are merely to guide the eye. The grey dotted line represents the optimal oxidation potential of water at pH=1.

PBE and BLYP deviate more, with a maximum error of 0.52 V (BLYP) and 0.45 V (PBE). The cheapest method, GFN-xTB shows a reasonable qualitative agreement but a significant overestimation of the oxidation potential for all reaction steps. The largest deviation from experiment is 1.28 V. While this shows that GFN-xTB is not reliable enough on its own, the results of the GFN-xTB+DFT combined methods show the reliability of geometries and frequencies of GFN-xTB: when using those in combination with single point energies of B3LYP and OPBE, the difference to the full DFT methods is small. For GFN-xTB+B3LYP, these differences range from 0.00 to 0.09 V vs the B3LYP, or a maximum of 0.27 V vs experiment. GFN-xTB+OPBE has an absolute deviation by a maximum of 0.16 V vs OPBE and

a maximum of 0.14 V when compared to experimental values. These values show that the combined GFN-xTB+DFT methods give significantly more reliable results than some of the full DFT based methods as BLYP and PBE. We also tested some double hybrid functionals, as the need for only a single point calculation in this method makes them computationally accessible. While all three tested double hybrid functionals agree very well with each other, they all significantly overestimate the oxidation potential for the oxidation to the $^{2}[Ru(V)=O]^{+}$ species. The deviation here ranges from 0.67 V (rev-DOD-PBE and rev-DOD-PBEP86) to 0.78 V (rev-DOD-BLYP). In contrast, the agreement with the other two oxidative steps is quite good. Since only one of the steps shows such a large deviation, the oxidation potential was also determined using B3LYP geometries and frequencies combined with rev-DOD-PBE single point energies. Here, the deviation remained over 0.7 V as well (see table 5A.7 in the appendix). The poor performance of the double hybrids in this case is most likely due to the fact that they are used on geometries not optimized at the same level of theory. Especially the $^{2}[Ru(V)=O]^{+}$ geometry is quite deformed due to the high number of coordinated ligands and the double bond between ruthenium and oxygen. B3LYP geometries perform as poorly as GFN-xTB. A more in-depth analysis of double hybrid performance and their sensitivity with regards to geometries would be interesting for future investigations.

The good performance of GFN-xTB with regards to geometries and frequencies could also provide a cheap method to investigate the effect of explicit solvent or other embedding environments on the thermodynamical properties. MD-based equilibrations of the involved reactants and products in full solvation at the GFN-xTB level can be followed by a vibrational analysis of selected snapshots, with a single point analysis on a DFT-basis for reliable Gibbs free energy differences in a fully solvated system.

All in all, the combination of GFN-xTB with higher level methods for a better description of the electronic structure seems quite reliable with a significant reduction of computational cost.

5.4 Conclusion

The full catalytic cycle of a ruthenium water oxidation catalyst was investigated using a wide range of DFT based methods as well as the tight binding approach GFN-xTB. While all tested computational methods predict the correct spin state and catalytic pathway, GFN-xTB fails to qualitatively describe the relative Gibbs free energy between the different catalytic steps, which is not surprising as this method was not developed to fulfill this purpose. B3LYP and OPBE both show the best performance in comparison to experiment, giving very similar results with an error of less than 0.2 eV/0.3 eV respectively. The other GGAs describe the process qualitatively correct but show larger deviations from experiment. As GFN-xTB provides excellent geometries and frequencies, a computational workflow that combines GFN-xTB geometries and frequencies with B3LYP single point energies is proposed and is found to closely reproduce relative Gibbs free energies of full B3LYP calculations while being at least 2 orders of magnitude faster than B3LYP. The same holds true when using OPBE. Usage of double hybrid functionals on the GFN-xTB geometries is computationally highly accessible, but while the results show good agreement with experiment for the first two oxidation steps (within 0.2 V), the last oxidative step shows larger deviation. The combination of GFN-xTB derived geometries and frequencies with higher level methods for a good electronic description of the WOC system shows great promise for fast, reliable determination of redox potentials, thermodynamic properties and electronic structure at a reasonable computational cost. The good description of both geometries and frequencies by GFN-xTB should allow for computationally accessible molecular dynamics simulations and embedding in extensive simulation boxes including potential photosensitizers or redox mediators and explicit solvation.

5.5 References

(1) Yu, Z.; Li, F.; Sun, L. Recent Advances in Dye-Sensitized Photoelectrochemical Cells for Solar Hydrogen Production Based on Molecular Components. *Energy Environ. Sci.* **2015**, *8* (3), 760–775. https://doi.org/10.1039/C4EE03565H.

(2) Nguyen, V.-H.; Do, H. H.; Van Nguyen, T.; Singh, P.; Raizada, P.; Sharma, A.; Sana, S. S.; Grace, A. N.; Shokouhimehr, M.; Ahn, S. H.; Xia, C.; Kim, S. Y.; Le, Q. V. Perovskite Oxide-Based Photocatalysts for Solar-Driven Hydrogen Production: Progress and Perspectives. *Sol. Energy* **2020**, *211*, 584–599. https://doi.org/10.1016/j.solener.2020.09.078.

(3) Niu, F.; Wang, D.; Li, F.; Liu, Y.; Shen, S.; Meyer, T. J. Hybrid Photoelectrochemical Water Splitting Systems: From Interface Design to System Assembly. *Adv. Energy Mat.* **2020**, *10* (11), 1900399. https://doi.org/10.1002/aenm.201900399.

(4) Duan, L.; Bozoglian, F.; Mandal, S.; Stewart, B.; Privalov, T.; Llobet, A.; Sun, L. A Molecular Ruthenium Catalyst with Water-Oxidation Activity Comparable to That of Photosystem II. *Nature Chem.* **2012**, *4* (5), 418–423. https://doi.org/10.1038/nchem.1301.

(5) Matheu, R.; Ertem, M. Z.; Benet-Buchholz, J.; Coronado, E.; Batista, V. S.; Sala, X.; Llobet, A. Intramolecular Proton Transfer Boosts Water Oxidation Catalyzed by a Ru Complex. *J. Am. Chem. Soc.* **2015**, *137* (33), 10786–10795. https://doi.org/10.1021/jacs.5b06541.

(6) Duan, L.; Wang, L.; Li, F.; Li, F.; Sun, L. Highly Efficient Bioinspired Molecular Ru Water Oxidation Catalysts with Negatively Charged Backbone Ligands. *Acc. Chem. Res.* **2015**, *48* (7), 2084–2096. https://doi.org/10.1021/acs.accounts.5b00149.

(7) Creus, J.; Matheu, R.; Peñafiel, I.; Moonshiram, D.; Blondeau, P.; Benet-Buchholz, J.; García-Antón, J.; Sala, X.; Godard, C.; Llobet, A. A Million Turnover Molecular Anode for Catalytic Water Oxidation. *Angew. Chem., Int. Ed.* **2016**, *55* (49), 15382–15386. https://doi.org/10.1002/anie.201609167.

(8) Matheu, R.; Ertem, M. Z.; Gimbert-Suriñach, C.; Sala, X.; Llobet, A. Seven Coordinated Molecular Ruthenium–Water Oxidation Catalysts: A Coordination Chemistry Journey. *Chem. Rev.* **2019**, *119* (6), 3453–3471. https://doi.org/10.1021/acs.chemrev.8b00537.

(9) Belić, J.; van Beek, B.; Menzel, J. P.; Buda, F.; Visscher, L. Systematic Computational Design and Optimization of Light Absorbing Dyes. *J. Phys. Chem. A* **2020**, *124* (31), 6380–6388. https://doi.org/10.1021/acs.jpca.0c04506.

(10) Menzel, J. P.; Papadopoulos, A.; Belić, J.; de Groot, H. J. M.; Visscher, L.; Buda, F. Photoinduced Electron Injection in a Fully Solvated Dye-Sensitized Photoanode: A Dynamical Semiempirical Study. *J. Phys. Chem. C* **2020**, *124* (51), 27965–27976. https://doi.org/10.1021/acs.jpcc.0c09551.

(11) Govindarajan, N.; Tiwari, A.; Ensing, B.; Meijer, E. J. Impact of the Ligand Flexibility and Solvent on the O–O Bond Formation Step in a Highly Active Ruthenium Water Oxidation Catalyst. *Inorg. Chem.* **2018**, *57* (21), 13063–13066. https://doi.org/10.1021/acs.inorgchem.8b00619.

(12) Govindarajan, N.; Meijer, E. J. Modeling the Catalyst Activation Step in a Metal–Ligand Radical Mechanism Based Water Oxidation System. *Inorganics* **2019**, *7* (5), 62. https://doi.org/10.3390/inorganics7050062.

(13) Schilling, M.; Cunha, R. A.; Luber, S. Zooming in on the O–O Bond Formation—An Ab Initio Molecular Dynamics Study Applying Enhanced Sampling Techniques. *J. Chem. Theory Comput.* **2020**, *16* (4), 2436–2449. https://doi.org/10.1021/acs.jctc.9b01207.

(14) Schilling, M.; Cunha, R. A.; Luber, S. Enhanced Ab Initio Molecular Dynamics Exploration Unveils the Complex Role of Different Intramolecular Bases on the Water Nucleophilic Attack Mechanism. *ACS Catal.* **2020**, *10* (14), 7657–7667. https://doi.org/10.1021/acscatal.0c01422.

(15) Ruiter, J. M. de; Buda, F. Introducing a Closed System Approach for the Investigation of Chemical Steps Involving Proton and Electron Transfer; as Illustrated by a Copper-Based Water Oxidation Catalyst. *Phys. Chem. Chem. Phys.* **2017**, *19* (6), 4208–4215. https://doi.org/10.1039/C6CP07454E.

(16) de Ruiter, J. M.; de Groot, H. J. M.; Buda, F. Energetic Effects of a Closed System Approach Including Explicit Proton and Electron Acceptors as Demonstrated by a Mononuclear Ruthenium Water Oxidation Catalyst. *ChemCatChem* **2018**, *10* (20), 4594–4601. https://doi.org/10.1002/cctc.201801093.

(17) Monti, A.; de Ruiter, J. M.; de Groot, H. J. M.; Buda, F. A Dynamic View of Proton-Coupled Electron Transfer in Photocatalytic Water Splitting. *J. Phys. Chem. C* **2016**, *120* (40), 23074–23082. https://doi.org/10.1021/acs.jpcc.6b08244.

(18) Shao, Y.; de Ruiter, J. M.; de Groot, H. J. M.; Buda, F. Photocatalytic Water Splitting Cycle in a Dye-Catalyst Supramolecular Complex: Ab Initio Molecular Dynamics Simulations. *J. Phys. Chem. C* **2019**, *123* (35), 21403–21414. https://doi.org/10.1021/acs.jpcc.9b06401.

(19) Shao, Y.; de Groot, H. J. M.; Buda, F. Proton Acceptor near the Active Site Lowers Dramatically the O–O Bond Formation Energy Barrier in Photocatalytic Water Splitting. *J. Phys. Chem. Lett.* **2019**, *10* (24), 7690–7697. https://doi.org/10.1021/acs.jpclett.9b02914.

(20) Shao, Y.; Groot, H. J. M. de; Buda, F. Tuning the Proton-Coupled Electron-Transfer Rate by Ligand Modification in Catalyst–Dye Supramolecular Complexes for Photocatalytic Water Splitting. *ChemSusChem* **2021**, *14* (1), 479–486. https://doi.org/10.1002/cssc.202001863.

(21) Grimme, S.; Bannwarth, C.; Shushkov, P. A Robust and Accurate Tight-Binding Quantum Chemical Method for Structures, Vibrational Frequencies, and Noncovalent Interactions of Large Molecular Systems Parametrized for All Spd-Block Elements (Z = 1–86). *J. Chem. Theory Comput.* **2017**, *13* (5), 1989–2009. https://doi.org/10.1021/acs.jctc.7b00118.

(22) Bursch, M.; Neugebauer, H.; Grimme, S. Structure Optimisation of Large Transition-Metal Complexes with Extended Tight-Binding Methods. *Angew. Chem., Int. Ed.* **2019**, *58* (32), 11078–11087. https://doi.org/10.1002/anie.201904021.

(23) Dohm, S.; Bursch, M.; Hansen, A.; Grimme, S. Semiautomated Transition State Localization for Organometallic Complexes with Semiempirical Quantum Chemical Methods. *J. Chem. Theory Comput.* **2020**, *16* (3), 2002–2012. https://doi.org/10.1021/acs.jctc.9b01266.

(24) Bursch, M.; Hansen, A.; Grimme, S. Fast and Reasonable Geometry Optimization of Lanthanoid Complexes with an Extended Tight Binding Quantum Chemical Method. *Inorg. Chem.* **2017**, *56* (20), 12485–12491. https://doi.org/10.1021/acs.inorgchem.7b01950.

(25) Bannwarth, C.; Ehlert, S.; Grimme, S. GFN2-XTB—An Accurate and Broadly Parametrized Self-Consistent Tight-Binding Quantum Chemical Method with Multipole Electrostatics and Density-Dependent Dispersion Contributions. *J. Chem. Theory Comput.* **2019**, *15* (3), 1652–1671. https://doi.org/10.1021/acs.jctc.8b01176.

(26) Spicher, S.; Grimme, S. Robust Atomistic Modeling of Materials, Organometallic, and Biochemical Systems. *Angew. Chem., Int. Ed.* **2020**, *59* (36), 15665–15673. https://doi.org/10.1002/anie.202004239.

(27) Neugebauer, H.; Bohle, F.; Bursch, M.; Hansen, A.; Grimme, S. Benchmark Study of Electrochemical Redox Potentials Calculated with Semiempirical and DFT Methods. *J. Phys. Chem. A* **2020**, *124* (35), 7166–7176. https://doi.org/10.1021/acs.jpca.0c05052.

(28) Sterling, C. M.; Bjornsson, R. Multistep Explicit Solvation Protocol for Calculation of Redox Potentials. *J. Chem. Theory Comput.* **2019**, *15* (1), 52–67. https://doi.org/10.1021/acs.jctc.8b00982.

(29) Spicher, S.; Grimme, S. Efficient Computation of Free Energy Contributions for Association Reactions of Large Molecules. *J. Phys. Chem. Lett.* **2020**, *11* (16), 6606–6611. https://doi.org/10.1021/acs.jpclett.0c01930.

(30) Bernasconi, L.; Kazaryan, A.; Belanzoni, P.; Baerends, E. J. Catalytic Oxidation of Water with High-Spin Iron(IV)–Oxo Species: Role of the Water Solvent. *ACS Catal.* **2017**, *7* (6), 4018–4025. https://doi.org/10.1021/acscatal.7b00568.

(31) Blakemore, J. D.; Schley, N. D.; Balcells, D.; Hull, J. F.; Olack, G. W.; Incarvito, C. D.; Eisenstein, O.; Brudvig, G. W.; Crabtree, R. H. Half-Sandwich Iridium Complexes for Homogeneous Water-Oxidation Catalysis. *J. Am. Chem. Soc.* **2010**, *132* (45), 16017–16029. https://doi.org/10.1021/ja104775j.

(32) Shaffer, D. W.; Xie, Y.; Concepcion, J. J. O–O Bond Formation in Ruthenium-Catalyzed Water Oxidation: Single-Site Nucleophilic Attack vs. O–O Radical Coupling. *Chem. Soc. Rev.* **2017**, *46* (20), 6170–6193. https://doi.org/10.1039/C7CS00542C.
(33) Hessels, J.; Detz, R. J.; Koper, M. T. M.; Reek, J. N. H. Rational Design Rules for Molecular Water Oxidation Catalysts Based on Scaling Relationships. *Chem. Eur. J.* **2017**, *23* (65), 16413–16418. https://doi.org/10.1002/chem.201702850.
(34) Abild-Pedersen, F.; Greeley, J.; Studt, F.; Rossmeisl, J.; Munter, T. R.; Moses, P. G.; Skúlason, E.; Bligaard, T.; Nørskov, J. K. Scaling Properties of Adsorption Energies for Hydrogen-Containing Molecules on Transition-Metal Surfaces. *Phys. Rev. Lett.* **2007**, *99* (1), 016105. https://doi.org/10.1103/PhysRevLett.99.016105.
(35) Anand, M.; Nørskov, J. K. Scaling Relations in Homogeneous Catalysis: Analyzing the Buchwald–Hartwig Amination Reaction. *ACS Catal.* **2020**, *10* (1), 336–345. https://doi.org/10.1021/acscatal.9b04323.
(36) Yu, F.; Poole, D.; Mathew, S.; Yan, N.; Hessels, J.; Orth, N.; Ivanović-Burmazović, I.; Reek, J. N. H. Control over Electrochemical Water Oxidation Catalysis by Preorganization of Molecular Ruthenium Catalysts in Self-Assembled Nanospheres. *Angew. Chem., Int. Ed.* **2018**, *57* (35), 11247–11251. https://doi.org/10.1002/anie.201805244.
(37) Matheu, R.; Ertem, M. Z.; Pipelier, M.; Lebreton, J.; Dubreuil, D.; Benet-Buchholz, J.; Sala, X.; Tessier, A.; Llobet, A. The Role of Seven-Coordination in Ru-Catalyzed Water Oxidation. *ACS Catal.* **2018**, *8* (3), 2039–2048. https://doi.org/10.1021/acscatal.7b03638.
(38) Wang, L.; Duan, L.; Stewart, B.; Pu, M.; Liu, J.; Privalov, T.; Sun, L. Toward Controlling Water Oxidation Catalysis: Tunable Activity of Ruthenium Complexes with Axial Imidazole/DMSO Ligands. *J. Am. Chem. Soc.* **2012**, *134* (45), 18868–18880. https://doi.org/10.1021/ja309805m.
(39) Fan, T.; Duan, L.; Huang, P.; Chen, H.; Daniel, Q.; Ahlquist, M. S. G.; Sun, L. The Ru-Tpc Water Oxidation Catalyst and Beyond: Water Nucleophilic Attack Pathway versus Radical Coupling Pathway. *ACS Catal.* **2017**, *7* (4), 2956–2966. https://doi.org/10.1021/acscatal.6b03393.
(40) Zhang, B.; Zhan, S.; Liu, T.; Wang, L.; Ken Inge, A.; Duan, L.; Timmer, B. J. J.; Kravchenko, O.; Li, F.; Ahlquist, M. S. G.; Sun, L. Switching OO Bond Formation Mechanism between WNA and I2M Pathways by Modifying the Ru-Bda Backbone Ligands of Water-Oxidation Catalysts. *J. Energy Chem.* **2021**, *54*, 815–821. https://doi.org/10.1016/j.jechem.2020.06.036.
(41) ADF 2019.3, SCM, Theoretical Chemistry, Vrije Universiteit, Amsterdam, The Netherlands, http://www.scm.com. .
(42) Velde, G. te; Bickelhaupt, F. M.; Baerends, E. J.; Fonseca Guerra, C.; van Gisbergen, S. J. A.; Snijders, J. G.; Ziegler, T. Chemistry with ADF. *J. Comput. Chem.* **2001**, *22* (9), 931–967.
(43) AMS DFTB 2019.3, SCM, Theoretical Chemistry, Vrije Universiteit, Amsterdam, The Netherlands, http://www.scm.com. .
(44) Nyhlén, J.; Duan, L.; Åkermark, B.; Sun, L.; Privalov, T. Evolution of O2 in a Seven-Coordinate RuIV Dimer Complex with a [HOHOH]− Bridge: A Computational Study. *Angew. Chem., Int. Ed.* **2010**, *49* (10), 1773–1777. https://doi.org/10.1002/anie.200906439.
(45) Becke, A. D. A New Mixing of Hartree–Fock and Local Density-functional Theories. *J. Chem. Phys.* **1993**, *98* (2), 1372–1377. https://doi.org/10.1063/1.464304.
(46) Lee, C.; Yang, W.; Parr, R. G. Development of the Colle-Salvetti Correlation-Energy Formula into a Functional of the Electron Density. *Phys. Rev. B* **1988**, *37* (2), 785–789.
(47) Becke, A. D. Density-Functional Exchange-Energy Approximation with Correct Asymptotic Behavior. *Phys. Rev. A* **1988**, *38* (6), 3098–3100.
(48) Perdew, J. P.; Burke, K.; Ernzerhof, M. Generalized Gradient Approximation Made Simple. *Phys. Rev. Lett.* **1996**, *77* (18), 3865–3868.
(49) Perdew, J. P.; Burke, K.; Ernzerhof, M. Generalized Gradient Approximation Made Simple [Phys. Rev. Lett. 77, 3865 (1996)]. *Phys. Rev. Lett.* **1997**, *78* (7), 1396–1396.
(50) Handy, N. C.; Cohen, A. J. Left-Right Correlation Energy. *Mol. Phys.* **2001**, *99* (5), 403–412. https://doi.org/10.1080/00268970010018431.

(51) Van Lenthe, E.; Baerends, E. J. Optimized Slater-Type Basis Sets for the Elements 1–118. *J. Comput. Chem.* **2003**, *24*, 1142–1156.
(52) Grimme, S.; Ehrlich, S.; Goerigk, L. Effect of the Damping Function in Dispersion Corrected Density Functional Theory. *J. Comput. Chem.* **2011**, *32* (7), 1456–1465. https://doi.org/10.1002/jcc.21759.
(53) Lenthe, E. van; Baerends, E. J.; Snijders, J. G. Relativistic Regular Two-component Hamiltonians. *J. Chem. Phys.* **1993**, *99* (6), 4597–4610. https://doi.org/10.1063/1.466059.
(54) van Lenthe, E.; Baerends, E. J.; Snijders, J. G. Relativistic Total Energy Using Regular Approximations. *J. Chem. Phys.* **1994**, *101* (11), 9783–9792. https://doi.org/10.1063/1.467943.
(55) van Lenthe, E.; Ehlers, A.; Baerends, E.-J. Geometry Optimizations in the Zero Order Regular Approximation for Relativistic Effects. *J. Chem. Phys.* **1999**, *110* (18), 8943–8953. https://doi.org/10.1063/1.478813.
(56) Pye, C. C.; Ziegler, T. An Implementation of the Conductor-like Screening Model of Solvation within the Amsterdam Density Functional Package. *Theor. Chem. Acc.* **1999**, *101* (6), 396–408. https://doi.org/10.1007/s002140050457.
(57) Bannwarth, C.; Caldeweyher, E.; Ehlert, S.; Hansen, A.; Pracht, P.; Seibert, J.; Spicher, S.; Grimme, S. Extended Tight-Binding Quantum Chemistry Methods. *WIREs Computational Molecular Science n/a* (n/a), e01493. https://doi.org/10.1002/wcms.1493.
(58) Nørskov, J. K.; Rossmeisl, J.; Logadottir, A.; Lindqvist, L.; Kitchin, J. R.; Bligaard, T.; Jónsson, H. Origin of the Overpotential for Oxygen Reduction at a Fuel-Cell Cathode. *J. Phys. Chem. B* **2004**, *108* (46), 17886–17892. https://doi.org/10.1021/jp047349j.
(59) Rossmeisl, J.; Logadottir, A.; Nørskov, J. K. Electrolysis of Water on (Oxidized) Metal Surfaces. *Chem. Phys.* **2005**, *319* (1), 178–184. https://doi.org/10.1016/j.chemphys.2005.05.038.
(60) Rossmeisl, J.; Qu, Z.-W.; Zhu, H.; Kroes, G.-J.; Nørskov, J. K. Electrolysis of Water on Oxide Surfaces. *J. Electroanal. Chem.* **2007**, *607* (1), 83–89. https://doi.org/10.1016/j.jelechem.2006.11.008.
(61) Gunnarsson, O.; Lundqvist, B. I. Exchange and Correlation in Atoms, Molecules, and Solids by the Spin-Density-Functional Formalism. *Phys. Rev. B* **1976**, *13* (10), 4274–4298. https://doi.org/10.1103/PhysRevB.13.4274.
(62) Jones, R. O.; Gunnarsson, O. The Density Functional Formalism, Its Applications and Prospects. *Rev. Mod. Phys.* **1989**, *61* (3), 689–746. https://doi.org/10.1103/RevModPhys.61.689.
(63) Santra, G.; Sylvetsky, N.; Martin, J. M. L. Minimally Empirical Double-Hybrid Functionals Trained against the GMTKN55 Database: RevDSD-PBEP86-D4, RevDOD-PBE-D4, and DOD-SCAN-D4. *J. Phys. Chem. A* **2019**, *123* (24), 5129–5143. https://doi.org/10.1021/acs.jpca.9b03157.
(64) Förster, A.; Visscher, L. Double Hybrid DFT Calculations with Slater Type Orbitals. *J. Comput. Chem.* **2020**, *41* (18), 1660–1684. https://doi.org/10.1002/jcc.26209.
(65) Förster, A.; Franchini, M.; van Lenthe, E.; Visscher, L. A Quadratic Pair Atomic Resolution of the Identity Based SOS-AO-MP2 Algorithm Using Slater Type Orbitals. *J. Chem. Theory Comput.* **2020**, *16* (2), 875–891. https://doi.org/10.1021/acs.jctc.9b00854.
(66) Spicher, S. Single-Point Hessian Calculations for Improved Vibrational Frequencies and Rigid-Rotor-Harmonic-Oscillator Thermodynamics. *J. Chem. Theory Comput.* 14.

5.A Appendix

5A.1 Energetically preferred spin states

All DFT based calculations were performed with the ADF2019[41,42] program by SCM using a TZP basis set,[51] D3 dispersion corrections with BJ-damping,[52] and COSMO implicit water[56]. Relativistic effects were included via the ZORA model.[53–55] The investigated exchange correlation functionals are B3LYP,[45,47] BLYP,[46,47] PBE[48,49] and OPBE[48–50]. The GFN-xTB[21] calculations were performed by the DFTB package included in AMS2019[43] by SCM, including GBSA implicit water as implemented in AMS.[57]

Table 5A.1: Energies in eV of viable spin states for all catalytic intermediates using B3LYP. The most favorable spin state is marked in bold.

Intermediate	Singlet	Doublet	Triplet	Quartet	Quintet	Sextet
[Ru(II)-OH_2]	**-430.06**	-	-428.94	-	-427.90	-
[Ru(III)-OH_2]$^+$	-	**-425.48**	-	-425.31	-	-423.26
[Ru(IV)-OH]$^+$	**-420.39**	-	-419.81	-	-418.38	-
[Ru(V)=O]$^+$	-	**-414.73**	-	-413.62	-	-
[Ru(III)-OOH_2]$^+$	-	**-431.26**	-	-429.99	-	-428.65
[Ru(IV)-OOH]$^+$	**-426.56**	-	-426.11	-	-424.92	-
[Ru(IV)-O-O-Ru(IV)]$^{2+}$	**-830.48**	-	-829.72	-	-828.92	-
H_2	**-7.71**	-	-	-	-	-
O_2	-10.77	**-**	**-13.41**	-	-	-
H_2O	**-17.25**	-	-	-	-	-

Table 5A.2: Energies in eV of viable spin states for all catalytic intermediates using BLYP. The most favorable spin state is marked in bold.

Intermediate	Singlet	Doublet	Triplet	Quartet	Quintet	Sextet
[Ru(II)-OH_2]	**-358.61**	-	-357.314	-	-355.94	-
[Ru(III)-OH_2]$^+$	-	**-354.14**	-	-352.92	-	-351.49
[Ru(IV)-OH]$^+$	**-349.98**	-	-349.24	-	-347.78	-
[Ru(V)=O]$^+$	-	**-345.19**	-	-344.09	-	-
[Ru(III)-OOH_2]$^+$	-	**-358.01**	-	-356.60	-	-355.80
[Ru(IV)-OOH]$^+$	**-354.20**	-	-353.44	-	-352.20	-
[Ru(IV)-O-O-Ru(IV)]$^{2+}$	**-691.14**	-	-690.23	-	-689.38	-
H_2	**-6.65**	-	-	-	-	-
O_2	-8.11	**-**	**-9.24**	-	-	-
H_2O	**-13.95**	-	-	-	-	-

Table 5A.3: Energies in eV of viable spin states for all catalytic intermediates using PBE. The most favorable spin state is marked in bold.

Intermediate	Singlet	Doublet	Triplet	Quartet	Quintet	Sextet
[Ru(II)-OH_2]	**-375.11**	-	-373.66	-	-372.24	-
[Ru(III)-OH_2]$^+$	-	**-370.52**	-	-369.04	-	-367.65
[Ru(IV)-OH]$^+$	**-366.25**	-	-365.42	-	-364.90	-
[Ru(V)=O]$^+$	-	**-361.25**	-	-360.09	-	-
[Ru(III)-OOH_2]$^+$	-	**-374.67**	-	-373.06	-	-371.46
[Ru(IV)-OOH]$^+$	**-370.71**	-	-369.98	-	368.61	-
[Ru(IV)-O-O-Ru(IV)]$^{2+}$	**-723.32**	-	-722.33	-	-721.48	-
H_2	**-6.75**	-	-	-	-	-
O_2	-8.59	**-**	**-9.72**	-	-	-
H_2O	**-14.39**	-	-	-	-	-

Table 5A.4: Energies in eV of viable spin states for all catalytic intermediates using OPBE. The most favorable spin state is marked in bold. The [Ru(II)-OH_2] species showed to be unstable in the triplet and quintet states, releasing the water molecule. As energies given here are therefore the [Ru(II)] and water in isolation.

Intermediate	Singlet	Doublet	Triplet	Quartet	Quintet	Sextet
[Ru(II)-OH_2]	**-383.01**	-	-381.74 Water released	-	-380.05 Water released	-
[Ru(III)-OH_2]$^+$	-	**-378.43**	-	-376.73	-	-357.57
[Ru(IV)-OH]$^+$	**-373.99**	-	-373.11	-	-371.48	-
[Ru(V)=O]$^+$	-	**-368.88**	-	-367.86	-	-
[Ru(III)-OOH_2]$^+$	-	**-382.64**	-	-376.73	-	-375.57
[Ru(IV)-OOH]$^+$	**-378.35**	-	-377.91	-	-376.15	-
[Ru(IV)-O-O-Ru(IV)]$^{2+}$	**-738.92**	-	-738.73	-	-738.80	-
H_2	**-6.79**	-	-	-	-	-
O_2	-8.89	**-**	**-10.19**	-	-	-
H_2O	**-14.58**	-	-	-	-	-

Table 5A.5: Energies in eV of viable spin states for all catalytic intermediates using GFN-xTB. The most favorable spin state is marked in bold.

Intermediate	Singlet	Doublet	Triplet	Quartet	Quintet	Sextet
[Ru(II)-OH_2]	**-2783.80**	-	-2782.48	-	-2780.47	-
[Ru(III)-OH_2]$^+$	-	**-2773.21**	-	-2771.59	-	-2768.75
[Ru(IV)-OH]$^+$	**-2757.21**	-	-2756.32	-	-2754.19	-
[Ru(V)=O]$^+$	-	**-2740.29**	-	-2738.94	-	-
[Ru(III)-OOH_2]$^+$	-	**-2897.88**	-	-2896.02	-	-2893.37
[Ru(IV)-OOH]$^+$	**-2882.50**	-	-2881.01	-	-2879.50	-
[Ru(IV)-O-O-Ru(IV)]$^{2+}$	**-5483.77**	-	-5482.93	-	-5482.02	-
H_2	**-28.15**	-	-	-	-	-
O_2	**-247.77**	**-**	**-247.77**	-	-	-
H_2O	**-156.935**	-	-	-	-	-

5A.2 6-coordinated ^{1}[Ru(II)-OH$_2$]

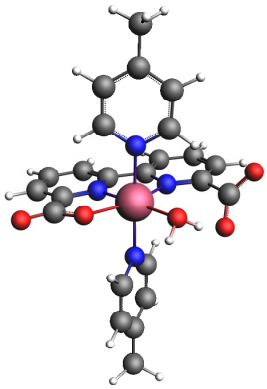

Figure 5A.1. Geometry of the ^{1}[Ru(II)-OH$_2$] complex. Note the breaking of the Ru-O bond from the carboxylate and hydrogen bond towards the bound water molecule to form a 6-coordinated complex.

5A.3 Energy Terms in Gibbs Free Energy and Computational Cost

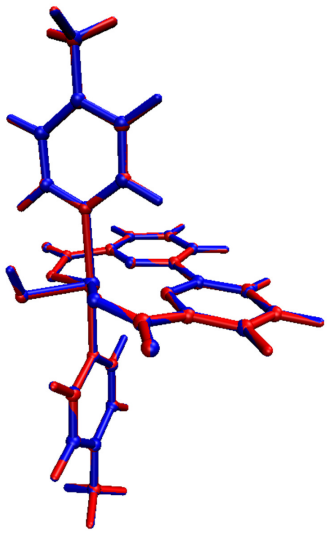

Figure 5A.2. Overlay of the molecular structures of the ^{1}[Ru(IV)-OH]$^{+}$ molecule optimized with the semi-empirical GFN-xTB (blue) and DFT using the B3LYP exchange correlation functional (red).

Table 5A.6: Energy decomposition of the different terms in the Gibbs free energy per catalytic intermediate for B3LYP and GFN-xTB. Also given is the computational cost for the vibrational analysis calculated on nodes with 24 cores. Root mean square displacements (RMSD) between GFN-xTB and B3LYP are given for the bond distances in the first coordination sphere.

Intermediate / Method	Bond Energy [eV]	Internal Energy [eV]	pV term [eV]	-TS [eV]	Gibbs Free Energy [eV]	Calculation time (*Nr. of nodes) [min]	RMSD [Å]
^{1}[Ru(II)-OH$_2$]							
B3LYP	-430,06	12,44	0.03	-2.63	-420.23	868(*4=3472)	0.052
GFN-xTB	-2783.80	12.06	0.03	-2.70	-2774.40	1	
^{2}[Ru(III)-OH$_2$]$^+$							
B3LYP	-425.48	12.47	0.03	-2.64	-415.63	1300(*4=5200)	0.248
GFN-xTB	-2773.21	12.09	0.03	-2.82	-2763.91	3	
^{1}[Ru(IV)-OH]$^+$							
B3LYP	-420.39	12.17	0.03	-2.57	-410.76	1243(*4=4972)	0.041
GFN-xTB	-2757.21	11.80	0.03	-2.73	-2748.12	1	
^{2}[Ru(V)=O]$^+$							
B3LYP	-414.74	11.85	0.03	-2.54	-405.39	1899(*4=7596)	0.061
GFN-xTB	-2740.29	11.46	0.03	-2.66	-2731.46	1	
^{2}[Ru(III)-OOH$_2$]$^+$							
B3LYP	-431.26	12.60	0.03	-2.74	-421.37	2200(*4=8800)	0.122
GFN-xTB	-2888.47	12.25	0.03	-2.86	-2888.47	1	
^{1}[Ru(IV)-OOH]$^+$							
B3LYP	-426.56	12.30	0.03	-2.62	-416.85	1484(*4=5936)	0.031
GFN-xTB	-2882.50	11.94	0.03	-2.78	-2873.31	1	
^{1}[Ru(IV)-O-O-Ru(IV)]$^{2+}$							
B3LYP	-830.48	23.82	0.03	-4,36	-810.99	16893(*2=33786)	0.036
GFN-xTB	-5483.76	23.06	0.03	-4.54	-5465.23	3	
H_2							
B3LYP	-7.71	0.34	0.03	-0.40	-7.75	1	0.011
GFN-xTB	-28.15	0.38	0.03	-0.40	-28.15	<<1	
O_2							
B3LYP	-13.41	0.16	0.03	-0.61	-13.83	1	0.006
GFN-xTB	-247.77	0.17	0.03	-0.61	-248.17	<<1	
H_2O							
B3LYP	-17.25	0.64	0.03	-0.58	-17.16	1	0.014
GFN-xTB	-156.94	0.62	0.03	-0.58	-156.87	<<1	

5A.4 Double hybrids on GFN-xTB and B3LYP geometries

Double hybrid single point calculations were performed using the same settings as described above (ZORA, COSMO, D3(BJ)) with the exception of using the higher TZ2P basis set. Calculations were performed with rev-DOD-PBE, rev-DOD-PBEP86 and rev-DOD-BLYP.[63,64] Single Point calculations were performed on GFN-xTB geometries. For comparison, a rev-DOD-PBE Single Point calculation was also done using geometry and frequencies obtained with B3LYP.

Table 5A.7. Determined oxidation potentials compared to experiment at pH=1 for the three investigated double hybrid functionals rev-DOD-PBE, rev-DOD-PBEP86 and rev-DOD-BLYP using COSMO and D3(BJ) on geometries obtained with GFN-xTB. Also added are determined oxidation potentials when using B3LYP geometries for the double hybrid rev-DOD-PBE.

Method	**[Ru(II)-OH$_2$] -> [Ru(III)-OH$_2$]$^+$**	**[Ru(III)-OH$_2$]$^+$ -> [Ru(IV)-OH]$^+$**	**[Ru(IV)-OH]$^+$ -> [Ru(V)=O]$^+$**
Rev-DOD-PBE on GFN-xTB geometry	0.76 V	0.88 V	1.92 V
Rev-DOD-PBEP86 on GFN-xTB geometry	0.73 V	0.91 V	1.92 V
Rev DOD-BLYP on GFN-xTB geometry	0.80 V	0.88 V	2.03 V
Rev-DOD-PBE on B3LYP geometry	0.79 V	0.77 V	1.98 V
Experiment	**0.60 V**	**1.07 V**	**1.25 V**

5A.5 References

(1) Velde, G. te; Bickelhaupt, F. M.; Baerends, E. J.; Fonseca Guerra, C.; van Gisbergen, S. J. A.; Snijders, J. G.; Ziegler, T. Chemistry with ADF. *J. Comput. Chem.* **2001**, *22* (9), 931–967.

(2) ADF 2019.3, SCM, Theoretical Chemistry, Vrije Universiteit, Amsterdam, The Netherlands, http://www.scm.com. .

(3) Van Lenthe, E.; Baerends, E. J. Optimized Slater-Type Basis Sets for the Elements 1–118. *J. Comput. Chem.* **2003**, *24*, 1142–1156.

(4) Grimme, S.; Ehrlich, S.; Goerigk, L. Effect of the Damping Function in Dispersion Corrected Density Functional Theory. *J. Comput. Chem.* **2011**, *32* (7), 1456–1465.

(5) Pye, C. C.; Ziegler, T. An Implementation of the Conductor-like Screening Model of Solvation within the Amsterdam Density Functional Package. *Theor. Chem. Acc.* **1999**, *101* (6), 396–

(6) Lenthe, E. van; Baerends, E. J.; Snijders, J. G. Relativistic Regular Two-component Hamiltonians. *J. Chem. Phys.* **1993**, *99* (6), 4597–4610.

(7) van Lenthe, E.; Baerends, E. J.; Snijders, J. G. Relativistic Total Energy Using Regular Approximations. *J. Chem. Phys.* **1994**, *101* (11), 9783–9792.

(8) van Lenthe, E.; Ehlers, A.; Baerends, E.-J. Geometry Optimizations in the Zero Order Regular Approximation for Relativistic Effects. *J. Chem. Phys.* **1999**, *110* (18), 8943–8953.

(9) Becke, A. D. A New Mixing of Hartree–Fock and Local Density-functional Theories. *J. Chem. Phys.* **1993**, *98* (2), 1372–1377.

(10) Becke, A. D. Density-Functional Exchange-Energy Approximation with Correct Asymptotic Behavior. *Phys. Rev. A* **1988**, *38* (6), 3098–3100.

(11) Lee, C.; Yang, W.; Parr, R. G. Development of the Colle-Salvetti Correlation-Energy Formula into a Functional of the Electron Density. *Phys. Rev. B* **1988**, *37* (2), 785–789.

(12) Perdew, J. P.; Burke, K.; Ernzerhof, M. Generalized Gradient Approximation Made Simple. *Phys. Rev. Lett.* **1996**, *77* (18), 3865–3868.

(13) Perdew, J. P.; Burke, K.; Ernzerhof, M. Generalized Gradient Approximation Made Simple [Phys. Rev. Lett. 77, 3865 (1996)]. *Phys. Rev. Lett.* **1997**, *78* (7), 1396–1396.

(14) Handy, N. C.; Cohen, A. J. Left-Right Correlation Energy. *Mol. Phys.* **2001**, *99* (5), 403–412.

(15) Grimme, S.; Bannwarth, C.; Shushkov, P. A Robust and Accurate Tight-Binding Quantum Chemical Method for Structures, Vibrational Frequencies, and Noncovalent Interactions of Large Molecular Systems Parametrized for All Spd-Block Elements (Z = 1–86). *J. Chem. Theory Comput.* **2017**, *13* (5), 1989–2009.

(16) AMS DFTB 2019.3, SCM, Theoretical Chemistry, Vrije Universiteit, Amsterdam, The Netherlands, http://www.scm.com. .

(17) Bannwarth, C.; Caldeweyher, E.; Ehlert, S.; Hansen, A.; Pracht, P.; Seibert, J.; Spicher, S.; Grimme, S. Extended Tight-Binding Quantum Chemistry Methods. *WIREs Computational Molecular Science n/a* (n/a), e01493.

(18) Santra, G.; Sylvetsky, N.; Martin, J. M. L. Minimally Empirical Double-Hybrid Functionals Trained against the GMTKN55 Database: RevDSD-PBEP86-D4, RevDOD-PBE-D4, and DOD-SCAN-D4. *J. Phys. Chem. A* **2019**, *123* (24), 5129–5143. h

(19) Förster, A.; Visscher, L. Double Hybrid DFT Calculations with Slater Type Orbitals. *J. Comput. Chem.* **2020**, *41* (18), 1660–1684.

CHAPTER 6

In silico Optimization of Charge Separating Dyes

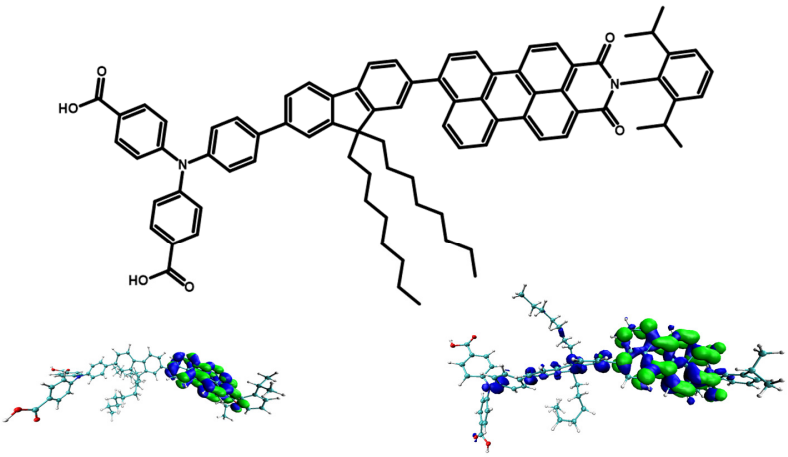

This Chapter is based in part on:

Tijmen M.A. Bakker, Jan Paul Menzel, Bas Vreugdenhil, Tessel Bouwens, Simon Mathew, Francesco Buda, Joost N.H. Reek; *to be submitted*

Jan Paul Menzel, Yorrick Boeije, Tijmen M.A. Bakker, Jelena Belić, Huub J.M. de Groot, Lucas Visscher, Joost N.H. Reek, Francesco Buda; *in preparation*

6

ABSTRACT

While DS-PECs are promising devices in solar energy conversion, a major loss pathway is the charge recombination of electron and hole at the dye-semiconductor interface. Charge separating dyes constructed as push-pull systems can increase the spatial separation of electron and hole, slow down the back-transfer and thereby decrease the recombination rate. In this chapter, we investigate a family of such dyes, consisting of polyphenylamine donors, fluorene bridges and perylene monoimide acceptors using a combination of semi-empirical GFN-xTB ground state dynamics and an AO/MO quantum propagation of photoexcited electron and hole. Several molecular design strategies to increase the charge separation efficiency are investigated *in silico*, including modifying the donor molecule, increasing the bridge length and decoupling the molecular components through steric effects. We find, in agreement with experiment, that exchanging the electron withdrawing formic acid anchors on the triphenylamine donor by electron donating acetic acid ones leads to a more efficient charge separation through hole accumulation on the donor. Triphenylamine donors lead to a more polarized charge transfer state than diphenylamines, while increasing the bridge from one to two fluorene fragments significantly enhances the dye's charge separation capabilities. Decoupling the different components by breaking the conjugation through steric hindrance from side groups results in a better charge separation in comparison to the planar molecule as well. Based on these findings an optimized charge separating dye for efficient suppression of charge recombination is proposed.

6.1 Introduction

DS-PECs have shown great promise for the production of renewable fuels, where semiconductor electrodes are sensitized with chromophores that absorb light in the visible range.[1] On the photoanode side, the photoexcited dyes inject the excited electrons into the semiconductor electrode, as discussed in chapter 4, to be used on the photocathode for fuel production. The hole left at the dye can then be picked up by a water oxidation catalyst (WOC) to split water into molecular oxygen and protons, regenerating the ground state of the molecular chromophore.[2]

Water oxidation however is a slow process involving storage of intermediates on long time scales in comparison to the electron injection from the photoexcited dye into the semiconductor anode.[3] Due to the slow consumption of holes by the chemical conversion of water to molecular oxygen and protons, they can be refilled as shown in figure 6.1. Reoccupation of the orbital may occur through a direct recombination of the photoexcited electron in the anode and the hole as seen in red in figure 6.1a, leading to a full deactivation and energetic losses through heat.

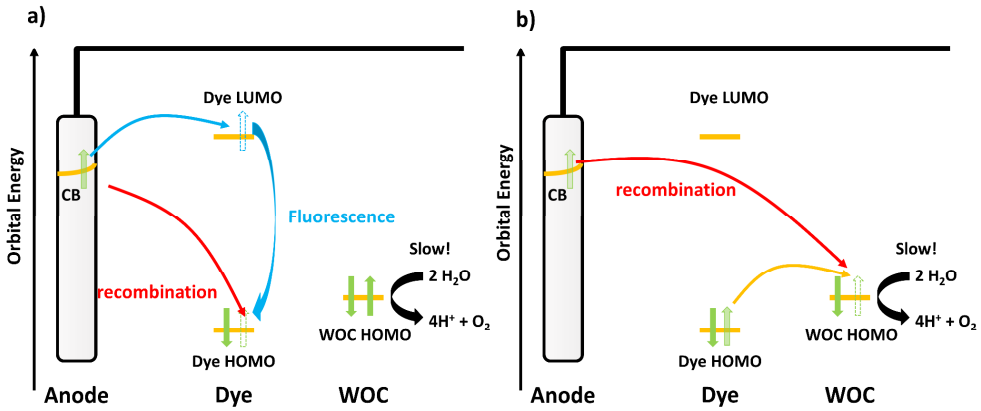

Figure 6.1. Energy loss pathways in a dye sensitized photoanode: **a)** After electron injection from the dye into the electrode, the hole on the dye can be either filled by direct recombination (red) with the photoexcited electron or by fluorescence after back transfer of the electron from the semiconductor (blue). **b)** Following the hole transfer to the WOC, recombination of the excited electron from the electrode (red) or back transfer to the dye's HOMO followed by the processes in a) can lead to the loss of the excited state energy.

Another loss pathway shown in blue is through back transfer of the excited electron to the dye followed by fluorescence, where the photoexcited electron falls back to the HOMO while releasing the excess energy in the form of a photon.

Deactivation is also possible after initially successful charge separation and hole transfer to the WOC: the hole at the WOC can be refilled as shown in figure 6.1b. This involves either direct recombination with the photoexcited electron from the semiconductor as shown in red, or back transfer of the hole to the dye as shown in yellow, opening up the loss pathways given in figure 6.1a. All these processes lead to the loss of the photon energy in the form of heat. The factor determining the losses is the ratio between the rates of the competing processes. As the creation of the charge separated state through the electron injection process into TiO_2 is extremely fast, often in the sub-picosecond or picosecond time frame[4] (see also chapter 4) and the rate of the slowest oxidation step of the WOC (^{1}[Ru(IV)-OH]$^+$ -> ^{2}[Ru(V)=O]$^+$) is, dependent on the concentration of the oxidant, in the order of micro to milliseconds (2.3×10^5 $M^{-1}s^{-1}$ at 35 °C with CeIV),[5] the time mismatch between these two processes is several orders of magnitude, over which the charge separated state needs to be stabilized. While the last decade has seen important improvements in the turnover frequency of WOCs,[5–9] reducing the charge recombination and back transfer rates is an important factor to minimize losses.

In general, several strategies can be applied to reduce the probability for back-transfer of an electron or hole in a donor-acceptor system. In figure 6.2, some of these possible approaches are schematically shown. When attaching the electron acceptor (such as the dye) directly to the donor, as shown in figure 6.2a, back transfer, though slower than forward charge transfer, can occur relatively unhindered. One way to reduce the rate of back transfer is to introduce a barrier between donor and acceptor by including a molecular system with a HOMO energy higher than that of both donor and acceptor as seen in figure 6.2b.

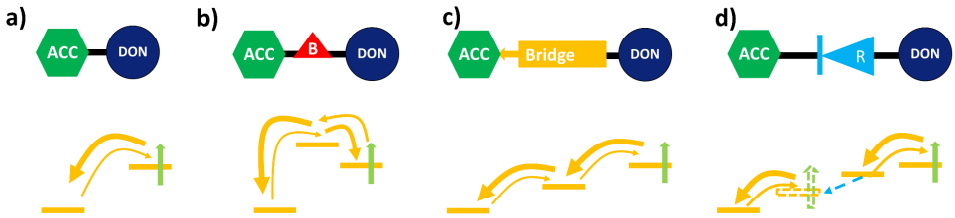

Figure 6.2. Schematic representation of different approaches to reduce the back transfer from the acceptor (ACC) towards the donor (DON) after initial charge transfer: **a)** Direct attachment of acceptor and donor allows for relatively easy back transfer. **b)** Introducing an energetic barrier reduces the rate of initial charge transfer, but also reduces the back transfer rate significantly. **c)** Spatial separation via a bridge leads to lower back transfer probability. **d)** Introduction of a molecular rectifier, that through asymmetrical HOMO and LUMO localization or resonant conformational changes increases charge flow in one direction, while decreasing it in the opposite.

While the initial transfer rate is decreased, since this barrier needs to be overtaken, the back transfer rate is even more reduced. Another possible strategy, for example used in natural photosynthesis,[10] is separating electron and hole spatially as quickly as possible by introducing a bridge consisting of one or more electronic systems with clear energy gradients of the involved orbitals as shown in figure 6.2c. Molecules, where HOMO and LUMO are on spatially different components, or molecules that change conformation upon population of the LUMO are efficient ways to allow for charge transfer in one direction but inhibit migration in the opposite direction as shown schematically in figure 6.2d. These molecules are called molecular rectifiers.[11–16]

A strategy combining some of the approaches described above for reducing charge recombination, is the introduction of charge separating dyes that are commonly used on the other half-cell reaction, the photodriven hydrogen evolution on the photocathode.[17–19] They consist of π-conjugated donor-acceptor molecules, with a donor component that accumulates hole density, an acceptor that accumulates electron density and a π-system bridging the two. This arrangement of donor – π system – acceptor (DON-π-ACC) is often also called a push-pull system, named after their respective properties of pushing (donor) or pulling (acceptor) electron

density.[20,21] The electronic properties of these systems are designed to allow for efficient intramolecular charge transfer. The explicit molecular systems can vary quite significantly, depending on the requirements on the molecules in their device implementation. Within the context of DSSCs and DS-PECs, some common donor molecules include diphenylamines (DPA)[17,18,20,22] and triphenylamines (TPA)[19,23–30] as well as their derivatives[31–33]. The π-conjugated molecular spacer or bridge is often an extended system, such as thiophene derivatives[19,24,27,31,34] or fluorenes.[18,17,20,29–31] The bridge can however also involve a photosensitizer such as porphyrin,[33,25,35] that donates an electron to the acceptor while the hole is transferred to the donor. If either the bridge or the donor is the photosensitizer, the acceptor can be non-photoactive, such as benzoic acids[24,25,33,35]. Cyano acrylic acids[22,31,34] are also used as acceptors, but various fragments can be chosen to tune the desired energy levels.[27] A common photoactive acceptor is perylene-monoimide (PMI).[17–19,29,30] The dyes are often equipped with alkyl or alkoxy chains to act as a protective layer for the respective electrode and anchoring groups, preventing electrolyte interference, but also dye aggregation.[17–19,24,31,33,35]

Implemented within a larger donor-acceptor system, these dyes can act as barrier, bridge or molecular rectifier, for either electron or hole, allowing for easy transfer in one direction, while inhibiting back transfer. Organic molecules with these charge separating qualities are therefore of interest in both half cells of DS-PECs whenever charge recombination becomes a major loss pathway.

Here, we do an *in silico* investigation and optimization of such push-pull systems for efficient charge separation and back-transfer suppression using a quantum-classical semi-empirical approach: GFN-xTB[36] based nuclear classical dynamics in the ground state are followed by an AO/MO quantum propagation of photoexcited electron and hole on these nuclear trajectories using an extended Hückel Hamiltonian.[37,38] GFN-xTB has been optimized for geometries and frequencies and has proven reliable in a wide variety of systems.[39–43] The general trends that can be extracted from this investigation should help to optimize charge separating

components for other systems as well, such as the dye-WOC complexes in the photoanode of a DS-PEC.

The structure of the investigated dyes is as follows: a Perylene Mono Imide (PMI) derived fragment acts as acceptor and photosensitizer. It is connected via a fluorene-based bridge (FLU) to a polyphenyl amine donor, here for example a triphenyl amine (TPA) with carboxylic acid groups. These organic molecules are based on charge separating dyes first synthesized and tested by Liu *et al.*[17,18] A schematic of the energetics obtained experimentally from Cyclic Voltammetry (CV) and UV-Vis experiments[44] of the involved fragments is shown in Figure 6.3.

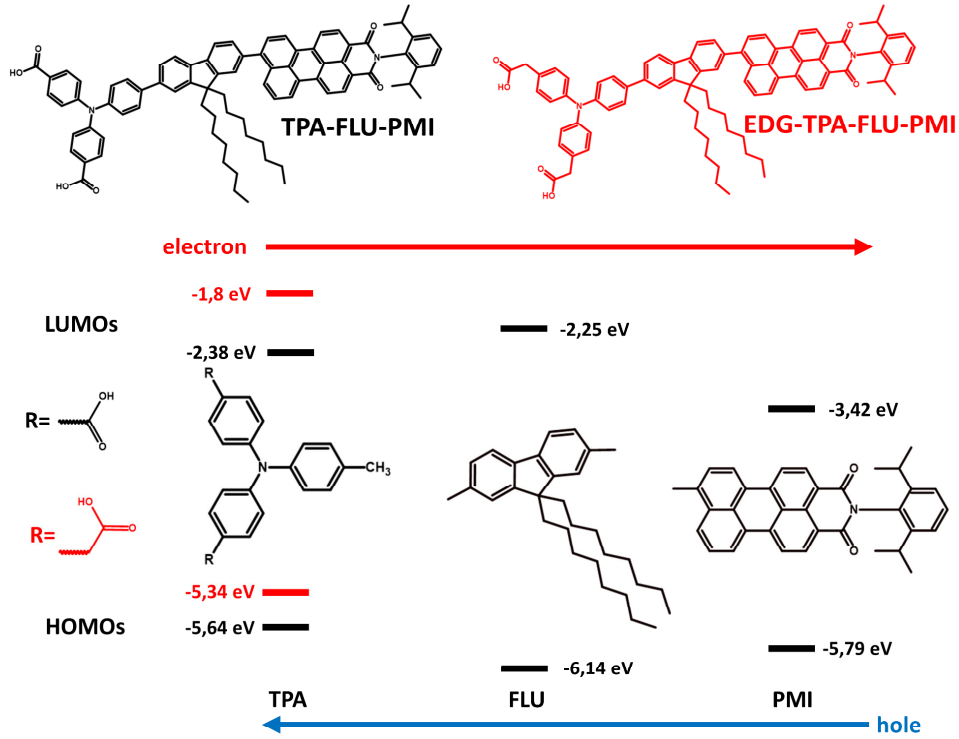

Figure 6.3. Molecular fragments of the TPA-FLU-PMI charge separating dye (chemical structure on top, black) with orbital energy levels obtained through experimental CV and UV-Vis redox potentials.[44] Due to the higher HOMO energy of the TPA fragment, the hole moves towards the TPA, while the electron moves towards the PMI. Exchanging the COOH groups of the TPA by CH_2COOH (red, EDG-TPA) leads to the EDG-TPA-FLU-PMI dye

(chemical structure on top in red) with a larger driving force for both the electron to move towards the PMI and the hole to move towards the EDG-TPA (red).

Due to the gradient in energy from the donor to the acceptor part of the molecule, the excited electron moves towards the acceptor, while the hole moves towards the polyphenyl amine donor.

The fluorene acts as both a bridge for the hole and as a barrier for the electron to prevent electron density from moving towards the donor. The electron can then be picked up by an oxidative agent, as *e.g.* on the photoanode side by the TiO_2 electrode, or on the photocathode by a hydrogen evolution catalyst (HEC) as shown in scheme 6.1. The hole is either injected from the donor into a semiconductor cathode or, for example, used to drive a water oxidation catalyst (WOC) on the photoanode side.

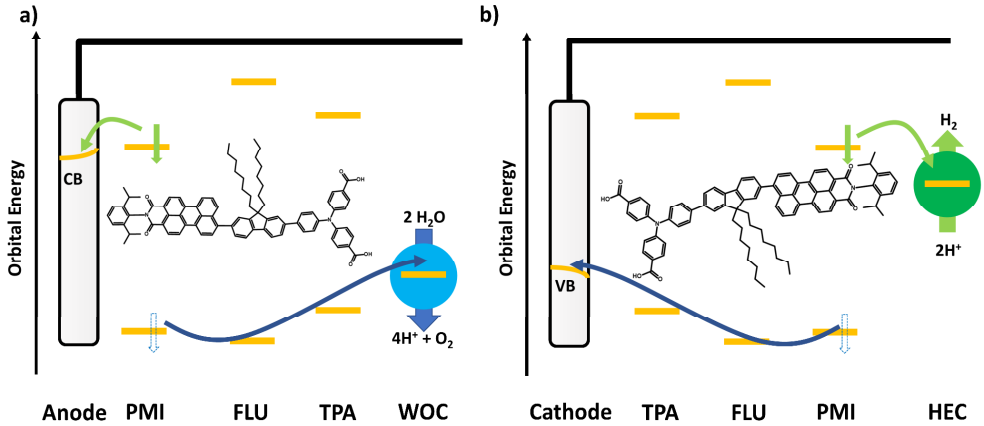

Scheme 6.1. Potential use of a charge separating dye in the context of a DS-PEC: **a)** on the photoanode side, where the photoexcited PMI donates the electron (green) into the CB of the anode, the hole (blue) is transferred via the FLU and TPA to a WOC to oxidize water, **b)** on the photocathode side, where the photoexcited PMI donates the electron (green) to a suitable HEC for hydrogen evolution, while the hole (blue) is transferred via FLU and TPA to be injected into the valence band (VB) of a suitable cathode.

Several strategies are tested to increase the charge separation efficiency of these dyes. Increasing the driving force between donor and acceptor should increase the charge separation efficiency. A comparison is therefore performed between two different donors with different energy levels: a diformate triphenyl amine group on

the TPA is exchanged by two acetate groups to change from an electron withdrawing substituent to an electron donating group (EDG-TPA), with the effect of a higher HOMO energy (see figure 6.3). This increase in driving force between the HOMO of the TPA and HOMO of the PMI should result in a larger polarization of the molecule, since more hole density should reside on the donor side.

However, since the donor as well as the acceptor part of the charge separating dyes might already have tuned energetic alignment with their respective reaction partners for further electron and hole transfer, it is also relevant to find ways to optimize these charge separating dyes without changing the energy levels of the donor and acceptor part of these molecules. Several different strategies are followed to obtain a better charge separation without increasing the driving force significantly. As mentioned before, here we use the triphenyl amine (TPA) as a donor. While the fluorene-PMI based dyes introduced by Liu *et al.* included a diphenylamine (DPA) donor[17,18], other successful push-pull systems were introduced with a TPA.[19,26,28] To estimate which donor would be more efficient in these systems, the effect of a DPA/TPA donor is investigated.

As the fluorene bridge acts as a spatial separation of the donor and acceptor, increasing the bridge length should have a relevant impact on the hole transfer dynamics, as has been shown experimentally in similar molecular systems.[18,19] Therefore, a further investigation of the effect of the number of fluorene bridge molecules on the charge separation is performed. The investigated dyes, including dyes with both DPA and TPA donors and one, two or three fluorene fragments, are given in table 6.1 including the nomenclature used throughout the chapter.

Table 6.1. Chemical structures and nomenclature used of the charge separating dyes, with different donors, triphenylamine (TPA) and diphenylamine (DPA), as well as increasing number of fluorenes in the bridge.

	Diphenylamine (DPA) donor	Triphenylamine (TPA) donor
1 fluorene	**DPA-FLU-PMI** 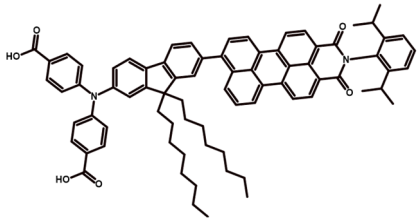	**TPA-FLU-PMI** 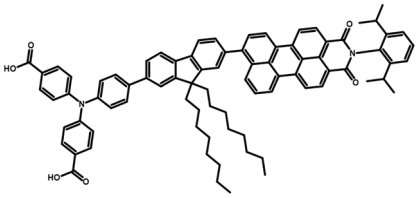
2 fluorenes	**DPA-2FLU-PMI** 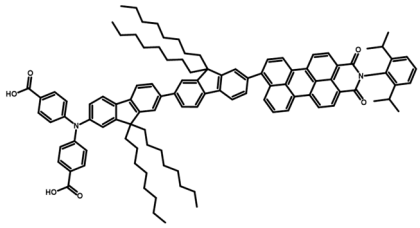	**TPA-2FLU-PMI** 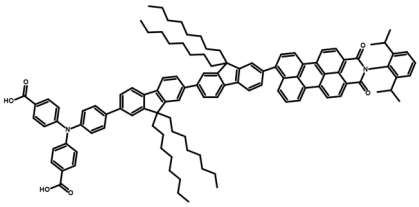
3 fluorenes	**DPA-3FLU-PMI** 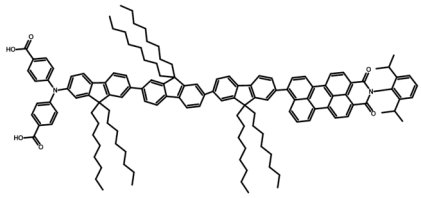	**TPA-3FLU-PMI** 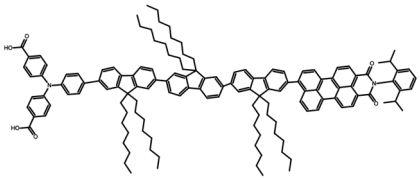

Finally, the close coupling between the different components of the charge separating dye diminishes the triad character of the dye, with the hole flowing freely between the different components, lowering the charge separation efficiency. To decrease the coupling between the components and reduce the back transfer of hole density towards the PMI, methyl groups are introduced to keep dihedral angles close to 90 degrees. In table 6.2, chemical structures of the sterically decoupled molecules are given, with the nomenclature used in the rest of the chapter.

Table 6.2. Chemical structures and nomenclature used throughout the chapter of investigated, decoupled dyes. The conjugation of the extended pi-systems is broken by introducing sterically demanding methyl groups to enforce approximately perpendicular dihedral angles on the TPA (TPAMe-FLU-PMI), the fluorene (TPA-FLUMe-PMI) or the PMI (TPA-FLU-PMIMe).

Methylated TPA:

TPAMe-FLU-PMI

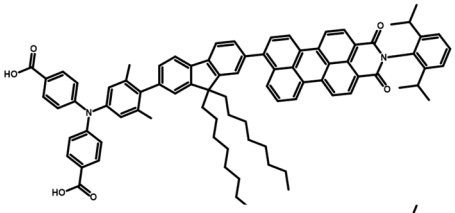

Methylated FLU:

TPA-FLUMe-PMI

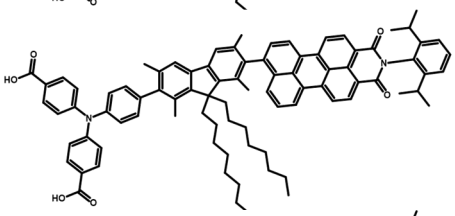

Methylated PMI:

TPA-FLU-PMIMe

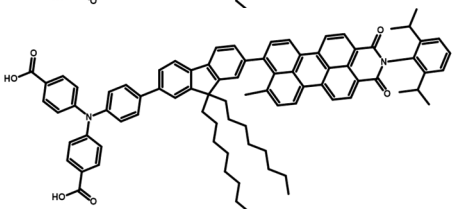

Our *in silico* investigation finds that the EDG-TPA donor increases charge separation efficiency in comparison to the TPA donor. TPAs give a larger spatial separation between electron and hole than DPAs, while the increasing chain length of fluorenes increases the separation efficiency up to two fluorenes, while adding a third fluorene does not significantly improve the charge separation, as measured by the equilibrium hole distributions. Introducing methyl groups to decouple the different fragments is most efficient when used on the fluorene bridge. Based on these results we propose an optimized dye that includes the TPA donor connected to the PMI via a bridge that contains two fluorenes, equipped with methyl groups to decouple the fragments. The proposed molecule is shown in scheme 6.2. This molecule shows indeed promise in a more efficient charge separation. The results obtained here are relevant for the optimization of charge transfer processes using push-pull systems for both photodriven water oxidation and hydrogen evolution.

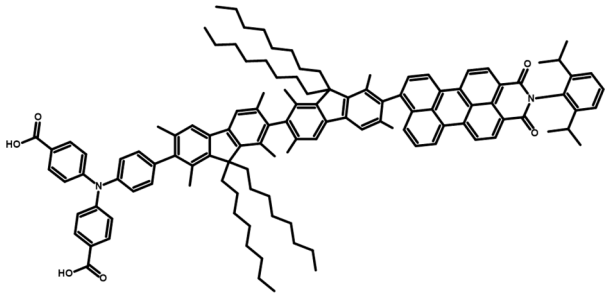

Scheme 6.2. Proposed optimized charge separating dye (TPA-2FLUMe-PMI): the TPA donor leads to a larger hole density on the donor in comparison to the fluorenes, the chain length of two fluorenes has been shown to give a more efficient charge separation, while the methyl groups on the fluorene molecules break conjugation, lowering the back transfer of hole density to the PMI.

6.2 Computational Methods

General Procedure

Simulations of photoinduced charge separation in these molecular dyes were performed by a combination of the semi-empirical GFN-xTB[36] approach to generate *a priori* classical nuclear trajectories and quantum dynamics simulations of the photoexcited electron and hole using the AO-MO propagator and an extended Hückel Hamiltonian.[37,38,45] Details of this method can be found in chapters 2 and 4. DFT and GFN-xTB based calculations were performed using the DFTB and ADF engines of the AMS2020 program package developed by SCM.[46–49] The quantum propagation was performed using the program developed by Rego and Batista.[37]

GFN-xTB-based Molecular Dynamics

The semi-empirical tight binding approach GFN-xTB was used to generate the nuclear trajectories. An equilibration run with a total simulation time of 15 ps in the NVT ensemble was performed using a Berendsen thermostat[50] at 293.15 K and a time step of 1 fs. This was followed by a MD production run in the NVE ensemble, with a total simulation time of 5 ps, and a time step of 0.1 fs. This trajectory was cut into 10 slices of 500 fs each. Those trajectories were then used in the charge transfer dynamics (CTDs).

Optimization of Extended Hückel Parameters

The extended Hückel parameters were optimized to reproduce experimental redox potentials. For this, geometry optimizations of the different molecular fragments were performed using both GFN-xTB and DFT. For the DFT optimizations, the B3LYP XC-functional[51,52] with a TZP basis set[53] and D3 dispersion corrections with BJ-damping,[54]were used. Both GFN-xTB and DFT lead to comparable geometries, with deviations mostly in the long, flexible alkyl chains. An example is shown for the TPA-FLU-PMI dye in figure 6A.1 in the appendix. The GFN-xTB geometries were used for the parameter optimization, while the DFT results were used for determining the spatial distribution of relevant orbitals. The experimental redox potentials were taken from a manuscript currently in preparation.[44] They were determined via Cyclic Voltammetry and, in cases where the reduction potential was out of measurable bounds, via the main absorption peak onset, which is commonly used to determine reduction potentials.[55,56] Conversion of these potentials to energies in eV of the frontier orbitals is done by following equation 6.1 and 6.2 for the oxidation potential/HOMO and reduction potential/LUMO, respectively. The target HOMO and LUMO energies $\varepsilon_{\mathrm{MOL}}^{\mathrm{HOMO}}$, $\varepsilon_{\mathrm{MOL}}^{\mathrm{LUMO}}$ can be estimated from these standard Redox Potentials versus NHE $E_{\mathrm{ox,NHE}}^{0}$, $E_{red,\mathrm{NHE}}^{0}$ with the use of the Faraday constant $F = N_A * e$ as given in equations 6.1 and 6.2:

$$\varepsilon_{\mathrm{MOL}}^{\mathrm{HOMO}} \approx -E_{\mathrm{ox,vacuum}}^{0} * nF = -\left(E_{\mathrm{ox,NHE}}^{0} + 4.44\,V\right) * e \tag{6.1}$$

$$\varepsilon_{\mathrm{MOL}}^{\mathrm{LUMO}} \approx -E_{\mathrm{red,vacuum}}^{0} * nF = -\left(E_{\mathrm{red,NHE}}^{0} + 4.44\,V\right) * e \tag{6.2}$$

Here $E_{\mathrm{ox,vacuum}}^{0}$and $E_{\mathrm{red,vacuum}}^{0}$ are the oxidation and reduction potential versus an electron at rest in vacuum, *n* the moles of electrons (here one electron, thus $\frac{1}{N_A}$), N_A the Avogadro constant and *e* the elemental charge. The resulting energies are then in units of eV. The determined target values can be found in table 6A.1 in the appendix. The optimization of the extended Hückel parameters was performed on the GFN-xTB geometries, so that the HOMO/LUMO energies of the respective molecules represent the target values determined in equations 6.1 and 6.2, while the spatial form

of the frontier orbitals was checked against the DFT results, to ensure that the obtained orbitals are physically meaningful. The procedure itself is based on a genetic algorithm described elsewhere.[57] The optimized energies can be found in table 6A.1, the spatial distribution of the frontier orbitals in table 6A.2 in the appendix. After optimization of the different fragment molecules on their experimental redox potentials, the TPA-FLU-PMI and EDG-TPA-FLU-PMI dyes gave remarkably close results to experiment without further optimization (see table 6A.1 in the appendix). For the methylated molecules, the parameters were not reoptimized as there is no corresponding experimental data available; however, the influence on the energies due to this small structural change is expected to be small.

Determination of Relevant Excitations

Relevant excitations in the 400-600 nm wavelength range were determined using LR-TDDFT. The long-range corrected hybrid functional camy-B3LYP as implemented in ADF[58–60] was used for all LR-TDDFT simulations, with a DZP basis, a small frozen core and D3-dispersion with BJ-damping. Excitation energies, oscillator strength and transition densities are given in tables 6A.5-6A.15 in the appendix. For all investigated molecules, the excitonic PMI HOMO-LUMO excitation was the most relevant due to its high oscillator strength and excitation energy in the visible light range.

Charge Transfer Dynamics

Simulations of Charge Transfer Dynamics (CTD) were performed on the pre-calculated nuclear trajectories. For each molecule, ten nuclear trajectories of 500 fs length with a time step of 0.1 fs were used, obtained as explained above and shown in scheme 6.3. Two wave packets representing photoexcited electron and hole were chosen based on the LR-TDDFT results: since in all cases, the excitonic PMI excitation is the most relevant in the visible region, the wave packets were prepared as the HOMO and LUMO of the PMI fragment. The wave packets were propagated

on these *a priori* nuclear trajectories, with a time step of 0.1 fs for the electronic propagation. After the CTDs, the populations of electron and hole on the different fragments over time were averaged over the 10 trajectories. The changes of charge over time were obtained by subtracting the electron populations from the hole population on each fragment. Average charges are determined over all CTDs and the last 200fs. since at that point the charges were stabilized in most simulations, and in this way quantitative measures of charge separation efficiencies were obtained. These results are collected for the fragments of all investigated dye molecules in table 6A.16 in the appendix. A representation of the full process of nuclear trajectory generation and CTDs is given in scheme 6.3.

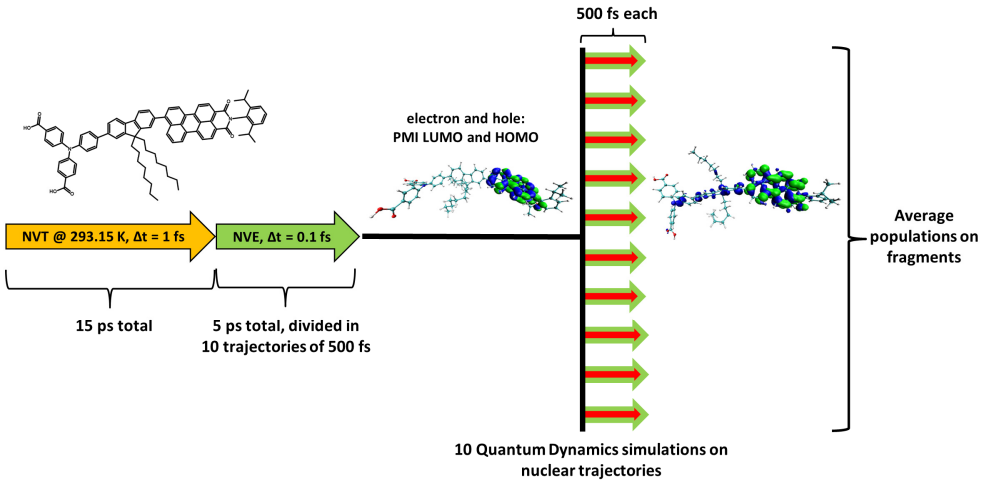

Scheme 6.3. Preparation of the nuclear trajectories and production of the CTDs. A 15 ps NVT equilibration run at 293.15 K is followed by a 5 ps long NVE run with a time step of 0.1 fs. This long trajectory is cut into 10 trajectories of 500 fs each in order to sample different initial conditions for the CTDs. On these nuclear trajectories, quantum propagation of electron and hole, represented by the PMI fragment LUMO and HOMO respectively is performed. From these 10 CTD runs, the populations of electron and hole on the respective molecular fragments is averaged to obtain the charge separation within the dye molecule.

6.3 Results

The photoinduced charge separation in the push pull system over time is shown for the TPA-FLU-PMI case in figure 6.4, where the charge corresponds to the hole minus electron population for the different fragments. The lines represent the mean average over the ten CTDs, while the shaded area represents the standard deviation.

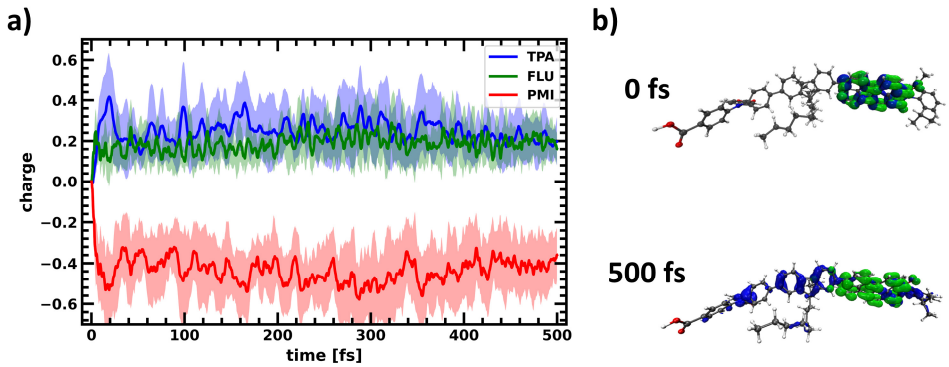

Figure 6.4. a) Charge separation in the TPA-FLU-PMI dye. Charges are determined as difference between hole and electron population on the respective fragments PMI (red), FLU (green) and TPA (blue). The lines denote mean averages over 10 trajectories, the shaded areas the standard deviation. **b)** electron (green) and hole (blue) densities at the beginning and end of one quantum dynamics trajectory.

Upon photoexcitation, both electron and hole reside on the PMI since the excitation is purely excitonic in character. Thus, the charge difference is initially zero on all fragments. Upon time evolution, the hole migrates to the fluorene and the TPA, while the electron stays at the PMI (see figure 6A.2 in the appendix), resulting in a negative charge accumulating on the PMI, while the FLU and TPA get positively charged. While the initial charge separation is relatively fast, the charges equilibrate after around 200 fs. In addition, hole transfer is not complete, most likely due to the delocalized character of the HOMO (see table 6A.4 in the appendix), and the nearly degenerate lower lying orbitals. Energetic separation is much larger for the unoccupied orbitals (figure 6.3). After the system reaches equilibrium, the average charge on the PMI corresponds to about -0.44, while the FLU obtains a

charge of approximately +0.20 and the TPA of +0.24, based on averaging over the last 200 fs. The TPA-FLU-PMI dye does show photoinduced charge separation, however to an extent that could be further improved.

Changing the Driving Force: TPA-FLU-PMI vs EDG-TPA-FLU-PMI Dye

Experimental work showed an increase in photoinduced hole injection when changing the donor from TPA to EDG-TPA by about 30 %.[44] In figure 6.5, we compare the charge separation over time of the PMI and TPA-derived fragments of the two dyes TPA-FLU-PMI and EDG-FLU-PMI. Here, the FLU has been omitted for clarity. (see table 6A.16 in the appendix).

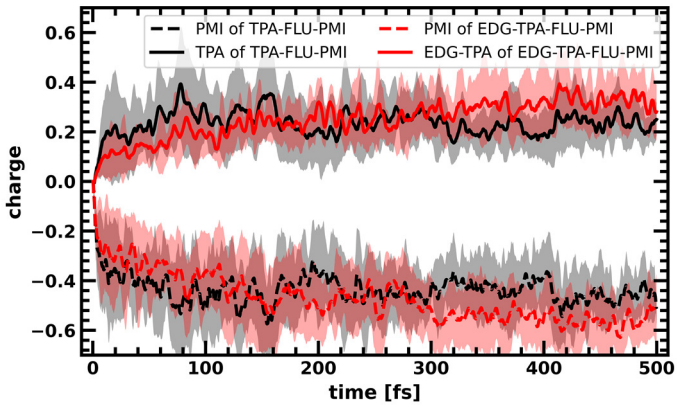

Figure 6.5. Charge separation in the TPA-FLU-PMI (black) and EDG-TPA-FLU-PMI (red) dyes. Charges are determined as difference between hole and electron population on the respective fragments PMI (dashed lines) and TPA (solid lines). The lines denote mean averages over 10 trajectories, the shaded areas the standard deviation.

The charge transfer dynamics of the EDG-TPA-FLU-PMI dye is qualitatively similar to the TPA-FLU-PMI, which reflects the close relation between the two dyes. Again, the excitonic excitation of the PMI leads to a neutral charge on all fragments at t=0. Upon time evolution, hole density is transferred towards the EDG-TPA via the FLU. While the initial charge transfer is delayed in comparison to the TPA-FLU-PMI, more hole density is transferred from the PMI to the EDG-TPA over time. Equilibration is also reached at a later stage. This decrease in initial charge separation

is most likely due to the less delocalized HOMO (see table 6A.4) of the EDG-TPA-FLU-PMI compared to the TPA-FLU-PMI, with weaker coupling between the PMI and EDG-TPA fragments. However, after the initial slow down, the larger driving force and spatial localization of the HOMO on the EDG-TPA leads to a stronger polarization compared to the TPA-FLU-PMI, as more hole density resides on average at the donor. When comparing the time average of the charge from the 300 fs mark on, where equilibrium appears to be achieved and the red and black curve clearly cross each other (see Figure 6.5), the EDG-TPA-FLU-PMI shows a significantly increased charge separation relative to the TPA-FLU-PMI: while the PMI had a charge of -0.43 in the TPA-FLU-PMI dye, this decreases to approximately -0.53 for the EDG-TPA-FLU-PMI dye. The positive charge of about +0.23 in the TPA is increased to an approximate value of 0.30 for the EDG-TPA, while the charge on the FLU increases a little less (+0.20 vs. +0.23). This points to a more efficient charge separation. The electron donating character of the methylene groups pulls the HOMO towards the EDG-TPA and increases its energy, leading to a larger driving force for the hole to move towards the donor. While dynamic disorder causes fluctuations in the orbital energies and therefore also to oscillations in hole population on the different fragments due to alternating forward and back transfer, the average hole population on the donor is increased in comparison to the TPA-FLU-PMI. This larger separation of electron and hole results in a lower charge recombination probability due to the lower spatial overlap of electron and hole densities for the EDG-TPA based dye than for the dye using a TPA donor. These findings are in line with the experimentally determined increased hole lifetimes for the EDG-TPA-FLU-PMI dye in comparison to the TPA-FLU-PMI.[44]

DPA vs TPA Donor

Introducing a TPA or DPA has little effect on the driving force in these charge separating dyes, as the HOMO energies are similar. This is supported by the density of states of these two fragments (figure 6.6). The peaks denoted HOMO (~-11.6 eV) and LUMO (~-8.4 eV) have almost the same energy for the two systems. Therefore, the boundary condition of a similar donor HOMO energy remains fulfilled when exchanging DPA and TPA.

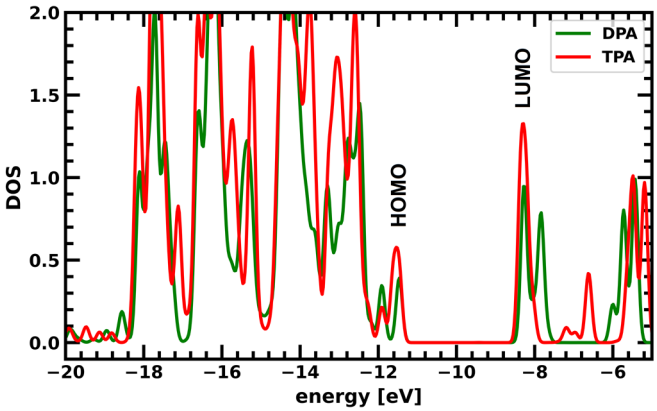

Figure 6.6. Partial Density Of States (PDOS) of the TPA (red) and DPA (green) donors.

A comparison between the TPA-FLU-PMI and DPA-FLU-PMI charge separation efficiency in the form of net charge on the PMI after photoexcitation is shown in figure 6.7a. Here, the other fragments as well as the standard deviation are omitted, the traces represent averages over 10 CTD simulations. The initial charge separation is slightly delayed with the DPA donor compared to the TPA as donor; however, this difference diminishes after around 100 fs. When averaging over the last 200fs, the charge on the PMI is -0.46 and -0.44 for the DPA-FLU-PMI and TPA-FLU-PMI dyes, respectively. While the charge on the PMI is not significantly changed, the TPA leads to a further polarization with a higher positive charge on the donor (+0.24) and lower on the fluorene (+0.20) in comparison to the DPA based dyes (+0.20 and +0.26 for DPA and FLU, respectively) as seen in figure 6.7b. This holds true also

when comparing the DPA-2FLU-PMI with the TPA-2FLU-PMI molecules (see figure 6A.3 and table 6A.16 in the appendix).

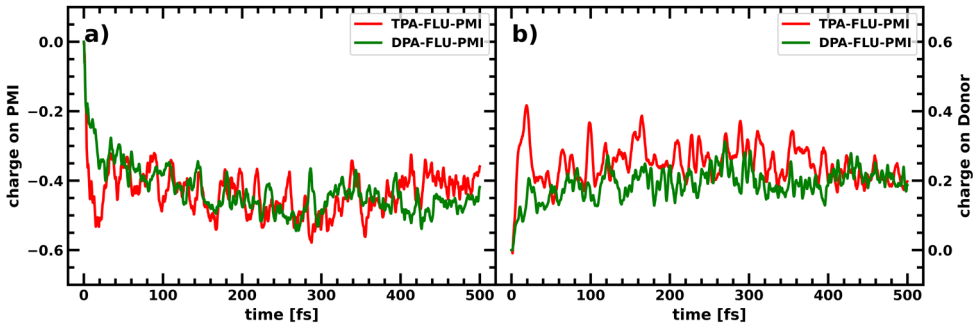

Figure 6.7. a) Average charge accumulation averaged over 10 CTDs on the PMI in the TPA-FLU-PMI (red) and DPA-FLU-PMI (green) dyes upon photoexcitation of the PMI. **b)** Average charge accumulation averaged over 10 CTDs on the donor (TPA/DPA) in the TPA-FLU-PMI (red) and DPA-FLU-PMI (green) dyes upon photoexcitation of the PMI.

While the same amount of hole density is transferred from the PMI, the charge separation is more efficient using a TPA instead of a DPA donor molecule: the TPA leads to larger polarization, as more hole density accumulates on the TPA instead of the FLU. For an efficient spatial separation, TPAs as donors are preferred.

Increasing the Bridge Length

In figure 6.8, the change in charge on each fragment of the charge separating dyes over time is shown for the TPA-XFLU-PMI and DPA-XFLU-PMI molecules, with the number of FLU fragments X changing from 1 to 3. While increasing the chain length from one fluorene to two fluorene molecules increases the charge separation efficiency significantly for both the TPA and DPA based dyes, introducing a third fluorene does not increase the charge separation any further for the TPA based dye, while the DPA-3FLU-PMI dye shows an initially better performance than the DPA-2FLU-PMI dye that diminishes after around 300 fs (see also table 6A.16 in the appendix).

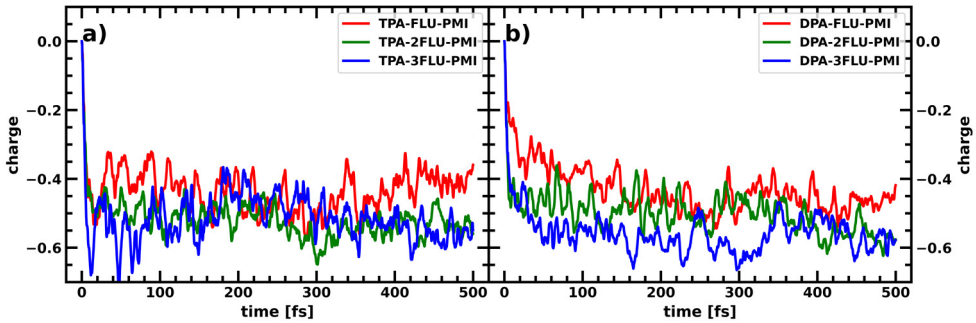

Figure 6.8. Average charge accumulation averaged over 10 CTDs on the PMI with increasing fluorene spacer bridge upon photoexcitation of the PMI: **a)** in the TPA-FLU-PMI (red), TPA-2FLU-PMI (green) and TPA-3FLU-PMI dyes. **b)** in the DPA-FLU-PMI (red), DPA-2FLU-PMI (green) and DPA-3FLU-PMI dyes.

Experimentally, an increase of fluorene chain length has been shown to increase the performance of the DPA-XFLU-PMI dyes (differing only in alkyl chain length), with the DPA-2FLU-PMI dye showing the best performance.[18] Our computational results also suggest that the charge separation efficiency does not significantly increase when moving from 2 fluorene bridges to using 3 fluorenes, since the hole mainly accumulates on the additional fluorenes with limited hole density on the donor (see table 6A.15 in the appendix). Liu et al. attribute the lower efficiency of DPA-3FLU-PMI in a photocathode to a lower loading of the molecule on the electrode in comparison to the DPA-FLU-PMI and DPA-2FLU-PMI molecules.[18] However, another influence on the decreased performance of the DPA-3FLU-PMI and TPA-3FLU-PMI molecules in comparison to their counterparts with one or two fluorenes might also be their different absorption behavior. With increasing fluorene length, the fluorene based excitonic excitation lowers in energy and increases in oscillator strength, becoming slightly competitive to the PMI based excitation as shown in figure 6A.4 in the appendix, also in agreement with experimental UV-VIS results.[18] A fluorene-based excitation leads to electron transfer towards not only the PMI but also the donor (TPA or DPA), increasing the likelihood of charge recombination.

All in all, increasing the chain length from one to two fluorene molecules leads to improved performance, while a three-fluorene bridge does not improve the charge

separation efficiency further and allows for competing pathways through the excitation of the fluorenes, that lead to recombination instead of charge separation, lowering the overall efficiency.

Decoupling the Fragments

One of the problems in the photoinduced charge separation process of these dyes is the relative delocalization of the molecular HOMO, as well as the nearly degenerate states, leading to a spread out of the hole. One approach to increase the average hole population on the donor is by increasing the driving force, pulling the hole towards the donor. Another possibility however would be to limit delocalization of the HOMO to the donor fragment, by decoupling the different fragments of the molecular dye. This can be achieved by breaking the conjugation between the different components, by forcing the dihedral angle towards a perpendicular orientation and thereby separating the fragments molecular orbitals from one another. Photoinduced charge separation should then still be possible, since dynamic fluctuations should also lead to changes in the dihedrals, allowing charge flow for certain nuclear conformations. While this might slow down initial charge transfer, it should lead to a distinct separation of fragment states, with the HOMO localized on the donor, reducing delocalization of the hole over the entire molecule and suppressing back transfer. The inclusion of methyl groups can help enforcing a near perpendicular arrangement of the fragment's π-systems, by introducing steric strain. Methyl groups were therefore introduced on different parts of the molecule to study the effect on the charge separation process. In figure 6.9, charge transfer within the dye is visualized through the net charge over time on the PMI fragment for the original TPA-FLU-PMI dye in comparison to dyes equipped with methyl groups at each respective fragment to break conjugation: TPAMe-FLU-PMI, TPA-FLUMe-PMI and TPA-FLU-PMIMe.

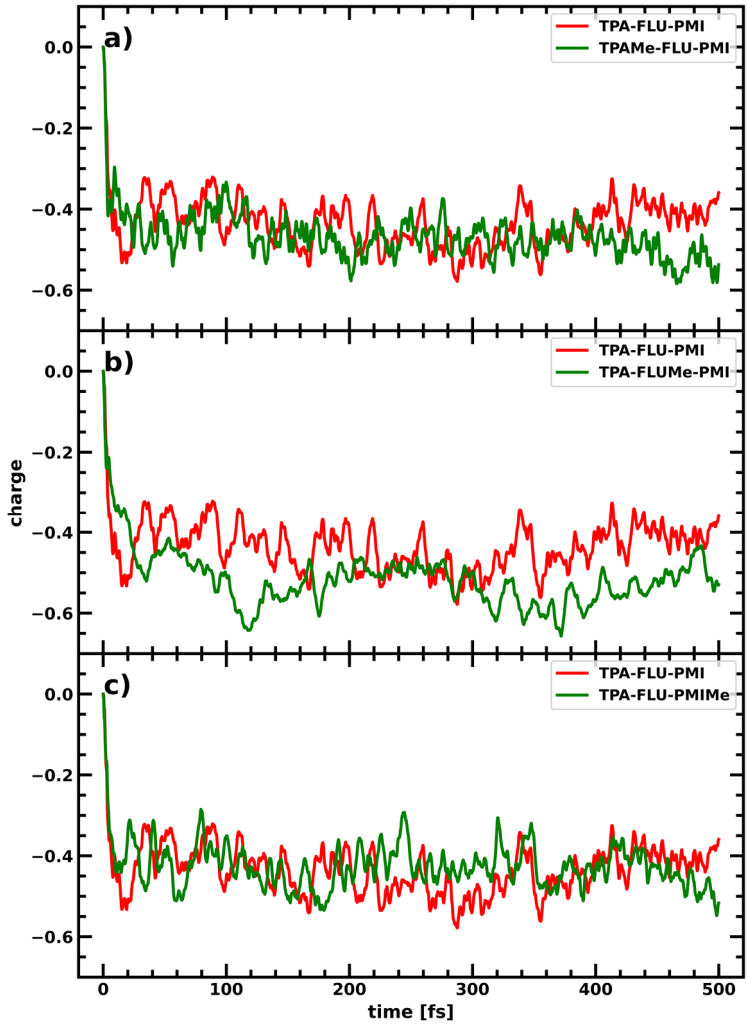

Figure 6.9. Average charge accumulation averaged over 10 CTDs on the PMI in the TPA-FLU-PMI case (red) compared to the respective methylated derivatives in green: **a)** TPAMe-FLU-PMI, **b)** TPA-FLUMe-PMI, **c)** TPA-FLU-PMIMe.

While a methyl group on the PMI does not lead to further hole transfer towards fluorene and TPA than for the TPA-FLU-PMI molecule, breaking the conjugation through methyl groups on the TPA and FLU leads to a lower net charge on the PMI (see table 6A.15 in the appendix), thus increasing charge separation in comparison to the planar molecule. Introducing methyl groups to the fluorene seems most promising, since more hole density is transferred to TPA and FLU, which is not

surprising since methyl groups on the FLU keep both dihedral angles at approximately 90 degrees. However, larger fluctuations are observable than for the coupled case. The charge separation process in the TPA-FLU-PMI dye becomes much more sensitive towards the respective nuclear conformation in comparison to the non-methylated dyes. Decoupling the fragments from another by breaking conjugation through dihedral angles of roughly 90 degrees can therefore increase the charge separation efficiency.

In Silico Optimization of Charge Separating Dyes

The results presented in the sections above of this systematic *in silico* investigation of effect of TPA vs. DPA donors, increasing the bridge length and decoupling the fragments can be used to guide the optimization of these fluorene/PMI based charge separating dyes. As the TPA resulted in more positive charge accumulation on the donor part than for the DPA, the TPA was chosen as the donor. Two fluorene molecules were chosen as bridge, as suggested by the results on optimal fluorene chain length. To decouple the different components and suppress the hole back transfer, these two fluorenes were equipped with methyl groups to keep the dihedral angles between all fragments of the molecular system close to 90 degrees, decoupling them and refining the different orbitals, keeping them localized. The resulting net charge evolution over time on the PMI averaged over 10 CTD trajectories is shown in figure 6.10.

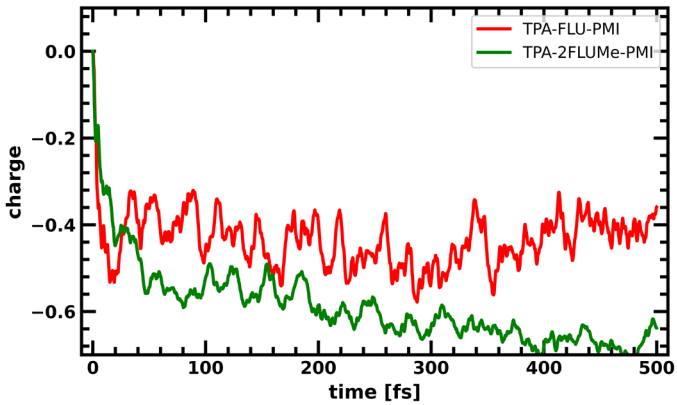

Figure 6.10. Average charge accumulation averaged over 10 CTDs on the PMI in the TPA-FLU-PMI (red) and the optimized TPA-2FLUMe-PMI (green) dye.

The combination of all of the modular optimizations of the different components of the dye (TPA donor, 2 fluorenes, decoupling through methyl groups) has led to a significantly enhanced charge separation. While the original TPA-FLU-PMI dye equilibrates to a charge of about -0.44 for the PMI, in the optimized TPA-2FLUMe-PMI dye, equilibrium was not yet reached yet after 500 fs, with the average charge on the PMI at -0.66 with a further negative tendency. Overall, combining the different strategies tested before, resulted in a dye optimized in silico that shows an impressive increase of charge accumulation by about 50% relative to the TPA-FLU-PMI.

6.4 Conclusion

Systematic investigations of phenylamine-fluorene-PMI based charge separating dyes were done on a semi-empirical quantum classical level to estimate the charge separation efficiency in this family of push-pull dyes. We find that exchanging the electron withdrawing character of the COOH substituent on the TPA by introducing an electron donating methylene group between the phenyl and carboxylic acid groups, the increased HOMO energy level and its localization on the donor side leads

to a more efficient charge separating dye with lower recombination rates, as confirmed by experiment. We also find that TPA donors lead to a more polarized charge transfer state than for their DPA relatives and should therefore be preferred. An increased bridge length between donor and acceptor from one fluorene fragment to two, leads to a better charge separation, however this effect decreases when expanding this to three fluorene fragments. Additionally, fluorene-based transitions shift towards the visible range, becoming more competitive with the desired PMI based excitation. Decoupling of the different components in the dyes by sterically demanding methyl groups is an effective way of decreasing back transfer and therefore decreasing the chance of recombination. This is most effective when used on the fluorene. The insight gained from these investigations were then used to propose an *in silico* optimized charge separating dye using a TPA donor, a bridge of two methylated fluorenes and a PMI acceptor. This dye showed remarkable enhancement in charge separation efficiency, with an increase of negative charge by about 50% on the PMI in comparison to the original TPA-FLU-PMI dye. The results gained from this *in silico* investigation and optimization of charge separating dyes should help in guiding experimental work on improving these molecules, to lower charge recombination and increase device efficiency.

6.5 References

(1) Yu, Z.; Li, F.; Sun, L. Recent Advances in Dye-Sensitized Photoelectrochemical Cells for Solar Hydrogen Production Based on Molecular Components. *Energy Environ. Sci.* **2015**, *8* (3), 760–775. https://doi.org/10.1039/C4EE03565H.

(2) Shao, Y.; de Ruiter, J. M.; de Groot, H. J. M.; Buda, F. Photocatalytic Water Splitting Cycle in a Dye-Catalyst Supramolecular Complex: Ab Initio Molecular Dynamics Simulations. *J. Phys. Chem. C* **2019**, *123* (35), 21403–21414. https://doi.org/10.1021/acs.jpcc.9b06401.

(3) Monti, A.; de Ruiter, J. M.; de Groot, H. J. M.; Buda, F. A Dynamic View of Proton-Coupled Electron Transfer in Photocatalytic Water Splitting. *J. Phys. Chem. C* **2016**, *120* (40), 23074–23082. https://doi.org/10.1021/acs.jpcc.6b08244.

(4) Bell, T. D. M.; Pagba, C.; Myahkostupov, M.; Hofkens, J.; Piotrowiak, P. Inhomogeneity of Electron Injection Rates in Dye-Sensitized TiO2: Comparison of the Mesoporous Film and Single Nanoparticle Behavior. *J. Phys. Chem. B* **2006**, *110* (50), 25314–25321. https://doi.org/10.1021/jp064005f.

(5) Duan, L.; Bozoglian, F.; Mandal, S.; Stewart, B.; Privalov, T.; Llobet, A.; Sun, L. A Molecular Ruthenium Catalyst with Water-Oxidation Activity Comparable to That of Photosystem II. *Nature Chem.* **2012**, *4* (5), 418–423. https://doi.org/10.1038/nchem.1301.

(6) Wang, L.; Duan, L.; Wang, Y.; Ahlquist, M. S. G.; Sun, L. Highly Efficient and Robust Molecular Water Oxidation Catalysts Based on Ruthenium Complexes. *Chem. Commun.* **2014**, *50* (85), 12947–12950. https://doi.org/10.1039/C4CC05069J.

(7) Duan, L.; Wang, L.; Li, F.; Li, F.; Sun, L. Highly Efficient Bioinspired Molecular Ru Water Oxidation Catalysts with Negatively Charged Backbone Ligands. *Acc. Chem. Res.* **2015**, *48* (7), 2084–2096. https://doi.org/10.1021/acs.accounts.5b00149.

(8) Zhang, B.; Sun, L. Artificial Photosynthesis: Opportunities and Challenges of Molecular Catalysts. *Chemical Society Reviews* **2019**, *48* (7), 2216–2264. https://doi.org/10.1039/C8CS00897C.

(9) Yang, J.; Wang, L.; Zhan, S.; Zou, H.; Chen, H.; Ahlquist, M. S. G.; Duan, L.; Sun, L. From Ru-Bda to Ru-Bds: A Step Forward to Highly Efficient Molecular Water Oxidation Electrocatalysts under Acidic and Neutral Conditions. *Nat Commun* **2021**, *12* (1), 373. https://doi.org/10.1038/s41467-020-20637-8.

(10) Rochaix, J.-D. Regulation of Photosynthetic Electron Transport. *Biochimica et Biophysica Acta (BBA) - Bioenergetics* **2011**, *1807* (3), 375–383. https://doi.org/10.1016/j.bbabio.2010.11.010.

(11) Aviram, A.; Ratner, M. A. Molecular Rectifiers. *Chemical Physics Letters* **1974**, *29* (2), 277–283. https://doi.org/10.1016/0009-2614(74)85031-1.

(12) Bera, A.; Pal, A. J. Molecular Rectifiers Based on Donor/Acceptor Assemblies: Effect of Orientation of the Components' Magnetic Moments. *Nanoscale* **2013**, *5* (14), 6518–6524. https://doi.org/10.1039/C3NR00493G.

(13) Ding, W.; Negre, C. F. A.; Vogt, L.; Batista, V. S. Single Molecule Rectification Induced by the Asymmetry of a Single Frontier Orbital. *J. Chem. Theory Comput.* **2014**, *10* (8), 3393–3400. https://doi.org/10.1021/ct5004687.

(14) Van Dyck, C.; Ratner, M. A. Molecular Rectifiers: A New Design Based on Asymmetric Anchoring Moieties. *Nano Lett.* **2015**, *15* (3), 1577–1584. https://doi.org/10.1021/nl504091v.

(15) Koepf, M.; Koenigsmann, C.; Ding, W.; Batra, A.; Negre, C. F. A.; Venkataraman, L.; Brudvig, G. W.; Batista, V. S.; Schmuttenmaer, C. A.; Crabtree, R. H. Controlling the Rectification Properties of Molecular Junctions through Molecule–Electrode Coupling. *Nanoscale* **2016**, *8* (36), 16357–16362. https://doi.org/10.1039/C6NR04830G.

(16) Ding, W.; Koepf, M.; Koenigsmann, C.; Batra, A.; Venkataraman, L.; Negre, C. F. A.; Brudvig, G. W.; Crabtree, R. H.; Schmuttenmaer, C. A.; Batista, V. S. Computational Design of Intrinsic Molecular Rectifiers Based on Asymmetric Functionalization of N-Phenylbenzamide. *J Chem Theory Comput* **2015**, *11* (12), 5888–5896. https://doi.org/10.1021/acs.jctc.5b00823.

(17) Liu, Z.; Xiong, D.; Xu, X.; Arooj, Q.; Wang, H.; Yin, L.; Li, W.; Wu, H.; Zhao, Z.; Chen, W.; Wang, M.; Wang, F.; Cheng, Y.-B.; He, H. Modulated Charge Injection in P-Type Dye-Sensitized Solar Cells Using Fluorene-Based Light Absorbers. *ACS Appl. Mater. Interfaces* **2014**, *6* (5), 3448–3454. https://doi.org/10.1021/am405610b.

(18) Liu, Z.; Li, W.; Topa, S.; Xu, X.; Zeng, X.; Zhao, Z.; Wang, M.; Chen, W.; Wang, F.; Cheng, Y.-B.; He, H. Fine Tuning of Fluorene-Based Dye Structures for High-Efficiency p-Type Dye-Sensitized Solar Cells. *ACS Appl. Mater. Interfaces* **2014**, *6* (13), 10614–10622. https://doi.org/10.1021/am5022396.

(19) Nattestad, A.; Mozer, A. J.; Fischer, M. K. R.; Cheng, Y.-B.; Mishra, A.; Bäuerle, P.; Bach, U. Highly Efficient Photocathodes for Dye-Sensitized Tandem Solar Cells. *Nature Mater* **2010**, *9* (1), 31–35. https://doi.org/10.1038/nmat2588.

(20) Rémond, M.; Hwang, J.; Kim, J.; Kim, S.; Kim, D.; Bucher, C.; Bretonnière, Y.; Andraud, C.; Kim, E. Push–Pull Dyes for Yellow to NIR Emitting Electrochemical Cells. *Advanced Functional Materials* **2020**, *30* (50), 2004831. https://doi.org/10.1002/adfm.202004831.

(21) Kundu, R.; Kulshreshtha, C. Design, Synthesis and Electronic Properties of Push–Pull–Push Type Dye. *RSC Adv.* **2015**, *5* (94), 77460–77468. https://doi.org/10.1039/C5RA13416A.

(22) Velusamy, M.; Justin Thomas, K. R.; Lin, J. T.; Hsu, Y.-C.; Ho, K.-C. Organic Dyes Incorporating Low-Band-Gap Chromophores for Dye-Sensitized Solar Cells. *Org. Lett.* **2005**, *7* (10), 1899–1902. https://doi.org/10.1021/ol050417f.

(23) Ren, S.; Zeng, D.; Zhong, H.; Wang, Y.; Qian, S.; Fang, Q. Star-Shaped Donor-π-Acceptor Conjugated Oligomers with 1,3,5-Triazine Cores: Convergent Synthesis and Multifunctional Properties. *J. Phys. Chem. B* **2010**, *114* (32), 10374–10383. https://doi.org/10.1021/jp104710y.

(24) Zhang, M.; Wang, Y.; Xu, M.; Ma, W.; Li, R.; Wang, P. Design of High-Efficiency Organic Dyes for Titania Solar Cells Based on the Chromophoric Core of Cyclopentadithiophene-Benzothiadiazole. *Energy Environ. Sci.* **2013**, *6* (10), 2944–2949. https://doi.org/10.1039/C3EE42331J.

(25) Chen, J.; Sheng, Y.; Ko, S.; Liu, L.; Han, H.; Li, X. Push–Pull Porphyrins with Different Anchoring Group Orientations for Fully Printable Monolithic Dye-Sensitized Solar Cells with Mesoscopic Carbon Counter Electrodes. *New J. Chem.* **2015**, *39* (7), 5231–5239. https://doi.org/10.1039/C5NJ00569H.

(26) Kaeffer, N.; Windle, C. D.; Brisse, R.; Gablin, C.; Leonard, D.; Jousselme, B.; Chavarot-Kerlidou, M.; Artero, V. Insights into the Mechanism and Aging of a Noble-Metal Free H2-Evolving Dye-Sensitized Photocathode. *Chem. Sci.* **2018**, *9* (32), 6721–6738. https://doi.org/10.1039/C8SC00899J.

(27) Brisse, R.; Praveen, C.; Maffeis, V.; Bourgeteau, T.; Tondelier, D.; Berthelot, T.; Geffroy, B.; Gustavsson, T.; Raimundo, J. M.; Jousselme, B. A Red to Blue Series of Push–Pull Dyes for NiO Based p-DSSCs. *Sustainable Energy Fuels* **2018**, *2* (3), 648–654. https://doi.org/10.1039/C7SE00474E.

(28) Massin, J.; Bräutigam, M.; Bold, S.; Wächtler, M.; Pavone, M.; Muñoz-García, A. B.; Dietzek, B.; Artero, V.; Chavarot-Kerlidou, M. Investigating Light-Driven Hole Injection and Hydrogen Evolution Catalysis at Dye-Sensitized NiO Photocathodes: A Combined Experimental–Theoretical Study. *J. Phys. Chem. C* **2019**, *123* (28), 17176–17184. https://doi.org/10.1021/acs.jpcc.9b04715.

(29) Powar, S.; Daeneke, T.; Ma, M. T.; Fu, D.; Duffy, N. W.; Götz, G.; Weidelener, M.; Mishra, A.; Bäuerle, P.; Spiccia, L.; Bach, U. Highly Efficient P-Type Dye-Sensitized Solar Cells Based on Tris(1,2-Diaminoethane)Cobalt(II)/(III) Electrolytes. *Angewandte Chemie* **2013**, *125* (2), 630–633. https://doi.org/10.1002/ange.201206219.

(30) Weidelener, M.; Mishra, A.; Nattestad, A.; Powar, S.; J. Mozer, A.; Mena-Osteritz, E.; Cheng, Y.-B.; Bach, U.; Bäuerle, P. Synthesis and Characterization of Perylene–Bithiophene–Triphenylamine Triads: Studies on the Effect of Alkyl-Substitution in p-Type NiO Based Photocathodes. *Journal of Materials Chemistry* **2012**, *22* (15), 7366–7379. https://doi.org/10.1039/C2JM16847B.

(31) Bai, Y.; Zhang, J.; Zhou, D.; Wang, Y.; Zhang, M.; Wang, P. Engineering Organic Sensitizers for Iodine-Free Dye-Sensitized Solar Cells: Red-Shifted Current Response Concomitant with

Attenuated Charge Recombination. *J. Am. Chem. Soc.* **2011**, *133* (30), 11442–11445. https://doi.org/10.1021/ja203708k.

(32) Gao, P.; Kim, Y. J.; Yum, J.-H.; Holcombe, T. W.; Nazeeruddin, M. K.; Grätzel, M. Facile Synthesis of a Bulky BPTPA Donor Group Suitable for Cobalt Electrolyte Based Dye Sensitized Solar Cells. *J. Mater. Chem. A* **2013**, *1* (18), 5535–5544. https://doi.org/10.1039/C3TA10632B.

(33) Mathew, S.; Yella, A.; Gao, P.; Humphry-Baker, R.; Curchod, B. F. E.; Ashari-Astani, N.; Tavernelli, I.; Rothlisberger, U.; Nazeeruddin, M. K.; Grätzel, M. Dye-Sensitized Solar Cells with 13% Efficiency Achieved through the Molecular Engineering of Porphyrin Sensitizers. *Nature Chem* **2014**, *6* (3), 242–247. https://doi.org/10.1038/nchem.1861.

(34) Choi, H.; Baik, C.; Kang, S. O.; Ko, J.; Kang, M.-S.; Nazeeruddin, M. K.; Grätzel, M. Highly Efficient and Thermally Stable Organic Sensitizers for Solvent-Free Dye-Sensitized Solar Cells. *Angewandte Chemie International Edition* **2008**, *47* (2), 327–330. https://doi.org/10.1002/anie.200703852.

(35) Tang, Y.; Wang, Y.; Li, X.; Ågren, H.; Zhu, W.-H.; Xie, Y. Porphyrins Containing a Triphenylamine Donor and up to Eight Alkoxy Chains for Dye-Sensitized Solar Cells: A High Efficiency of 10.9%. *ACS Appl. Mater. Interfaces* **2015**, *7* (50), 27976–27985. https://doi.org/10.1021/acsami.5b10624.

(36) Grimme, S.; Bannwarth, C.; Shushkov, P. A Robust and Accurate Tight-Binding Quantum Chemical Method for Structures, Vibrational Frequencies, and Noncovalent Interactions of Large Molecular Systems Parametrized for All Spd-Block Elements (Z = 1–86). *J. Chem. Theory Comput.* **2017**, *13* (5), 1989–2009. https://doi.org/10.1021/acs.jctc.7b00118.

(37) Rego, L. G. C.; Batista, V. S. Quantum Dynamics Simulations of Interfacial Electron Transfer in Sensitized TiO_2 Semiconductors. *J. Am. Chem. Soc.* **2003**, *125* (26), 7989–7997. https://doi.org/10.1021/ja0346330.

(38) da Silva, R.; Hoff, D. A.; Rego, L. G. C. Coupled Quantum-Classical Method for Long Range Charge Transfer: Relevance of the Nuclear Motion to the Quantum Electron Dynamics. *J. Phys.: Condens. Matter* **2015**, *27* (13), 134206. https://doi.org/10.1088/0953-8984/27/13/134206.

(39) Dohm, S.; Bursch, M.; Hansen, A.; Grimme, S. Semiautomated Transition State Localization for Organometallic Complexes with Semiempirical Quantum Chemical Methods. *J. Chem. Theory Comput.* **2020**, *16* (3), 2002–2012. https://doi.org/10.1021/acs.jctc.9b01266.

(40) Bursch, M.; Hansen, A.; Grimme, S. Fast and Reasonable Geometry Optimization of Lanthanoid Complexes with an Extended Tight Binding Quantum Chemical Method. *Inorg. Chem.* **2017**, *56* (20), 12485–12491. https://doi.org/10.1021/acs.inorgchem.7b01950.

(41) Bursch, M.; Neugebauer, H.; Grimme, S. Structure Optimisation of Large Transition-Metal Complexes with Extended Tight-Binding Methods. *Angew. Chem., Int. Ed.* **2019**, *58* (32), 11078–11087. https://doi.org/10.1002/anie.201904021.

(42) Bannwarth, C.; Caldeweyher, E.; Ehlert, S.; Hansen, A.; Pracht, P.; Seibert, J.; Spicher, S.; Grimme, S. Extended Tight-Binding Quantum Chemistry Methods. *WIREs Computational Molecular Science n/a* (n/a), e01493. https://doi.org/10.1002/wcms.1493.

(43) Menzel, J. P.; Kloppenburg, M.; Belić, J.; Groot, H. J. M. de; Visscher, L.; Buda, F. Efficient Workflow for the Investigation of the Catalytic Cycle of Water Oxidation Catalysts: Combining GFN-XTB and Density Functional Theory. *Journal of Computational Chemistry* **2021**, *42* (26), 1885–1894. https://doi.org/10.1002/jcc.26721.

(44) Bakker, T. M. A.; Menzel, J. P.; Vreugdenhil, B.; Bouwens, T.; Mathew, S.; Buda, F.; Reek, J. N. H. Increased Photocurrent by Improving the Donating Properties of the Anchoring Group in P-Type Dye Sensitized Solar Cells. *to be submitted*.

(45) Hoff, D. A.; da Silva, R.; Rego, L. G. C. Coupled Electron–Hole Quantum Dynamics on D–π–A Dye-Sensitized TiO_2 Semiconductors. *J. Phys. Chem. C* **2012**, *116* (40), 21169–21178. https://doi.org/10.1021/jp303647x.

(46) Velde, G. te; Bickelhaupt, F. M.; Baerends, E. J.; Fonseca Guerra, C.; van Gisbergen, S. J. A.; Snijders, J. G.; Ziegler, T. Chemistry with ADF. *J. Comput. Chem.* **2001**, *22* (9), 931–967.

(47) ADF 2020.3, SCM, Theoretical Chemistry, Vrije Universiteit, Amsterdam, The Netherlands, http://www.scm.com. .
(48) AMS2020.3, SCM, Theoretical Chemistry, Vrije Universiteit, Amsterdam, The Netherlands, http://www.scm.com. .
(49) AMS DFTB 2020.3, SCM, Theoretical Chemistry, Vrije Universiteit, Amsterdam, The Netherlands, http://www.scm.com. .
(50) Berendsen, H. J. C.; Postma, J. P. M.; van Gunsteren, W. F.; DiNola, A.; Haak, J. R. Molecular Dynamics with Coupling to an External Bath. *J. Chem. Phys.* **1984**, *81* (8), 3684–3690. https://doi.org/10.1063/1.448118.
(51) Becke, A. D. A New Mixing of Hartree–Fock and Local Density-functional Theories. *J. Chem. Phys.* **1993**, *98* (2), 1372–1377. https://doi.org/10.1063/1.464304.
(52) Lee, C.; Yang, W.; Parr, R. G. Development of the Colle-Salvetti Correlation-Energy Formula into a Functional of the Electron Density. *Phys. Rev. B* **1988**, *37* (2), 785–789.
(53) Van Lenthe, E.; Baerends, E. J. Optimized Slater-Type Basis Sets for the Elements 1–118. *J. Comput. Chem.* **2003**, *24*, 1142–1156.
(54) Grimme, S.; Ehrlich, S.; Goerigk, L. Effect of the Damping Function in Dispersion Corrected Density Functional Theory. *J. Comput. Chem.* **2011**, *32* (7), 1456–1465. https://doi.org/10.1002/jcc.21759.
(55) Sakai, N.; Mareda, J.; Vauthey, E.; Matile, S. Core-Substituted Naphthalenediimides. *Chem. Commun.* **2010**, *46* (24), 4225–4237.
(56) Ooyama, Y.; Yamaji, K.; Ohshita, J. Photovoltaic Performances of Type-II Dye-Sensitized Solar Cells Based on Catechol Dye Sensitizers: Retardation of Back-Electron Transfer by PET (Photo-Induced Electron Transfer). *Mater. Chem. Front.* **2017**, *1* (11), 2243–2255. https://doi.org/10.1039/C7QM00211D.
(57) Monti, A.; Negre, C. F. A.; Batista, V. S.; Rego, L. G. C.; de Groot, H. J. M.; Buda, F. Crucial Role of Nuclear Dynamics for Electron Injection in a Dye–Semiconductor Complex. *J. Phys. Chem. Lett.* **2015**, *6* (12), 2393–2398.
(58) Yanai, T.; Tew, D. P.; Handy, N. C. A New Hybrid Exchange–Correlation Functional Using the Coulomb-Attenuating Method (CAM-B3LYP). *Chem. Phys. Lett.* **2004**, *393* (1), 51–57. https://doi.org/10.1016/j.cplett.2004.06.011.
(59) Akinaga, Y.; Ten-no, S. Range-Separation by the Yukawa Potential in Long-Range Corrected Density Functional Theory with Gaussian-Type Basis Functions. *Chem. Phys. Lett.* **2008**, *462* (4), 348–351. https://doi.org/10.1016/j.cplett.2008.07.103.
(60) Seth, M.; Ziegler, T. Range-Separated Exchange Functionals with Slater-Type Functions. *J. Chem. Theory Comput.* **2012**, *8* (3), 901–907. https://doi.org/10.1021/ct300006h.

6.A Appendix

6A.1 Geometry Comparison between GFN-xTB and B3LYP

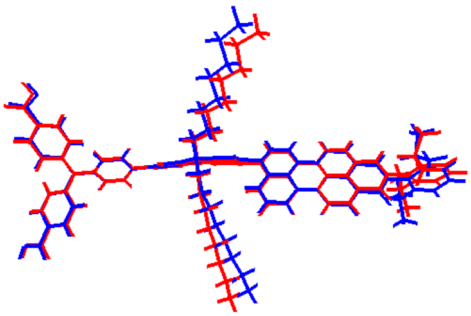

Figure 6A.1 Comparison of the GFN-xTB optimized geometry (red) with the B3LYP optimized geometry (blue) for the TPA-FLU-PMI dye.

6A.2 Optimization of Extended Hückel Parameters

Table 6A.1: *Experimental redox potentials vs. NHE and vacuum from CV measurements, onset of absorbtion peak in UV-VIS and estimated reduction potential for the four fragment molecules and two push-pull dyes*

Molecule	**Oxidation Potential [V] (CV)**	**Reduction Potential [V] (CV)**	**UV-VIS absorbtion onset [nm]/(eV)**	**Red. Pot. estimate (Ox. Pot - UV-VIS onset) [V]**
TPA	1.20	-	380 nm (3.26 eV)	-2.06
EDG-TPA	0.90	-	350 nm (3.54 eV)	-2.64
Fluorene	1.70	-	315 nm (3.94 eV)	-2.55
PMI	1.35	-1.02	-	-
TPA-FLU-PMI	1.05	-1.00	-	-
EDG-TPA-FLU-PMI	0.85	-1.00	-	-

Since the relative alignment of these energies is important, first the PMI was optimized to provide a realistic estimate of the HOMO-LUMO gap. The energies obtained with these optimized parameters (HOMO: -11.80 eV, LUMO: -9.43 eV) had a total shift of 6.01 eV in comparison to the targeted orbital energies, so all target energies were shifted by this 6.01 eV. All other molecules were then optimized to give the same energetic alignment as the experimental values using this 6.01 eV shift. The TPA-FLU-PMI and EDG-TPA-FLU-PMI dyes were not reoptimized, but the parameters for the molecular fragments were used. The agreement with the target values derived from experiment were very good with deviations in the range 0.02 – 0.05 eV.

Table 6A.2: *HOMO and LUMO energies for TPA, EDG-TPA, Fluorene, PMI, TPA-FLU-PMI and EDG-TPA-FLU-PMI obtained with standard Hückel parameters, target values generated with a linear shift of -6.01 eV and obtained with the optimized Hückel parameters.*

Molecule	**Standard Hückel Parameters [eV]**		**Target values [eV]**		**Optimized Hückel parameters [eV]**	
	HOMO	LUMO	HOMO	LUMO	HOMO	LUMO
TPA	-11.56	-9.45	-11.65	-8.39	-11.64	-8.38
EDG-TPA	-11.36	-8.51	-11.35	-7.81	-11.35	-7.80
Fluorene	-12.11	-8.89	-12.15	-8.26	-12.15	-8.25
PMI	-11.74	-10.33	-11.80	-9.43	-11.80	-9.42
TPA-FLU-PMI	-11.47	-10.30	-11.50	-9.45	-11.47	-9.40
EDG-TPA-FLU-PMI	-11.30	-10.30	-11.30	-9.45	-11.32	-9.40

Table 6A.3: *Spatial distribution of HOMO and LUMO for the four fragment molecules, using B3LYP and the Extended Hückel method with optimized parameters.*

Molecule /Method	**HOMO** B3LYP	**HOMO** Extended Hückel	**LUMO** B3LYP	**LUMO** Extended Hückel
TPA	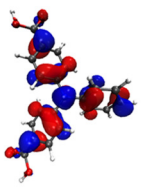	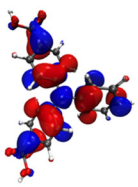	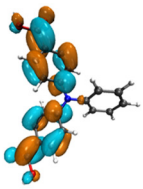	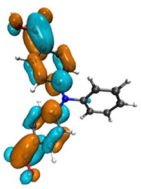
EDG-TPA	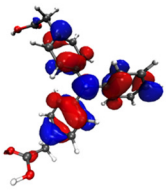	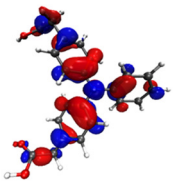	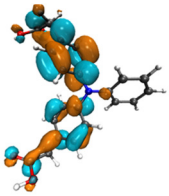	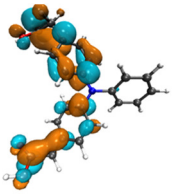
Fluorene	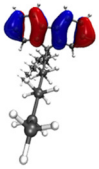	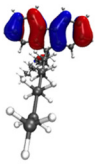	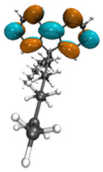	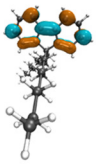
PMI	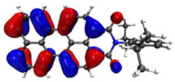	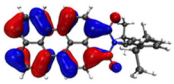	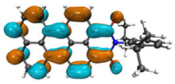	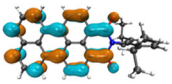

Table 6A.4: *Spatial distribution of HOMO-1, HOMO, LUMO and LUMO+1 for the TPA-FLU-PMI and EDG-TPA-FLU-PMI dyes, using B3LYP and Extended Hückel method with optimized parameters. Note the different LUMO+1 localization between the dyes.*

Molecule	**TPA-FLU-PMI**		**EDG-TPA-FLU-PMI**	
Method	B3LYP	Extended Hückel	B3LYP	Extended Hückel
LUMO+1	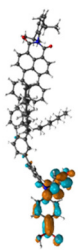	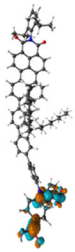	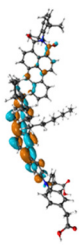	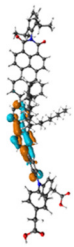
LUMO	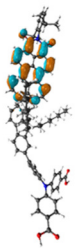	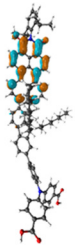	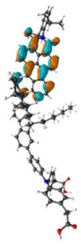	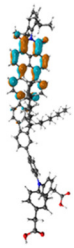
HOMO	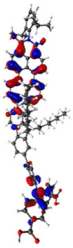	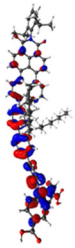	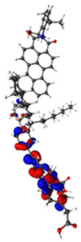	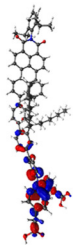
HOMO-1	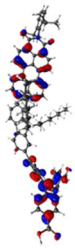	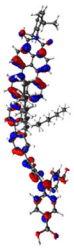	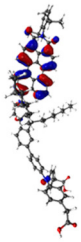	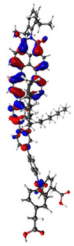

6A.3 Relevant Excitations

Table 6A.5: *TDDFT transitions for the COOH-TPA-FLU-PMI dye, including excitation energy, oscillator strength and transition densities.*

Transition Nr.	Excitation energy [nm]	Oscillator strength	Transition density
1	466 nm	1.117	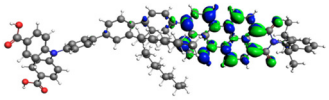
2	352 nm	0.109	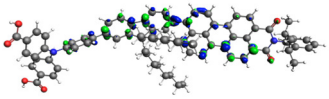
3	330 nm	0.000	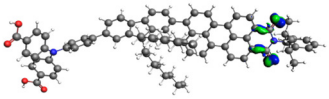
4	329 nm	0.001	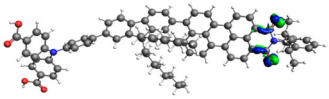
5	327 nm	0.1030	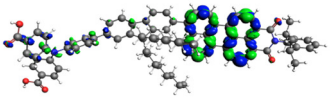

Table 6A.6: *TDDFT transitions for the EDG-TPA-FLU-PMI dye, including excitation energy, oscillator strength and transition densities.*

Transition Nr.	Excitation energy [nm]	Oscillator strength	Transition density
1	464 nm	1.082	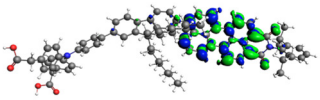
2	379 nm	0.016	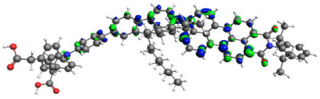
3	331 nm	1.248	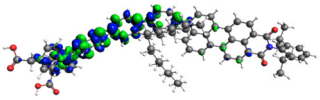
4	329 nm	0.019	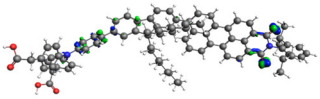
5	328 nm	0.000	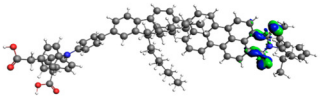

Table 6A.7: *TDDFT transitions for the DPA-FLU-PMI dye, including excitation energy, oscillator strength and transition densities.*

Transition Nr.	Excitation energy [nm]	Oscillator strength	Transition density
1	466 nm	1.090	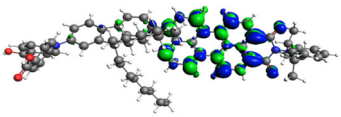
2	365 nm	0.045	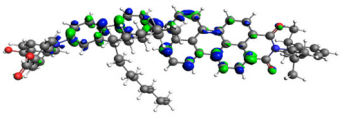
3	333 nm	0.436	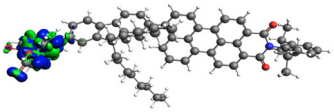
4	330 nm	0.000	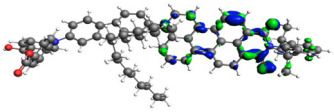
5	330 nm	0.000	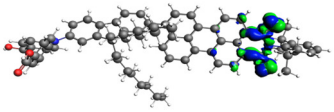

Table 6A.8: *TDDFT transitions for the TPA-2FLU-PMI dye, including excitation energy, oscillator strength and transition densities.*

Transition Nr.	Excitation energy [nm]	Oscillator strength	Transition density
1	470 nm	1.280	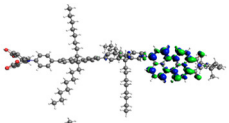
2	359 nm	0.215	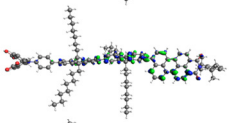
3	332 nm	2.139	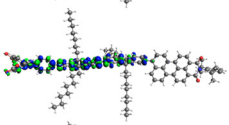
4	330 nm	0.007	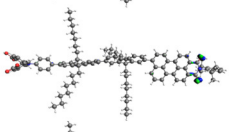
5	329 nm	0.006	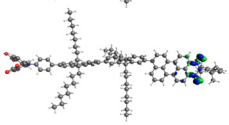

Table 6A.9: *TDDFT transitions for the DPA-2FLU-PMI dye, including excitation energy, oscillator strength and transition densities.*

Transition Nr.	Excitation energy [nm]	Oscillator strength	Transition density
1	470 nm	1.254	
2	356 nm	0.213	
3	331 nm	0.006	
4	330 nm	1.081	
5	329 nm	0.281	

Table 6A.10: *TDDFT transitions for the TPA-3FLU-PMI dye, including excitation energy, oscillator strength and transition densities.*

Transition Nr.	Excitation energy [nm]	Oscillator strength	Transition density
1	469 nm	1.228	
2	356 nm	0.215	
3	335 nm	2.682	
4	330 nm	0.000	
5	329 nm	0.001	

Table 6A.11: *TDDFT transitions for the DPA-3FLU-PMI dye, including excitation energy, oscillator strength and transition densities.*

Transition Nr.	Excitation energy [nm]	Oscillator strength	Transition density
1	468 nm	1.213	
2	354 nm	0.202	
3	336 nm	1.858	
4	330 nm	0.000	
5	327 nm	0.031	

Table 6A.12: *TDDFT transitions for the TPAMe-FLU-PMI dye, including excitation energy, oscillator strength and transition densities.*

Transition Nr.	Excitation energy [nm]	Oscillator strength	Transition density
1	465 nm	1.044	
2	337 nm	0.036	
3	330 nm	0.001	
4	330 nm	0.000	
5	324 nm	0.001	

Table 6A.13: *TDDFT transitions for the TPA-FLUMe-PMI dye, including excitation energy, oscillator strength and transition densities.*

Transition Nr.	Excitation energy [nm]	Oscillator strength	Transition density
1	459 nm	0.914	
2	365 nm	0.000	
3	328 nm	0.000	
4	328 nm	0.000	
5	313 nm	0.000	

Table 6A.14: *TDDFT transitions for the TPA-FLU-PMIMe dye, including excitation energy, oscillator strength and transition densities.*

Transition Nr.	Excitation energy [nm]	Oscillator strength	Transition density
1	477 nm	1.165	
2	353 nm	0.194	
3	330 nm	0.022	
4	329 nm	0.004	
5	328 nm	0.001	

Table 6A.15: *TDDFT transitions for the TPA-2FLUMe-PMI dye, including excitation energy, oscillator strength and transition densities.*

Transition Nr.	Excitation energy [nm]	Oscillator strength	Transition density
1	460 nm	1.038	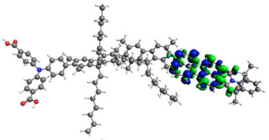
2	369 nm	0.000	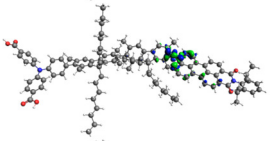
3	329 nm	0.000	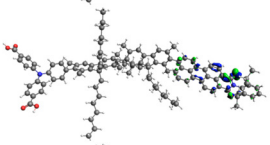
4	328 nm	0.002	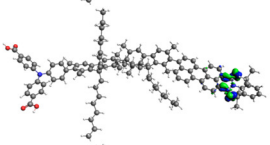
5	327 nm	0.001	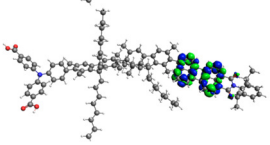

6A.4 Electron and hole migration in the TPA-FLU-PMI dye

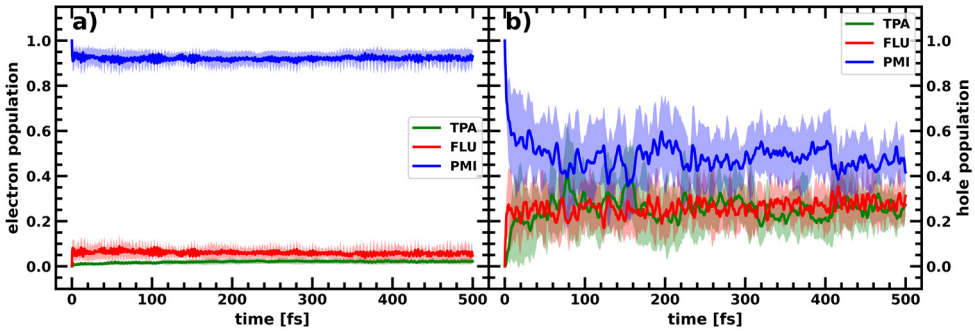

Figure 6A.2. Electron (**a**) and hole (**b**) populations over time on the fragments TPA (green), FLU (red) and PMI (blue) of the TPA-FLU-PMI dye. Only the hole shows significant population transfer.

6A.5 Average charges on fragments of all investigated dyes

Table 6A.16: *Mean charge on the fragments of all investigated dyes, averaged over 10 CTDs and the last 200fs. The TPA-FLU-PMI simulations were performed twice for comparison with EDG-TPA-FLU-PMI and the other molecules, with high quantitative agreement.*

Dye	Charge on Donor	Charge on FLU	Charge on PMI
TPA-FLU-PMI	+0.23/+0.24	+0.20/+0.20	-0.43/-0.44
EDG-TPA-FLU-PMI	+0.30	+0.23	-0.53
DPA-FLU-PMI	+0.20	+0.26	-0.46
TPA-2FLU-PMI	+0.21	+0.33	-0.54
DPA-2FLU-PMI	+0.16	+0.37	-0.53
TPA-3FLU-PMI	+0.13	+0.41	-0.54
DPA-3FLU-PMI	+0.13	+0.43	-0.56
TPAMe-FLU-PMI	+0.28	+0.21	-0.49
TPA-FLUMe-PMI	+0.26	+0.29	-0.55
TPA-FLU-PMIMe	+0.22	+0.22	-0.43
TPA-2FLUMe-PMI	+0.19	+0.47	-0.66

6A.6 Charge accumulation on the Donor: TPA-2FLU-PMI vs DPA-2FLU-PMI

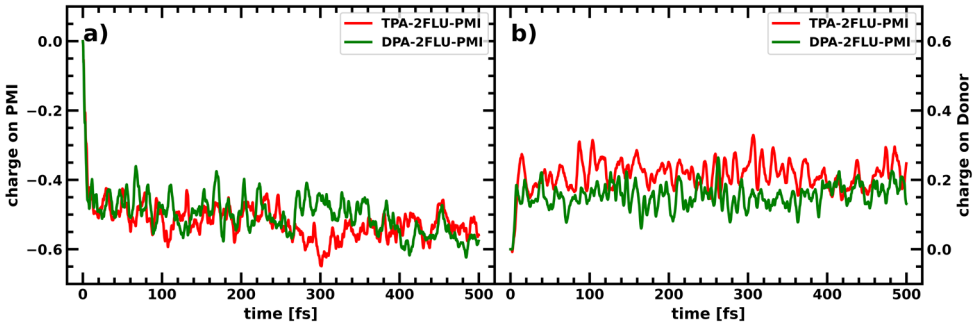

Figure 6.A3. a) Average charge accumulation averaged over 10 CTDs on the PMI in the TPA-2FLU-PMI (red) and DPA-2FLU-PMI (green) dyes upon photoexcitation of the PMI. **b)** Average charge accumulation averaged over 10 CTDs on the donor (TPA/DPA) in the TPA-2FLU-PMI (red) and DPA-2FLU-PMI (green) dyes upon photoexcitation of the PMI.

6A.7 UV-VIS spectra of DPA-XFLU-PMI dyes

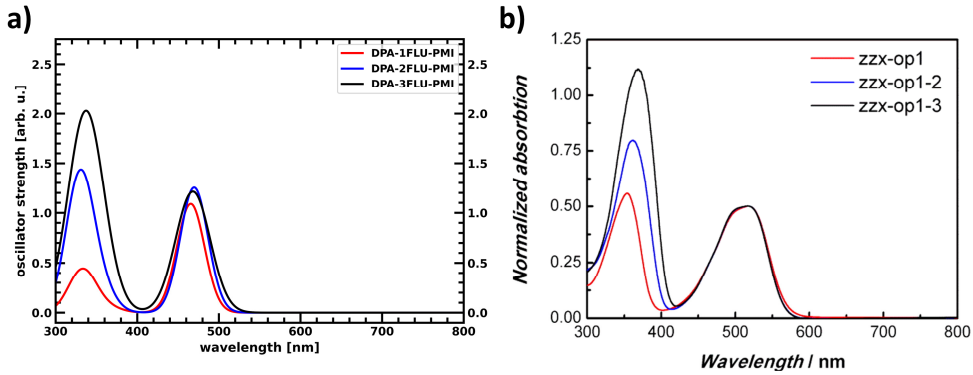

Figure 6.A4. UV-VIS spectra of the charge separating dyes with DPA-xFLU-PMI structure. Note the increasing oscillator strength/absorption of the lower energetic peak with increasing number of fluorenes. **a)** obtained by TDDFT calculations above (tables 6A7, 6A.9 and 6A.11), **b)** experimental UV-VIS spectra with zzx-op1 corresponding to DPA-1FLU-PMI, zzx-op1-2 corresponding to DPA-2FLU-PMI and zzx-op1-3 corresponding to DPA-3FLU-PMI. Adapted with permission from: Liu, Z.; Li, W.; Topa, S.; Xu, X.; Zeng, X.; Zhao, Z.; Wang, M.; Chen, W.; Wang, F.; Cheng, Y.-B.; He, H. Fine Tuning of Fluorene-Based Dye Structures for High-Efficiency p-Type Dye-Sensitized Solar Cells. *ACS Appl. Mater. Interfaces* 2014, *6* (13), 10614–10622 (reference [18]). Copyright 2014 American Chemical Society.

CHAPTER 7

Conclusions and Outlook

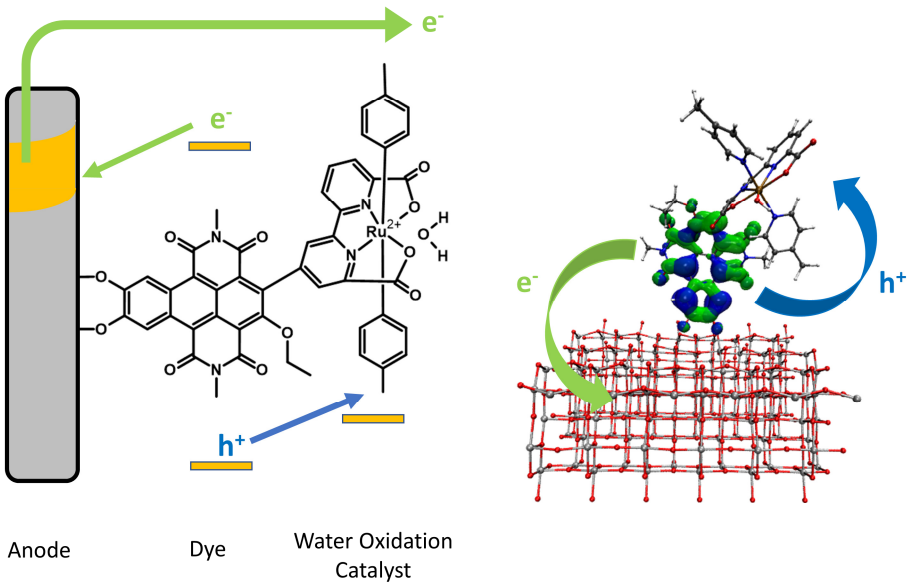

This Chapter is based in part on:

Jan Paul Menzel, Justina Moss, Jelena Belić, Huub J.M. de Groot, Lucas Visscher, Francesco Buda; *in preparation*

7

7.1 Conclusions

Increasing the efficiency of Dye-Sensitized Photoelectrochemical Cells remains a prime objective in solar fuel production.[1] Using computational methods to design and optimize the different components and interfaces in a dye-sensitized photoanode can support and facilitate experimental work in assembling and improving these devices.[2–4] This work aims at moving further towards this goal and several steps have been executed

In **chapter 3**, the fundamental process of photoinduced coherent charge transfer was investigated in a pseudo base pair donor-acceptor molecular complex to understand the requirements for this ultrafast process. Our simulations underline how nuclear modes vibronically couple to the electronic system and drive population exchange from the exciton to the charge transfer state.[5] Through adjusting the frequency of the relevant nuclear vibrations by isotope exchange, we successfully modulated the resonance associated to the coherent charge transfer process and disentangled how nuclear modes are selected. The importance of symmetry is revealed, as we find that coherent charge transfer requires dynamical symmetry breaking to proceed. This suggests that chiral systems should be preferred when trying to take advantage of ultrafast coherent charge transfer. We also find evidence of angular momentum exchange between the (classical) nuclear and (quantum mechanical) electronic subsystems.[6]

Photoinduced electron injection into a TiO_2 semiconductor sensitized by several NDI-based dyes were simulated in **chapter 4**. For these simulations, a computational strategy was developed using a combination of DFTB[7–10] based nuclear dynamics and quantum propagation using the AO/MO propagator and an extended Hückel Hamiltonian.[11–13] We find that nuclear dynamics and trajectory averaging are crucial for a realistic description of the injection process. Furthermore, explicit solvation is important for the correct exploration of conformational space in the nuclear dynamics. Taking these findings into account, the semi-empirical quantum-classical simulation of photoinduced electron injection can be used for qualitative

determination of electron injection capabilities of anchoring groups and potential molecular chromophores.[14]

In **chapter 5**, an efficient approach to calculate Gibbs free energy differences and oxidation potentials in a ruthenium-based water oxidation catalyst has been introduced. In this workflow, GFN-xTB[15] is used for geometry optimizations and frequency analysis, followed by a single point calculation by a higher-level method, such as B3LYP based DFT,[16,17] to determine Gibbs free energies of all catalytic intermediates. The method predicts the experimentally determined catalytic cycle and reaction mechanism and gives Gibbs free energy differences in close agreement with full B3LYP/DFT results, while reducing the computational cost by 2 orders of magnitude. Oxidation potentials determined by this approach also agree very well with experimental results.[18]

To decrease charge recombination losses, push-pull dyes can be used to spatially separate electron and hole.[19–22] A family of such dyes consisting of polyphenylamine donors, fluorene bridges and perylene monoamide acceptors was investigated in **chapter 6**. We performed a systematic investigation on the effects of different molecular designs on the charge separation efficiency. We found that increasing the electron donating character of substituents on the donor increase the charge separation efficiency considerably. While using a TPA vs. DPA anchor does not increase the hole transfer from the acceptor, more hole density localizes at the donor rather than the bridge, leading to a larger polarization of the molecule. Increasing the bridge length by a second additional fluorene moiety leads to a better charge separation in comparison to the molecule with one fluorene, with more hole density residing on the fluorene and donor and less back transfer to the PMI, while a further increase in the number of fluorenes towards 3 does not increase further the performance. Decoupling the different components by breaking conjugation through methyl groups forcing the dihedral angles between the components close to 90 degrees also leads to a better charge separation in comparison to the planar molecule, especially when the fluorene is equipped with methyl groups. An *in silico*

optimization of a nonplanar charge separating dye was then performed, taking advantage of the insight gained by the systematic investigations, resulting in a significant increase of charge separation capability compared to planar systems.

Simulating at an atomistic level the whole photocatalytic water splitting reaction at the photoanode of a DS-PEC device remains a challenging task due to the large size of the system, and the broad range of time scales of the complex processes involved that require different computational approaches. In this work we have made significant progress in simulating a dye sensitized photoanode, including semiconductor, anchor molecule, molecular dye and taking into account the electrolyte environment. With the semiclassical multiscale approach that combines tight binding based nuclear dynamics with quantum propagation of electron and hole, simulations of charge migration in a full photoanode system become viable, while remaining flexible and reliable due to its parametrization on either experimental redox potentials or higher level computational methods.

7.2 Outlook

Charge Transfer in a Photocatalytic Dye-WOC Complex

While we investigated the photoinduced electron injection from an NDI-based dye into a semiconductor electrode in chapter 4 and showed that GFN-xTB is a viable method for geometries and frequencies of a ruthenium based WOC, it would be interesting to combine these two approaches to investigate the hole transfer in a photocatalytic dye-WOC complex upon irradiation. An example of such a photocatalytic molecular complex is given in scheme 7.1.

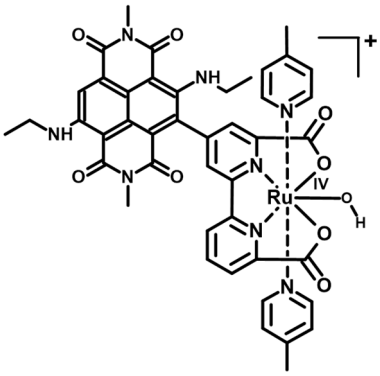

Scheme 7.1. Example of a molecular photocatalytic water splitting complex consisting of the WOC investigated in chapter 5 and an NDI based dye, here with two ethylamino groups, connected via a core carbon to the WOC.

Simulating this hole transfer is quite challenging due to several properties intrinsic to the WOC's catalytic cycle and the chemical environment. First, the HOMO and LUMO energies of the WOC change quite significantly over the course of the catalytic steps, as the WOC oxidizes the water and is itself oxidized by the photoexcited dye. This is sketched in scheme 7.2.

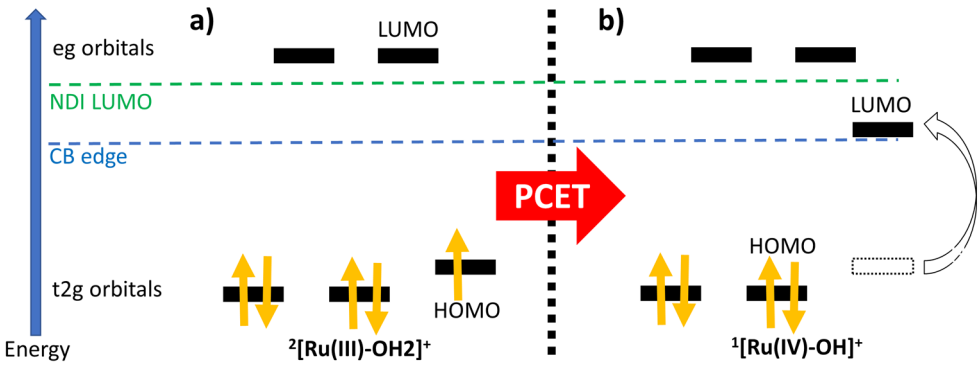

Scheme 7.2. Electron configuration and HOMO/ LUMO energies of the ruthenium based WOC for different catalytic intermediates. The singly occupied HOMO of the ^{2}[Ru(III)-OH$_2$]$^+$ (**a**) has a higher energy and the complex is thus more easily oxidized by a photoexcited dye compared to the catalytic intermediate ^{1}[Ru(IV)-OH]$^+$ (**b**). After the PCET step indeed the third t2g orbital is slightly higher energetically due to the deformed octahedral environment. Additionally, the unoccupied orbital is pushed up in energy as the geometric structure relaxes towards a new minimum with the new electron configuration. The LUMO energy of the ^{1}[Ru(IV)-OH]$^+$ is therefore significantly lower than the LUMO of the ^{2}[Ru(III)-OH$_2$]$^+$, closely above the conduction band edge of TiO_2.

The challenge is that the same molecular dye needs to have enough oxidative power to drive the WOC through its entire cycle. Since here, we use a WOC that reacts via a radical coupling mechanism, only two oxidative states are relevant for photooxidation. However, their respective HOMO and LUMO energies change significantly. The HOMO of the ^{2}[Ru(III)-OH$_2$]$^+$, is unoccupied in the ^{1}[Ru(IV)-OH]$^+$, and is pushed up in energy through geometric rearrangement of the WOC, such that the resulting LUMO of the ^{1}[Ru(IV)-OH]$^+$ is close in energy to the TiO_2 conduction band edge, below the LUMO energies of feasible molecular dyes (see Scheme 7.2). This makes the energetic difference between the two oxidative steps quite large and finding suitable dyes a challenging task. Another problem is the influence of the pH on the oxidation potential. We have simulated hole transfer from the photoexcited dye to the WOC in the ^{1}[Ru(IV)-OH]$^+$ state, since this is the most difficult to oxidize, with the same method as in chapters 4 and 6, using GFN-xTB as a suitable ground state MD method (see chapter 5). Furthermore, since the

^{1}[Ru(IV)-OH]$^+$ is in the singlet state, the simulations can be performed in a restricted manner. The Computational details can be found in the appendix. Figure 7.1 shows the photoinduced hole transfer upon exciting the NDI in the dye-WOC complex of scheme 7.1. As is visible, we are able to follow the hole transfer towards the WOC, suggesting that the dye has enough oxidative power when photoexcited to oxidize the ^{1}[Ru(IV)-OH]$^+$. Including full explicit solvation is an obvious next step, which is in progress.

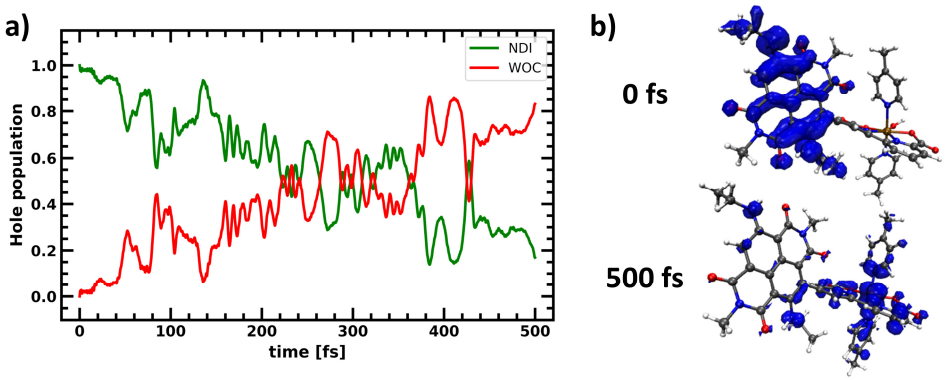

Figure 7.1. a) Hole population on the NDI (green) and WOC (red) over time after photoexcitation of the NDI. **b)** initial and final hole density on the complex.

Since the LUMO of the ^{1}[Ru(IV)-OH]$^+$ is energetically close to the LUMO of the NDI, an important challenge is to prevent back transfer of a photoexcited electron from the dye to the WOC, which would enable regeneration of the ^{2}[Ru(III)-OH$_2$]$^+$. We can follow the transfer of a photoexcited electron from the NDI to the WOC in its ^{1}[Ru(IV)-OH]$^+$ state in our simulations, where electron population is transferred from the photoexcited dye towards the WOC, as shown in (figure 7.2).

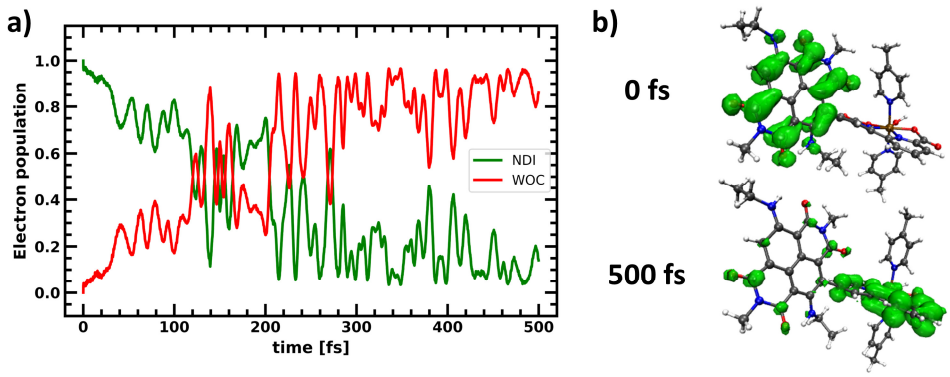

Figure 7.2. a) Electron population on the NDI (green) and WOC (red) over time after photoexcitation of the NDI. **b)** initial and final electron density on the complex.

To prevent such a transfer on short time scales, molecular moieties might be included, as discussed in chapter 6, that allow for hole transfer but inhibit electron transfer, such as a molecular barrier, a charge separating bridge, or a molecular rectifier. The search for a suitable module is one of our currently ongoing investigations. It is however quite promising that photoinduced electron and hole transfer in such challenging systems, including a transition metal complex, can be simulated using this quantum-classical, semi-empirical approach.

Simulating Charge Separation in a Full Photoanode System

The ultimate goal however would be to follow electron and hole transfer in a full photoanode system, including semiconductor electrode, anchoring group, molecular dye, the WOC, potential charge separating dyes or molecular rectifiers and explicit solvent. The combination of GFN-xTB for the nuclear dynamics and the AO/MO quantum propagation of electron and hole potentially allows for the treatment of such extended systems. We have already been successful in performing simulations of photoinduced electron injection and hole transfer for the system shown in figure 7.3: a semiconductor-dye-WOC complex. Here, we chose the cat-NDI dye from chapter 4, since the LUMO lies energetically well within the conduction band of the TiO_2 at a large density of states (figure 4A.3 in the appendix of chapter 4) and the HOMO is

low enough in energy for potential hole transfer to the most demanding catalytic step of the WOC, the ^{1}[Ru(IV)-OH]$^{+}$ (see chapters 4 and 5).

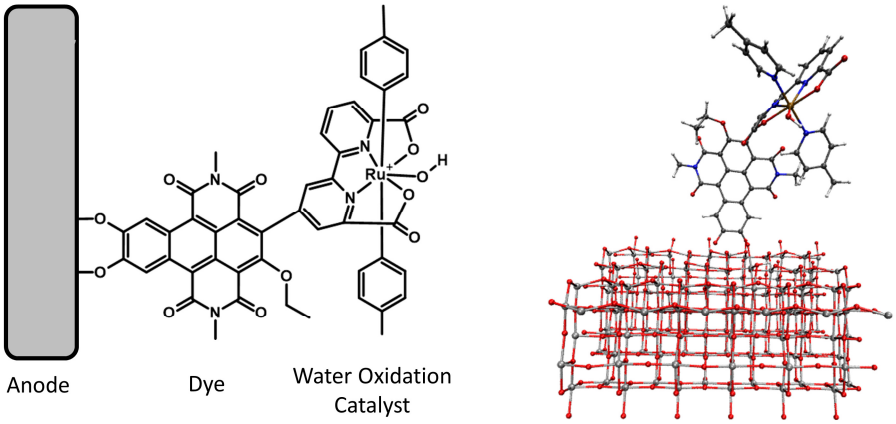

Figure 7.3. Chemical structure and geometry of the TiO_2-Dye-WOC complex investigated.

Moreover, we expect that for this case the effect of including explicit solvation is relatively minor (see chapter 4). However, for a more rigorous description especially of the interaction between WOC and electrolyte, we are currently working on including explicit solvent. The optimized extended Hückel parameters of chapter 4 were used for the cat-NDI dye, with the optimized parameters for the ^{1}[Ru(IV)-OH]$^{+}$ from the previous section.

In figure 7.4, electron and hole populations on the different fragments over time are shown after photoexcitation of the dye. As can be seen, electron injection is quite fast and finished within the first 20 fs. The low lying LUMO of the WOC does not seem to be too problematic, as only a low quantity of electron density is donated to the WOC.

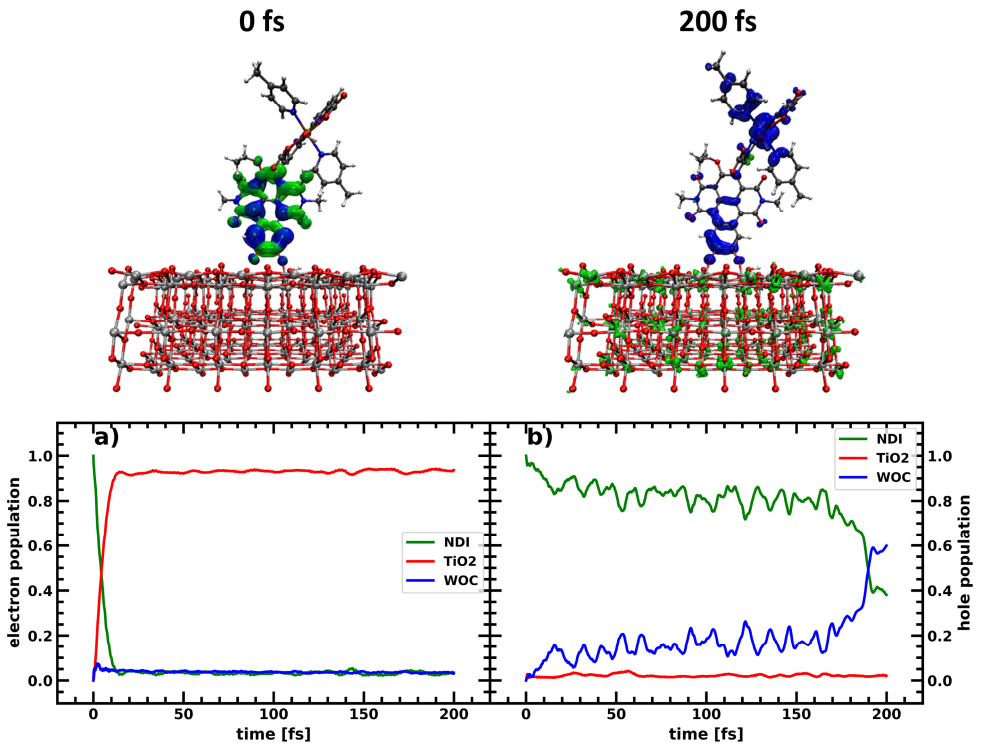

Figure 7.4. a) Electron population on the NDI (green), TiO_2 (red) and WOC (blue) over time after photoexcitation of the NDI. **b)** Hole population on the NDI (green), TiO_2 (red) and WOC (blue) over time after photoexcitation of the NDI. On top the electron (green) and hole (blue) densities at the initial time step and after 200 fs.

Hole transfer takes longer, but after 200 fs, about 50 % of the hole is transferred towards the WOC. While these are only preliminary results, this illustrates the great potential of the semi-empirical, quantum classical approach in simulating photoinduced processes in dye-sensitized photoelectrochemical cells, with an *in silico* treatment of the full photoanode system well within reach.

7.3 References

(1) Yu, Z.; Li, F.; Sun, L. Recent Advances in Dye-Sensitized Photoelectrochemical Cells for Solar Hydrogen Production Based on Molecular Components. *Energy Environ. Sci.* **2015**, *8* (3), 760–775. https://doi.org/10.1039/C4EE03565H.

(2) Pastore, M.; Mosconi, E.; De Angelis, F.; Grätzel, M. A Computational Investigation of Organic Dyes for Dye-Sensitized Solar Cells: Benchmark, Strategies, and Open Issues. *J. Phys. Chem. C* **2010**, *114* (15), 7205–7212. https://doi.org/10.1021/jp100713r.

(3) Ding, W.; Koepf, M.; Koenigsmann, C.; Batra, A.; Venkataraman, L.; Negre, C. F. A.; Brudvig, G. W.; Crabtree, R. H.; Schmuttenmaer, C. A.; Batista, V. S. Computational Design of Intrinsic Molecular Rectifiers Based on Asymmetric Functionalization of N-Phenylbenzamide. *J. Chem. Theory Comput.* **2015**, *11* (12), 5888–5896. https://doi.org/10.1021/acs.jctc.5b00823.

(4) Belić, J.; van Beek, B.; Menzel, J. P.; Buda, F.; Visscher, L. Systematic Computational Design and Optimization of Light Absorbing Dyes. *J. Phys. Chem. A* **2020**, *124* (31), 6380–6388. https://doi.org/10.1021/acs.jpca.0c04506.

(5) Rafiq, S.; Scholes, G. D. From Fundamental Theories to Quantum Coherences in Electron Transfer. *J. Am. Chem. Soc.* **2019**, *141* (2), 708–722. https://doi.org/10.1021/jacs.8b09059.

(6) Menzel, J. P.; de Groot, H. J. M.; Buda, F. Photoinduced Electron Transfer in Donor–Acceptor Complexes: Isotope Effect and Dynamic Symmetry Breaking. *J. Phys. Chem. Lett.* **2019**, *10* (21), 6504–6511. https://doi.org/10.1021/acs.jpclett.9b02408.

(7) Porezag, D.; Frauenheim, Th.; Köhler, Th.; Seifert, G.; Kaschner, R. Construction of Tight-Binding-like Potentials on the Basis of Density-Functional Theory: Application to Carbon. *Phys. Rev. B* **1995**, *51* (19), 12947–12957. https://doi.org/10.1103/PhysRevB.51.12947.

(8) Elstner, M.; Porezag, D.; Jungnickel, G.; Elsner, J.; Haugk, M.; Frauenheim, Th.; Suhai, S.; Seifert, G. Self-Consistent-Charge Density-Functional Tight-Binding Method for Simulations of Complex Materials Properties. *Phys. Rev. B* **1998**, *58* (11), 7260–7268. https://doi.org/10.1103/PhysRevB.58.7260.

(9) Elstner, M.; Frauenheim, T.; Kaxiras, E.; Seifert, G.; Suhai, S. A Self-Consistent Charge Density-Functional Based Tight-Binding Scheme for Large Biomolecules. *Phys. Status Solidi B* **2000**, *217* (1), 357–376. https://doi.org/10.1002/(SICI)1521-3951(200001)217:1<357::AID-PSSB357>3.0.CO;2-J.

(10) Frauenheim, T.; Seifert, G.; Elsterner, M.; Hajnal, Z.; Jungnickel, G.; Porezag, D.; Suhai, S.; Scholz, R. A Self-Consistent Charge Density-Functional Based Tight-Binding Method for Predictive Materials Simulations in Physics, Chemistry and Biology. *physica status solidi (b)* **2000**, *217* (1), 41–62. https://doi.org/10.1002/(SICI)1521-3951(200001)217:1<41::AID-PSSB41>3.0.CO;2-V.

(11) Rego, L. G. C.; Batista, V. S. Quantum Dynamics Simulations of Interfacial Electron Transfer in Sensitized TiO_2 Semiconductors. *J. Am. Chem. Soc.* **2003**, *125* (26), 7989–7997. https://doi.org/10.1021/ja0346330.

(12) Monti, A.; Negre, C. F. A.; Batista, V. S.; Rego, L. G. C.; de Groot, H. J. M.; Buda, F. Crucial Role of Nuclear Dynamics for Electron Injection in a Dye–Semiconductor Complex. *J. Phys. Chem. Lett.* **2015**, *6* (12), 2393–2398.

(13) da Silva, R.; Hoff, D. A.; Rego, L. G. C. Coupled Quantum-Classical Method for Long Range Charge Transfer: Relevance of the Nuclear Motion to the Quantum Electron Dynamics. *J. Phys.: Condens. Matter* **2015**, *27* (13), 134206. https://doi.org/10.1088/0953-8984/27/13/134206.

(14) Menzel, J. P.; Papadopoulos, A.; Belić, J.; de Groot, H. J. M.; Visscher, L.; Buda, F. Photoinduced Electron Injection in a Fully Solvated Dye-Sensitized Photoanode: A Dynamical Semiempirical Study. *J. Phys. Chem. C* **2020**, *124* (51), 27965–27976. https://doi.org/10.1021/acs.jpcc.0c09551.

(15) Grimme, S.; Bannwarth, C.; Shushkov, P. A Robust and Accurate Tight-Binding Quantum Chemical Method for Structures, Vibrational Frequencies, and Noncovalent Interactions of

Large Molecular Systems Parametrized for All Spd-Block Elements (Z = 1–86). *J. Chem. Theory Comput.* **2017**, *13* (5), 1989–2009. https://doi.org/10.1021/acs.jctc.7b00118.

(16) Becke, A. D. A New Mixing of Hartree–Fock and Local Density-functional Theories. *J. Chem. Phys.* **1993**, *98* (2), 1372–1377. https://doi.org/10.1063/1.464304.

(17) Lee, C.; Yang, W.; Parr, R. G. Development of the Colle-Salvetti Correlation-Energy Formula into a Functional of the Electron Density. *Phys. Rev. B* **1988**, *37* (2), 785–789.

(18) Menzel, J. P.; Kloppenburg, M.; Belić, J.; Groot, H. J. M. de; Visscher, L.; Buda, F. Efficient Workflow for the Investigation of the Catalytic Cycle of Water Oxidation Catalysts: Combining GFN-XTB and Density Functional Theory. *Journal of Computational Chemistry* **2021**, *42* (26), 1885–1894. https://doi.org/10.1002/jcc.26721.

(19) Bakker, T. M. A.; Menzel, J. P.; Vreugdenhil, B.; Bouwens, T.; Mathew, S.; Buda, F.; Reek, J. N. H. Increased Photocurrent by Improving the Donating Properties of the Anchoring Group in P-Type Dye Sensitized Solar Cells. *to be submitted*.

(20) Nattestad, A.; Mozer, A. J.; Fischer, M. K. R.; Cheng, Y.-B.; Mishra, A.; Bäuerle, P.; Bach, U. Highly Efficient Photocathodes for Dye-Sensitized Tandem Solar Cells. *Nature Mater* **2010**, *9* (1), 31–35. https://doi.org/10.1038/nmat2588.

(21) Liu, Z.; Xiong, D.; Xu, X.; Arooj, Q.; Wang, H.; Yin, L.; Li, W.; Wu, H.; Zhao, Z.; Chen, W.; Wang, M.; Wang, F.; Cheng, Y.-B.; He, H. Modulated Charge Injection in P-Type Dye-Sensitized Solar Cells Using Fluorene-Based Light Absorbers. *ACS Appl. Mater. Interfaces* **2014**, *6* (5), 3448–3454. https://doi.org/10.1021/am405610b.

(22) Liu, Z.; Li, W.; Topa, S.; Xu, X.; Zeng, X.; Zhao, Z.; Wang, M.; Chen, W.; Wang, F.; Cheng, Y.-B.; He, H. Fine Tuning of Fluorene-Based Dye Structures for High-Efficiency p-Type Dye-Sensitized Solar Cells. *ACS Appl. Mater. Interfaces* **2014**, *6* (13), 10614–10622. https://doi.org/10.1021/am5022396.

7.A Appendix

7A.1 Computational Details

Nuclear trajectories were prepared using GFN-xTB.[1] We have optimized Extended Hückel parameters, similar to chapter 6, on experimental oxidation potentials of the involved NDIs and the WOC in its ^{1}[Ru(IV)-OH]$^+$ state. For the WOC, we use the Nernst equation to shift the oxidation potential vs NHE at pH=0 to a pH value of 7, translated towards absolute potential vs. an electron at rest in vacuum and used this as target HOMO energy of the respective oxidative state. For the LUMO energy, we used Δ SCF derived values given in table 7A.1. The Δ SCF calculations were performed using the B3LYP[2,3] XC-functional with D3 dispersion corrections and BJ-damping[4] and a TZP basis[5]. Relativistic effects were included using ZORA,[6–8] while implicit solvent water was modelled using COSMO.[9] The target values and results obtained with optimized Extended Hückel parameters can be found in table 7A.2.

Table 7A.1: *Experimental Redox potentials vs. NHE and vacuum from CV measurements for the WOC (converted to ph=7 using Nernst equation) and ethylamine NDI dyes, approximated LUMO energy of the WOC with ΔSCF vs NHE and vacuum*

Molecule	**^{1}[Ru(IV)-OH]$^+$**	**2NHEt-NDI**
CV Oxidation Potential vs NHE (vs. vacuum)	pH=1 : 1.25 V (5.69 V)[10] pH=7 : 0.90 V (5.34 V)	0.91 V (5.35 V)[11]
CV Reduction Potential vs NHE (vs vacuum)	-	-0.88 V (3.56 V)[11]
ΔSCF Reduction Potential vs NHE (vs vacuum)	-0.68 V (3.76 V)	-

Table 7A.2: *HOMO and LUMO energies for WOC and NDI: target values generated with a linear shift of -5.95 eV and values obtained with the optimized Hückel parameters.*

Molecule	**Target values [eV]**		**Optimized Hückel parameters [eV]**	
	HOMO	LUMO	HOMO	LUMO
WOC (^{1}[Ru(IV)-OH]$^+$)	-11.29	-9.72	-11.28	-9.72
2NHEt-NDI	-11.30	-9.51	-11.31	-9.52

7A.2 References

(1) Grimme, S.; Bannwarth, C.; Shushkov, P. A Robust and Accurate Tight-Binding Quantum Chemical Method for Structures, Vibrational Frequencies, and Noncovalent Interactions of Large Molecular Systems Parametrized for All Spd-Block Elements (Z = 1–86). *J. Chem. Theory Comput.* **2017**, *13* (5), 1989–2009. https://doi.org/10.1021/acs.jctc.7b00118.

(2) Becke, A. D. A New Mixing of Hartree–Fock and Local Density-functional Theories. *J. Chem. Phys.* **1993**, *98* (2), 1372–1377. https://doi.org/10.1063/1.464304.

(3) Lee, C.; Yang, W.; Parr, R. G. Development of the Colle-Salvetti Correlation-Energy Formula into a Functional of the Electron Density. *Phys. Rev. B* **1988**, *37* (2), 785–789.

(4) Grimme, S.; Antony, J.; Ehrlich, S.; Krieg, H. A Consistent and Accurate Ab Initio Parametrization of Density Functional Dispersion Correction (DFT-D) for the 94 Elements H-Pu. *J. Chem. Phys.* **2010**, *132* (15), 154104. https://doi.org/10.1063/1.3382344.

(5) Van Lenthe, E.; Baerends, E. J. Optimized Slater-Type Basis Sets for the Elements 1–118. *J. Comput. Chem.* **2003**, *24*, 1142–1156.

(6) Lenthe, E. van; Baerends, E. J.; Snijders, J. G. Relativistic Regular Two-component Hamiltonians. *J. Chem. Phys.* **1993**, *99* (6), 4597–4610. https://doi.org/10.1063/1.466059.

(7) van Lenthe, E.; Baerends, E. J.; Snijders, J. G. Relativistic Total Energy Using Regular Approximations. *J. Chem. Phys.* **1994**, *101* (11), 9783–9792. https://doi.org/10.1063/1.467943.

(8) van Lenthe, E.; Ehlers, A.; Baerends, E.-J. Geometry Optimizations in the Zero Order Regular Approximation for Relativistic Effects. *J. Chem. Phys.* **1999**, *110* (18), 8943–8953. https://doi.org/10.1063/1.478813.

(9) Pye, C. C.; Ziegler, T. An Implementation of the Conductor-like Screening Model of Solvation within the Amsterdam Density Functional Package. *Theor. Chem. Acc.* **1999**, *101* (6), 396–408. https://doi.org/10.1007/s002140050457.

(10) Duan, L.; Bozoglian, F.; Mandal, S.; Stewart, B.; Privalov, T.; Llobet, A.; Sun, L. A Molecular Ruthenium Catalyst with Water-Oxidation Activity Comparable to That of Photosystem II. *Nature Chem.* **2012**, *4* (5), 418–423. https://doi.org/10.1038/nchem.1301.

(11) Sakai, N.; Mareda, J.; Vauthey, E.; Matile, S. Core-Substituted Naphthalenediimides. *Chem. Commun.* **2010**, *46* (24), 4225–4237. https://doi.org/10.1039/C0CC00078G.

Summary

Since the advent of the industrial revolution, the rate of technological development, increasing productivity, and population growth has started to reach unprecedented heights. This however has been achieved by exploitation of exhaustible fossil resources, carbon based fuels emitting CO_2 that has been captured through natural photosynthesis hundreds of millions of years ago. Not only are these resources limited, but the increase in CO_2 levels has also been closely linked to climate change, with detrimental effects to the planet's ecosystem and our habitat. Exchanging fossil resources by renewables is crucial for reducing carbon emissions and to mitigate climate change.

Chapter 1 of this work discusses these problems and shines light on how solar energy can be used for carbon-neutral manufacturing of synthetic fuels: natural and artificial photosynthesis are introduced, drawing parallels between them and underlying the common fundamental processes involved. Dye-Sensitized Photoelectrochemical Cells are promising artificial photosynthesis devices for carbon neutral solar fuels production, however, the efficiency of these devices remains too low for upscaling and industrial production at affordable cost. This work is focused on understanding photoinduced processes in DS-PECs and proposing potential components with improved properties through computational investigation.

Due to the different time, spatial and materials dimensions in these complex devices, a wide array of computational tools is used to bridge these multi scale processes. In **Chapter 2** an overview is provided of the theory behind the different computational methods employed, starting from the Born Oppenheimer Approximation. DFT as well as semi-empirical methods are described, with which large scale simulations of DS-PEC components become viable. Furthermore, non-adiabatic molecular dynamics are discussed, including the mean field Ehrenfest dynamics and semi-classical AO-MO propagation, that allow for real time simulations of photoinduced electron transfer processes.

Improving the design of DS-PECs can only be achieved if important fundamental processes are understood. One crucial step in natural as well as artificial photosynthesis is the initial, photoinduced charge transfer step. In nature, there is growing evidence that this ultrafast process involves resonances at the frequencies of specific nuclear vibrations to establish the coherent superposition of excitonic and charge transfer electronic states in the form of vibronic coupling. To understand and disentangle these effects, the coherent charge transfer in a pseudo base model system is investigated in **chapter 3**. It is found that the N-H stretching couples to the electronic motion, driving population transfer from the excitonic to the charge transfer state. Isotope exchange of H by D to shift the frequencies of this mode does not suppress coherent charge transfer, as it leads to a shift in electronic oscillations, allowing different nuclear modes to fulfill resonance condition and couple to the charge transfer process. Furthermore, dynamical symmetry breaking proves crucial for coherent charge transfer. Concerted electronic and nuclear angular motion in the coherent charge transfer process suggests exchange of angular momentum.

In **chapter 4**, the photoinduced electron injection from an NDI based dye into a TiO_2 electrode is simulated including full explicit solvation. To be able to simulate these massive extended systems, a quantum-classical, semi-empirical method is used that combines nuclear trajectory generation by DFTB with an AO-MO quantum propagation of photoexcited electron and hole based on an extended Hückel Hamiltonian. The effects of nuclear motion, conformational and trajectory averaging, as well as explicit solvation are disentangled: the results suggest that nuclear motion and trajectory averaging are absolutely crucial to describe the injection process satisfactorily, while explicit solvation is important for correct sampling of conformational space. Using these findings, NDI based dyes with three different anchoring moieties are evaluated with regards to their electron injection properties, with the NDI attached via a catechol anchor showing the greatest promise.

Chapter 5 deals with the oxidation of water to molecular oxygen and protons through a Ru-based molecular water oxidation catalyst. A thorough computational study on the catalytic cycle, including Gibbs free energies and preferred reaction mechanism, was performed using a variety of functionals and the semi empirical GFN-xTB. While all methods predict the experimentally observed reaction mechanism correctly, the Gibbs free energies remain highly dependent on the employed method. Although B3LYP proved the most reliable, the large computational cost involved limits its applicability. Therefore, an efficient work flow to evaluate Gibbs free energies of the catalytic steps in a water oxidation cycle by combining geometries and frequencies obtained by GFN-xTB with electronic energies by the hybrid functional B3LYP is proposed and validated. This combination shows good agreement with full B3LYP and experimental oxidation potentials, with a decrease of computational time by 2 orders of magnitude. With this speed up, computational screening of oxidation potentials or extended molecular dynamics equilibrations including full explicit solvation become viable.

Chapter 6 discusses the problem of back transfer of separated electron and hole, increasing the likelihood of recombination and therefore lowering the overall efficiency. To tackle this problem, a series of charge separating dyes of the structure D-π-A with a polyphenyl amine as donor, fluorenes as bridging π-systems and a PMI as acceptor, are investigated for an efficient, spatial charge separation that reduces back transfer. It is found that TPA donors lead to larger spatial separation between hole and electron than DPA donors. Increasing the bridge length by introducing one additional fluorene leads to a better charge separation efficiency in comparison with dyes including only one fluorene, while additional fluorenes do not increase the efficiency any further. Furthermore, decoupling of the different components through breaking the conjugation via introduction of methyl groups also results in better hole transfer away from the acceptor in comparison to the planar dye. This is most efficient when decoupling all three components through methyl groups on the fluorene. Finally, the insights from these investigations are used to design *in silico*

an optimized charge separating dye that shows an impressively increased hole transfer in comparison to all other investigated dyes.

Concluding this thesis, **Chapter 7** gives an additional outlook that combines findings and methods from the different chapters to demonstrate that simulating the photoinduced processes *in silico* in an extended photoanode system including electrode, dye and water oxidation catalyst might well be in reach. In conclusion, valuable insight into fundamental photoinduced processes can be gained by computational simulation. *In silico* investigations allow for screening of a large number of potential molecular components and optimization of their properties and interfaces in a DS-PEC, potentially guiding experimental research before tedious synthetic realization.

Samenvatting

Sinds de opkomst van de industriële revolutie is het tempo van technologische ontwikkelingen, toename in productiviteit, en bevolkingsgroei tot ongekende hoogtes gestegen. Dit is echter bereikt door de exploitatie van uitputbare fossiele grondstoffen, ofwel koolstof bevattende brandstoffen die bij verbranding CO_2 uitstoten dat honderden miljoenen jaren geleden is opgeslagen in de grond door natuurlijke fotosynthese. De totale hoeveelheid fossiele brandstoffen is niet alleen eindig, de CO_2 die vrijkomt bij het verbranden ervan is een van de oorzaken van klimaatverandering, wat schadelijke gevolgen heeft voor het ecosysteem van de planeet en onze leefomgeving. Het vervangen van fossiele brandstoffen voor hernieuwbare energiebronnen is cruciaal voor het verminderen van de CO_2 uitstoot en het beperken van klimaatverandering.

Hoofdstuk 1 van dit proefschrift behandelt deze problemen en verschaft inzichten in hoe zonne-energie gebruikt kan worden voor het koolstof-neutraal fabriceren van synthetische brandstoffen: natuurlijke en kunstmatige fotosynthese worden geïntroduceerd waarbij parallellen en overlappende fundamentele processen worden onderschreven. Kleurstof-gebaseerde foto-elektrochemische cellen (DS-PEC's) zijn veelbelovende, kunstmatige fotosynthese apparaten voor het produceren van zonne-brandstoffen zonder uitstoot van koolstof. De efficiëntie van deze apparaten is echter te laag om op te schalen en daarmee een industriële productie te leveren tegen betaalbare kosten. Dit proefschrift is gericht op het begrijpen van deze door licht veroorzaakte processen in DS-PEC's en het aandragen van mogelijke onderdelen met verbeterde eigenschappen op basis van computationeel onderzoek.

Een breed scala aan computationeel gereedschap moet worden toegepast om de verschillende tijds-, ruimte- en materiaaldimensies van deze complexe apparaten te verenigen. In **hoofdstuk 2** wordt een overzicht gegeven van de theorie achter de verschillende toegepaste computationele methodes, te beginnen met de Born-Oppenheimer benadering. DFT wordt beschreven, evenals semi-empirische

methodes waarmee het mogelijk wordt om grootschalige simulaties uit te voeren van onderdelen van een DS-PEC. Verder worden non-adiabatische moleculaire dynamica methoden behandeld, waaronder Ehrenfest dynamica en semi-klassieke AO-MO propagatie waarmee het mogelijk is om door licht veroorzaakte elektronoverdrachtsprocessen te simuleren.

Het ontwerp van een DS-PEC zal alleen verbeterd kunnen worden wanneer men de werking begrijpt van de belangrijke fundamentele processen binnen het apparaat. Een cruciale stap in zowel natuurlijke als kunstmatige fotosynthese is de eerste door licht veroorzaakte ladingsoverdrachtstap. In de natuur zijn er steeds meer aanwijzingen dat bij dit ultrasnelle proces resonanties betrokken zijn met frequenties van specifieke nucleaire vibraties die een coherente superpositie tot stand brengen tussen excitonische en ladingsoverdrachttoestanden in de vorm van vibronische koppeling. Om deze processen te begrijpen en te onderscheiden, is coherente ladingsoverdracht in een pseudo-base modelsysteem onderzocht in **hoofdstuk 3**. Het blijkt dat de N-H rekvibratie koppelt aan de elektronische beweging in het systeem, waardoor populatieoverdracht van de excitonische naar de ladingsoverdrachtstoestand wordt bevorderd. Het aanpassen van deze vibraties, door isotoopuitwisseling van H door D, onderdrukt de coherente ladingsoverdracht echter niet. Het leidt namelijk tot een verandering in elektronische oscillaties, waardoor andere nucleaire vibraties aan de resonantievoorwaarde kunnen voldoen en aan het ladingsoverdrachtsproces kunnen koppelen. Tevens blijkt dat dynamische symmetriebreking cruciaal is voor coherente ladingsoverdracht. De samenvallende elektronische en nucleaire draaibeweging in het coherente ladingsoverdrachtproces suggereert de uitwisseling van impulsmoment tussen deze componenten.

In **hoofdstuk 4** wordt de door licht veroorzaakte elektroneninjectie van een NDI-achtige kleurstof in een TiO_2 elektrode gesimuleerd inclusief expliciete oplosmiddel-moleculen. Om deze systemen van enorme omvang te kunnen simuleren, wordt gebruik gemaakt van een kwantum-klassieke, semi-empirische methode. De nucleaire trajecten worden gegenereerd op basis van DFTB en vervolgens wordt een

AO-MO kwantum methode (gebaseerd op een uitgebreide Hückel Hamiltoniaan) toegepast om het foto-geëxciteerde elektron en elektronengat te simuleren. Drie verschillende effecten worden ontleed, de nucleaire bewegingen, het middelen over verschillende conformaties en trajecten, alsmede het in beschouwing nemen van een expliciet oplosmiddel. De resultaten suggereren dat nucleaire beweging en het middelen van trajecten absoluut cruciaal zijn om het injectieproces adequaat te beschrijven, terwijl expliciete solvatatie belangrijk is voor een statistisch correcte afname van de conformatie-ruimte. Op basis van deze bevindingen worden op NDI-gebaseerde kleurstoffen met drie verschillende verankeringsmoleculen geëvalueerd met betrekking tot hun elektroneninjectie-eigenschappen, waarbij de NDI bevestigd via een catechol verankermolecuul het meest veelbelovend blijkt.

Hoofdstuk 5 behandelt de oxidatie van water tot zuurstofmoleculen en protonen door een op Ru gebaseerde moleculaire water-oxidatiekatalysator. Een grondige computationele studie van de katalytische cyclus, inclusief Gibbs vrije energieën en het geprefereerde reactiemechanisme, werd uitgevoerd met behulp van een verscheidenheid aan functionalen en de semi-empirische GFN-xTB methode. Hoewel alle methoden het experimenteel waargenomen reactiemechanisme correct voorspellen, blijven de Gibbs vrije energieën sterk afhankelijk van de gebruikte methode. Alhoewel B3LYP het meest degelijk bleek, beperkt de hoge rekenkost de toepasbaarheid ervan. Daarom wordt een efficiënte werkwijze voorgesteld en gevalideerd om de Gibbs vrije energieën van de katalytische stappen in een wateroxidatiecyclus te evalueren door de geometrieën en frequenties verkregen met GFN-xTB, te combineren met elektronische energieën die zijn verkregen met de hybride B3LYP functionaal. Deze combinatie toont een goede overeenkomst met zowel de volledige B3LYP berekeningen als experimentele oxidatiepotentiëlen, terwijl de rekentijd verminderd wordt met twee orden van grootte. Met deze tijdswinst wordt het haalbaar om computationeel oxidatiepotentialen te screenen en uitgebreide moleculaire dynamica equilibraties uit te voeren met een volledige beschrijving van het oplosmiddel.

Hoofdstuk 6 beschrijft het probleem waarbij een gescheiden elektron en elektrongat terug-combineren en daarmee het ladingsscheidings rendement verlagen. Om dit probleem aan te pakken wordt een serie lading scheidende kleurstoffen van de structuur D-π-A onderzocht op een efficiënte, ruimtelijke ladingsscheiding die terug overdracht van het elektron vermindert. Het onderzoek beschouwt specifiek een polyfenyl amine als donor, fluorenen als overbruggende π-systemen en een PMI als acceptor. Het blijkt dat TPA donoren leiden tot een grotere ruimtelijke scheiding tussen het elektrongat en het elektron dan DPA donoren. Vergroting van de bruglengte door de introductie van één extra fluoreen leidt tot een betere ladingsscheidingsefficiëntie in vergelijking met kleurstoffen met slechts één fluoreen, terwijl extra fluoreen de efficiëntie niet verder verhoogt. Bovendien leidt ontkoppeling van de verschillende componenten, door het verbreken van de conjugatie via het introduceren van methylgroepen, ook tot een betere verplaatsing van het elektrongat. Dit is het efficiëntst wanneer alle drie de componenten worden ontkoppeld via methylgroepen op het fluoreen. Tenslotte worden de inzichten uit deze onderzoeken gebruikt om, *in silico*, een geoptimaliseerde ladingsscheidende kleurstof te ontwerpen die een indrukwekkende verhoogde elektrongat verplaatsing laat zien in vergelijking met alle andere onderzochte kleurstoffen.

Ter afsluiting van dit proefschrift, geeft **hoofdstuk 7** een vooruitzicht waarin de bevindingen en methoden uit de verschillende hoofdstukken worden gecombineerd om aan te tonen dat het *in silico* simuleren van de door licht veroorzaakte processen in een uitgebreid fotoanode systeem inclusief elektrode, kleurstof en water-oxidatiekatalysator binnen handbereik zou kunnen liggen. Er kan concluderend gesteld worden dat met behulp van computationele simulaties een waardevol inzicht in de fundamentele, door licht veroorzaakte, processen kan worden verkregen. *In silico* onderzoek maakt het mogelijk om een groot aantal potentiële moleculaire componenten te screenen en om hun individuele eigenschappen en verbindingen met elkaar te optimaliseren in een DS-PEC. Dit kan mogelijk als leidraad dienen in experimenteel onderzoek zodat moeizame synthese kan worden voorkomen.

Zusammenfassung

Die Geschwindigkeit der technologischen Entwicklung, Produktivitätssteigerung und des Bevölkerungsanstiegs hat seit Beginn der industriellen Revolution zuvor unerreichbare Werte erzielt. Dieser Anstieg wurde jedoch durch Ausbeutung begrenzter fossiler, vor Jahrmillionen durch natürliche Photosynthese fixierter, kohlenstoffbasierter und Kohlendioxid emittierender Brennstoffe erkauft. Da diese Ressourcen nicht nur begrenzt sind, sondern das durch ihre Verbrennung ansteigende CO_2-Niveau in der Atmosphäre auch eng mit dem Klimawandel verbunden ist - mit katastrophalen Folgen für das Ökosystem und unseren eigenen Lebensraum - ist der Austausch fossiler durch erneuerbare Rohstoffe unverzichtbar, um die Folgen des Klimawandels zu begrenzen.

Kapitel 1 dieser Arbeit beschäftigt sich mit dieser Problematik und der möglichen Nutzung von Solarenergie zur CO_2-neutralen Synthese von Brennstoffen: Eine Einführung in natürliche und künstliche Photosynthese zeigt deren Parallelen und zugrundeliegende Prozesse auf. Farbstoffbasierte Photoelektrochemische Zellen (DS-PECs) sind vielversprechende Kandidaten zur CO_2-neutralen Herstellung von Brennstoffen auf Solarbasis, deren Effizienz allerdings bisher zur Aufskalierung und kostengünstigen industriellen Fertigung zu gering bleibt. Diese Arbeit beschäftigt sich mit der Aufklärung lichtinduzierter Vorgänge in DS-PECs durch computergestützte Untersuchungen und empfiehlt potenzielle Komponenten mit verbesserten Eigenschaften.

Durch die großen zeitlichen, räumlichen und materiellen Unterschiede innerhalb dieser komplexen Zellen wird eine breite Auswahl von Computermethoden genutzt, um diese Größenordnungen zu überbrücken. **Kapitel 2** gibt einen Überblick über deren theoretische Hintergründe, beginnend bei der Born-Oppenheimer Näherung, über DFT und semi-empirische Methoden, mit deren Hilfe ausgedehnte Simulationen von DS-PEC Komponenten möglich werden, zu nicht-adiabatischen

Moleküldynamiksimulationen wie Ehrenfestdynamik und semiklassischer AO-MO Propagation, welche Simulationen lichtinduzierter Prozesse in Echtzeit erlauben.

Verbesserungen von DS-PECs sind nur möglich, wenn die zugrunde liegenden Prozesse aufgeklärt und verstanden sind. Ein wichtiger Schritt innerhalb natürlicher sowie künstlicher Photosynthese ist die lichtinduzierte Ladungstrennung, für die in zunehmenden Maß Hinweise darauf hindeuten, dass in diesem ultraschnellen Prozess Resonanzen zwischen den Frequenzen spezifischer nuklearer Schwingungen und der kohärenten Überlagerung von exzitonischem und ladungsgetrenntem Elektronenzustand, sogenannter vibronischer Kopplung, involviert sind. Um diese Effekte zu entwirren und zu verstehen, wird die kohärente lichtinduzierte Ladungstrennung in einem Pseudo-Basenpaar Modellsystem in **Kapitel 3** untersucht, wobei sich zeigt, dass die N-H Streckschwingungen zur Elektronenbewegung koppeln und Populationsübertragung vom exzitonischem zum ladungsgetrennten Zustand vorantreiben. Durch Isotopenaustausch von H zu D werden die Frequenzen dieser Schwingung verschoben, was allerdings nicht zum Unterdrücken des kohärenten Ladungstransfers führt, aber zur Änderung der Elektronenoszillationen, was Resonanzen mit zusätzlichen Molekülschwingungen erlaubt, die daher ebenso zum Prozess koppeln. Zusätzlich ist dynamische Symmetriebrechung für kohärenten Ladungstransfer nötig, während gemeinsame Elektronen- und Kernrotationsbewegung Austausch von Drehimpuls zwischen den beiden suggeriert.

Die lichtinduzierte Elektroneninjektion von einem angeregten Farbstoffmolekül auf NDI Basis in eine TiO_2 Elektrode inklusive expliziter Lösungsmittelmoleküle wird in **Kapitel 4** untersucht. Um solch herausfordernde Systeme simulieren zu können, wird eine quanten-klassische, semiempirische Methode genutzt, welche Kernbewegungen mittels DFTB bestimmt und diese mit einer AO-MO Quantenpropagation von angeregtem Elektron und Elektronenloch auf Basis eines erweiterten Hückel Hamiltonoperators kombiniert. Der Einfluss der Kernbewegungen, Konformations- und Trajektorienmittelung sowie explizite

Solvatation wird geklärt: Kernbewegung und Mittelung von Konformationen und Trajektorien sind nach diesen Ergebnissen notwendig, um den Injektionsprozess zufriedenstellend zu beschreiben, während explizite Solvatation wichtig für die korrekte Konformationsraumerhebung ist. Farbmoleküle auf NDI-Basis mit drei unterschiedlichen Ankergruppen werden, diese Erkenntnisse nutzend, in Bezug zu deren Injektionseigenschaften bewertet, wobei das NDI-Molekül mit Brenzkatechin als Anker am vielversprechendsten scheint.

Kapitel 5 beschäftigt sich mit der Oxidation von Wasser zu elementarem Sauerstoff und Protonen durch Rutheniumhaltige Wasseroxidationskatalysatoren. Gründliche computergestützte Untersuchungen des Katalysezyklus – inklusive Analyse der freien Enthalpien und des bevorzugten Reaktionsmechanismus - mit unterschiedlichen Funktionalen und dem semiempirischen GFN-xTB zeigen, dass alle untersuchten Methoden den experimentellen Reaktionsmechanismus vorhersagen, die freien Enthalpien jedoch stark von diesen abhängig sind. Obwohl das B3LYP Funktional am zuverlässigsten scheint, limitieren hohe Kosten dessen Anwendbarkeit. Aus diesem Grund wird ein effizienter Workflow, bestehend aus Geometrien und Frequenzen bestimmt durch GFN-xTB und Energien mit dem hybriden B3LYP Funktional, entwickelt und getestet, um freie Enthalpien entlang des Katalysezyklus zu bestimmen. Diese Kombination ergibt Werte, die gut mit B3LYP errechneten, aber auch mit experimentellen Redoxpotentialen übereinstimmen, bei einer Verringerung der Rechenkosten um zwei Größenordnungen. Diese Beschleunigung macht computergestützte Voraussagen von Oxidationspotentialen oder längere Moleküldynamiken mit expliziten Lösungsmittelmolekülen durchführbar.

Die Problematik von Rückübertragung des voneinander getrennten Elektrons und Elektronenlochs, was Rekombination begünstigt und dadurch die Effizienz senkt, ist das Thema des **6. Kapitels**. Um dieses Problem anzugehen, werden eine Reihe von ladungstrennenden Farbstoffen mit Donator-π-Akzeptor Struktur mit Polyphenyldonator, Fluorenbrücke und Perylenmonoimidakzeptor, auf die Effizienz

derer räumlichen Ladungstrennung untersucht, welche Rücktransfer unterdrückt. Donatoren aus Triphenylamin (TPA) ergeben dabei eine größere räumliche Trennung der Ladungen als aus Diphenylamin (DPA). Einfügen eines zusätzlichen Fluorens in der π-Brücke führt auch zu besserer Ladungstrennung, wobei ein drittes Fluoren die Effizienz nicht weiter steigert. Ein besserer Transfer des Elektronenlochs kann auch durch Entkopplung der Komponenten durch Konjugationsunterbrechung mit Hilfe von sterisch anspruchsvollen Methylgruppen erreicht werden, wobei Methylierung des Fluorens und dadurch Entkopplung aller drei Komponenten die deutlichste Verbesserung im Vergleich zum planaren Molekül darstellt. Die Erkenntnisse dieser Untersuchungen werden dann zur *in silico* Optimierung der ladungstrennenden Farbstoffe genutzt, was zu einer eindrucksvollen Steigerung der Elektronenlochübertragung führt.

Zum Abschluss der Arbeit gibt **Kapitel 7** einen Über- und Ausblick, in welchem Ergebnisse und Methoden der Kapitel zusammengeführt werden und demonstriert wird, dass *in silico* Simulationen von lichtinduzierten Prozessen in Photoanodensystemen inklusive Elektrode, Farbstoff und Wasseroxidationskatalysator in Reichweite scheinen. Zusammenfassend können computergestützte Simulationen wertvolle Einblicke in fundamentale, lichtinduzierte Prozesse geben und zur Evaluierung einer großen Anzahl potenzieller molekularer Komponenten, sowie Optimierung derer Eigenschaften und Schnittstellen in einer DS-PEC genutzt werden, um ohne aufwändige synthetische Darstellung experimentelle Forschung anzuleiten.

List of Publications

Main Publications in this Thesis:

1. **Jan Paul Menzel**, Huub J.M. de Groot, Francesco Buda: "Photoinduced Electron Transfer in Donor-Acceptor Complexes: Isotope Effect and Dynamic Symmetry Breaking", *Journal of Physical Chemistry Letters,* **2019**, *10*, 6504-6511 **(Chapter 3 of this Thesis)**

2. **Jan Paul Menzel**, Anastasios Papadopoulos, Jelena Belić, Huub J.M. de Groot, Lucas Visscher, Francesco Buda: "Photoinduced Electron Injection in a Fully Solvated Dye-Sensitized Photoanode: A Dynamical Semi-Empirical Study", *Journal of Physical Chemistry C*, **2020**, *124*, 27965-27976 **(Chapter 4 of this Thesis)**

3. **Jan Paul Menzel**, Martijn Kloppenburg, Jelena Belić, Huub J.M. de Groot, Lucas Visscher, Francesco Buda: "Efficient Workflow for the Investigation of the Catalytic Cycle of a Water Oxidation Catalyst: Combining GFN-xTB and Density Functional Theory", *Journal of Computational Chemistry*, **2021**, *42*, 1885-1894 **(Chapter 5 of this Thesis)**

4. Tijmen M.A. Bakker, **Jan Paul Menzel**, Bas Vreugdenhil, Tessel Bouwens, Simon Mathew, Francesco Buda, Joost N.H. Reek: "Increased Photocurrent by Improving the Donating Properties of the Anchoring Group in P-Type Dye Sensitized Solar Cells", *to be submitted* **(Part of Chapter 6 of this Thesis)**

5. **Jan Paul Menzel**, Yorrick Boeije, Tijmen M.A. Bakker, Jelena Belić, Huub J.M. de Groot, Lucas Visscher, Joost N.H. Reek, Francesco Buda: "In Silico Optimization of Charge Separating Dyes", *to be submitted* **(Part of Chapter 6 of this Thesis)**

6. **Jan Paul Menzel**, Justina Moss, Jelena Belić, Huub J.M. de Groot, Lucas Visscher, Francesco Buda, *in preparation* **(Part of Chapter 7 of this Thesis)**

Publications not included in this Thesis:

1. Helen Chadwick, Han Guo, Ana Gutiérrez-González, **Jan Paul Menzel**, Bret Jackson, Rainer D. Beck: "Methane Dissociation on the Steps and Terraces of Pt(211) Resolved by Quantum State and Impact Site", *Journal of Chemical Physics*, **2018**, *148*, 014701

2. Han Guo, **Jan Paul Menzel**, Bret Jackson: "Quantum Dynamics Studies of the Dissociative Chemisorption of CH4 on the Steps and Terraces of Ni(211)", *Journal of Chemical Physics*, **2018**, *149*, 244704

3. Jelena Belić, Bas van Beek, **Jan Paul Menzel**, Francesco Buda, Lucas Visscher: "Systematic Computational Design and Optimization of Light Absorbing Dyes", *Journal of Physical Chemistry A*, **2020**, *124*, 6380-6388

4. Jelena Belić, Arno Förster, **Jan Paul Menzel**, Francesco Buda, Lucas Visscher: "Automated Assessment of Redox Potentials for Dyes in Dye-Sensitized Photoelectrochemical Cells", *Phys. Chem. Chem. Phys*, **2022**, *24*, 197-210

5. Michael S. Meijer, **Jan Paul Menzel**, Matthijs Hakkenes, Francesco Buda, Anne Goetz, Roy van Duijn, Maxime A. Siegler, Sylvestre Bonnet, *in preparation*

Curriculum Vitae

Jan Paul Menzel was born on the 31st of January 1992 in the federal city of Bonn (Germany), founded by the Romans on the bank of the river Rhine. Jan Paul grew up with his sister and brother in the part of Bonn that lies on the left bank of the river, where he also went to school at the *Carl-von-Ossietzky Gymnasium* from 2002-2011. After obtaining his *Abitur* with specialization in mathematics and chemistry, he decided to pursue a bachelor's degree in chemistry (2011-2014) in Jena, Thuringia, moving 400 km east over the old inner German border. While living there required some cultural adjustments he soon found fellow chemistry students that quickly became friends and had three wonderful years at the town on the Saale river. While Jan Paul imagined how wonderful chemistry could be without having to worry about yield, he first came into contact with theoretical chemistry. After spending a 5-months ERASMUS period at the NTNU (2013) in Trondheim, Norway, he performed his Bachelor Thesis (Detection and Classification of mycobacteria using Lab-on-Chip SERS) under the supervision of Anna Mühlig, Dr. Dana Cialla-May and Prof. Jürgen Popp in 2014.

Following his Bachelor, Jan Paul decided to leave Germany for the Netherlands to pursue a master's degree in physical chemistry (2015-2017). He furthered his interest in theory and computation through several courses, finalizing his studies with his Thesis (Real time Simulations of Photoinduced Charge Transfer in Molecular Complexes) under guidance of Dr. Francesco Buda and Prof. Huub de Groot. During his master he also went to the University of Massachusetts in Amherst, USA for half a year in 2016 to perform simulations on stepped metal surfaces under supervision of Prof. Bret Jackson and Prof. Geert-Jan Kroes. He obtained his master's degree *cum laude* in April of 2017.

Jan Paul then continued his studies of photoinduced processes using computational tools with Dr. Francesco Buda and Prof. Huub de Groot, culminating in this doctoral thesis (2017-2022). During this time, he supervised first year *Biopharmaceutical*

Science students at organic synthesis labs, he prepared exercises and taught and supervised second year *Molecular Science and Technology* students in theoretical chemistry exercise classes. He tutored a total of 4 *Leren Onderzoeken* students, 3 HRSMC research internship students and 5 students performing their master thesis research under his supervision.

Jan Paul presented his research work at a variety of national and international conferences with poster presentations at the PPES conference in Pisa (2018), HRSMC symposium (Leiden, 2018), CTC symposium (Amsterdam, 2019), ISTCP (Tromsø, Norway 2019), Reedijk Symposium (Leiden, 2019), Solar to Products Symposium (Eindhoven, 2019), CHAINS (Veldhoven, 2019, 2021), and ISF Conference (Online, 2021). At this conference he won a poster prize. Oral presentations were given at Han-sur-Lesse Winterschool (2018), CHAINS (Veldhoven/online, 2018, 2020), the HRSMC symposium (Amsterdam, 2019), Physics at Veldhoven (online, 2021) and the Dutch Photochemistry Days (2021).

Acknowledgements

With this manuscript, over four years of research come to an end. Over the course of this period (and also before), there have been many people involved in my work and life, who enabled me to reach my achievements and who I would dearly like to thank.

First and most of all, I am very much indebted to my supervisor and copromotor **Francesco Buda**. I want to thank you **Franco**, for an incredible experience. I cannot thank you enough for the trust you put in me, the understanding you have provided and the persistent kindness you show throughout all possible and impossible situations. Thank you for expertise and guidance, for helping me grow as a scientist. You really are the best mentor one can wish for.

I also owe gratitude to my promotor **Huub de Groot** for the great opportunity to perform research at his BPOC/SSNMR group in Leiden. Thank you for your great insight, persistence to put everything on a sound scientific basis and support during this time. Thank you also for the many, sometimes enthusiastic but always productive discussions in both science and other subjects.

I would also like to thank **Jelena**, **Tijmen** and **Lucas Visscher** for fruitful collaborations and scientific discussions during our many meetings.

During my time as a PhD candidate, I had the luck to be able to supervise many talented students: **Stan**, **Klaas**, **Anne**, **Martijn**, **Samantha**, **Yorrick**, **Matthijs** and **Justina**, thank you for your hard work and all the best for your future careers in Science, Business and Education!

A special thanks also to my fellow computational PhD colleagues, **Jessica**, **Yang**, **Xinmeng**, **Dario**, **Rianne**, **Titus** and (now as a PhD student) **Matthijs**, for a great

working atmosphere, helpful discussions and out-of-work social life. **Liesbeth**, thank you very much for all the help and hard work you put in to make sure that everyone feels part of the group and can make the most of the time given to us here. To the many people of the BPOC/SSNMR group: **Alia, Agur, Anjali, Fons, Karthick, Adriano, Emanuela, Remco, Dieuwertje, Maithili, Rubin, Vidya, Zhongwu, Fatemeh, Laura, Faezeh, Kiran, Rico, Lolita, Tirong, Chuang,** thank you for a wonderful time, all the lunches together, the coffees drank and (scientific) discussions. I wish you all the best.

Gabi and **Raimund** I want to thank for making it possible and even pleasant for me to perform research on parts of this thesis during my Covid 19-induced exile in the spring of 2020. **Celina** and **Tilman**, thank you for, among many other things, a live long companionship and enthusiastic discussions at the dinner table.

My Parents for their love and support in all the things I did and do, for motivating me when things don't work out as wanted and accepting my stubbornness. I am grateful for all the opportunities you have given me. I cannot thank you enough.

Finally, **Anna**, for all and everything.